Continental Convergence: Length-Scales, Aspect Ratios, and Styles of Crustal Deformation

by

Susan Ellis

A thesis submitted
in partial fulfillment of the requirements
for the Degree of Doctor of Philosophy

at

Department of Oceanography
Dalhousie University
Halifax, Nova Scotia
April, 1995

ISBN 0-612-05266-4

Name SUSAN ELLIS

Dissertation Abstracts International is arranged by broad, general subject categories Please select the one subject which most nearly describes the content of your dissertation Enter the corresponding four-digit code in the spaces provided

Geophysics
SUBJECT TERM

0373
SUBJECT CODE

U·M·I

Subject Categories

THE HUMANITIES AND SOCIAL SCIENCES

COMMUNICATIONS AND THE ARTS

Architecture 0729
Art History 0377
Cinema 0900
Dance 0378
Fine Arts 0357
Information Science 0723
Journalism 0391
Library Science 0399
Mass Communications 0708
Music 0413
Speech Communication 0459
Theater 0465

EDUCATION

General 0515
Administration 0514
Adult and Continuing 0516
Agricultural 0517
[illegible]
[illegible]
[illegible]
[illegible]
[illegible]
Early Childhood 0518
Elementary 0524
Finance 0277
Guidance and Counseling 0519
Health 0680
Higher 0745
History of 0520
Home Economics 0278
Industrial 0521
Language and Literature 0279
Mathematics 0280
Music 0522
Philosophy of 0998
Physical 0523
Psychology 0525
Reading 0535
Religious 0527
Sciences 0714
Secondary 0533
Social Sciences 0534
Sociology of 0340
Special 0529
Teacher Training 0530
Technology 0710
Tests and Measurements 0288
Vocational 0747

LANGUAGE, LITERATURE AND LINGUISTICS

Language
- General 0679
- Ancient 0289
- Linguistics 0290
- Modern 0291

Literature
- General 0401
- Classical 0294
- Comparative 0295
- Medieval 0297
- Modern 0298
- African 0316
- American 0591
- Asian 0305
- Canadian (English) 0352
- Canadian (French) 0355
- English 0593
- Germanic 0311
- Latin American 0312
- Middle Eastern 0315
- Romance 0313
- Slavic and East European 0314

PHILOSOPHY, RELIGION AND THEOLOGY

Philosophy 0422
Religion
- General 0318
- Biblical Studies 0321
- Clergy 0319
- History of 0320
- Philosophy of 0322

Theology 0469

SOCIAL SCIENCES

American Studies 0323
Anthropology
- Archaeology 0324
- Cultural 0326
- Physical 0327

Business Administration
- General 0310
- Accounting 0272
- Banking 0770
- Management 0454
- Marketing 0338

Canadian Studies 0385
Economics
- General 0501
- [illegible]
- [illegible]
- History 0509
- Labor 0510
- Theory 0511

Folklore 0358
Geography 0366
Gerontology 0351
History
- General 0578
- Ancient 0579
- Medieval 0581
- Modern 0582
- Black 0328
- African 0331
- Asia, Australia and Oceania 0332
- Canadian 0334
- European 0335
- Latin American 0336
- Middle Eastern 0333
- United States 0337

History of Science 0585
Law 0398
Political Science
- General 0615
- International Law and Relations 0616
- Public Administration 0617

Recreation 0814
Social Work 0452
Sociology
- General 0626
- Criminology and Penology 0627
- Demography 0938
- Ethnic and Racial Studies 0631
- Individual and Family Studies 0628
- Industrial and Labor Relations 0629
- Public and Social Welfare 0630
- Social Structure and Development 0700
- Theory and Methods 0344

Transportation 0709
Urban and Regional Planning 0999
Women's Studies 0453

THE SCIENCES AND ENGINEERING

BIOLOGICAL SCIENCES

Agriculture
- General 0473
- Agronomy 0285
- Animal Culture and Nutrition 0475
- Animal Pathology 0476
- Food Science and Technology 0359
- Forestry and Wildlife 0478
- Plant Culture 0479
- Plant Pathology 0480
- Plant Physiology 0817
- Range Management 0777
- Wood Technology 0746

Biology
- General 0306
- Anatomy 0287
- Biostatistics 0308
- Botany 0309
- Cell 0379
- Ecology 0329
- Entomology 0353
- Genetics 0369
- Limnology 0793
- Microbiology 0410
- Molecular 0307
- Neuroscience 0317
- Oceanography 0416
- Physiology 0433
- Radiation 0821
- Veterinary Science 0778
- Zoology 0472

Biophysics
- General 0786
- Medical 0760

EARTH SCIENCES

Biogeochemistry 0425
Geochemistry 0996
Geodesy 0370
Geology 0372
Geophysics 0373
Hydrology 0388
Mineralogy 0411
Paleobotany 0345
Paleoecology 0426
Paleontology 0418
Paleozoology 0985
Palynology 0427
Physical Geography 0368
Physical Oceanography 0415

HEALTH AND ENVIRONMENTAL SCIENCES

Environmental Sciences 0768
Health Sciences
- General 0566
- Audiology 0300
- Chemotherapy 0992
- Dentistry 0567
- Education 0350
- Hospital Management 0769
- Human Development 0758
- Immunology 0982
- Medicine and Surgery 0564
- Mental Health 0347
- Nursing 0569
- Nutrition 0570
- Obstetrics and Gynecology 0380
- Occupational Health and Therapy 0354
- Ophthalmology 0381
- Pathology 0571
- Pharmacology 0419
- Pharmacy 0572
- Physical Therapy 0382
- Public Health 0573
- Radiology 0574
- Recreation 0575
- Speech Pathology 0460
- Toxicology 0383

Home Economics 0386

PHYSICAL SCIENCES

Pure Sciences

Chemistry
- General 0485
- Agricultural 0749
- Analytical 0486
- Biochemistry 0487
- Inorganic 0488
- Nuclear 0738
- Organic 0490
- Pharmaceutical 0491
- Physical 0494
- Polymer 0495
- Radiation 0754

Mathematics 0405
Physics
- General 0605
- Acoustics 0986
- Astronomy and Astrophysics 0606
- Atmospheric Science 0608
- Atomic 0748
- Electronics and Electricity 0607
- Elementary Particles and High Energy 0798
- Fluid and Plasma 0759
- Molecular 0609
- Nuclear 0610
- Optics 0752
- Radiation 0756
- Solid State 0611

Statistics 0463

Applied Sciences

Applied Mechanics 0346
Computer Science 0984

Engineering
- General 0537
- Aerospace 0538
- [illegible]
- Marine 0547
- Materials Science 0794
- Mechanical 0548
- Metallurgy 0743
- Mining 0551
- Nuclear 0552
- Packaging 0549
- Petroleum 0765
- Sanitary and Municipal 0554
- System Science 0790

Geotechnology 0428
Operations Research 0796
Plastics Technology 0795
Textile Technology 0994

PSYCHOLOGY

General 0621
Behavioral 0384
Clinical 0622
Developmental 0620
Experimental 0623
Industrial 0624
Personality 0625
Physiological 0989
Psychobiology 0349
Psychometrics 0632
Social 0451

to Kirby.

TABLE OF CONTENTS

List of Figures | Page

List of Tables

List of Symbols

α	normal:transcurrent length-scale ratio	Ω	domain of deforming region
Am	Ampferer number	p	pressure
Ar	Argand number	ρ_c	density of crust
B_c	vertically averaged material constant for a power law viscous crust	ρ_m	density of mantle
B_b	vertically averaged material constant for a power law viscous simple shear layer	Pe (ch 2)	Péclet number: tectonic advection vs. surface diffusion
D	lateral extent of (kinematic) indenter	Pe (ch 6)	Péclet number: tectonic advection vs. thermal diffusion
$\dot{E}$	second invariant of the strain-rate tensor	P_0	pressure at depth of compensation
$\dot{\varepsilon}_0$	reference strain-rate	Q	creep activation energy
$\dot{\varepsilon}_{ij}$	strain-rate tensor	r	obliquity of convergence
f	crustal thickening factor	Σ	integrated sectional thickening
h	thickness of basal layer	ϕ	isostatic amplification factor
J_{2D}	second invariant of the stress tensor	ϕ_P	flux of material entering pro-side of convergent zone
K_H	Surface process diffusivity	ϕ_S	subducted crustal flux
L	Depth of compensation	t'	dimensionless time (= normalized convergence)
ΔM	quantitative integral of thickness difference	τ_{ij}	deviatoric stress tensor
$\Delta\dot{M}$	quantitative integral of thickening difference	τ_{max}	maximum shear stress
n	power law exponent	T^b_{xz}	basal shear traction
${}^m t_{RES}$	mantle residence time	μ_c	crustal viscosity
${}^c t_{RES}$	crustal residence time	w	deflection of Moho

S	crustal thickness
S_0	initial crustal thickness
T	temperature
μ_b	basal viscosity
μ_{eff}	effective viscosity
$\bar{u}$	crustal velocity
u_0	imposed boundary velocity
u_m	imposed velocity at the top of the mantle lithosphere
V_P	material velocity of pro-lithosphere
V_S	velocity of singularity
w_f	flexural perturbation on local isostatic compensation
λ_{NB}	normal length-scale for basally-driven deformation
λ_{NS}	normal length-scale for side-driven deformation
λ_{NO}	normal length-scale for observed deformation
$v\lambda$	velocity length-scale
$t\lambda$	thickening length-scale
$s\lambda$	strain-rate length-scale
λ_m	basal detachment length-scale
λ_N	crustal response length-scale for normal convergence
λ_T	crustal response length-scale for transcurrent motion

List of Numbered Equations | Page

ABSTRACT

The processes involved when continents collide can often only be inferred from studies of rocks exposed at the surface of the Earth. To determine the forces which cause the deformation seen at the surface, we can use analytical and numerical models, where the behaviour of the lithosphere is simplified into a set of end-member styles.

In this thesis, two possible end-member styles for convergent plate boundaries are investigated using simple analytical and numerical models, which represent the crust and/or lithosphere as a non-linear viscous thin-sheet. The thin-sheet approximation reduces the complexity of three-dimensional lithospheric behaviour to two (planform) dimensions. Use of the thin-sheet approximation restricts the study to large-scale plate boundary interactions.

Using the models, differences for the length-scale of deformation seen at the surface are predicted for the two contrasting styles of forcing: (a) where the lithosphere deforms as one layer, and is indented from the side by a convergent plate of finite extent; and (b) where the crust detaches from the underlying mantle lithosphere, which subducts at the plate boundary. Style (a) is referred to as the side-driven model, and has already been used to explain large-scale continental convergent settings, such as the India-Eurasia collision. Style (b) is referred to as the basally-driven model, and has not previously been investigated using a thin-sheet tectonic model.

The first part of this thesis develops analytical and numerical models for the basally-driven model, and shows that when crustal deformation is controlled by detachment and subduction of mantle lithosphere, the scale of the deformation can be parameterized in terms of a new scaling number, the Ampferer number. In contrast, length-scale predictions for the side-driven model depend on the lateral scale of the indenter. Predicted length-scale ratios for convergent vs. strike-slip settings are different for the two cases. A case with a combination of basal forcing and indenter mechanics is also investigated, and deforms over length-scales which depend on the strongest forcing parameter.

The predictions of the two end-member styles are tested in a comparison with natural examples in the latter half of the thesis. On the basis of this comparison, neither end-member can be rejected as a candidate for deformation style. A further investigation for large amounts of convergence, indicates that a combination of indentation and basal forcing may best represent large-scale continental convergence. However, the large uncertainties in the model-data comparisons suggest that length-scale analyses by themselves cannot be used to distinguish first-order controls on mountain building, and that further direct measurements of deep lithospheric processes are required.

ACKNOWLEDGEMENTS

The work represented by this thesis has benefited greatly from the exacting and enthusiastic supervision of Chris Beaumont. I thank him for his encouragement and guidance during the long process of learning to become a scientist. I have been fortunate in having an additional mentor, Philippe Fullsack, who is also responsible for developing the code which, in modified form, is used throughout this thesis. Discussions with Owen Hertzman, Becky Jamieson, Peter Molnar, Shimon Wdowinski and Sean Willett helped to improve the manuscript.

As well as Chris and Philippe, I would like to thank all the other people who are, or have been, members of the Dalhousie Geodynamics Group in the last few years: Jean Braun, Kevin Brown, Alan Gilchrist, Juliet Hamilton, Dave Johnson, Henk Kooi, Paula Waschbusch, and Sean Willett. Their friendship, advice, and encouragement have been much appreciated over the years. Many thanks as well to all my friends at the Departments of Oceanography and Earth Sciences.

In addition to my Dalhousie colleagues, I would like to thank the Early Music community, who have allowed me to sometimes forget about my thesis for a night or two. I would also like to express my appreciation to the staff and doctors of the Victoria General Hospital, Halifax, for their care which allowed me to get back to work after a prolonged illness.

I owe a big debt of gratitude to my 'life support system': my adopted family in Cape Breton, the MacLeods and Howies, who have shown me a true Nova Scotian welcome; my sister and grandmother; and my parents, whose encouragement and support for the past 30 years has been unfailing, and who can finally say that their daughter has finished her PhD (!). Lastly, to Kirby, who has made it all seem worthwhile.

My study at Dalhousie University was supported by a Canadian Commonwealth Scholarship and a Dalhousie Fellowship.

Chapter One

INTRODUCTION

§1.1 Preamble

".... les structures qui composent un édifice tectonique ne sont pas tout : il y a le mouvement qui anima, qui anime encore ces choses, car l'histoire continue et nous vivons, sans privilège d'aucune sorte, à un instant quelconque de cette grande affaire."

".... the structures that compose a tectonic edifice are not all there is to it; there is a movement that has vitalised them and that still does so, because history continues and we live, without any privilege of any sort, at an arbitrary moment of this grand affair."

(Argand, La Tectonique de l'Asie, 1924, p.172)

When Emile Argand presented his classic synthesis of the tectonic evolution of Eurasia in 1922, the exposed rocks and structures of mountain belts clearly provided the evidence that the outer layers of the Earth were the product of a long history of movement and deformation. Plate tectonics theory has since helped to explain orogenesis (mountain building) in terms of the processes occurring at convergent lithospheric plate boundaries (Wilson, 1965). Faulting, folding and thrusting are thought to occur whenever converging lithospheric plates experience net shortening and compression. This is typically the case for convergence of buoyant continental lithospheric plates, but may also occur at oceanic-continental active margins (e.g. the Andes).

Despite the advances in our understanding of orogenesis since 1922, plate tectonics theory by itself cannot provide a complete explanation for the dynamic interactions which lead to such impressive, large-scale movements of the lithosphere. Processes for which we have only an incomplete understanding include: the mechanisms by which compressive stress at plate boundaries is transmitted (i.e. what are the boundary conditions of the system); the role of rheology (the deformation of material in response to applied stresses); the interaction between temperature, pressure and deformation in the lithosphere; and how an orogenic system evolves for a given set of initial and boundary conditions.

Deformation of the lithosphere progresses over timescales much longer than the duration of a human life. For this reason, many of the processes of orogenesis cannot be directly measured as they occur, but must be inferred from the past record contained in the structure of rocks exhumed at the surface, and imaged using geophysical techniques. In addition, hypotheses can be tested by utilizing models of the crust or lithosphere. The results from forward modelling are compared with observations in order to refine our ideas about the deformation of the Earth's crust and mantle.

This study makes use of a simple geodynamic model (containing the 'thin-sheet' approximations) in order to investigate the processes causing deformation at convergent plate boundaries. (Similar processes which occur as intra-plate convergence are also investigated). Before describing the model in detail, I summarize in the following sections the motivation for my approach.

§1.2 Deformation at Convergent Margins: Background Setting, Theories and Observations

The assumption that lithospheric plates act as essentially rigid bodies is successful in explaining the geometry and kinematics of the plates at the largest scale, but fails to adequately account for the deformation at convergent plate boundaries. A map showing the extent of tertiary and recent deformation at convergent plate boundaries (figure 1) illustrates that in many cases, especially those involving buoyant continental crust, deformation extends for hundreds of kilometres into the plates, and certainly cannot be approximated by the collision of rigid bodies (England and Jackson, 1989). A particular example is the India-Asia collision zone, which has a width of 2000 km about the suture zone marking the contact between India and Asia.

Sites of Orogenesis

The type of processes operating at a convergent plate boundary depend on the relative buoyancy of the respective lithospheres compared to the underlying asthenosphere, i.e. the gravitational stability of the lithospheric plates. Convergence involving oceanic lithosphere, with typically thin (~6km) crust, leads to subduction, and generally the coldest (i.e. most dense) lithospheric plate is consumed at the trench. Deformation in the overlying plate may be compressional or extensional, depending on whether the net convergence rate is exceeded by the rate of slab subduction (*retreating* plate boundaries) or vice-versa (*advancing* subduction boundaries), as defined by Royden (1993a).

Typically, convergence of two oceanic plates creates a small-scale (< 100 km wide) topographic expression, due to the off-scraping of oceanic sediments at the trench to form an accretionary wedge, and the development of a volcanic arc above the down-going slab. If extension is present in the upper plate, marginal basins (e.g. the Aleutian basin) may form behind the arc. Similar types of basin may also be present for cases of subduction along continental margins (e.g. the western edge of the Pacific), where the plate boundary may also be classified as retreating (Doglioni, 1992).

Figure 1: Map showing the Tertiary and Recent sub-aerial extent of mountain ranges and island arcs (shaded). Figure modified from Bott, 1982.

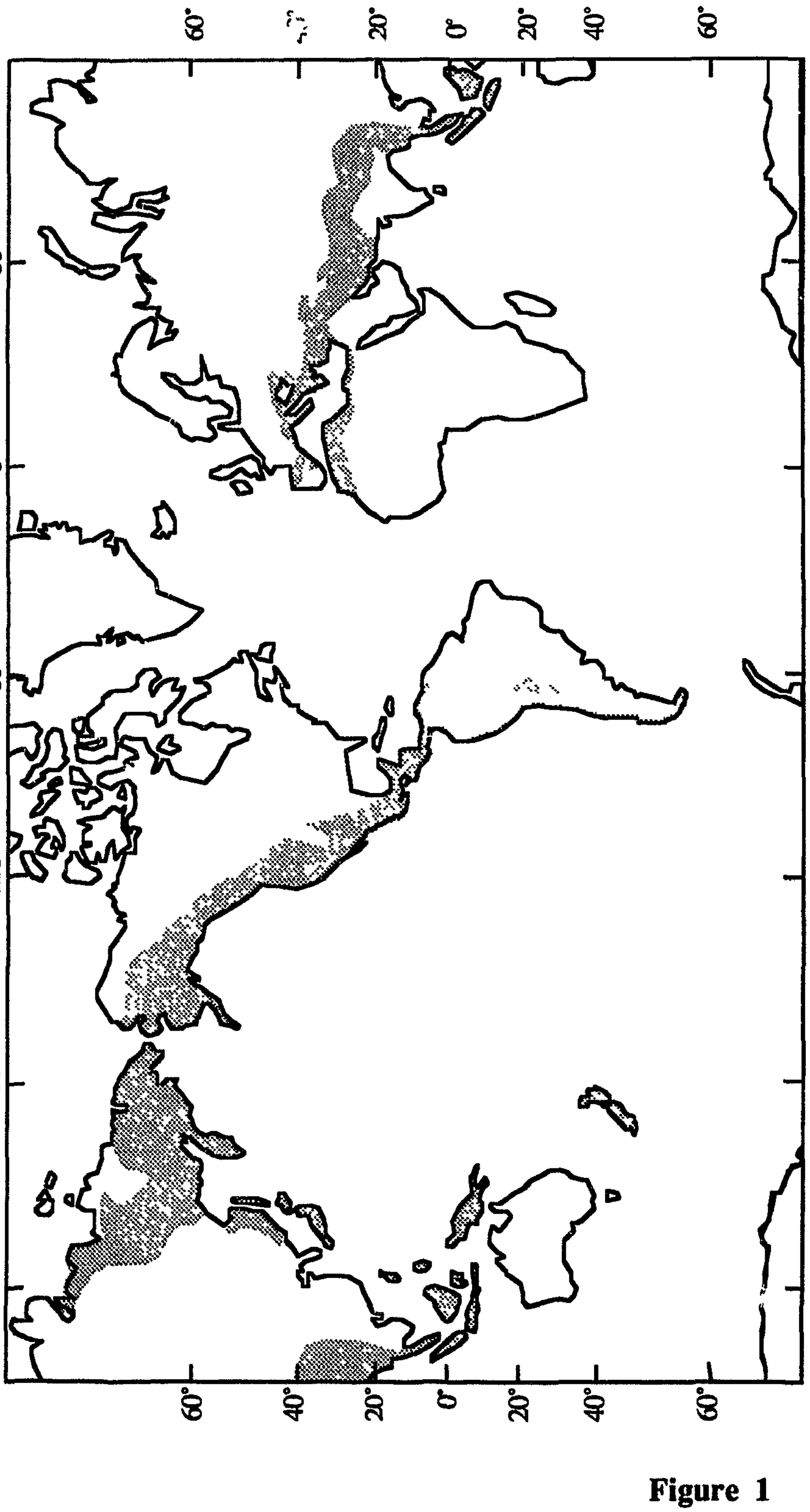

Figure 1

Significant orogenesis is only likely at (a) advancing subduction boundaries where the upper lithospheric plate is continental; and (b) continent-continent convergent boundaries. Both (a) and (b) are the subject of this study. For significant durations of convergence, the continental lithospheric plates in these cases may exhibit considerable thickening and deformation. This may occur by processes such as (a) thin-skinned folds and thrusts along a shallow detachment surface, and (b) thick-skinned deformation of the crust and/or mantle lithosphere.

Models of Orogenesis

The mechanics and topographic expression of accretionary wedges and thin-skinned fold and thrust belts have been successfully modelled using the static analysis of a self-similar critical wedge (Chapple, 1978; Stockmal, 1983; Davis et al., 1983; Dahlen, 1984; Dahlen and Suppe, 1988, Platt et al., 1986, and others). Most of these models assume a Coulomb (frictional) rheology with a basal shear stress everywhere on the verge of frictional yield. The self-similar topographic expression predicted by critical wedge theory is analogous to the shape created when sand is pushed along a slope by a bulldozer. Most critical wedge studies assume an indenter of infinite vertical extent above the basal decollement. However, when the indenter has a finite height, or is replaced by a corresponding boundary condition at the base of the model, two oppositely verging wedges are produced (Malavieille, 1984; Koons, 1990; Willett et al., 1993).

Static wedge analysis is only useful for predicting the geometry of systems which have attained, or are close to, steady state (i.e. for which there is no net change in the geometry of the orogen) (Barr and Dahlen, 1989; Dahlen and Barr, 1989). The necessary assumptions of self-similarity, and static critical topography, precludes a mechanical analysis of the development from small to large-scale crustal thickening, and subsequent variations in the state of the orogen (whether it is in a constructive, steady-state or destructive phase) (Jamieson and Beaumont, 1988). These limitations have motivated the development of dynamic cross-sectional models of the crust, such as numerical models which employ the plane-strain approximation. Willett (1992) and Willett et al. (1993) use the assumption of an incompressible plastic-viscous crust, with prescribed velocity boundary conditions, to explore the behaviour of compressional orogens. Their basic assumption is that deformation is driven by the detachment and subduction of underlying mantle lithosphere at the site of convergence. Although simple, the velocity boundary conditions can be shown to produce several features that are strikingly similar to observations from structural geology, exhumation patterns, and deep seismic reflector patterns (Beaumont and Quinlan, 1994).

Cross-sectional models of the crust, such as that discussed above, preclude the investigation of oblique convergence and variations in the shape of plate boundary zones. An alternative set of two-dimensional models have been developed to investigate these cases, using the thin-sheet approximations (England and McKenzie, 1982; Vilotte et al., 1982; Bird and Piper, 1980), which neglect cross-sectional shear stress. The lithosphere may generally be treated as a thin-sheet provided the deformation being investigated takes place on a large planform scale, in comparison to the thickness of the lithosphere. Thin-sheet models have primarily been used to investigate the effects of indenters of finite lateral extent (e.g. whether India is indenting Asia (England and Houseman, 1986)), and also to determine approximate length-scale relationships between indenter shape, obliquity of the convergence, and the rheology of the lithosphere (England et al., 1985). These investigations generally prescribe velocity boundary conditions along the sides of the model domain, and assume that the crust and mantle do not deform independently.

More recently, fully three-dimensional numerical models of the crust have been developed (Braun, 1993). These models promise to unite the concepts investigated in cross-sectional and planform models of the crust and lithosphere. However, one- and two-dimensional approximations are still be useful in providing a first-order intuitive grasp of the processes of orogenesis.

Forces Driving Deformation

In order to develop a set of valid boundary conditions for models of orogenesis, the forces that drive deformation at convergent plate boundaries must be specified. They will be a combination of: (a) forcing at the sides of the deforming region, caused by exterior body forces (crudely, 'ridge push' and 'slab pull' forces, which are caused by gravity acting on variations in density (Forsyth and Uyeda, 1975)); (b) forces at the bottom of the deforming region, due to the movement of lower layers; and (c) body forces such as the effect of topographic loads (excess crustal thickness).

The mechanical models of convergence discussed above have expressed a dichotomy in postulated driving mechanisms. Thin-sheet models have mostly been used to investigate large-scale deformation using velocity or stress boundary conditions applied to the sides of the modelled region, as illustrated in Table 1, which summarizes some of the thin-sheet studies to date. The implicit assumption is that horizontally transmitted stress (e.g. ridge push or slab pull) drives deformation, and that tractions on the base of the lithosphere are negligible. In contrast, some plane-strain models of the crust assume that continental collision is driven by the detachment and subduction of the underlying mantle lithosphere (Willett et al., 1993). In this instance, the driving mechanism is forcing along the base of the crust or deforming layer. The contrasting assumptions produce different predictions of first-order deformation styles.

Table 1: Summary of Thin-Sheet Tectonic Studies

Authors	*Description of model*	*Boundary conditions*	*areas investigated*
Molnar and Tapponnier (1975); Tapponnier and Molnar (1976)	Planform plane strain model of lithosphere; used rigid dies to indent a rigid-plastic medium	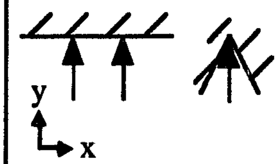	India-Asia collision
Bird and Piper (1980)	Thin sheet model of crust; rigid-plastic upper crust; viscous lower crust	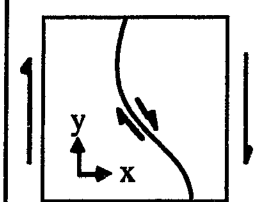	California
England and McKenzie (1982), (1983); England and Houseman (1985), (1986)	Thin sheet model of lithosphere; viscous power-law rheology; side indentation by (kinematic) indenter	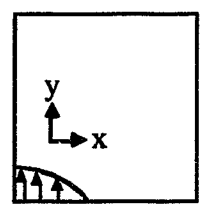	India-Asia collision
England et al. (1985)	Analytical solutions for thin sheet, plane strain cases with sinusoidal boundary conditions	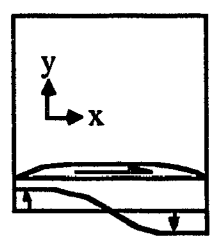	General investigation of strike-slip and convergent deformation
Sonder et al. (1986)	Thin sheet model of lithosphere; strike-slip velocity/ stress boundary conditions	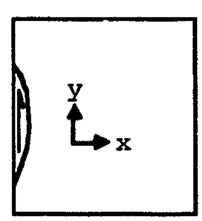	California

Vilotte et al. (1982)	Thin sheet model of lithosphere with (kinematic) indenter	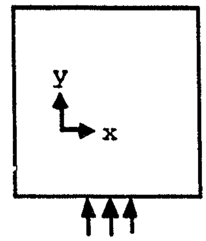	India-Asia collision
Bird and Baumgardner (1984)	Thin sheet model of crust with basal boundary conditions, non-deforming mantle	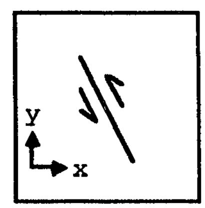	Western US
Bird (1989)	Thin sheet; full 2-sheet solution (crust and mantle)	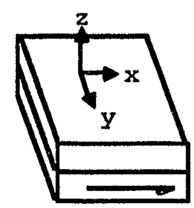	Western US
Wdowinski et al. (1989)	1D thin sheet model of lithosphere with fluid mantle asthenosphere, basal coupling	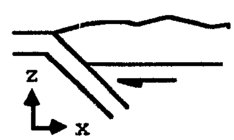	Andes, Aegean
This study	2D thin sheet model of crust with basal coupling to mantle through weak layer; mantle kinematically specified	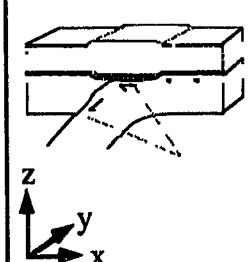	Oblique convergence

§1.3 Motivation for this Study

This study attempts to distinguish which of the two different end-member hypotheses discussed above (that convergent deformation is driven by side or basal forcing) better represents the driving forces causing deformation at convergent plate boundaries. The crustal sheet is isostatically compensated by assuming that the mantle lithosphere acts as an elastic plate. I use a planform thin-sheet model of the crust which is driven by basal forcing. I also investigate cases where side forcing, or a combination of side and basal forcing, is present.

Part of the thesis focusses on finding the range of parameters for which the model is valid, because the use of a traction at the base of the crust is not strictly compatible with the thin-sheet assumptions. I also investigate how the assumptions concerning the behaviour of the mantle lithosphere modify the isostatic balance of the crustal thin-sheet, by comparison with a local compensation mechanism.

I compare the length-scale relationships predicted by the models to various geological examples of previously and currently active orogens. Although the comparisons are primarily conducted using scale analysis, I also use numerical models to investigate some of the features of large-scale orogenesis, such as the effect of crustal thickening on buoyancy-driven forces and crust-mantle coupling.

§1.4 Summary of Thesis Chapters

Following from the general background described in chapter one, I start the second chapter with a brief discussion of possible choices for boundary conditions in geodynamic models of lithospheric convergence. I also discuss the basal boundary conditions used in this study, which use the assumption that crustal deformation is driven by basal forcing from the underlying mantle lithosphere, and then outline the formulation and implementation of the basic model. In chapter three the model is tested by comparing one-dimensional model results with the equivalent problem solved using the plane-strain method. After finding the valid parameter range for the thin-sheet approximation, I discuss the rheological basis for my choice of model parameters, and investigate the effect of these parameters on basic, one-dimensional model behaviour.

The basally-driven thin-sheet model is used to investigate a simple problem of oblique lithospheric convergence in chapter four, and by considering the resulting strain partitioning between normal and transcurrent deformation, demonstrates both analytically and numerically that the side-driven and basally-driven models predict different results. The case with both side and basally-driven deformation is also investigated. The implications of these results are discussed in the subsequent chapter, in which I conduct some simple scale analyses of active convergent margins.

In chapter six, some predictions are made concerning the evolution of length-scales with increased normalized convergence, and compared to the length-scale data from natural examples. The chapter also includes some suggestions for physical plate boundary settings which may correspond to the end-member ideas investigated in the thesis. Chapter seven concludes the thesis, by reviewing some of the length-scale results, and the predicted differences between crustal deformation driven by indentation from the side, vs. detachment and subduction of mantle lithosphere.

Chapter Two

METHOD

§ 2.1 Crust-Mantle Interactions in Continental Convergence

The behaviour of the lithosphere under compression is a consequence of complex interactions between boundary forces, body forces, and the distribution of mechanical strength in the crust and mantle. Geodynamic models reduce this complexity by investigating simple end-member types of lithospheric behaviour. One of the simplest end-member assumptions that may be made when using numerical models of continental convergence, is that the crust and upper mantle deform together in a vertically averaged way, without detachment, and with no shear between them (figure 2(a)). Under this assumption, the crust and mantle deformation length-scales (λ_N, where the subscript N indicates that the length-scale is for deformation normal to the plate boundary, and λ_m, with the subscript denoting 'mantle') are necessarily the same.

In thin-sheet models of the case where crust and mantle lithosphere deform together (figure 2(a)), local compensation is commonly assumed, and the density contrast at the bottom of the lithosphere is neglected so that the effect of mantle thickening is not incorporated in the deformation (England and McKenzie, 1982). When shear stress at the base of the lithosphere is also neglected, the lithosphere is considered to be driven by horizontally transmitted stresses, so that the length-scales are determined by the dimensions of the indenter along-strike (England et al., 1985). If shear stresses from the asthenosphere are assumed to be significant, the length-scales also depend on the strength and style of forcing from the base of the lithosphere (Wdowinski et al., 1989).

Reviews of the rheological stratification of the continental crust and mantle

(Ranalli and Murphy, 1987; Ord and Hobbs, 1989; Carter and Tsenn, 1987) suggest that, for a typical range of geotherms, one or more local strength minima may be present at intermediate depths in the lithosphere. In particular, for a limited range of crustal geotherms and rheologies (Ord and Hobbs, 1989) a local strength minimum will coincide with the base of the crust. The existence of such a 'crustal asthenosphere', or 'asthenolayer' (Lobkovsky and Kerchman, 1991), as a region of low strength or effective viscosity, permits the crust and mantle lithosphere to decouple along this weak detachment layer.

Figure 2(b) illustrates how the crust and mantle may decouple along the weak layer, and deform with different characteristic length-scales, so that $\lambda_N \neq \lambda_m$ (figure 2(b)). In the thin-sheet approximation of this problem either two coupled thin-sheets are used to represent the crust and mantle lithosphere (Bird, 1989), or the velocity field of the lower region is specified (Bird and Baumgardner, 1984).

Figure 2: A diagram depicting possible end-member styles of lithospheric deformation. λ_N is the length-scale of deformation in the crust normal to the direction of convergence, and λ_m is the length-scale of deformation or detachment in the mantle lithosphere. (a) case where the whole lithosphere deforms with no shear between crust and mantle lithosphere, so that $\lambda_N = \lambda_m$; (b) partial detachment between crust and mantle lithosphere such that the mantle contracts with a different length-scale to the crust, $\lambda_N \neq \lambda_m$; (c) subduction of mantle lithosphere, $\lambda_m \to 0$. The lightly shaded regions indicate areas of contraction and deformation. The dark shading in (b) and (c) shows the position of a weak layer between the crust and mantle lithosphere. The style of deformation will depend upon the rheological layering in the lithosphere and the type of mantle deformation. This study explores cases (c) and compares results to previous studies of case (a).

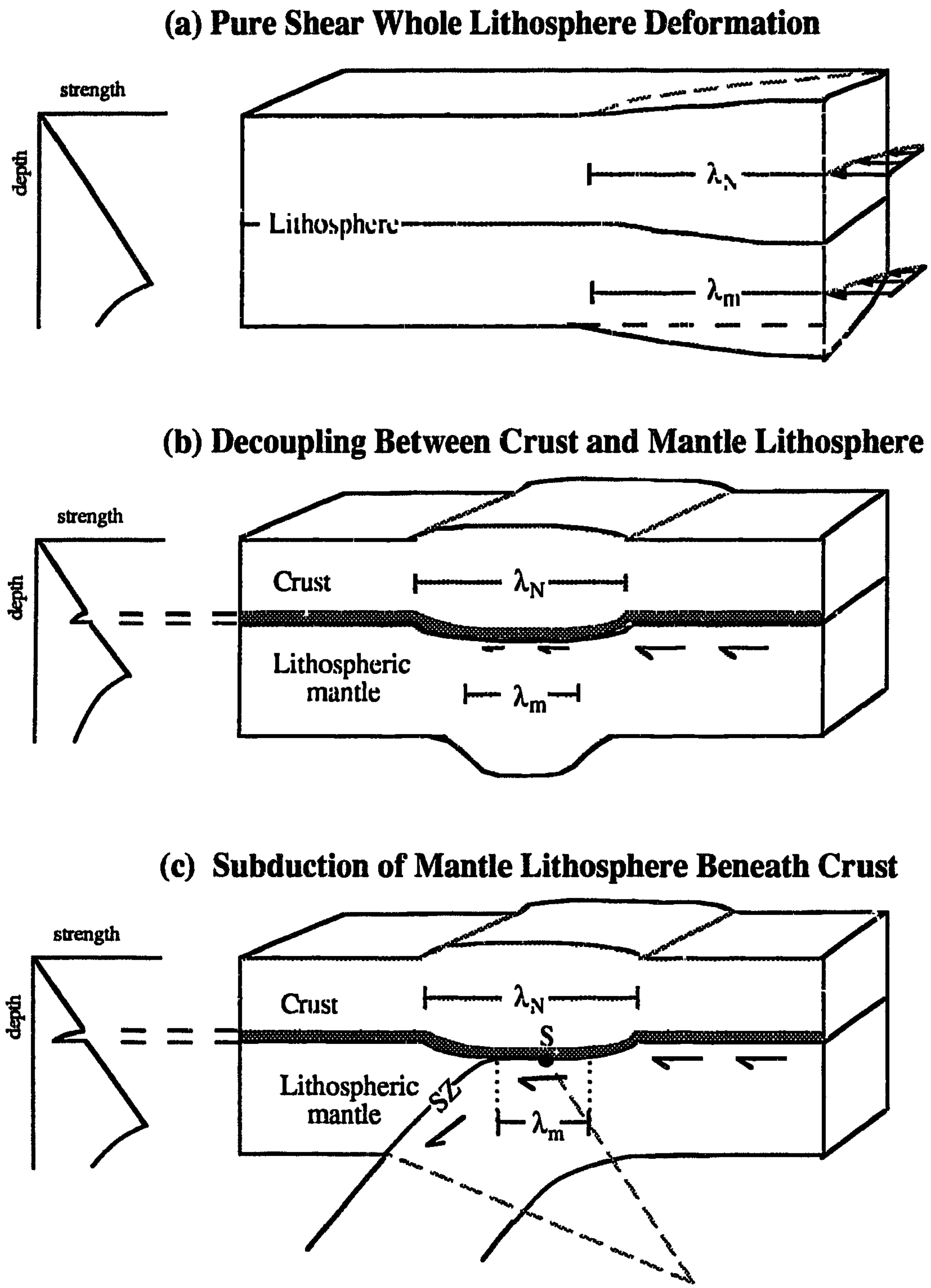
(a) Pure Shear Whole Lithosphere Deformation
strength
depth
λ_N
Lithosphere
λ_m
(b) Decoupling Between Crust and Mantle Lithosphere
strength
depth
Crust
λ_N
Lithospheric mantle
λ_m
(c) Subduction of Mantle Lithosphere Beneath Crust
strength
depth
Crust
λ_N
S
Lithospheric mantle
SZ
λ_m

Figure 2

If the negatively-buoyant mantle lithosphere is much stronger than the crust, it may detach along the weak layer, and subduct without significant internal deformation (figure 2(c)). The subducting layer will pass down below the neighbouring region of mantle lithosphere along another weak, sheared layer, represented by the symbol 'SZ' (for 'Shear Zone') in figure 2(c)). In the limit that the mantle length-scale $\lambda_m \rightarrow 0$, the crust experiences a velocity discontinuity at point S, where the mantle lithosphere detaches. More generally, $\lambda_m \neq 0$, and in numerical models its value may either be specified kinematically, or determined dynamically.

The 'mantle subduction' assumption of figure 2(c) was used by Willett et al. (1993) to interpret the large-scale structure and mechanical behaviour of convergent orogens. Use of these boundary conditions with a non-cohesive Coulomb rheology produces a doubly-vergent wedge, which at the largest scale reproduces many of the features of convergent orogens.

In order to investigate the effect of basal forcing on crustal deformation, this study also investigates the boundary conditions of figure 2(c). Predictions concerning length-scales of deformation for this case, are compared with the results of previous studies which use the boundary conditions of figure 2(a). For convenience, I refer to the model style illustrated in figure 2(a) as the 'side-driven' model, and the model style in figure 2(c) as the 'basally-driven' model. I caution that, as is evident from the discussion in this section, there are many alternative views of crust-mantle interactions during continental convergence (e.g. England and McKenzie, 1983; Bird, 1989). Differences between the predictions of the cases investigated here, and the deformation length-scales of natural orogens (e.g. see chapter five), give an indication of the excessive simplification of the models compared to the real processes involved in collisional orogenesis.

§ 2.2 Applying the Basally-Driven Model to Other Convergent Settings

The similarity between the mantle subduction boundary conditions illustrated in figure 2(c) and lithospheric subduction has led to the idea that there may be a continuous range of convergent behaviour from continental collision, where the mantle lithosphere detaches and subducts, to oceanic subduction, where both crust and mantle detach at a lithospheric shear zone and subduct. This idea was used by Willett et al. (1993) and Beaumont et al. (1994b), and is shown in figure 3.

Figure 3(a) corresponds to the continental collision, basally-driven model of figure 2(c), with the weak detachment layer (not shown) at the Moho, so that only mantle lithosphere subducts. Partial crustal subduction is illustrated in figure 3(b), where the weak layer does not correspond to the Moho, but to a shallower depth in the crust. Finally, total subduction of the lithosphere is illustrated in figure 3(c), and corresponds to ocean-continent, or ocean-ocean, subduction.

Figure 3: Proposed boundary conditions for the basally-driven model, with progressively more crust subducted along with the mantle lithosphere. ϕ_P is the crustal mass flux entering the pro side of the orogen, and S represents the singularity. (a) Continental convergence, where detachment occurs at the Moho, and the subducted crustal flux ϕ_S=0. (b) Partial crustal subduction, where detachment occurs along a crustal asthenolayer above the Moho (dashed line), and $0< \phi_S< \phi_P$. (c) Lithospheric subduction shown for oceanic-continental convergence, with $\phi_S = \phi_P$, and the thinner, denser oceanic crust subducting along with the mantle. Nails on left-hand side of figure represent fixed crust and mantle lithosphere.

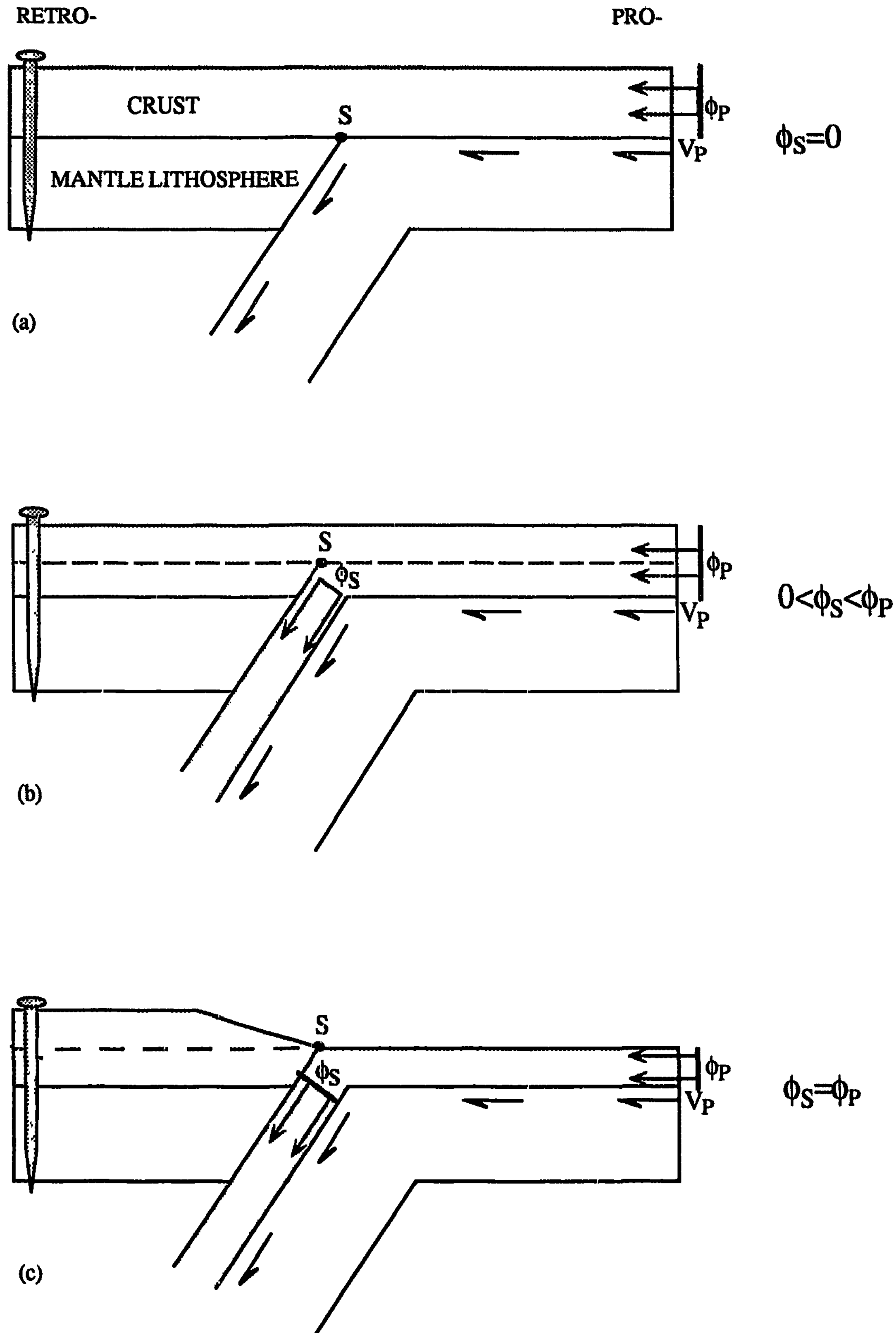

RETRO-
PRO-
CRUST
S
MANTLE LITHOSPHERE
ϕ_P
V_P
$\phi_S=0$
(a)
S
ϕ_S
ϕ_P
V_P
$0<\phi_S<\phi_P$
(b)
S
ϕ_S
ϕ_P
V_P
$\phi_S=\phi_P$
(c)

Figure 3

Figure 3 also shows the mass fluxes ϕ_P (Beaumont et al., 1994b), where the 'P' indicates flux of mass entering from the 'pro' (upstream) side of the singularity, and ϕ_S, the amount of crustal flux which is subducted along with the mantle lithosphere (the terminology 'pro' and 'retro', indicating the upstream and downstream sides of the singularity, comes from Willett et al., 1993).

Willett et al. (1993) also suggested another range of possible detachment behaviours, where the initial point of detachment (S) moves with respect to the retro side of the lithosphere. Figure 4 shows the two possible behaviours for continental convergence. Motion of the singularity in the pro-direction will cause advance, and the opposite motion will cause retreat, of the subducting layer (figure 4). Retreat and advance may cause mass to be added or removed from the retro-side of the lithosphere (Beaumont et al., 1994b).

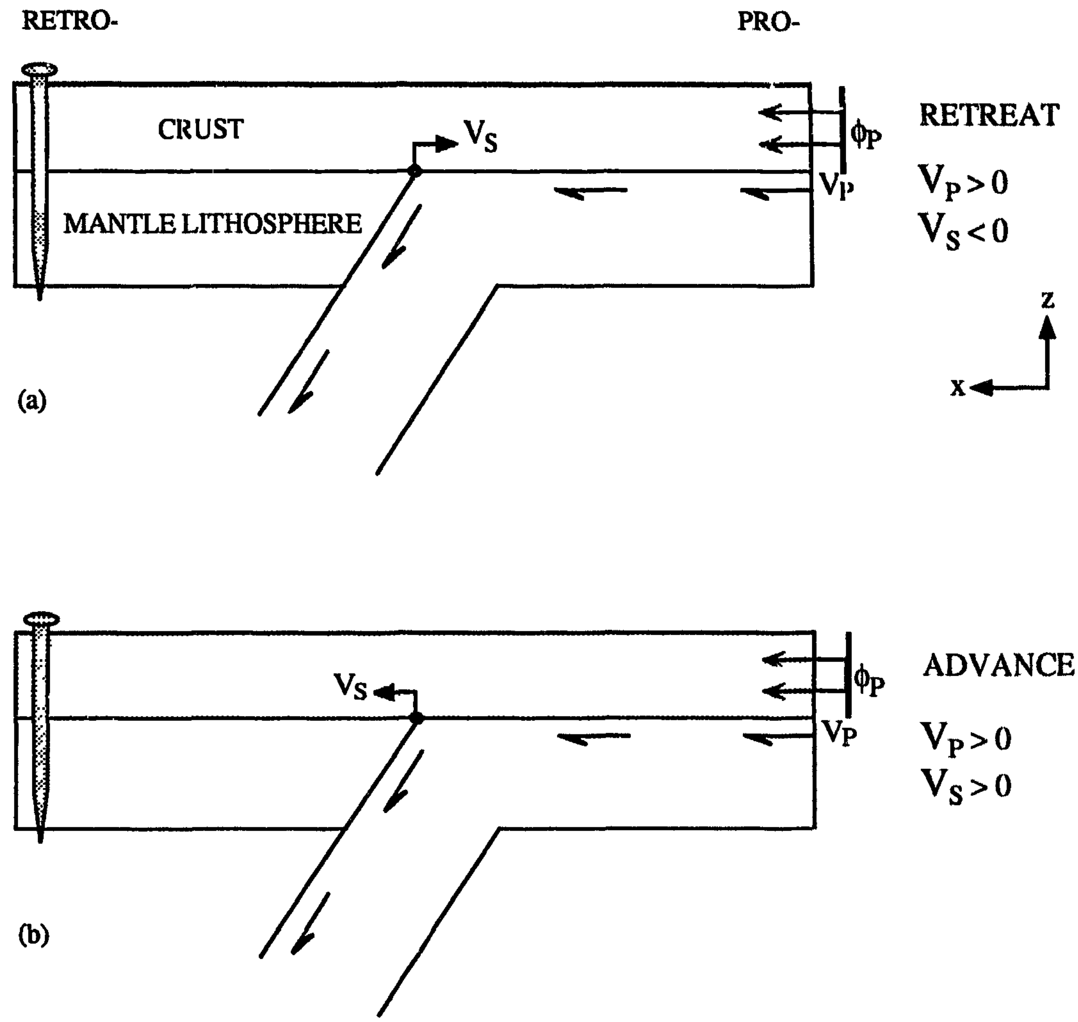

Figure 4: Retreating ($V_P > 0$, $V_S < 0$) and advancing ($V_P > 0$, $V_S > 0$) mantle subduction, shown for the continental convergence case (figure 3(a)). The singularity moves with velocity V_S relative to the fixed (retro) reference frame. The velocity V_P is a material velocity.

§ 2.3 Boundary Conditions used in this Study

Continent-Continent Convergence

In this study it is assumed that some aspects of continental convergence involve the detachment and subduction of mantle lithosphere beneath the crust, as discussed above and illustrated in figure 2(c). The crust and mantle are separated by a weak asthenolayer. Because the mantle lithosphere is assumed to be much stronger than the overlying crust, it is assumed to be below yield stress, and remains elastic. The mantle lithosphere is therefore assumed to subduct with little internal deformation. If the subduction occurs by elastic flexure, without exceeding the yield stress in the mantle except along the shear zone SZ (figure 2(c)), an appropriate model for the crust is a thin viscous sheet, deformed by the application of a specified mantle velocity field through a weak layer, which causes a traction on the base of the model crust. The weak basal layer is assumed to be thin in comparison to the thickness of the sheet. The model is isostatically compensated by elastic flexure in the strong part of the mantle lithosphere. (Elastic flexure is defined as the elastic bending of a layer in response to an applied load. The layer will return to its original shape if the load is removed).

Figure 5: A schematic illustration of the basally-driven thin-sheet model. (a) the velocity boundary conditions applied at the crust-mantle interface. The darkly shaded region is the thin weak layer at the base of the crust through which the specified mantle velocity field acts on the crust. (b) the material properties of the model crust and weak basal layer; (c) the compensation mechanism for the model. The crust is supported by elastic flexure of the strong part of the mantle lithosphere.

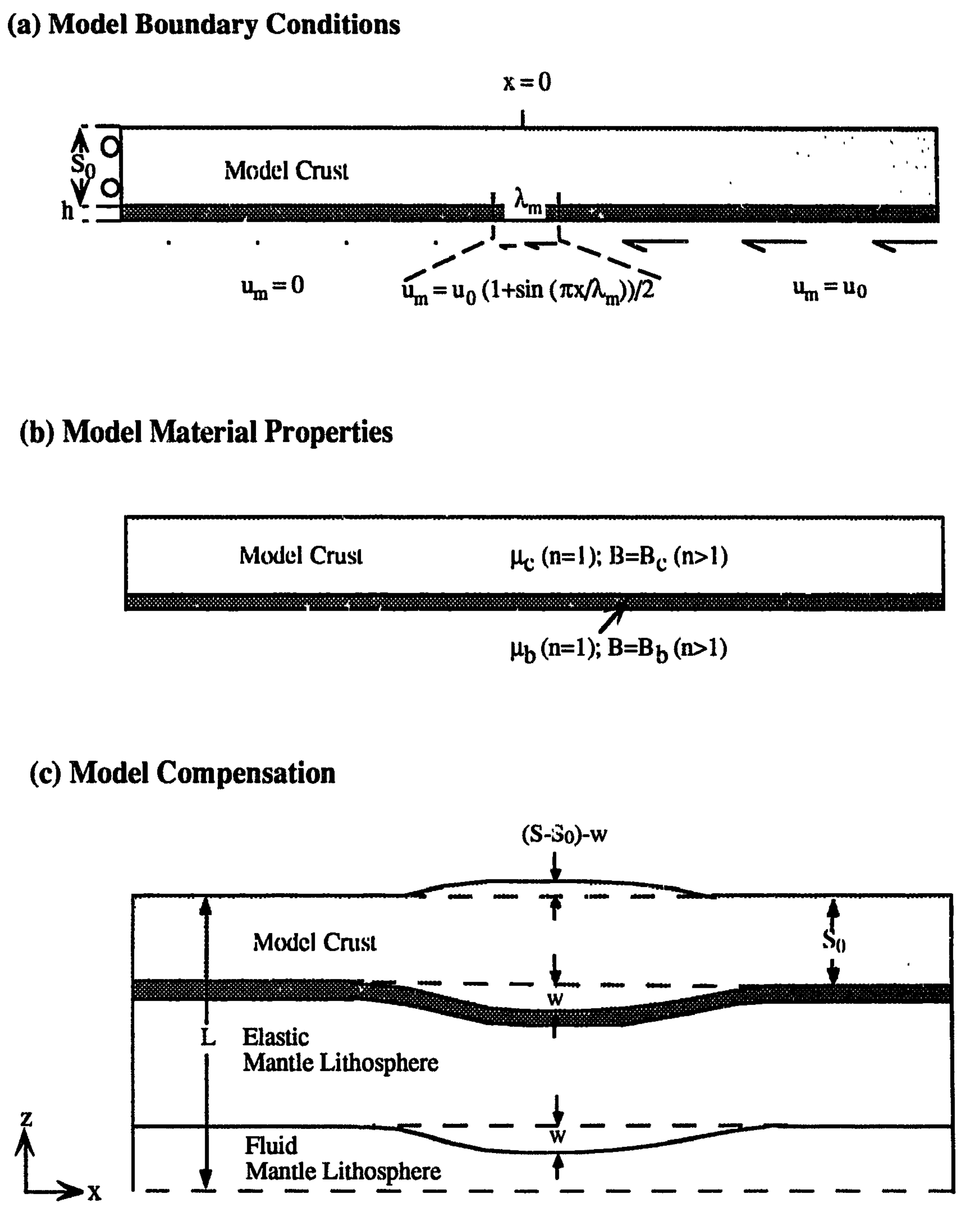

(a) Model Boundary Conditions
x = 0
Model Crust
S_0
h
λ_m
$u_m = 0$
$u_m = u_0 (1+\sin(\pi x/\lambda_m))/2$
$u_m = u_0$
(b) Model Material Properties
Model Crust
μ_c (n=1); B=B_c (n>1)
μ_b (n=1); B=B_b (n>1)
(c) Model Compensation
$(S-S_0)-w$
Model Crust
S_0
w
L
Elastic
Mantle Lithosphere
w
Fluid
Mantle Lithosphere
z
x

Figure 5

The formulation follows the approach of Bird (1989) and Bird and Baumgardner (1984) by modelling the continental lithosphere as two separate layers (crust and mantle lithosphere). Like Bird and Baumgardner (1984), the mantle is not modelled as a viscous thin-sheet, but has specified velocity and flexural properties. Although I continue to use the term lithosphere, in reality the crustal thin-sheet is planar and does not follow the curvature of the earth. The crust and mantle are linked by the vertical force balance, and by the simple shear boundary layer, which transmits the specified mantle lithosphere velocity as a traction to the base of the crust (figure 5).

The parameters used in the model are shown in figure 5, and the standard parameter values are listed in Table 2. For a linear viscous crustal rheology, the thin-sheet has viscosity μ_c and initial thickness S_0, and is subject to the specified basal velocity field $\mathbf{u}_m(x,y)$, which acts through the low viscosity simple shear boundary layer, with viscosity μ_b and thickness h ($<< S_0$), to apply a traction to the base of the sheet (figure 5(a)). The corresponding non-linear creep parameters, B_c and B_b, are also shown on figure 5, and are discussed in Appendix C. In the far-field away from the plate boundary, $\mathbf{u}_m(x,y) = \mathbf{u}_0$. The initial horizontal detachment length-scale for detachment between the crust and subducting mantle lithosphere (figures 2(c), 5(a)) is λ_m. The crustal sheet is isostatically compensated as it thickens (figure 5(b)).

Modifications for Other Types of Convergence

Although the model boundary conditions discussed above are formulated for the case of continent-continent collision, other types of convergence, as discussed in section 2.2 and illustrated in figures 3 and 4, may also be modelled by changing the position of the weak detachment layer and singularity, and by modifying the thickness and material properties of the crust. The corresponding model boundary conditions for these cases are discussed in chapter six.

Table 2: Parameters used in the model

ρ_c	density of crust	h	thickness of basal layer
ρ_m	density of mantle	L	Depth of compensation
μ_c	crustal viscosity	$\bar{u}$	crustal velocity
μ_b	basal viscosity	u_0	imposed boundary velocity
B_c	vertically averaged material constant for a power law viscous crust	u_m	imposed velocity at the top of the mantle lithosphere
B_b	vertically averaged material constant for a power law viscous simple shear layer	λ_m	basal detachment length-scale
n	power law exponent	λ_N	crustal response length-scale for normal convergence
S	crustal thickness	λ_T	crustal response length-scale for transcurrent motion
S_0	initial crustal thickness		

§ 2.4 A Crustal Thin-Sheet Model Driven by Basal Velocity Conditions

Formulation

Neglecting inertial acceleration in the Earth's frame of reference, the force balance in the crust and mantle lithosphere is:

$$\frac{\partial \sigma_{ij}}{\partial x_j} + \rho g a_i = 0 \qquad (\mathbf{a} = (0,0,-1)) \qquad .....(1)$$

where σ_{ij} is a component of the stress tensor, ρ is the density, and g the acceleration due to gravity. The force balance equation is combined with the equation for deviatoric stress:

$$\tau_{ij} = \sigma_{ij} + p\delta_{ij} \qquad .....(2)$$

where p is the pressure, and $p = -(1/3)\sigma_{kk}$. Firstly, consider deformation in the x-z (i=x, z) plane only, where z is measured vertically upward. Combining (1) and (2), the horizontal force balance is:

$$\frac{\partial \sigma_{xx}}{\partial x} + \frac{\partial \sigma_{xz}}{\partial z} = \frac{\partial \tau_{xx}}{\partial x} + \frac{\partial \tau_{xz}}{\partial z} - \frac{\partial p}{\partial x} = 0 \qquad .....(3)$$

The horizontal force balance can be vertically integrated over the lithosphere, provided we can estimate the pressure gradient, $\partial p/\partial x$. The vertical force balance in the lithosphere is:

$$\frac{\partial \sigma_{zz}}{\partial z} + \frac{\partial \sigma_{zx}}{\partial x} = \frac{\partial \tau_{zz}}{\partial z} + \frac{\partial \tau_{zx}}{\partial x} - \frac{\partial p}{\partial z} = \rho g \qquad .....(4)$$

Although the shear τ_{xz} from the boundary layer propagates into the mantle lithosphere, it does not cause significant horizontal shear, because the mantle lithosphere is assumed to be elastic. Within the crust, the contribution of the horizontal derivative of shear stress ($\partial\tau_{zx}/\partial x$) to the vertically integrated force balance is negligible, provided, as shown in Appendix A, that the effective strength of the basal layer is much less than that of the crust. The contribution of $\partial\tau_{zx}/\partial x$ to the integrated vertical force balance in the basal simple shear layer will also be very small, provided the simple shear layer thickness is much less than the crustal thickness S. Therefore the term $\partial\tau_{zx}/\partial x$ can be neglected when integrating (4) with respect to depth to get an expression for the pressure p(z):

$$p(z) = P_0 - \int_0^z \rho g dz' + \int_0^z \frac{\partial\tau_{zz}}{\partial z'} dz'$$

The lithosphere is assumed to be isostatically compensated, with pressure P_0, at z=0, below the elastic mantle lithosphere (figure 5(c)). For a crustal load S(x), the elastic portion of the mantle will be deflected by an amount w(x). Because the strong part of the mantle lithosphere is elastic, it does not contribute a dynamical term to the pressure, and so the deflection w(x) can be calculated from the equation for an elastic beam (Turcotte and Schubert, 1982).

The vertically integrated pressure to the bottom of a general lithospheric column, as shown in figure 5(c), is:

$$P_L = (L+S-w)P_0 - \int_0^{L-w} \rho_m g z \, dz - \int_{L-w}^{L+S-w} \rho_c g z \, dz + \int_0^{L+S-w} \tau_{zz} \, dz$$

where L is the thickness of the lithosphere for a reference vertical column with no crustal thickening, S(x) is the thickness of the crust, ρ_c is the crustal density, ρ_m the mantle density, and w(x) is the deflection of the elastic beam. The deflection w(x) may be written in terms of a flexural perturbation $w_f(x)$ on the locally compensated deflection $S\rho_c/\rho_m$:

$$w(x) = \frac{\rho_c}{\rho_m} S(x) - w_f(x)$$

Substituting this into the vertically integrated pressure gives:

$$P_L = \left[(L + S\phi)\rho_m g L - \int_0^{L - S\frac{\rho_c}{\rho_m}} \rho_m g z \, dz - \int_{L - S\frac{\rho_c}{\rho_m}}^{L+S\phi} \rho_c g z \, dz \right] +$$

$$\left[\rho_m g L w_f - \int_{L - S\frac{\rho_c}{\rho_m}}^{L - S\frac{\rho_c}{\rho_m} + w_f} \rho_m g z \, dz + \int_{L - S\frac{\rho_c}{\rho_m}}^{L - S\frac{\rho_c}{\rho_m} + w_f} \rho_c g z \, dz - \int_{L-S\phi}^{L-S\phi+w_f} \rho_c g z \, dz \right] + \int_0^{L+S\phi+w_f} \tau_{zz} \, dz$$

where ϕ is the isostatic amplification factor:

$$\phi = 1 - \frac{\rho_c}{\rho_m}$$

This expression simplifies to:

$$P_L = \frac{\rho_c g \phi S^2}{2} + \frac{\rho_m g L^2}{2} - \frac{\rho_m g w_f^2}{2} + \int_0^{L+S\phi+w_f} \tau_{zz} \, dz \qquad \text{.....(5)}$$

The effect of flexure on the pressure is to add the extra terms in w_f to the vertically integrated pressure for the locally compensated case (cf. England and McKenzie, 1983). The vertically integrated pressure gradient is:

$$\frac{\rho_c g \phi}{2} \frac{\partial S^2}{\partial x} - \frac{\rho_m g}{2} \frac{\partial w_f^2}{\partial x} + \int_0^{L+S\phi+w_f} \frac{\partial \tau_{zz}}{\partial x} \, dz \qquad \text{.....(6)}$$

Integrating the horizontal force balance (3) over the lithosphere and combining with (6) gives:

$$\int_0^{L+S\phi+w_f} \frac{\partial \tau_{xx}}{\partial x} dz + \int_0^{L+S\phi+w_f} \frac{\partial \tau_{xz}}{\partial z} dz$$
$$= \left(\frac{\rho_c g \phi}{2} \frac{\partial S^2}{\partial x} + \frac{\rho_m g}{2} \frac{\partial {w_f}^2}{\partial x}\right) + \int_0^{L+S\phi+w_f} \frac{\partial \tau_{zz}}{\partial x} dz \qquad .....(7)$$

The perturbation in mantle deflection, w_f, will compensate crustal thickness variations over a length-scale determined by the flexural parameters. However, it is shown in Appendix B that w_f is not significant, provided the crust thickens over a length-scale greater than approximately twice the flexural wavelength. This length-scale restriction on locally compensated crustal deformation approximately concurs with the length-scale restrictions placed on the model due to the thin-sheet approximation (see chapter 3). Terms in $w_f(x)$ are therefore neglected for subsequent derivations, although an incorporation of this term into the force balance may be necessary for cases where significant amounts of thickening of the crust are expected.

The elastic mantle lithosphere is below yield, and it is assumed that one limb subducts passively beneath the other by elastic flexure, under the weight of the subducted limb. Consistent with this assumption and the kinematic treatment of the horizontal boundary conditions at the base of the simple shear layer, the contributions from shear stress gradients in the mantle to the horizontal force balance are not included when integrating eq. (7).

Within the crustal layer, following the thin-sheet assumption, the vertical derivative of shear stress τ_{xz} is taken to be zero, so that the second term in eq. (7) reduces to T^b_{xz}, the shear traction applied at the base of the crust. The validity of this approximation is established by comparing the thin-sheet solution to the complete plane-strain solution of crustal deformation in chapter 3.

With these simplifications, eq. (7) becomes:

$$2\frac{\partial(S\bar{\tau}_{xx})}{\partial x}+T^{b}{}_{xz}=\frac{\rho_c g\phi}{2}\frac{\partial S^2}{\partial x} \qquad .....(8)$$

where the overbar denotes a quantity vertically averaged over crustal thickness S, so that:

$$\bar{\tau}_{xx}=\frac{1}{S}\int_{L-S\frac{\rho_c}{\rho_m}}^{L+S\phi}\tau_{xx}\,dz$$

and the incompressibility condition $\tau_{zz} = -\tau_{xx}$ has been used to eliminate τ_{zz}.

Stresses are averaged over S(x), so the horizontal derivative on the left-hand side of eq. (8) must include both the crustal thickness and average deviatoric stress terms. This differs from thin-sheet models where stresses are averaged over L, the lithospheric thickness (e.g. England and McKenzie, 1982). For these 'whole lithosphere' thin-sheet models, sheet thickness variations due to excess crustal thickness ΔS are of order $\Delta S\phi$ which is much less than L, so the horizontal derivative $\partial L/\partial x$ may be neglected. For a crustal thin-sheet, variations in crustal thickness are of order ΔS which may be a significant fraction of S, so the horizontal derivative $\partial S/\partial x$ may be significant.

The mantle lithosphere, which has horizontal velocity $u_m(x)$, interacts with the model crust, with vertically averaged velocity $\bar{u}(x)$, via the thin basal boundary layer of thickness h. If the boundary layer has a linear viscosity, μ_b, the horizontally-applied traction at the base of the crust can be found from Couette flow[1] (Turcotte and Schubert,

[1] The assumption of Couette flow in the basal layer is justified for cases where the thickness of the weak basal layer is much less than total crustal thickness (h<<S), and for reasonable viscosity contrasts between the basal layer and average crustal values ($\mu_b/\mu_c > 10^{-6}$). For extreme cases, where h is a much larger fraction of S, and/or viscosity contrasts are large, channel flow may dominate in the basal layer beneath areas with significant crustal thickness contrasts (Royden, submitted). The likelihood of a change to

1982) to be:

$$T^{b}_{xz} = -\frac{\mu_b}{h}(\bar{u} - u_m) \qquad .....(9)$$

For a crust with linear viscosity μ_c, the constitutive relation is:

$$\bar{\tau}_{xx} = 2\mu_c\bar{\dot{\varepsilon}}_{xx} = 2\mu_c\frac{\partial \bar{u}}{\partial x} \qquad ....(10)$$

where, as before, the overbar denotes a quantity vertically averaged over crustal thickness S. Eq. (8) becomes, in terms of the vertically averaged horizontal velocity:

$$4\mu_c S\frac{\partial^2 \bar{u}}{\partial x^2} + 4\mu_c\frac{\partial S}{\partial x}\frac{\partial \bar{u}}{\partial x} = \frac{\rho_c g\phi}{2}\frac{\partial S^2}{\partial x} + \frac{\mu_b}{h}(\bar{u} - u_m) \qquad ....(11)$$

Eq. (11) is similar to the expression found by Wdowinski et al.(1989), except that it solves for average crustal, instead of lithospheric, velocity. Normalizing the equation using the horizontal mantle detachment length-scale λ_m, the velocity in the far-field where the crust and mantle lithosphere are moving with no shear between them, u_0, and a vertical length-scale, the initial crustal thickness S_0:

$$u' = \frac{u}{u_0}; \qquad S' = \frac{S}{S_0}; \qquad x' = \frac{x}{\lambda_m}; \qquad t' = t\frac{u_0}{S_0}$$

gives:

$$S'\frac{\partial^2 \bar{u}'}{\partial x'^2} + \frac{\partial S'}{\partial x'}\frac{\partial \bar{u}'}{\partial x'} = \frac{\rho_c g\phi S_0\lambda_m}{8\mu_c u_0}\frac{\partial S'^2}{\partial x'} + \frac{\mu_b}{4\mu_c}\frac{\lambda_m{}^2}{hS_0}(\bar{u}' - u'_m)$$

---

channel flow behaviour during contractional thickening is discussed in chapter three, with reference to the results of Royden (submitted).

which can also be written as:

$$S'\frac{\partial^2\overline{u}'}{\partial x'^2}+\frac{\partial S'}{\partial x'}\frac{\partial \overline{u}'}{\partial x'}=\frac{Ar}{4}\frac{\partial S'^2}{\partial x'}+\frac{Am}{4}(\overline{u}'-u'_m) \qquad \text{....(12)}$$

where:

$$Ar=\frac{\rho_c g\phi S_0\lambda_m}{2\mu_c u_0} \qquad \text{and} \qquad Am=\frac{\mu_b{\lambda_m}^2}{\mu_c h S_0}$$

The form of eq. (12) shows that for the linear viscous case, variations in all important parameters can be represented by the three dimensionless numbers Ar, Am and t' (Table 3, figure 6). The two dimensional form of eq. (12) in normalized tensor notation can be shown to be:

$$2\frac{\partial}{\partial x'_i}(S'\frac{\partial\overline{u}'_j}{\partial x'_j})+\frac{\partial}{\partial x'_j}(S'\frac{\partial\overline{u}'_i}{\partial x'_j}+S'\frac{\partial\overline{u}'_j}{\partial x'_i})=Ar\frac{\partial S'^2}{\partial x'_i}+Am(\overline{u}'_i-u'_{mi}) \qquad \text{...(13)}$$

where repeated indices imply summation, and if the strike of the applied boundary conditions is in the y-direction, i=x gives the equation for the normal component of velocity, and i=y the equation for the transverse component. $\overline{u}'_i$ and u'_{mi} are the ith component of the average crustal and mantle velocities, respectively. In the absence of a basal shear, the last term of eq. (13) may be dropped, and the equation reduces to a form similar to that found by England and McKenzie (1983), but with velocity terms now averaged over model crustal thickness S rather than constant lithospheric thickness L. The equivalent equation for a non-linear viscous rheology is derived in Appendix C.

The equation (13) can be solved using the finite element technique on a deforming (Lagrangian) grid. Crustal thickness $S'(x,y)$ is updated at each timestep using conservation of mass:

$$\frac{\partial S'}{\partial t'} = -\frac{\partial (S'\overline{u}'_j)}{\partial x'_j} \qquad \text{....(14)}$$

Table 3: Table of dimensionless parameters

Ar	Argand number (ratio of gravitational buoyancy force: compressive force in crust)
Am	Ampferer number (ratio of basal traction force: compressive force in crust)
t'	dimensionless time
n	power-law exponent

Figure 6: A diagram summarizing the controlling parameters of the thin-sheet problem into the ratio between three forces influencing crustal deformation: (a) the compressive force in the crust, F_1; (b) the gravitational buoyancy force due to excess crustal thickness, F_2; and (c) the basal traction force, F_3. The ratio between F_2 and F_1 gives the Argand number, Ar, which can also be written as the ratio of two stresses, since both F_1 and F_2 scale with S_0. The ratio between forces F_3 and F_1 gives the Ampferer number Am, which can also be written as the ratio between two stresses, scaled by the length scale ratio (λ_m/S_0).

(a)

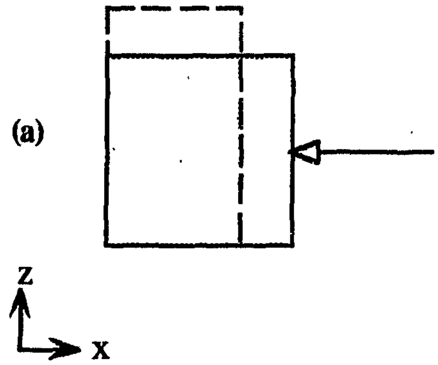

Compressive force $F_1 = \left(\frac{\mu_c u_0}{\lambda_m}\right) S_0$

(b)

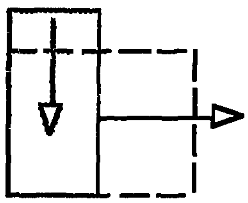

Gravitational force $F_2 = \left(\frac{\rho_c g \phi S_0}{2}\right) S_0$

(c)

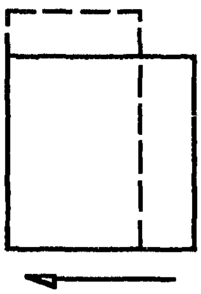

Basal traction force $F_3 = \left(\frac{\mu_b u_0}{h}\right) \lambda_m$

$$Ar = F_2/F_1 = \frac{\rho_c g \phi S_0 \lambda_m}{2 \mu_c u_0} = \frac{\tau_g}{\tau_c}$$

$$Am = F_3/F_1 = \frac{\mu_b \lambda_m^2}{h \mu_c S_0} = \frac{\tau_b}{\tau_c} \frac{\lambda_m}{S_0}$$

Figure 6

The Argand and Ampferer Numbers

Gravity acts to diffuse the crustal thickness contrasts created by crust-mantle interactions. The Argand number, Ar, represents the relative importance of gravitational forces generated by crustal thickness gradients compared to the compressive forces present in the model crust (figure 6). The consequence of a non-zero Argand number increases with dimensionless time as the orogen grows. England and McKenzie (1982) proposed the name 'Argand' to describe a derived non-dimensional scaling quantity, representing the ratio of excess pressure caused by crustal thickness contrasts vs. the stress required to deform the lithosphere at a characteristic strain-rate, $\dot{\varepsilon}_0$:

$$Ar^{\substack{\text{England \&} \\ \text{McKenzie}}} = \frac{\rho_c g \phi L^2}{2\mu_c u_0} \qquad (n = 1)$$

(England and McKenzie, 1982), where L is the thickness of the lithosphere.

Emile Argand was a Swiss geologist who was instrumental in applying Wegener's ideas of continental drift to explain the large horizontal movement of the Alpine nappes, and later to other orogens in Eurasia, including the Himalayas and Tibet. The Argand number is thus, appropriately, a measure of the ratio between two horizontal stresses or forces. The definition for Ar used in this study is similar to the Argand numbers of England and McKenzie (1982), and also Wdowinski et al. (1989), but now includes both horizontal and vertical reference length-scales, and therefore must be interpreted as a force ratio, rather than a stress ratio.

In a similar manner to the introduction of the Argand number by England and McKenzie (1982), Ellis et al. (1995) proposed the name Ampferer number (Am), to represent the amount of coupling between the crust and underlying mantle (figure 6). Otto Ampferer postulated that crustal compression was related to the apparent underthrusting of forelands beneath orogenic belts (Ampferer, 1906). Ampferer and Hammer (1911) termed the process 'Verschlukung', in which a series of sub-crustal currents dragged the overlying crustal rocks beneath the growing orogen. Ampferer in many ways anticipated the more modern idea of A-type subduction (Bally and Oldow, 1984), in which part of the continental crust is subducted, creating large-scale decollement folding and thrusting in the overlying crust.

The Ampferer number as defined is similar to the dimensionless parameter used by Wdowinski et al. (1989):

$$\frac{\mu_a D}{4\mu_l L}$$

for a lithospheric sheet, where μ_a and μ_l are the asthenospheric and lithospheric viscosities, respectively, L is the thickness of the lithosphere, and D is the horizontal extent of deformation. However, the dimensionless parameter Am used in this study differs from Wdowinski et al. because of the use of two length-scales to normalize the equation (13): crustal thickness S_0, and the horizontal mantle detachment length-scale λ_m. The Ampferer number thus contrasts the basal traction force with the level of compressive force present in the crust, as characterized by the relative strengths of the crust and basal layer, and the length-scale ratio (λ_m/S_0). Appendix E and chapter 4 show that Am may be used to derive the natural response length-scale of the crust (λ_N for normal convergence) to basal forcing at length-scale λ_m. In the limit as μ_b becomes much less than μ_c, $\lambda_m/\lambda_N \rightarrow 0$ and coupling becomes weak.

Although the definition for Am is related to the applied boundary conditions used in the model, a general Ampferer number will exist for any situation where crustal or lithospheric deformation is influenced by basal forcing, and will be the ratio of the basal traction force to compressive force in the deforming layer. For example, Platt (1993) developed descriptions of the velocity distributions for critical topography in obliquely convergent wedges, with three different assumed rheologies (linear viscous, perfectly plastic, and non-cohesive Coulomb). For each case, the velocity distributions were shown to depend on the relative strengths of the wedge and the coupling with the base and backstop. For a wedge with velocity dependent shear stress boundary conditions, where coupling to the base and backstop is proportional to constants p and q, the resultant velocities within the wedge are scaled by an equival ıpferer number, containing the ratio of a function of the coupling constants p and q to the material strength of the wedge (Platt, 1993).

If the mantle detaches at a singularity (i.e. λ_m is zero), the equation (13) may be normalized using only the vertical length-scale S_0, so that Am may be written as:

$$Am = \frac{\mu_b S_0}{\mu_c h}$$

The form of the normalized equation (13), and the dimensionless parameters Ar and Am, demonstrate that the thickening in the crustal sheet is a result of a competition between the viscous resistance to deformation, basal traction forces, and the gravitational forces due crustal thickness gradients.

§ 2.5 Numerical Implementation of the Basally-Driven Thin-Sheet Model

Introduction

The governing equation (13) may be solved analytically for certain cases (see section 4.2). More generally, a two-dimensional finite element numerical method is used to solve (13) at a finite number of nodal points, with velocity boundary conditions applied to the base and sides of the domain, Ω (figure D1). I use a finite element code adapted from a program written by Philippe Fullsack (Fullsack, 1995; Willett, 1992; Beaumont et al., 1992). This section and Appendix D summarize the particular modifications of the code to solve the governing thin-sheet equation (13), and the interaction of basal and crustal layers. For a general overview of the finite element numerical method, the reader is referred to the wide assortment of books written on the topic (e.g. Zienkiewicz, 1977; Norrie and deVries, 1978).

Prescribing the Grid and Velocity Boundary Conditions

A simple mesher routine is used to linearly interpolate grid coordinates between prescribed points from the input files. The grid covering the crustal domain may be regularly spaced on input (e.g. figure 7), or may have increased resolution near the basal detachment point. To minimize numerical errors, care must be taken when designing the grid to avoid juxtaposing elements of extremely different size (Akin, 1986). Because the representation of the crust is two-dimensional (planform), the vertical description of the model crust is restricted to a value of the crustal thickness $S(x,y)$ for each element, from which the corresponding height field can be computed, assuming local isostatic compensation and an initial crustal thickness, S_0.

The crustal grid has dimensions big enough so that throughout the model run, at the edges of the grid, the velocity can be assumed to represent the 'far-field' velocity, where the crust is not detached from its base, and so the net basal traction is zero. The velocities at the sides of the model domain may be specified directly (Dirichlet boundary conditions), or a symmetry condition (no shear on the boundaries ≡ Neumann boundary conditions)) may be assumed, where the derivatives of velocity normal to the boundary are taken to be zero.

Figure 7: An illustration of a typical model crustal grid and boundary conditions at (a) $t'=0$, and (b) deformation after significant convergence time, t'. A constant velocity u_0 is applied at the side of the domain, and a sinusoidal basal detachment zone of dimension $2S_0$ causes the grid to deform as shown in the lower figure. Grid spacing is $(1/3)S_0$.

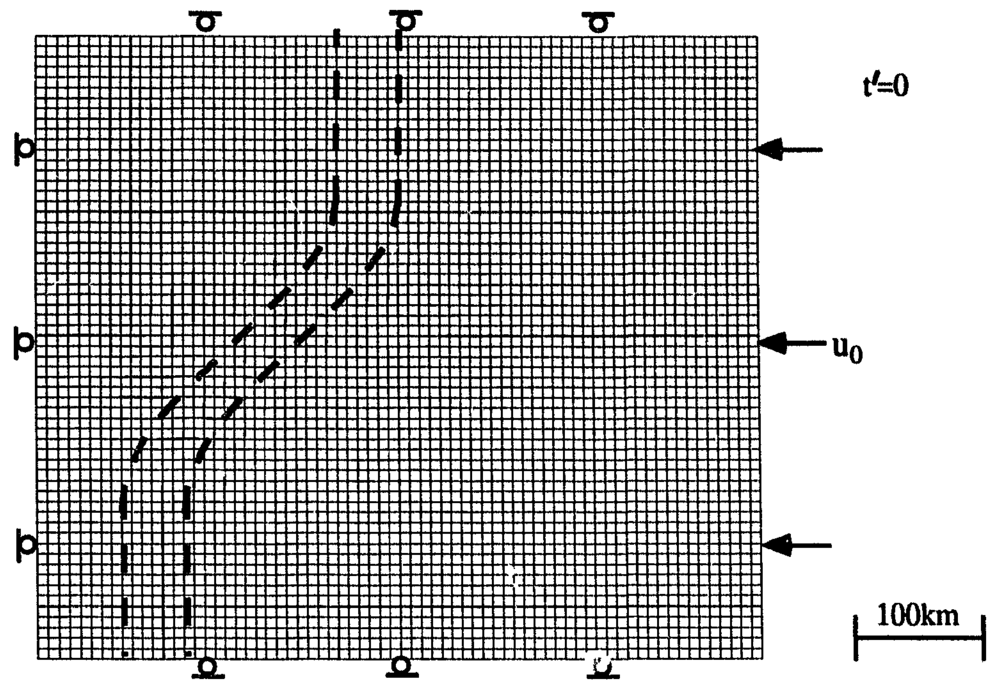

(a)

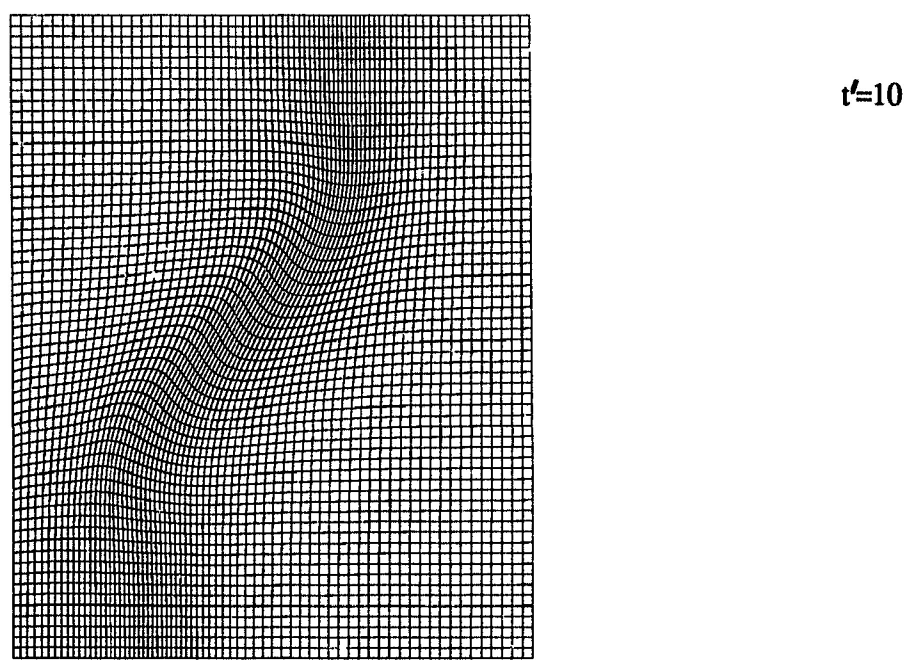

(b)

Figure 7

Basal velocity boundary conditions are applied as discussed in section 2.3, by application of a basal traction as a force on the right hand side of eq. (13). As discussed in section 2.3, a simple shear layer of constant thickness, h, and viscosity μ_b, is assumed at the base of the model crust, so that the basal traction is given by:

$$\mathbf{T}^b = \frac{\mu_b}{h}(\mathbf{u}(x,y) - \mathbf{u}_m(x,y))$$

The velocity at the top of the mantle lithosphere, $\mathbf{u}_m$, must be evaluated at the nodal coordinates of the model crustal grid (x,y). The basal velocity field is specified for a grid which will not correspond, in general, to the crustal grid, which is deforming with time. For a given timestep and nodal coordinate, the basal velocity is found by determining the surrounding basal node numbers using a search algorithm, and then interpolating linearly between them. If the node has been advected outside of the basal grid, the velocity $\mathbf{u}_m(x,y)$ is prescribed to be the basal velocity at the closest basal boundary point.

The model mantle detaches and subducts over width λ_m, where (as discussed in section 2.1) λ_m may be on the order of the crustal thickness, or vanishingly small for the case of detachment at a singularity (figure 2(c)). For the case where $\lambda_m \rightarrow 0$, the smallest representation of the singularity on a numerical grid is the minimum cell size for the grid. For most of this thesis, I investigate the case where $\lambda_m = S_0$. For smaller values of λ_m, I refine the mesh near the singularity so that in all cases the bottom velocity condition decreases to zero across more than one gridpoint, in a smooth (sinusoidal) manner, ensuring that velocity components and their derivatives vary smoothly across the mantle detachment zone.

Computing the Velocity Solution

Once the initial crustal grid and velocity boundary conditions have been defined, a numerical solution for the crustal velocity is found at each timestep using the finite element calculations. The computation alternates between calculations performed at the global level (over the whole domain), and the local (element) level (see Appendix D). The step-by-step numerical procedure for a linear viscous crustal rheology is as follows:

- Assuming a rectangular global connectivity, compute an array linking global and local nodal numberings
- Loop over each element:
  - Transform the element coordinates to a square (bilinear transformation)
  - Compute the Jacobian
  - Evaluate the local element stiffness matrix using Gaussian quadrature and the shape functions for the transformed element
- Assemble the global stiffness matrix by nodes (x degrees of freedom)
- Assemble the right hand side
- Substitute in for the Dirichlet boundary conditions
- Solve the matrix equation ($\sum K_{pq} u_p = F_q$) using the Linpack SPBFA matrix solver routine (Dongarra et al., 1979).

Solving for a Non-Linear Rheology

The non-linear equivalent to equation (13) is described in Appendix C. The dimensioned form of eq. (C2) may be written as:

$$2\frac{\partial}{\partial x_i}\left(S\mu_{eff}\frac{\partial \bar{u}_j}{\partial x_j}\right)+\frac{\partial}{\partial x_j}\left(S\mu_{eff}\left(\frac{\partial \bar{u}_i}{\partial x_j}+\frac{\partial \bar{u}_j}{\partial x_i}\right)\right)= \frac{\rho_c g\phi}{2}\frac{\partial S^2}{\partial x_i}+\frac{\mu_b}{h}(\bar{u}_i - u_{mi})^{\frac{1}{n}}$$

where the effective viscosity, μ_{eff}, is given by:

$$\mu_{eff} = \mu_0 \left(\frac{\dot{\bar{E}}}{\dot{\varepsilon}_0} \right)^{\frac{1}{n}-1}$$

The effective viscosity depends on the velocity field, via $\dot{\bar{E}}$, and a reference strain-rate, $\dot{\varepsilon}_0$, which is determined by the scaling parameters used to normalize the equation, so that $\dot{\varepsilon}_0 = u_0/\lambda_m$. The parameterization of the creep rheology by μ_0 and $\dot{\varepsilon}_0$ is equivalent to a special choice of B:

$$B = \mu_{eff} \dot{E}^{1-\frac{1}{n}}$$

where B averages the temperature dependence of the creep throughout the crust.

As for the linear solution described in Appendix D, the non-linear equation is split into a left hand side, which is a partial differential equation in **u**(x,y), and a right hand side containing the remaining terms. The basal coupling term is split between the left and right-hand sides in the following manner:

$$2\frac{\partial}{\partial x_i}\left(S\mu_{eff} \frac{\partial \bar{u}_j}{\partial x_j} \right) + \frac{\partial}{\partial x_j}\left(S\mu_{eff}\left(\frac{\partial \bar{u}_i}{\partial x_j} + \frac{\partial \bar{u}_j}{\partial x_i} \right)\right) - \frac{\mu_b}{h}(\bar{u}_i - u_{mi})^{\frac{1}{n}-1}\bar{u}_i$$
$$= \frac{\rho_c g \phi}{2}\frac{\partial S^2}{\partial x_i} - \frac{\mu_b}{h}(\bar{u}_i - u_{mi})^{\frac{1}{n}-1} u_{mi} \qquad \text{....(15)}$$

where u_{mi} is the ith component of basal velocity. The program uses an iterative technique to solve for μ_{eff} and **u**, as follows:

<u>First pass</u>: solve the linear equation (13), using $\mu_{eff} = \mu_0$

<u>Subsequent passes</u>: solve equation (15), using $\mu_{eff} = \mu_0 \left(\dot{\bar{E}} / \dot{\varepsilon}_0 \right)^{\frac{1}{n}-1}$ where $\dot{\bar{E}}$ and the term in $(\bar{u}_i - u_{mi})^{\frac{1}{n}-1}$ are calculated from the previous iteration.

In general, solving the equation for a non-linear rheology in the crust and basal layer (n between 2 and 10) requires between 1-20 iterations to converge.

Updating the Crustal Grid

The crust is represented by a Lagrangian grid, so that after solving for **u**(x,y) at the nodes, the grid positions are updated as follows:

$$x_n = x_n + u_n \Delta t$$
$$y_n = y_n + v_n \Delta t$$

where (u_n, v_n) are the components of velocity **u**(x,y) at the nth node, and Δt is the time step interval, chosen so that:

$$|u_n \Delta t| << \Delta x$$
$$|v_n \Delta t| << \Delta y$$

for cell dimensions Δx and Δy in the x and y directions, respectively.

The advantage to using a Lagrangian grid is that the nodes follows the deformation of the viscous material. However, the grid may also become distorted, and this can be a problem numerically, if the aspect ratios of the elements become to large. (The aspect ratio of an element is defined to be the ratio of the element size in the x and y directions). Fortunately, for the large-scale problems investigated in this thesis, the grid does not become distorted enough for numerical problems of this type to occur.

Updating Crustal Thickness

After each timestep, with time interval Δt, the change in crustal thickness for each element is computed using the (Lagrangian) incompressibility condition:

$$\frac{\partial S}{\partial t} = S\dot{\varepsilon}_{zz}$$

The total volume is calculated at each timestep, to make sure that the program is conserving mass.

Calculation of the Height Field

The model assumes local isostatic compensation (see section 2.3), so the height H(x,y) is related to the crustal thickness, S, by:

$$H = (S - S_0)\left(1 - \frac{\rho_c}{\rho_m}\right)$$

Preliminary Testing of the Code

The code was tested against simple analytical solutions (Table 4(a)-(c)), giving agreement to within 1%. The code was also compared to the thin-sheet results of England and McKenzie (1983) and Houseman and England, 1986 (Table 4(d,e)), and showed qualitative agreement with velocities, strain-rates, and crustal thickness. Further one-dimensional tests of the type of boundary conditions discussed in section 2.3 (Table 4(f)) were performed by comparison with a fully cross-sectional plane-strain code results (see chapter 3).

Table 4: Testing the Thin-Sheet Code Against Analytical Solutions and Previous Numerical Results

Boundary Conditions[2]	Predicted Quantities
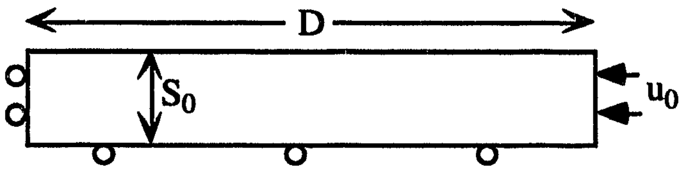 (a) Pure Shear	$\frac{\partial S}{\partial t} = \frac{u_0 S_0}{D}$ $(t'=0)$
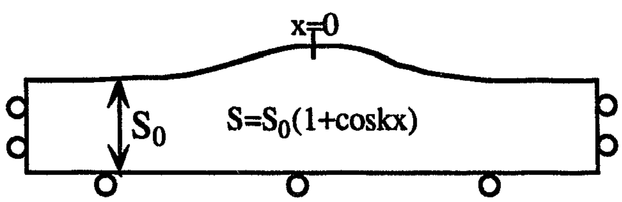 (b) Decay of Sinusoidal Topography	$\frac{\partial S}{\partial t}\Big\vert_{x=0} = -Ar\,u_0$ $(t'=0;\ n=1)$
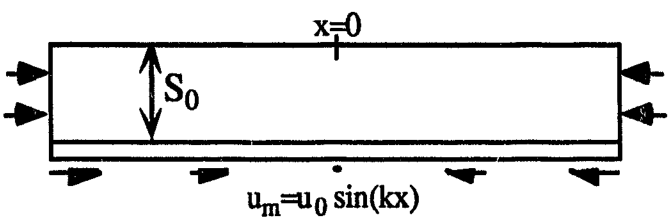 (c) Sinusoidal Basal Traction	$\frac{\partial S}{\partial t}\Big\vert_{x=0} = \left(\frac{k}{1+4k^2}\right)u_0$ $(t'=0;\ n=1)$

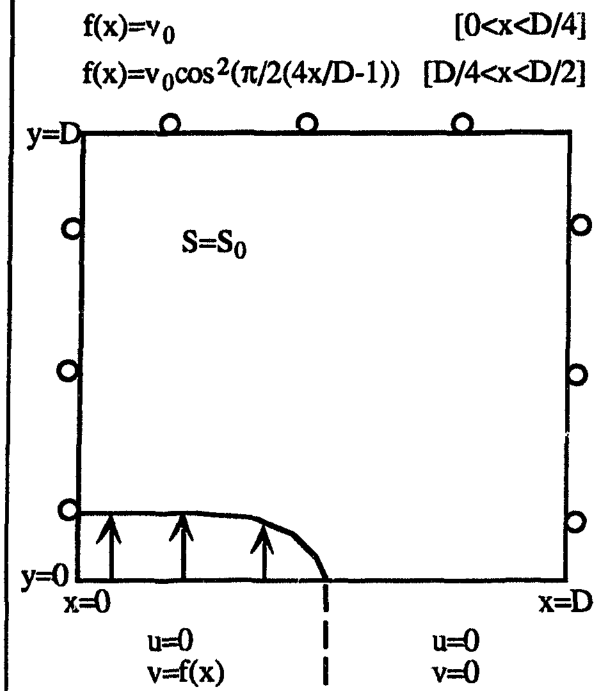

(d) England and McKenzie, 1983
(e) Houseman and England, 1986

(d) (for t′=0;
Ar=0,1,3,10,30;
n=1,3,5)

- velocity fields
- strain rates

(e) (for Ar=0,1,3,10;
n=1,3,10)

- velocity fields (t′=0)
- strain rates (t′=0)
- crustal thickness (t′=0 to 20)

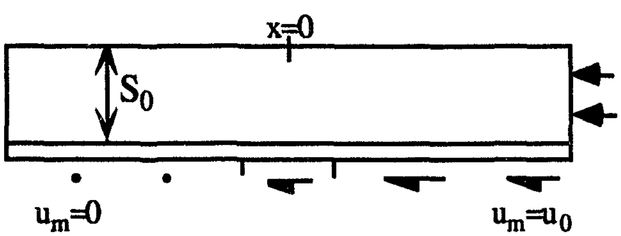

(f) Basal Detachment

- crustal thickness
- strain rates
- velocity fields

(See Chapter 3)

2 Unfilled circles on diagram represent 'roller' boundary conditions (i.e. no shear). Arrows represent velocities, and filled dots under figures indicate zero velocity. Initial crustal thickness is S_0.

§ 2.6 Modelling Syn-tectonic Surface Processes

Model Rationale

Tectonic processes such as those discussed in sections 2.1 and 2.2 do not provide the only mass fluxes in an orogenic system. Mass may also be transported and redistributed through *surface processes*, the erosion and deposition of material due to the interaction of topography and climate. Syn-tectonic surface processes can affect the deformation state of an orogen (Jamieson and Beaumont, 1988, 1989). Erosion may focus exhumation (the progressive exposure of rocks at the surface), creating or strengthening crustal shear zones, and thus considerably influencing the development of topography (Koons, 1990; Beaumont et al., 1992). Deposition of sediments can redistribute the topographic load into the flanking foreland basins, which form by flexural isostatic compensation in response to the tectonic loading of the convergent orogen (Flemings and Jordan, 1989; Johnson and Beaumont, 1995).

Surface mass redistribution is the result of a complicated set of processes such as soil creep, landslides, rainsplash, surface and subsurface wash on hill slopes (loosely grouped together as 'diffusive' processes), and long-range transport and deposition as bedload and suspended load in fluvial systems ('advective' processes) (Beaumont et al., 1992). Physical laws may be used to represent surface mass redistribution at the smallest spatial and temporal scales (i.e. length-scales on the order of meters, and timescales of days or months), but extension of this technique to larger scales is numerically difficult (Dietrich et al., 1992). A simpler approach to modelling larger spatial and temporal scale processes is to explore relationships between diffusion and advection on a topographic grid (Chase, 1988; Willgoose et al., 1991a,b; Beaumont et al., 1992). This approach implicitly assumes that the non-linearity of smaller scale processes, when integrated over larger resolution topographic cells, can be represented by linear or simple non-linear relationships, in a similar manner to using the laws of thermodynamics as an

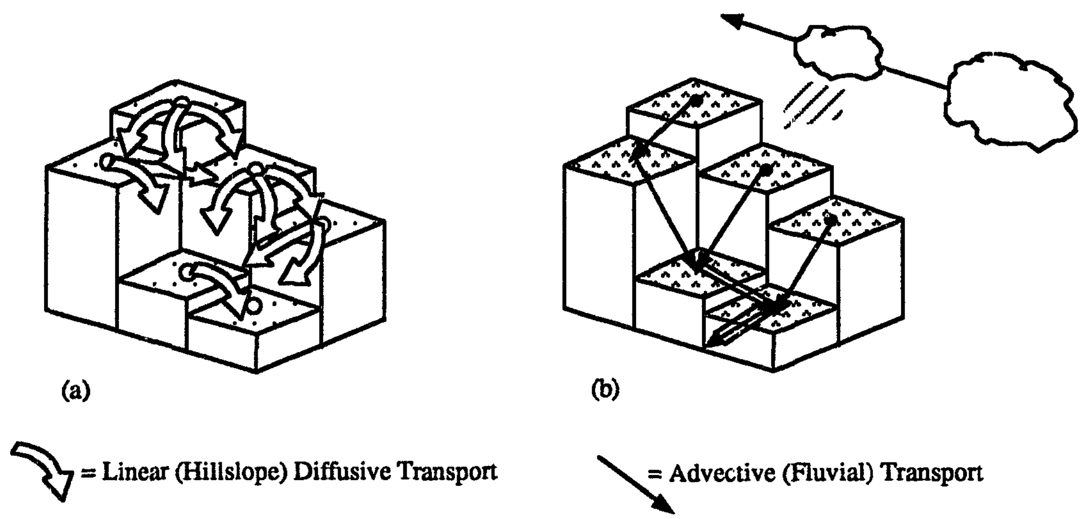

$$\frac{\partial H}{\partial t} = K_H \frac{\partial^2 H}{\partial x_i^2}$$

$$q_f^{eqb} = -K_f q_r \frac{\partial H}{\partial l}$$

equilibrium carrying capacity — fluvial transport coefficient — river discharge

Figure 8: A schematic illustration of (a) short range, hillslope diffusive transport, and (b) long range, advective (fluvial) transport on a topographic grid (modified after Johnson and Beaumont, 1995, and Beaumont et al., 1992). The arrows represent material flux between neighbouring topographic cells. Symbols not explained on the figure are H, the height of a cell; K_H, the diffusion coefficient; and l, the length-scale for a river segment.

approximation of the individual interactions between many molecules (Kooi and Beaumont, 1994).

Figure 8 illustrates the method behind the surface process model used by Beaumont et al. (1992). Mass transport is the sum of short range (diffusive) and long range (advective) transport down a topographic grid. The model tracks the cumulative fluvial discharge down a drainage network, and calculates river power (as a function of slope and discharge) in order to determine the carrying capacity of each river segment. The effect of spatial scale on the division between diffusive and advective surface processes is discussed by Kooi and Beaumont (1994). The model cannot represent sub-grid fluvial processes, as only one river is modelled per cell. A model drainage density greater than the grid resolution is therefore represented by diffusive processes. Diffusion in surface process models based on a topographic grid thus includes not only the true diffusive processes, but also fluvial transport at the sub-grid level (Kooi and Beaumont, 1994). This simplifiying assumption follows from measurement of diffusivity values from escarpment studies (figure 9). The measurements indicate that, as the scale of the escarpment increases, so does the effective diffusivity.

The models in this thesis do not include the syn-tectonic surface processes discussed above. Results from the next chapter will show that the thin-sheet model is only valid for large scale orogens, where deformation extends for horizontal distances several times larger than the crustal thickness. The spatial scale of the topographic grid is large in comparison to most of the studies illustrated in figure 9, so that if surface processes were included in the models, only diffusive effects need be considered. This simplification could be made because of the increasing use of diffusion to represent both true diffusive and sub-scale advective processes as the spatial scale of the model increases.

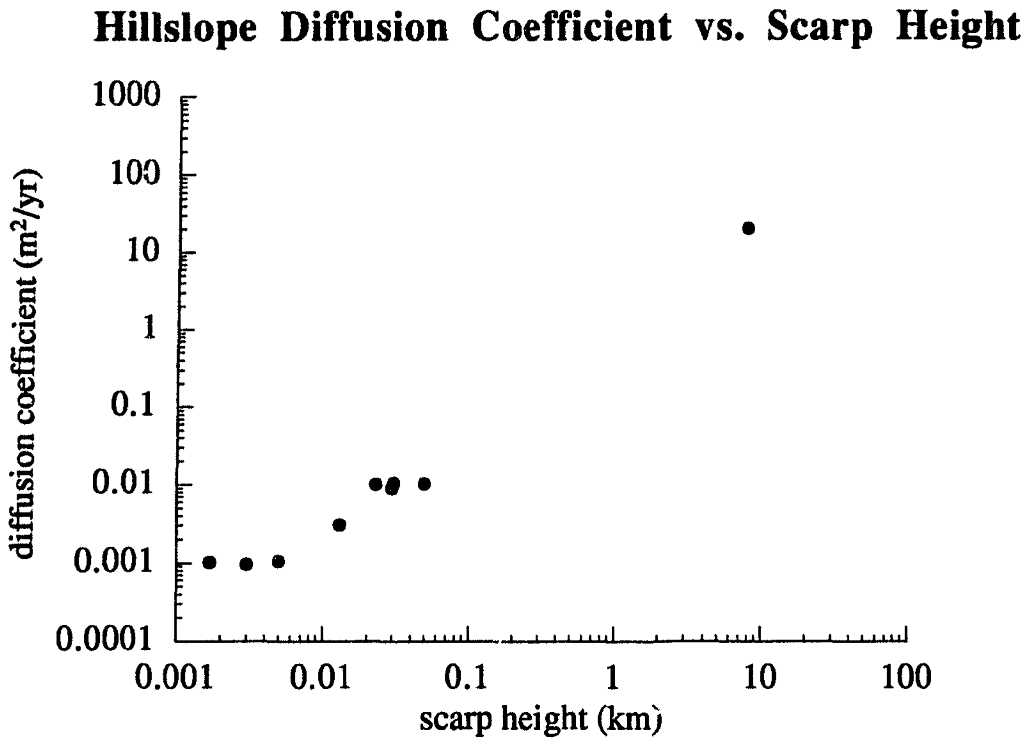

Figure 9: A plot of the empirically-derived diffusion coefficient, K_H, vs. scarp height. Values are derived from Hanks et al. (1984), Colman and Watson (1983), Nash (1980), and Moretti and Turcotte (1985).

An interesting study would be to use a planform coupled tectonic/surface process model to determine whether the redistribution of mass at the surface is as important a control on the development of a convergent orogen as the effects of gravity acting on crustal thickness contrasts (represented by Ar), and basal forcing (Am). Studies have already been conducted for the cross-sectional case (e.g. Beaumont et al., 1992), but results for a planform tectonic model, especially if it involved a simple scale analysis, may be useful in determining first-order controls for cases of oblique collision, or where convergence varies along-strike. Note that the asymmetrical erosion caused by orographic precipitation acting on the fluvial system, which was found to be important for the cross-sectional case (Beaumont et al., 1992), could not be represented by a simple diffusional model, unless a discharge term was incorporated into the diffusion coefficient (e.g. Paola et al., 1992).

Below, I outline the method that could be used to add a simple (uniform) surface process diffusion coefficient to the model.

Surface Process Formulation

Mass transport by diffusion obeys an equation of the form:

$$\frac{\partial H}{\partial t} = K_H \frac{\partial^2 H}{\partial x_i^2}$$

where H is the height of excess topography, K_H is a diffusion coefficient (m^2s^{-1}), and summation over index i is implied. When local isostatic compensation is assumed, the excess height $H=(S-S_0)\phi$, and the diffusion equation can be rewritten in terms of crustal thickness, S:

$$\frac{\partial S}{\partial t} = K_H \frac{\partial^2 S}{\partial x_i^2}$$

Adding this term to the equation for conservation of mass:

$$\frac{\partial S}{\partial t} = -\frac{\partial (S\bar{u}_j)}{\partial x_j} + K_H \frac{\partial^2 S}{\partial x_j^2}$$

and normalizing for the case where λ_m -> S_0 ($t'=tu_0/S_0$, $S'=S/S_0$, $u'=u/u_0$, $x'=x/S_0$) gives:

$$\frac{\partial S'}{\partial t'} = -\frac{\partial (S'\bar{u}'_j)}{\partial x'_j} + \frac{K_H}{u_0 S_0}\frac{\partial^2 S'}{\partial x'^2_j} = -\frac{\partial (S'\bar{u}'_j)}{\partial x'_j} + \left(\frac{1}{Pe}\right)\frac{\partial^2 S'}{\partial x'^2_j} \qquad \text{....(16)}$$

where Pe (= K_H/u_0S_0), a dimensionless Peclet number, represents the relative importance of tectonic advection and horizontal (surface process) diffusion.

Incorporating the Diffusive Surface Process Model in the Numerical Code

When the tectonic thickening has been computed, mass can be redistributed (according to diffusive surface processes) by a geometric update of the topography, using a diffusive surface process algorithm developed by Beaumont et al., 1992. The diffusive transport is directly related to the height field H, by the diffusion equation:

$$\frac{\partial H}{\partial t} = K_H \frac{\partial^2 H}{\partial {x_j}^2}$$

The diffusion coefficient K_H can also be thought of as the product of a transport speed, u_S, and a vertical height scale of the erodable surface boundary layer, h_S (Beaumont et al., 1992).

The diffusive algorithm loops from the highest to the lowest cell. Mass is redistributed to adjacent cells by an amount proportional to the slope between cell midpoints (figure 8(a)). Transport to each topographic cell is the linear sum of mass transport from each of the eight neighbours. The total change in height of cell j due to possible mass fluxes from the eight adjacent cells is given by:

$$(D_s)_j = \frac{1}{\Delta L^2}\sum_{i=1}^{8}(Q_s)_{ij}$$

The incremental diffusion amounts, (D_S), can be added to the height field at the end of each erosion timestep. The boundaries of the grid are assumed to be in the far-field zone where there is no crustal thickening, so that the diffusive erosion flux at the boundaries is set to zero.

An alternative method for incorporating diffusive surface processes into the tectonic model would be by an implicit numerical solution of the diffusion equation over the planform height field.

Chapter Three

TESTING THE MODEL

Before exploring the two dimensional[3] behaviour of the model, it is necessary to find the range of parameters for which it can be considered to be a good approximation of the behaviour of the crust. This chapter is divided into three sections, each of which investigates a different aspect of the model parameterization. The first section determines the rheological basis for using the Ampferer number to describe crust-mantle interactions. This is achieved using a series of cross-sectional, frictional[3]-viscous models of the crust.

The thin-sheet approximation limits the application of the model to large-scale (weakly coupled) cases. These model limitations are quantitatively described in section 3.2, using a comparison between the one-dimensional thin-sheet model and the equivalent, cross-sectional model which uses the plane-strain approximation. In the last section, the effect of the model parameters Am, n, and Ar on the style of deformation is investigated.

§ 3.1 Choice of Parameters for Basal Coupling

Review of Rheological Models of the Lithosphere

Depth distributions of continental earthquake foci, laboratory studies of rock specimens subjected to strain-rates at various pressures and temperatures, and styles of deformation evident from exhumed crustal rocks, all indicate that shallow crustal rocks

---

[3] Throughout this discussion, I avoid the use of the term 'plastic', because the definition for plastic used by rock mechanicists and rock materialists is different (Mandl, 1988). The preferred definition is that a plastic material has a finite yield strength, which (if exceeded) leads to continuous irrecoverable deformation. The term 'frictional' refers to a specific type of plastic behaviour, where deformation is pressure sensitive, and thus includes brittle deformation.

fail by brittle fracture[4], generating earthquakes, whereas deep crustal rocks deform anelastically by ductile flow[5]. These observations suggest a rheological stratification of the crust, with transitions between different rheological layers occurring at depths dependent on the thermal thickness of the lithosphere. The rheological stratification depends strongly on the compositional layering of the lithosphere.

In an effort to quantify the presumed rheological stratification of the lithosphere, Ranalli and Murphy (1987), Strehlau and Meissner (1987), and others have constructed *strength profiles* based on empirically derived laws for given material layers, and an assumed geotherm for the lithosphere. A strength profile $\sigma(z)$ represents the maximum deviatoric stress difference able to be sustained in the brittle regime, and the flow stress for a given strain-rate in the ductile regime. The maximum stress difference $\sigma(z)$ is defined as:

$$\begin{aligned} \sigma &= \sigma_1 - \sigma_3 \\ &= 2\tau_{max} \end{aligned}$$

where σ_1 and σ_3 are the maximum and minimum principal stresses, respectively, and τ_{max} is the maximum shear stress. The choice of whether crustal material deforms in the brittle or ductile regime is determined by which style of deformation that requires the smaller stress difference, $\sigma_{brittle}$ vs. $\sigma_{ductile}$ (i.e. if $\sigma_{brittle} < \sigma_{ductile}$, the material will deform by brittle processes, and vice-versa).

Strength profiles are constructed using geophysical data and the results from laboratory measurements, extrapolated via theoretical creep mechanisms. A representative rheology must be assumed for the lithosphere, most commonly a simplified rheology

---

[4] Brittle fracture is discontinous deformation by a combination of elastic and anelastic (strain-rate dependent) processes.

[5] Ductile flow is defined as viscous behaviour where there is a direct relationship between shear stress and strain rate (Mandl, 1988).

with a quartz-rich crust and olivine-rich mantle, although the rheology may be determined from the particular geological history of the study area (eg: Ranalli and Murphy, 1987). The mechanical layering that results from simplified rheological models is not necessarily considered to be a layering of rock types, but a layering in which various minerals (Qz, Fsp, Ol) are the dominant contributors to the observed strength of the crust (Ord and Hobbs, 1989).

The variation of temperature with depth is chosen using representative geotherms for particular geological situations, constrained at the surface by T = 300K, and at the bottom of the lithosphere by Tm = 1500K. Knowledge of the variation of temperature and radiogenic heat production with increasing depth is essential in order to construct appropriate strength profiles. A geotherm may be perturbed from steady-state by magmatic activity, or tectonic displacement of crustal material. It is claimed that data from surface heat flow measurements, and an accurate petrological model for the crust and mantle, can constrain lithospheric temperatures to within ± 100 K (Ranalli, 1987).

Following Goetze and Evans (1979), it is generally assumed that the shear strength of the upper crust is controlled by frictional sliding within a well-fractured material. For this case, the frictional relationship is given by:

$$\tau = \eta \sigma_n$$

(Brace and Byerlee, 1966; Byerlee, 1968) where τ and σ_n are the shear and normal stress on a plane, and η is the coefficient of friction along surfaces within the material. The coefficient of friction may also be written as tan ϕ, where ϕ is the angle of internal friction.

The frictional relationship may also be modified by the presence of rock cohesion, C, giving the Coulomb yield stress:

$$\tau = \tan\phi\,\sigma_n + C \qquad \text{...(17)}$$

If it is assumed that the maximum normal stress is due to the weight of the overburden, eq. (17) may also be written as:

$$\tau \approx \tan\phi\,\rho g z(1-\delta) + C$$

where δ is the pore fluid factor:

$$\delta = \frac{p_f}{\rho g z}$$

defined as the ratio of pore fluid pressure, p_f, to the lithostatic (overburden) pressure.

The yield stress τ defines the necessary shear stress for frictional sliding to occur. Neglecting the cohesion term, and assuming that the pore fluid factor is incorporated into the frictional coefficient, the stress difference in the brittle regime may therefore be written as:

$$\sigma = 2\tau \approx (2\tan\phi)\rho g z$$

The maximum ductile stress difference is calculated by assuming a strain-rate $\dot{\varepsilon}$, to be:

$$\sigma = B\exp\left(Q/_{nRT}\right)(\dot{\varepsilon})^{\frac{1}{n}} \qquad \text{...(18)}$$

where B is a material parameter, Q is the creep activation enthalpy and n is the power law exponent (Ranalli and Murphy, 1987). This equation was derived empirically from laboratory studies of rock deformation. The experiments are mostly performed by keeping the strain-rate constant, under triaxial stress conditions (where $\sigma_1 > \sigma_2 = \sigma_3$), yielding an equation of the form:

$$\mu = A\, J_{2D}^{(1-n)/2} \exp\left(-Q/_{RT}\right)$$

where J_{2D} is the second invariant of the stress tensor. The relationship between A and B is not straightforward, because a geometrical factor must be included in order to translate the triaxial confining pressure into the stresses found in the earth (Braun, 1988).

Most materials under laboratory conditions in the ductile field exhibit a power-law rheology (i.e. n>1), and the exponent n generally increases with stress if experiments are conducted over more than two orders of stress magnitude, due to the dominance of different creep mechanisms at different stresses or pressure/temperature conditions.

Sources of Uncertainty in the Construction of Strength Profiles

(1) Depth to the Brittle-Ductile Transition

The strength profiles discussed above assume that shear stress increases linearly with depth until the frictional relation intersects the ductile yield stress for a given rock type and strain-rate . Sibson (1982) suggested that the cutoff depth for earthquakes (the base of the seismogenic zone) is equivalent to the depth of transition from brittle to ductile behaviour, with the presence of large earthquakes at depth attributed to the increasing shear strength with depth. However, for low geothermal gradients (i.e. where ductile yield stress remains large to quite considerable depths), the Byerlee relation predicts that seismogenic activity should be present throughout the crust and lower mantle, but this is not observed. If the frictional relation does not give a good representation of rock deformation beyond moderate temperatures and pressures, then the maximum stress levels sustainable will be much lower (Ord and Hobbs, 1989). Empirical estimates of the maximum stresses sustainable by the lithosphere using seismic data indicate that stresses beyond 300 MPa cannot be sustained, bringing the upper stress estimates for the crust from 700 MPa (in thrust regimes) down to about 300 MPa.

Evidence for a Byerlee law breakdown can also be found in laboratory studies. The transition from brittle to ductile behaviour observed in quartz indicates that several different deformation mechanisms are involved (Hirth and Tullis, 1994), suggesting that the brittle-ductile transition occurs over a wide range of depths in the crust.

(2) Extrapolation of Microphysical Creep Models

Because of the impossibility of conducting laboratory measurements at the strain-rates of the lower lithosphere, a means must be found of observing the relevant process in the laboratory in order to establish its dynamic characteristics. Extrapolation must then be made to geological conditions by assuming that the mechanism of the geological process is the same as that in the laboratory (Paterson, 1990). This is a major source of uncertainty in the characterization of flow laws for the lower crust. An excellent summary of the sources of error in laboratory measurements may be found in Strehlau and Meissner (1987).

Flow stress decreases with increasing temperature and increases with increasing strain-rate, because both temperature and strain-rate affect the creep activation energy. Consequently, the deformation produced by an increase in temperature is equivalent to that caused by a decrease in strain-rate. This equivalence is often used to justify the extrapolation of laboratory results (where strain-rates cannot be measured below $10^{-8}\ s^{-1}$) to geodynamical conditions (where $10^{-15} \leq \dot{\varepsilon} \leq 10^{-10}\ s^{-1}$). The extrapolation of empirical steady-state flow equations derived from laboratory experiments to the much lower strain-rates of the lithosphere, is partly justified by the observation that rocks deformed under natural high temperature creep conditions appear almost identical to minerals deformed in the laboratory (Carter and Tsenn, 1987). There is also considerable support in microphysical creep theory for a Dorn-type power law equation operating at high temperatures. Extrapolation to the lithosphere is achieved for each constituent mineral by using empirically derived values for A, n, E, and V, constrained by deformation maps. However, only processes that can be studied readily in the laboratory, such as dislocation creep, are well understood. Natural processes that operate too slowly for convenient laboratory study, such as pressure solution, are much less well understood. The extrapolation of laboratory data may therefore produce a biased representation of the true deformation processes of the lithosphere.

(3) Hydrolytic Weakening

A quantitative constitutive relation describing the effect of hydrolytic weakening on rocks is still lacking. Purely mechanical effects of fluids on rock deformation are reasonably well understood, but equally important chemical effects are yet to be quantitatively explained (Carter et al., 1990). Within the field of brittle deformation, research suggests that rock strengths are much lower than those predicted by Byerlee's relation, because even trace quantities of water present on frictional surfaces will result in a marked lowering of the frictional coefficient, due to formation of gouge surfaces (Carter et al., 1990).

Within the ductile field, shear localization is enhanced by fluid penetration and weakening. Water related defects may gain access to grain interiors via fluid infiltration along open microcracks, where present. Laboratory experiments show that wet rock strengths, where 'wet' indicates significant water within the mineral structure, are often an order of magnitude lower than strengths of dry rocks (Ranalli, 1987). The weakening effect is only present above a threshold temperature and confining pressure, and seems to increase with grain boundary area, suggesting that hydrolytic weakening concentrates at grain boundaries. As yet there is no unambiguous model for hydrolytic weakening in creep processes. It is an important factor in the lower crust wherever hydrous minerals (e.g. amphiboles) become unstable.

(4) Localization of shear zones

Localized shear zones within ductile regions are thought to be widespread in the crust (Rutter and Brodie, 1988), and possibly the upper mantle. Their presence may substantially alter the distribution of stress in the continental crust (Kirby, 1985).

Rock strength in the ductile regime may be locally reduced by strain softening processes such as *dynamic recrystallization*, which takes place during high temperature deformation of minerals undergoing power law creep. Dynamic recrystallization is related to the rearrangement of dislocations within grains into new, lower energy configurations. It is an important process over approximately the same range of temperature and stress fields as power law creep, and leads to transient episodes of accelerated flow on the creep curve. Changes in grain size with increasing strain may also localize deformation, by causing a change in the deformation mechanism.

The temperature dependance of a strain softening process such as dynamic recrystallization leads to the interesting result that for a given rock type, low temperature shear zones are narrower and have higher strain gradients than high temperature shear zones (Handy, 1989). Construction of strain-dependent yield profiles over the temperature range of the subcontinental mantle (Rutter and Brodie, 1988) shows that the effect of dynamic recrystallization is to reduce the strength contrast otherwise found at the Moho, and may actually cause a strength minimum within the upper mantle.

(5) Poly-mineralic Assemblages

The extrapolation of flow laws from the laboratory to the lithosphere is generally made under the assumption that lithosphere rheology can be adequately represented by the weakest or most abundant mineral present at each 'layer' of the sandwich. However, studies of polymineralic rocks usually show that several minerals, rather than just the weakest, are deformed and collectively determine the rheology of the aggregate (Handy, 1990; Hirth and Tullis, 1994).

Deformation of rocks containing two or more minerals undergoing different deformation styles (eg: an aggregate of semibrittle calcite and ductile halite) is complex and not yet thoroughly understood (Evans and Dresen, 1991). Elementary microphysics can be used to show that stress becomes magnified around an isolated rigid inclusion in an isotropic elastic medium (Jaeger and Cook, 1979). Rigid inclusions in ductile materials can increase the plastic flow strength, as the rigid minerals form obstacles for dislocation glide.

In summary, fundamental criticisms of the use of strength profiles include the necessity for extrapolation of rate laws from the scale of the laboratory to that of the lithosphere. The region of transition from shallow crustal, brittle faulting to deeper crustal ductile flow is a complex and wide zone that has been mostly ignored in the construction of strength envelopes. It is unclear whether Byerlee's law is valid at the deeper crustal range of the brittle field, and this may lead to significant overestimates of lithospheric strength. In extrapolations to the ductile regime most rock experiments are carried out on monomineralic rocks, whereas the lithosphere contains complex polyphase aggregates of minerals. The role of hydrolytic weakening, shear localization and recrystallization in deformation styles of the lower crust have not been fully explored, and relatively little effort has been made to understand the transient rheology of rocks (Rutter and Brodie, 1991).

Generic and Dynamic Strength Profiles for Continental Crust of Uniform Composition

(a) Introduction

Strength profiles constructed using the assumption of overburden pressure in eq.

17, and an assumed strain-rate in eq. 18, are 'generic' in the sense that they are not specific to a particular deformation history. The main weakness of generic strength profiles is that they assume a uniform strain-rate $\dot{\varepsilon}_0$ throughout the ductile region. In reality, strain-rates will vary in space and time, depending on the configuration of boundary stresses and the material properties of the lithosphere.

A more dynamic determination of strength profiles can be obtained by using the equations (17) and (18) directly in a geodynamic model, which computes strain-rates and stresses implicitly. Strength profiles produced in this manner are specific to the problem being solved. I construct both generic and dynamic strength profiles below, in order to determine the range of geotherms for which a weak layer is present at the Moho. Although dynamically determined strength profiles create a more internally consistent model of the rheological stratification of the lithosphere than generic profiles, they still suffer from the uncertainties inherent in defining a rheology and mechanical behaviour of the crust.

(b) Choice of boundary conditions and material properties

Generic and dynamic strength profiles are determined for the boundary conditions of figure 5(a). The generic strength profiles are calculated for the three representative crustal types described in Table 5, and dynamic strength profiles are found for the two continental crust cases described in Table 5. A linear crustal geotherm is assumed, from 0 °C at the surface to a specified temperature at the Moho. The continental crust is represented by a uniform layer with the properties of wet feldspar, where 'wet' indicates that the properties were determined for a sample which was dried in air at a low temperature (160 °C), thus removing surficial water, but retaining the water within the crystal structure. The oceanic crust is represented by a uniform layer with the material properties of diabase (a polyphase basic igneous rock). Material properties are taken from Braun (1988) who calculated the parameter B for wet feldspar and diabase from the laboratory measurements of Shelton and Tullis (1981).

Table 5: Representative cases used in determining strength profiles

type of crust	*surface temperature (℃)*	*Moho temperature (℃)*	*Material properties*
30km thick, cold continental	0	450	wet feldspar[6]
30km thick, hot continental	0	600	wet feldspar[6]
10km thick, oceanic	0	200	diabase[7]

[6]wet feldspar; B=3e6 Pa $s^{1/n}$; Q=2.4e5 mol J^{-1}; n=3.2
[7]diabase; B=1.22e7 Pa $s^{1/n}$; Q=2.6e5 mol J^{-1}; n=3.4

The strain-rates used in the generic profiles are estimated from the average strain-rates over the singularity derived from the geodynamic model results. Dynamic strength profiles are computed with a geodynamic model which uses the plane-strain approximation, and the boundary conditions of figure 5(a). The edges of the model domain are taken to be sufficiently far away so that no thickening occurs along them. At the right hand boundary, the mantle velocity u_m is equal to the far-field velocity of the lithospheric plate, u_0. The formulation of the finite element plane-strain model is similar to the thin-sheet model, except that it is cross-sectional rather than planform, and so does not need to assume constant velocity with depth. I use a model based on the method of Fullsack (1995). Deformation in the brittle layer follows a Coulomb rheology (eq. 17):

$$\tau_{max} = (\tan\phi)\sigma$$

where τ_{max} ($=1/2(\sigma_1-\sigma_3)$) is the maximum shear stress that may be obtained in the material before deformation, ϕ is the angle of internal friction in the material, taken to be 15°, and σ is the normal stress on the plane of failure. Deformation in the ductile regime follows equation (18). To highlight the comparisons between figures, the crust is not isostatically compensated.

(c) Comparison between generic and dynamic strength profiles

The computed generic strength profiles and equivalent effective viscosities for hot and cold continental crust, and oceanic crust, are shown in figure 10. The effective viscosity is estimated by straightforward division of components of the stress tensor by the corresponding strain-rate components. Within the layer dominated by Coulomb behaviour, the effective viscosity therefore gives an estimate of the equivalent 'viscous' behaviour for each increment of deformation. Note that the continental profiles are calculated for a crustal thickness of 30km. This thickness may be an underestimate for geologically old continental crust.

Figure 10: (a) Generic strength profiles, and (b) effective viscosities, for cold and hot continental crust, and oceanic crust. The reference strain-rates for ductile deformation are taken from the dynamic profiles of the next sub-section (see figures 12 and 13). The crust is assumed to be 30km thick, and $\sigma = \sigma_1 - \sigma_3$ as described in section 3.1.

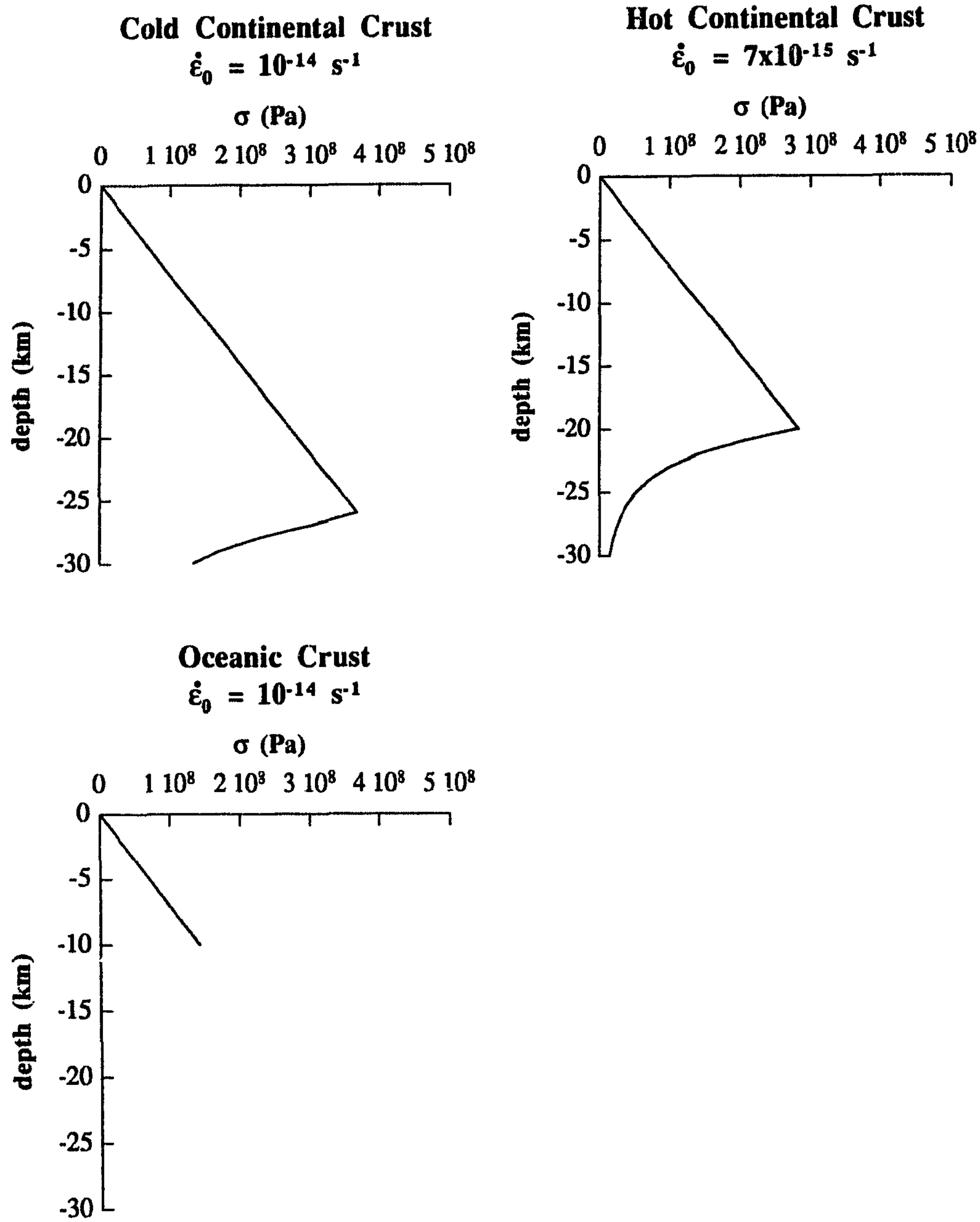

Cold Continental Crust
$\dot{\varepsilon}_0 = 10^{-14}\ s^{-1}$
σ (Pa)
0 1 10⁸ 2 10⁸ 3 10⁸ 4 10⁸ 5 10⁸
depth (km)
0 -5 -10 -15 -20 -25 -30
Hot Continental Crust
$\dot{\varepsilon}_0 = 7x10^{-15}\ s^{-1}$
σ (Pa)
0 1 10⁸ 2 10⁸ 3 10⁸ 4 10⁸ 5 10⁸
depth (km)
0 -5 -10 -15 -20 -25 -30
Oceanic Crust
$\dot{\varepsilon}_0 = 10^{-14}\ s^{-1}$
σ (Pa)
0 1 10⁸ 2 10⁸ 3 10⁸ 4 10⁸ 5 10⁸
depth (km)
0 -5 -10 -15 -20 -25 -30

Figure 10(a)

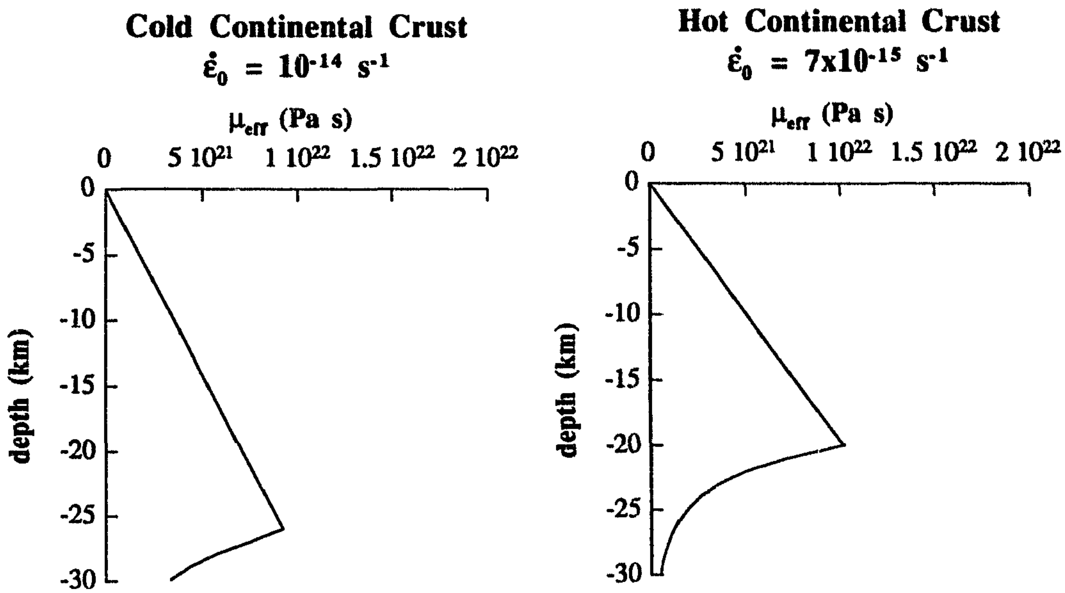

Cold Continental Crust
$\dot{\varepsilon}_0 = 10^{-14}\ s^{-1}$
μ_{eff} (Pa s)
0
5 10²¹
1 10²²
1.5 10²²
2 10²²
0
-5
-10
-15
-20
-25
-30
depth (km)
Hot Continental Crust
$\dot{\varepsilon}_0 = 7x10^{-15}\ s^{-1}$
μ_{eff} (Pa s)
0
5 10²¹
1 10²²
1.5 10²²
2 10²²
0
-5
-10
-15
-20
-25
-30
depth (km)

Figure 10(b)

In the generic strength profiles, the two continental cases have a strength minimum near the Moho; this minimum is most marked for the hot continental crust case. The presence of a weak detachment layer at the Moho is consistent with the interpretation of many seismic reflection profiles of convergent orogens (e.g. Cook and Varsek, 1994). The oceanic crust has increasing strength down to the Moho.

The dynamic strength profiles for hot and cold continental crust (figure 11) also exhibit strength minima at the Moho similar to the generic strength profiles; however, the maximum stresses sustained in the brittle regions are slightly higher than for the generic profiles, and vary spatially. The maximum stress difference is largest near the singularity, where strain-rates are highest. The stress difference peak near the singularity is especially marked for the cold continental case.

Figure 11: Dynamic strength profiles and contour plots for (a) cold continental, and (b) hot continental crust. Contours are of maximum deviatoric stress difference, σ. Stresses are computed using the boundary conditions of figure 5(a), with crustal thickness S_0=30km, far-field velocity u_0=2cm/yr, and mantle detachment length λ_m=20km. The zone of basal detachment is indicated by the box drawn underneath the contour plots.

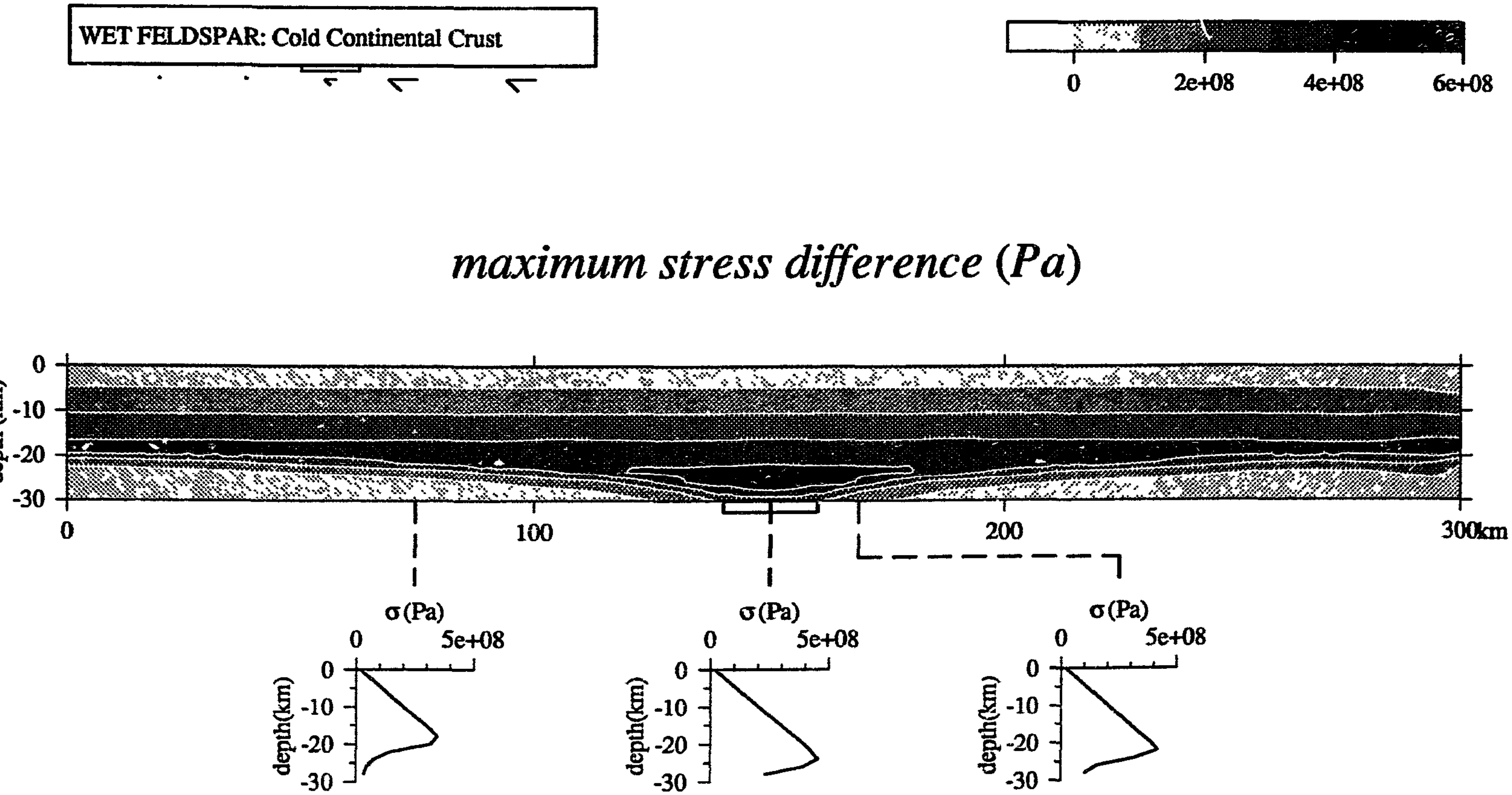
WET FELDSPAR: Cold Continental Crust
0
2e+08
4e+08
6e+08
maximum stress difference (Pa)
depth (km)
0
-10
-20
-30
0
100
200
300km
σ (Pa)
0
5e+08
depth(km)
0
-10
-20
-30
σ (Pa)
0
5e+08
depth(km)
0
-10
-20
-30
σ (Pa)
0
5e+08
depth(km)
0
-10
-20
-30

Figure 11(a)

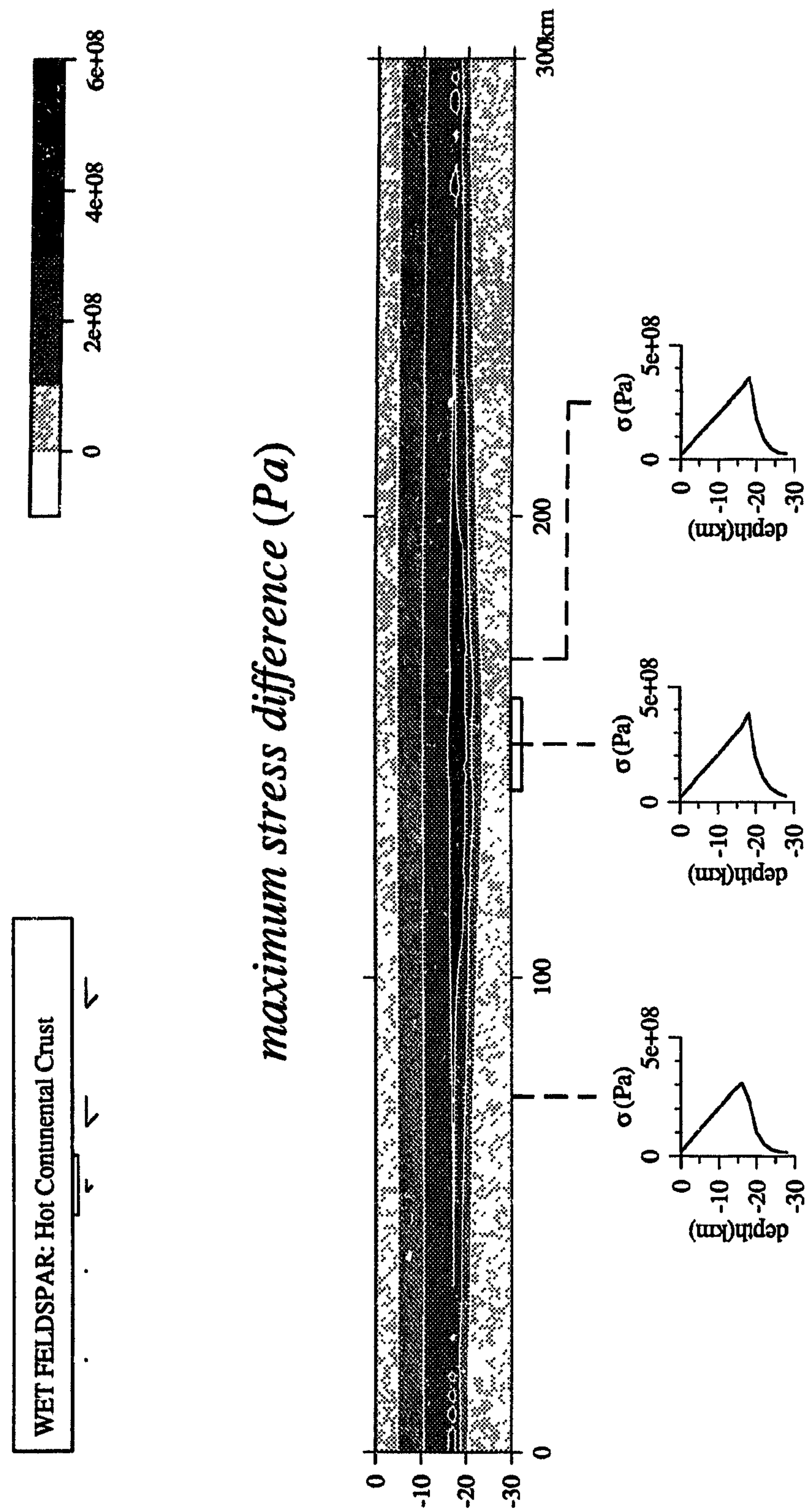
WET FELDSPAR: Hot Continental Crust
maximum stress difference (Pa)
0
2e+08
4e+08
6e+08
depth (km)
0
100
200
300km
σ (Pa)
5e+08
depth(km)

Figure 11(b)

Despite the appearance of close agreement between the generic and dynamic strength profiles, there are major differences, as can be demonstrated by comparing the estimated effective viscosity for the generic cases (figure 10(b)) with those for the geodynamic model (figures 12(c) and 13(c)). In particular, there is no spatial variation in effective viscosity for the generic model, because the strain-rate is assumed to be uniform.

Determining an Equivalent Two-Layer Viscous Rheology

The thin-sheet model formulation with a weak detachment layer, described in chapter two, parameterizes the behaviour of the crust using the scaling parameter Am. The Ampferer number represents the degree of coupling between the crust and mantle lithosphere, using the ratio of viscosities for the weak detachment layer and the crust (e.g. μ_b/μ_c for a linear viscous case). To determine a rheologically valid range for Am, it is necessary to consider the dependence of (effective) crustal and basal viscosities on the compositional layering, temperature, and pressure conditions in the crust. This is achieved using the strength profiles discussed in the previous sub-section, by finding an equivalent two-layer viscous rheology, in order to determine μ_b and μ_c.

Figure 12: Contour plots and vertical profiles of (a) horizontal strain-rate; (b) vertical shear strain-rate, and (c) effective viscosity, for the cold continental geotherm case. Boundary conditions are the same as for figure 11.

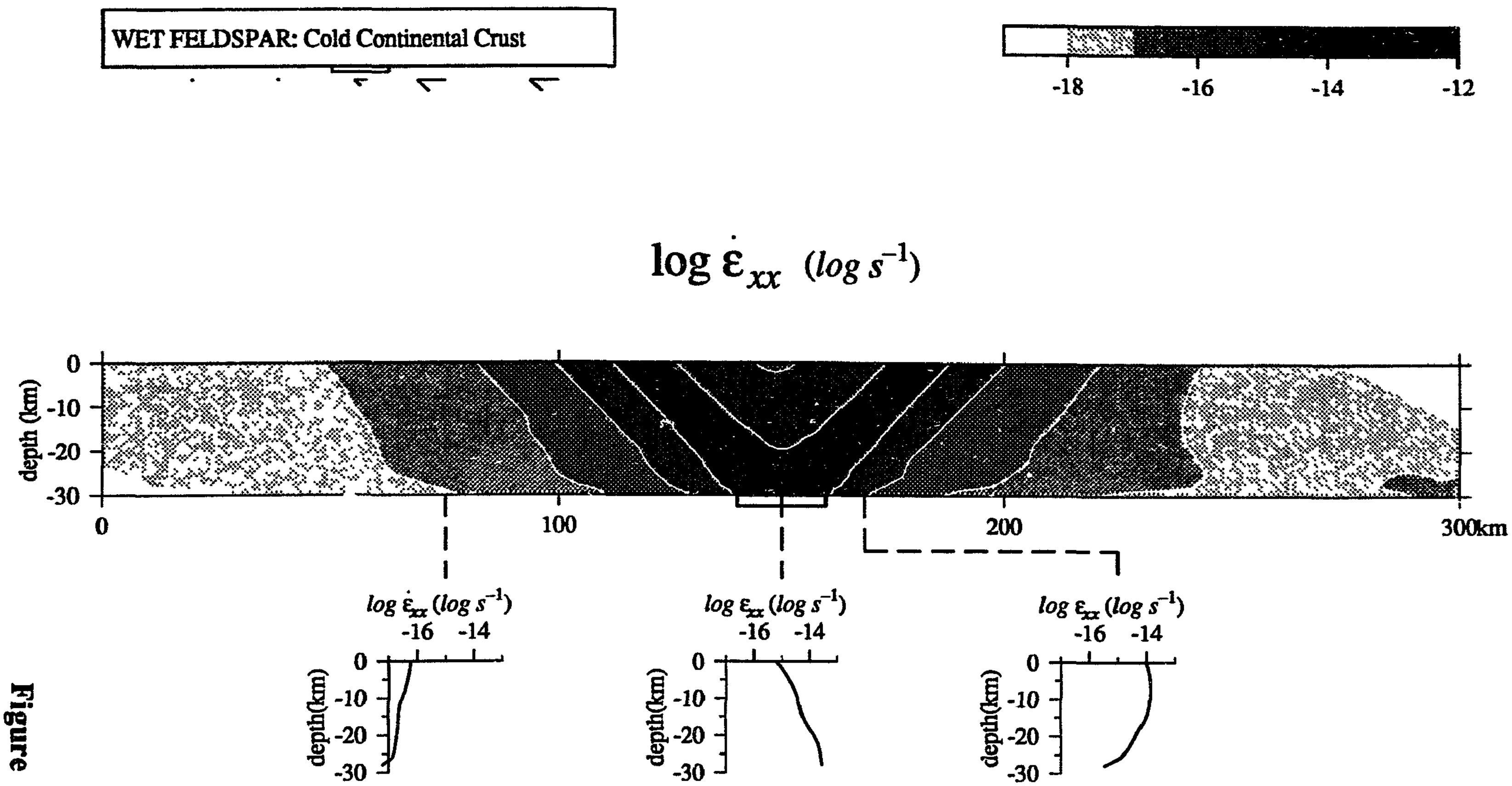

WET FELDSPAR: Cold Continental Crust
-18
-16
-14
-12
log $\dot{\varepsilon}_{xx}$ (log s^{-1})
depth (km)
0
-10
-20
-30
0
100
200
300km
log $\dot{\varepsilon}_{xx}$ (log s^{-1})
-16 -14
depth(km)
0
-10
-20
-30
log $\dot{\varepsilon}_{xx}$ (log s^{-1})
-16 -14
depth(km)
0
-10
-20
-30
log $\dot{\varepsilon}_{xx}$ (log s^{-1})
-16 -14
depth(km)
0
-10
-20
-30

Figure 12(a)

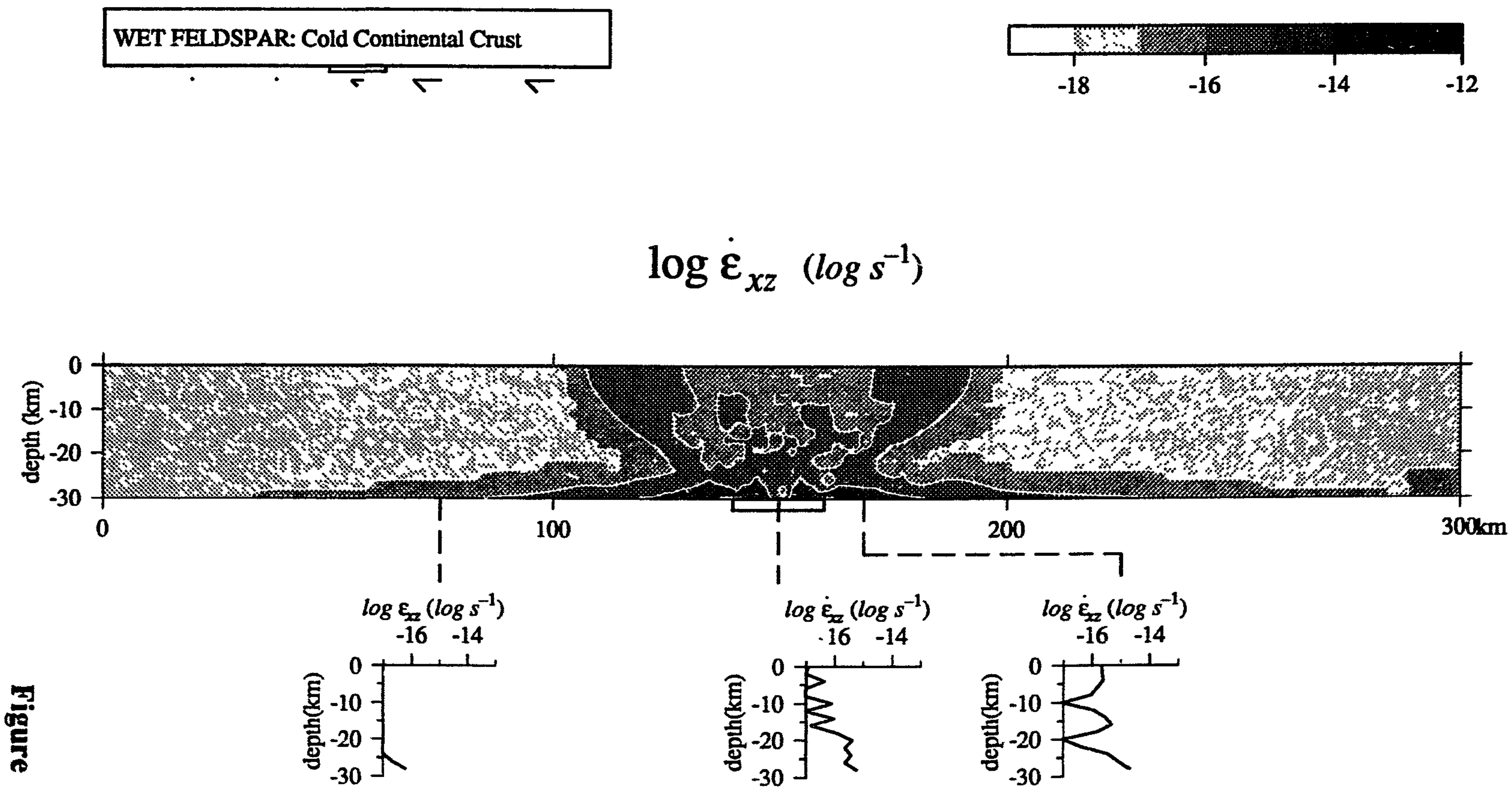
WET FELDSPAR: Cold Continental Crust
-18
-16
-14
-12
log ε̇xz (log s-1)
0
-10
-20
-30
depth (km)
0
100
200
300km
log ε̇xz (log s-1)
-16 -14
depth(km)
log ε̇xz (log s-1)
-16 -14
depth(km)
log ε̇xz (log s-1)
-16 -14
depth(km)

Figure 12(b)

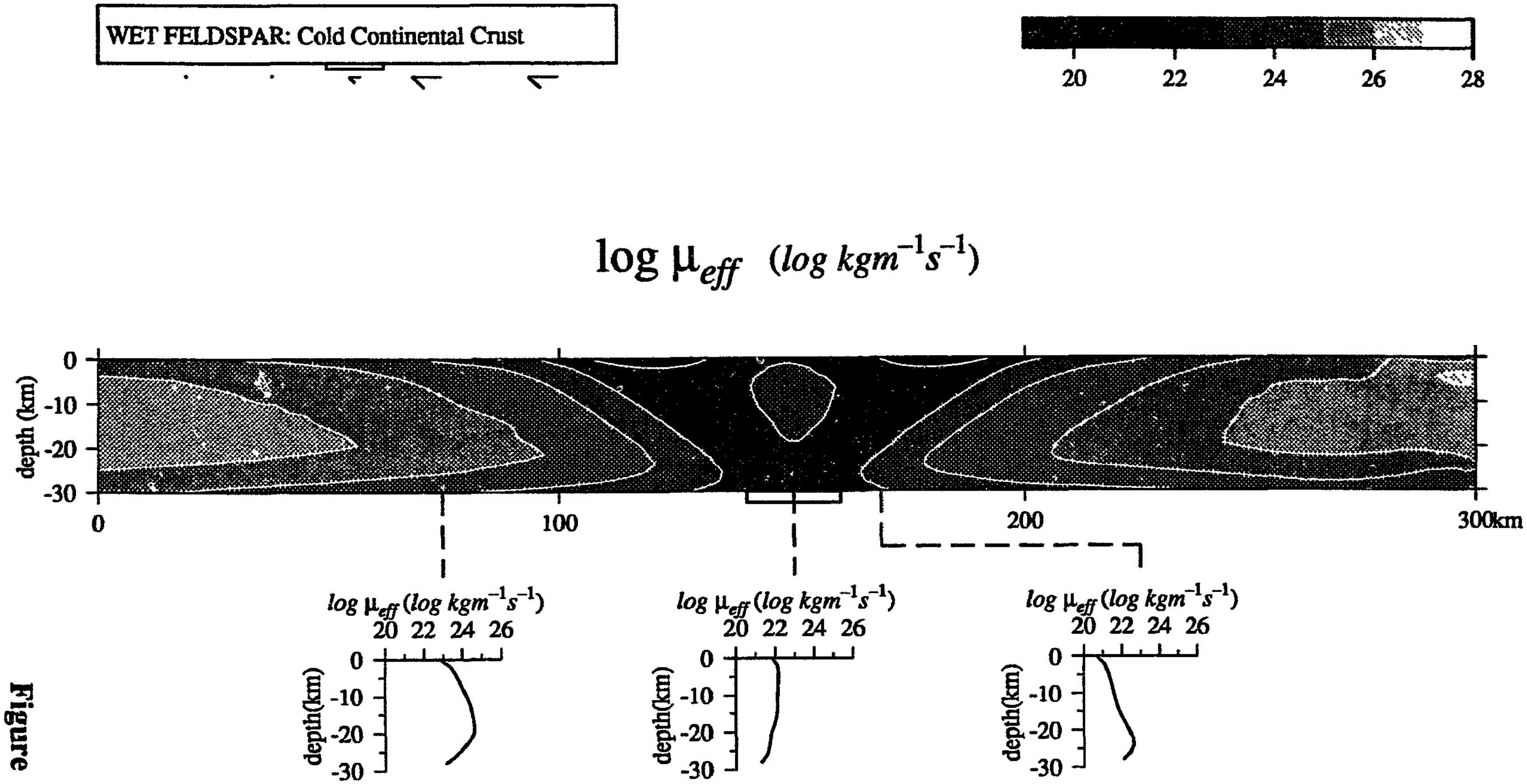

WET FELDSPAR: Cold Continental Crust
20
22
24
26
28
log μeff (log kgm-1s-1)
depth (km)
0
-10
-20
-30
0
100
200
300km
log μeff (log kgm-1s-1)
20 22 24 26
depth(km)
0
-10
-20
-30
log μeff (log kgm-1s-1)
20 22 24 26
depth(km)
0
-10
-20
-30
log μeff (log kgm-1s-1)
20 22 24 26
depth(km)
0
-10
-20
-30

Figure 12(c)

Figure 13: Contour plots and vertical profiles of (a) horizontal strain-rate; (b) vertical shear strain-rate, and (c) effective viscosity, for the hot continental geotherm case. Boundary conditions are the same as for figure 11.

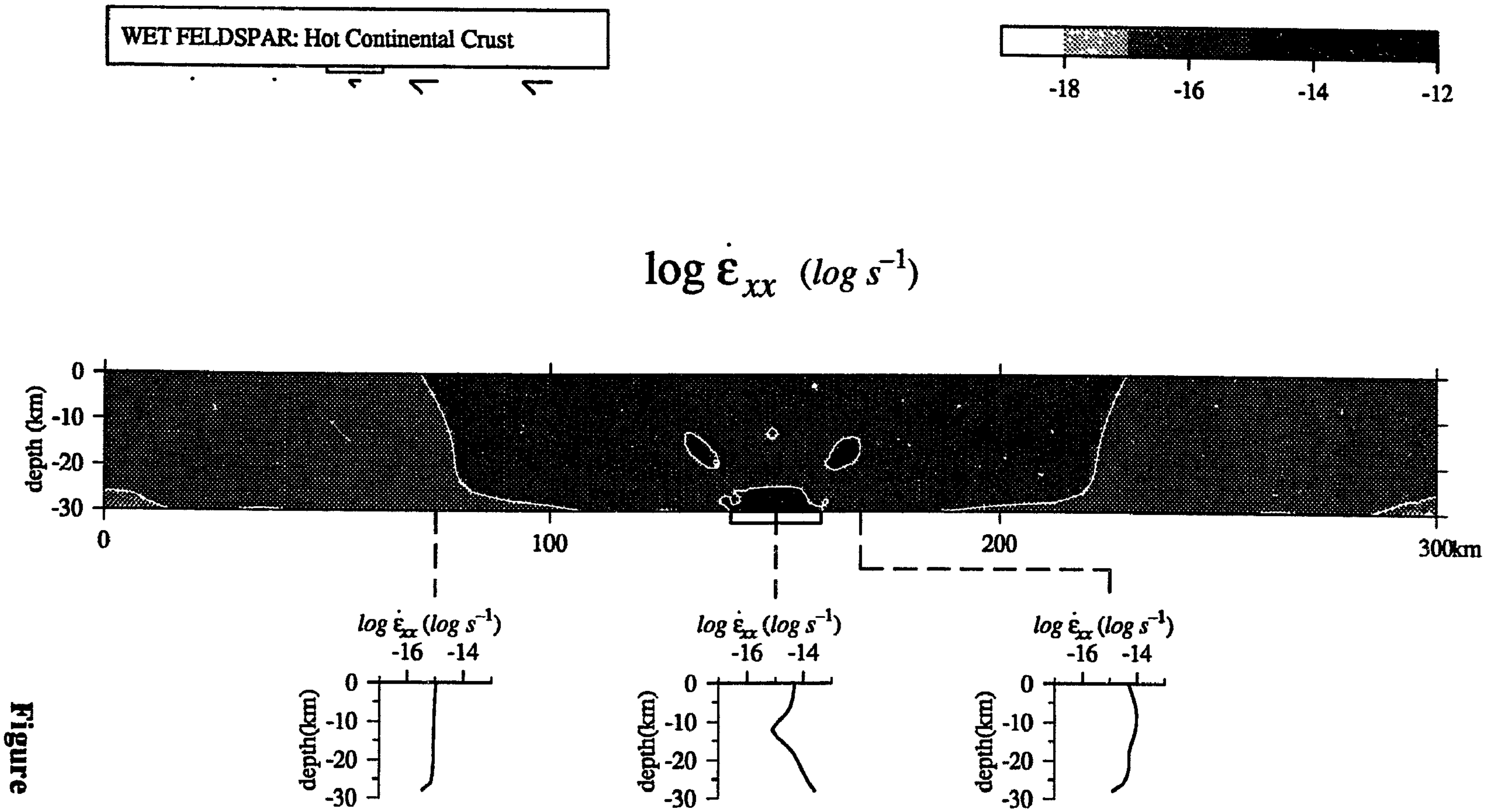
WET FELDSPAR: Hot Continental Crust
-18
-16
-14
-12
log ε̇xx (log s⁻¹)
0
-10
-20
-30
depth (km)
0
100
200
300km
log ε̇xx (log s⁻¹)
-16 -14
depth(km)

Figure 13(a)

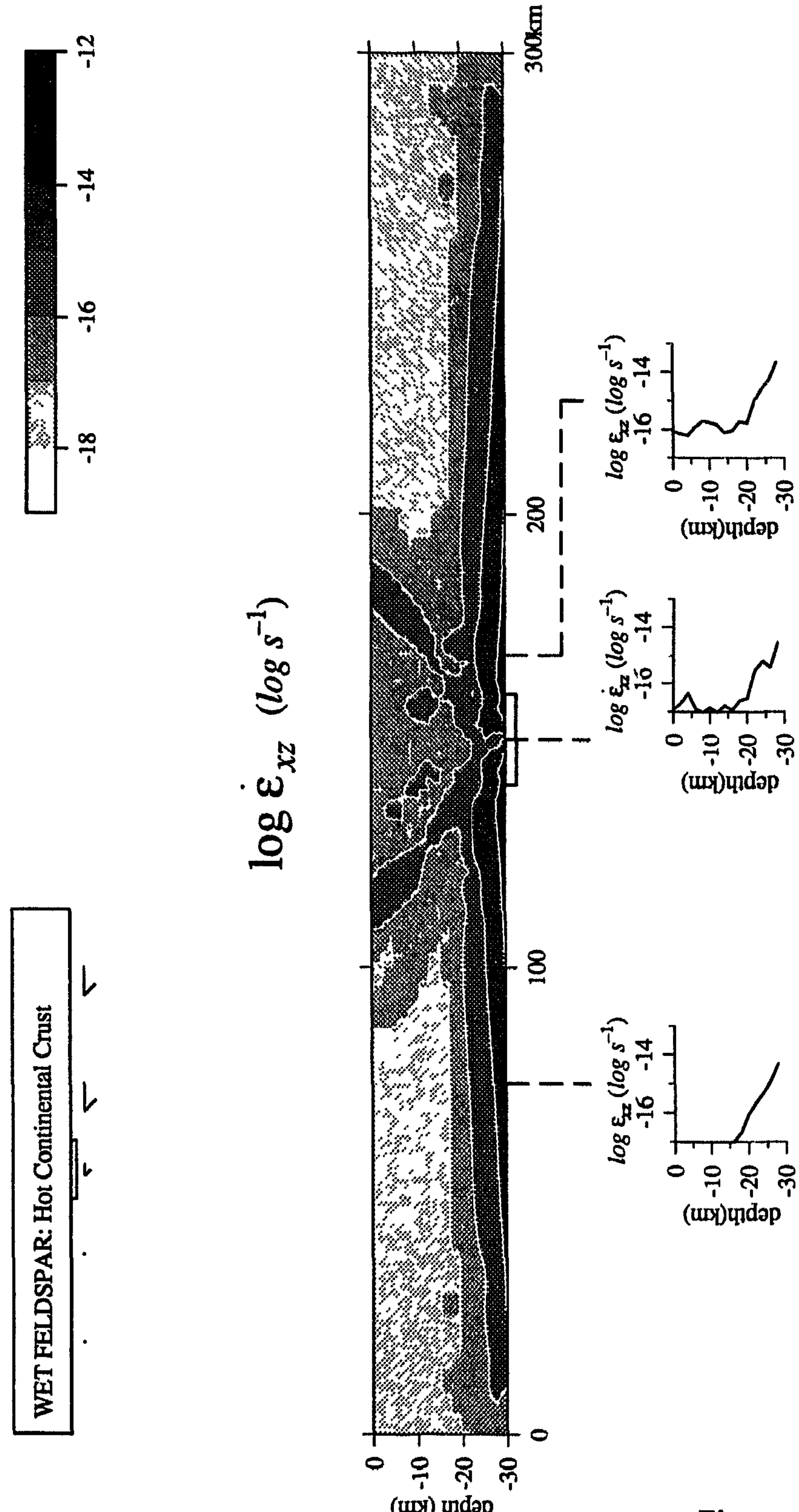
WET FELDSPAR: Hot Continental Crust
log $\dot{\varepsilon}_{xz}$ $(log\ s^{-1})$
-18
-16
-14
-12
0
100
200
300km
0
-10
-20
-30
depth (km)
log $\dot{\varepsilon}_{xz}$ $(log\ s^{-1})$
-16
-14
depth(km)

Figure 13(b)

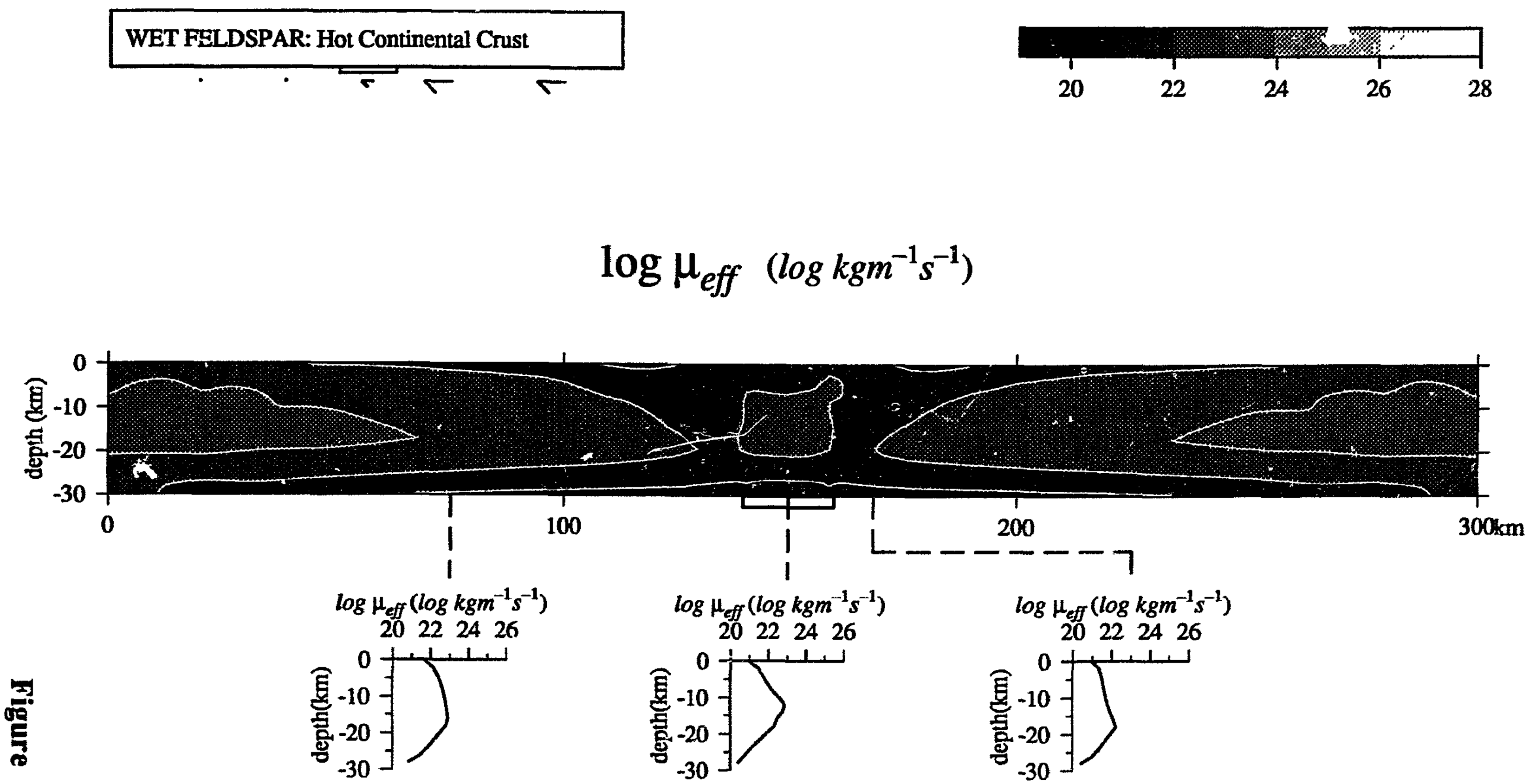
WET FELDSPAR: Hot Continental Crust
20
22
24
26
28
log μeff (log kgm-1s-1)
depth (km)
0
-10
-20
-30
0
100
200
300km
log μeff (log kgm-1s-1)
20 22 24 26
depth(km)

Figure 13(c)

The strain-rate contours $\dot{\varepsilon}_{xz}$ for the cold and hot continental geotherm cases (figures 12(b) and 13(b)), taken from a model run at $t' \sim 0$, indicate that most of the simple shear takes place near the Moho. This result suggests that it is possible to represent the frictional-viscous case by a two-layer viscous rheology, where the lower layer is relatively weak and incorporates most of the simple shear. The top of the weak layer is chosen to be the depth at which the normalized cumulative shear strain-rate ratio:

$$\sum_{0}^{z} \dot{\varepsilon}_{xz} \Big/ \sum_{0}^{S_0} \dot{\varepsilon}_{xz}$$

reaches a value of 1/e. The bottom of the weak layer is at the Moho. Over most of the model domain, for both cold and hot continental geotherms, the thickness of the lower layer (h) is less than 2km (figure 14), which is at the limit of the grid resolution. Near the singularity, h may be larger. I take the minimum estimated value for h, but the effect of the discrepancy between the maximum and minimum values for h will be demonstrated below.

Figure 14: Contours and vertical profiles of cumulative vertical shear strain-rate for (a) cold, and (b) hot continental geotherms, and the boundary conditions as described for figure 11.

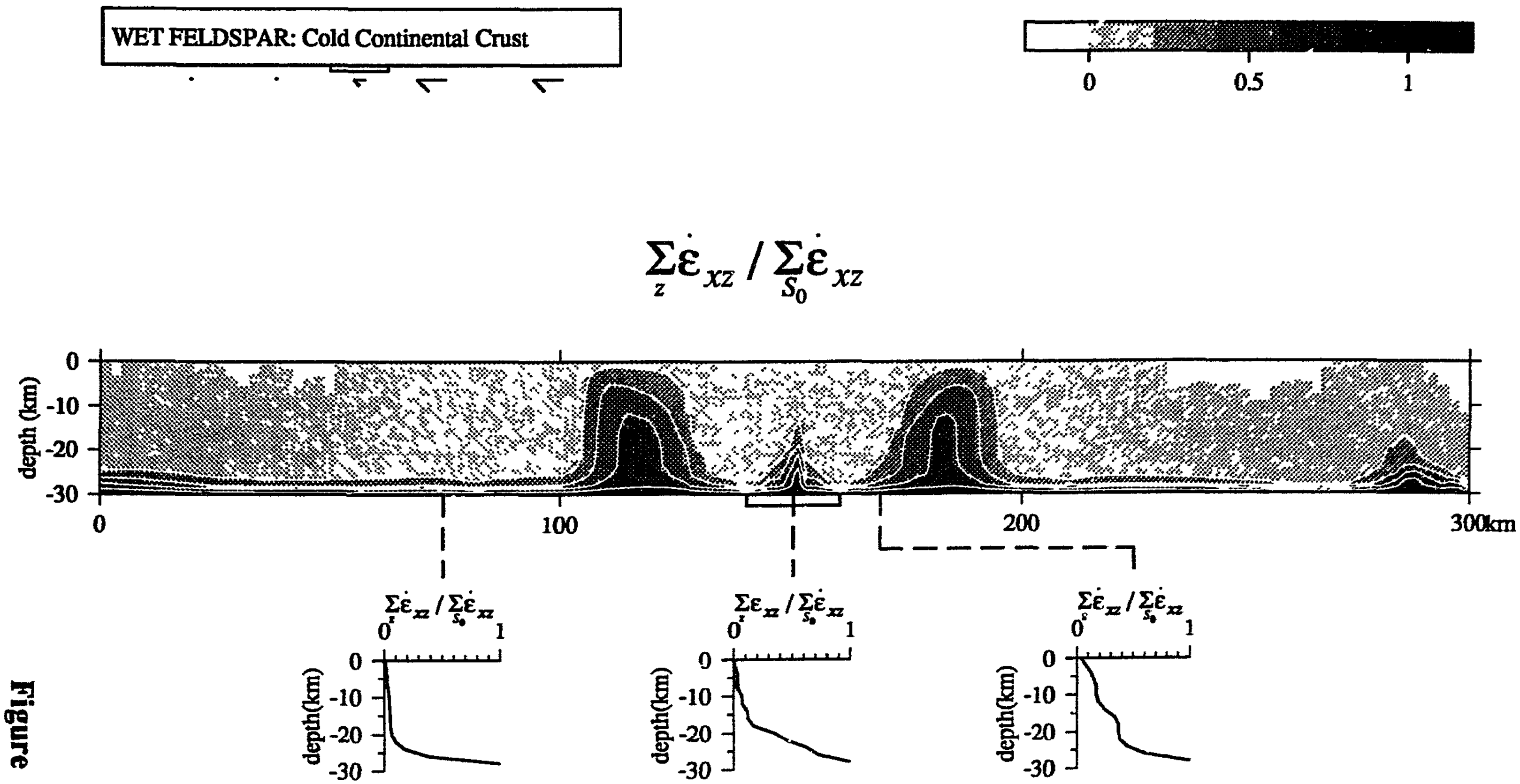

WET FELDSPAR: Cold Continental Crust
0
0.5
1
$\sum_z \dot{\varepsilon}_{xz} / \sum_{S_0} \dot{\varepsilon}_{xz}$
depth (km)
0
-10
-20
-30
0
100
200
300km
depth(km)

Figure 14(a)

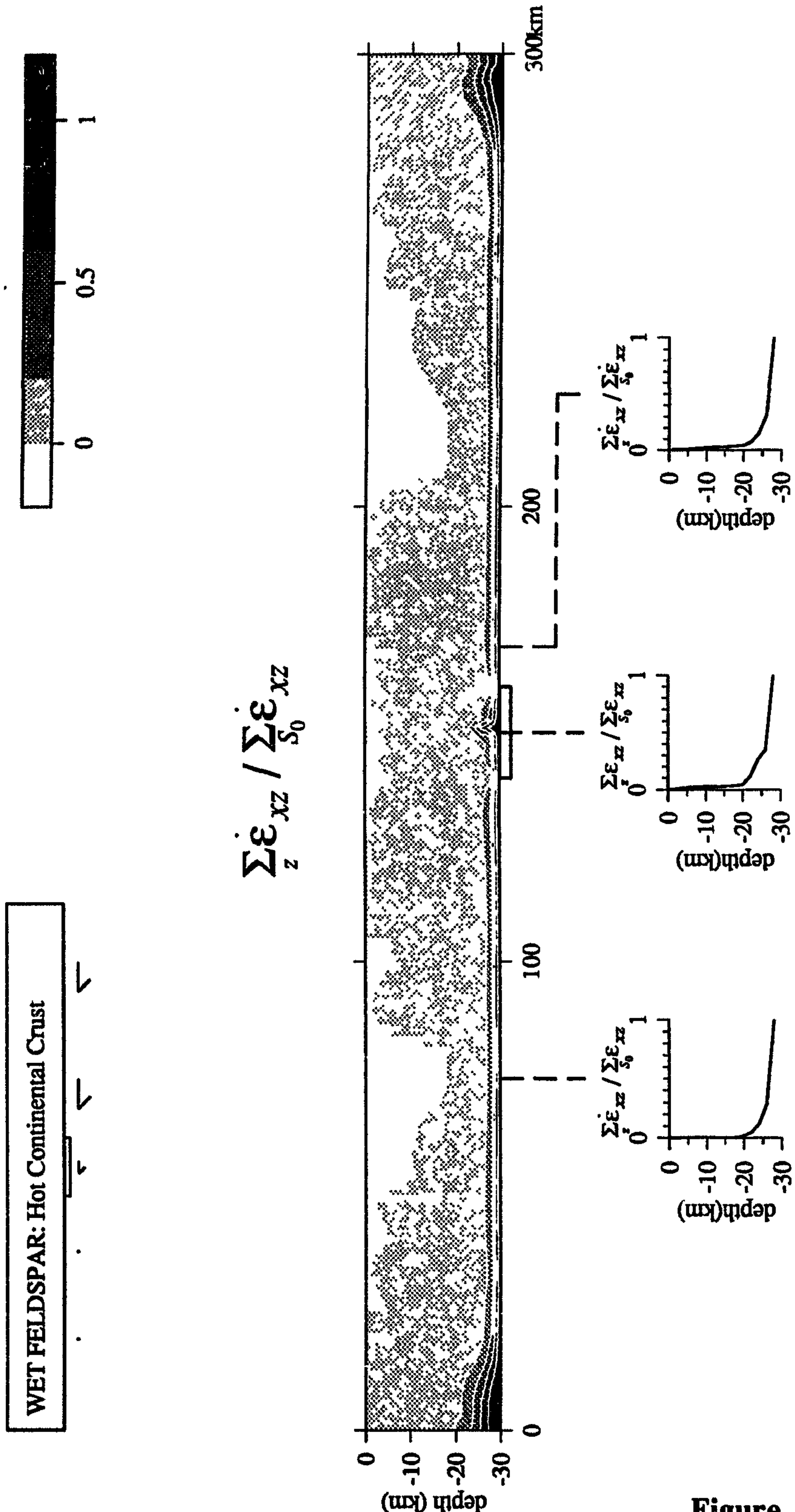
WET FELDSPAR: Hot Continental Crust
0
0.5
1
$\sum_z \dot{\varepsilon}_{xz} / \sum_{S_0} \dot{\varepsilon}_{xz}$
depth (km)
0
-10
-20
-30
0
100
200
300km
depth(km)

Figure 14(b)

To find the equivalent material parameters for the two-layer viscous approximation of the frictional-viscous case, the effective two-layer viscosities must also be found. For each layer, the viscosity is assumed to be constant with depth, so that:

$$\tau_{ij} = B\dot{\varepsilon}_{ij}^{1/n} = \mu_{eff}\,\dot{\varepsilon}_{ij}$$

where μ_{eff} is the effective viscosity. The material parameter B may therefore be estimated from a shear stress, τ, and an effective viscosity, using the following relationship:

$$B = 2^{\frac{1}{n}-1}\,\tau^{1-\frac{1}{n}}\,\mu^{\frac{1}{n}}$$

Figure 15: Estimating equivalent viscous parameter values for cold and hot continental geotherm models. The weak basal layer is indicated by the shaded region on the: (a) strength, (b) effective viscosity, and (c) strain-rate (second invariant) profiles. The thickness of the weak layer is arbitrarily assigned to be 2 km, which is the minimum value established from estimates of normalized shear strain-rate in section 3.1. Estimates for maximum stress difference and effective viscosity may be made either by assuming a layer is represented by its peak values (solid circles), or by average values (dashed lines). The material parameter B for each layer is computed from the estimates for shear stress (=0.5σ), and effective viscosity.

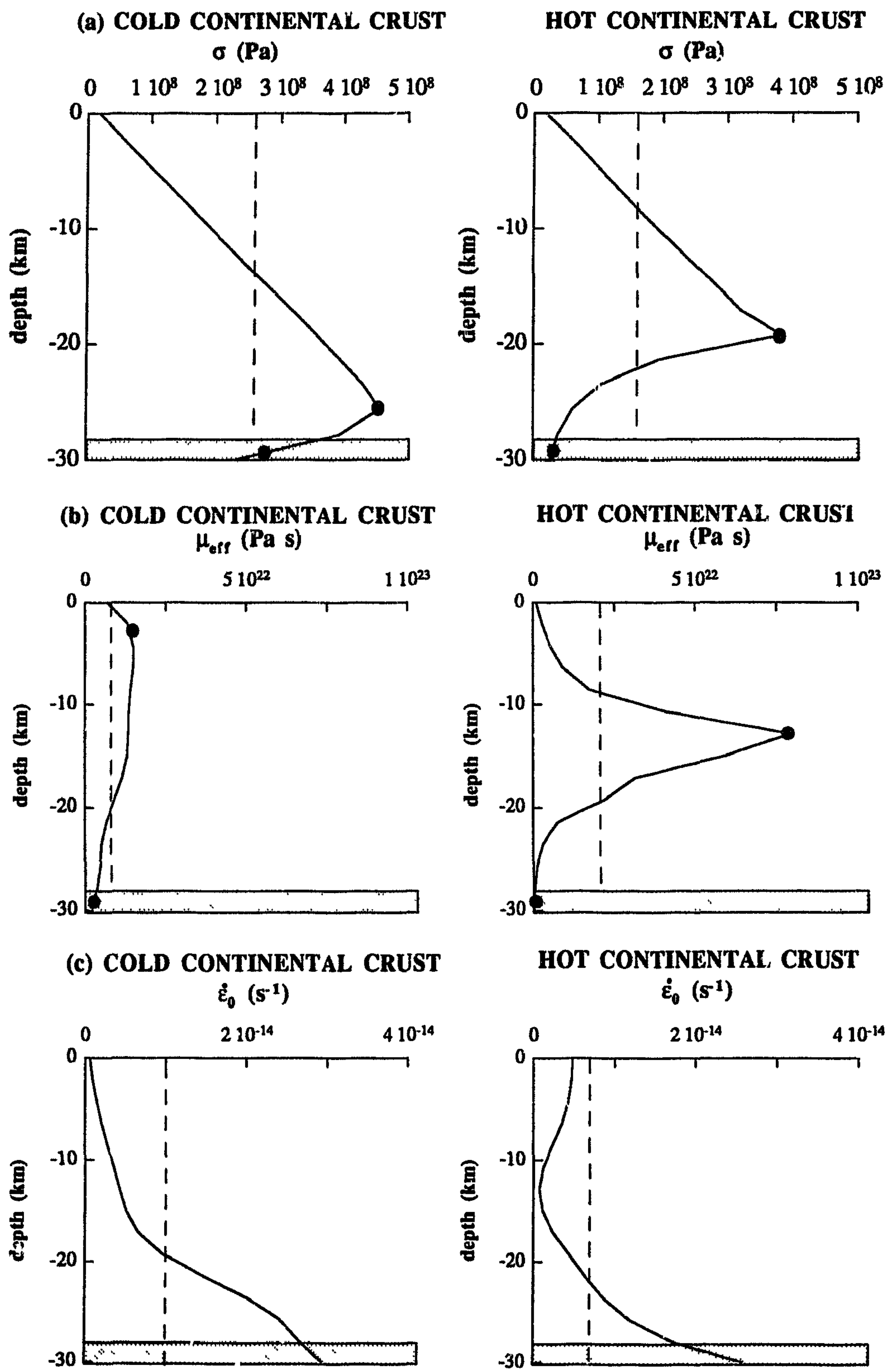

(a) COLD CONTINENTAL CRUST
σ (Pa)
0 1 10⁸ 2 10⁸ 3 10⁸ 4 10⁸ 5 10⁸
depth (km)
0
-10
-20
-30
HOT CONTINENTAL CRUST
σ (Pa)
(b) COLD CONTINENTAL CRUST
μeff (Pa s)
0 5 10²² 1 10²³
HOT CONTINENTAL CRUST
μeff (Pa s)
(c) COLD CONTINENTAL CRUST
ε̇0 (s-1)
0 2 10-14 4 10-14
HOT CONTINENTAL CRUST
ε̇0 (s-1)

Figure 15

There are several possible choices for the viscous parameters τ, B, and μ_{eff}, because of their spatial dependence. Firstly, there is the dependence of parameter values on horizontal distance from the singularity. I assume that the parameter values estimated *directly above* the singularity are most important in controlling deformation style. Secondly, there is the change in parameter values with depth. If the strength of a layer is controlled by the *peak* maximum stress difference, the parameter values should be chosen to represent this maximum. Alternatively, the *average* values may give the best two-layer representation. I explore these alternatives in figure 15 for the cold and hot continental crust cases. The maximum values (represented by the solid circles) give lower (minimum) estimates of the coupling (as represented by the non-linear Ampferer number (Appendix C)) between the two layers than the averages. I also estimate the average strain-rates in figure 15(c), which were used to construct the generic strength profiles in the last sub-section.

Figure 16(a) compares the deformation and crustal thickening for the cold continental geotherm case at normalized convergence time $t'=2$, for (i) the Coulomb-viscous model; (ii) a non-linear two-layer viscous representation where it is assumed that the strength of the crust and basal layer are controlled by the average parameter values (Tables 6, 7); and (iii) the same as case (ii), but assuming the strength of the layers are controlled by their strongest regions. The figure demonstrates that even for the strongly-coupled case, the deformation produced using the two-layer viscous approximation gives a fair agreement with the fully Coulomb-viscous case. The slight discrepancies in thickening occur because, as already shown in figure 14(a), the cross-sectional shear is not confined to a thin basal layer, but extends in 2 shear zones on either side of the mantle detachment zone. Agreement is even better for the hot continental geotherm case shown in figure 16(b), where the cross-sectional shear is primarily within the basal layer (cf. figure 14(b)). Linear viscous approximations to the Coulomb-viscous model can also be made, by using the estimates for effective viscosity from figure 15. As for the non-linear viscous approximations, agreement is best for the weak-based (hot) continental crust (figure 17).

Figure 16: Comparisons in the deformation and thickening after normalized convergence time $t'=2$, for (a) cold continental geotherm; (b) hot continental geotherm, and the boundary conditions of figure 11. (i) Fully plastic-viscous crust; (ii) two-layer viscous (plane-strain model) representation, assuming average parameter values; (iii) same as (ii), assuming layer strength is controlled by maximum parameter values.

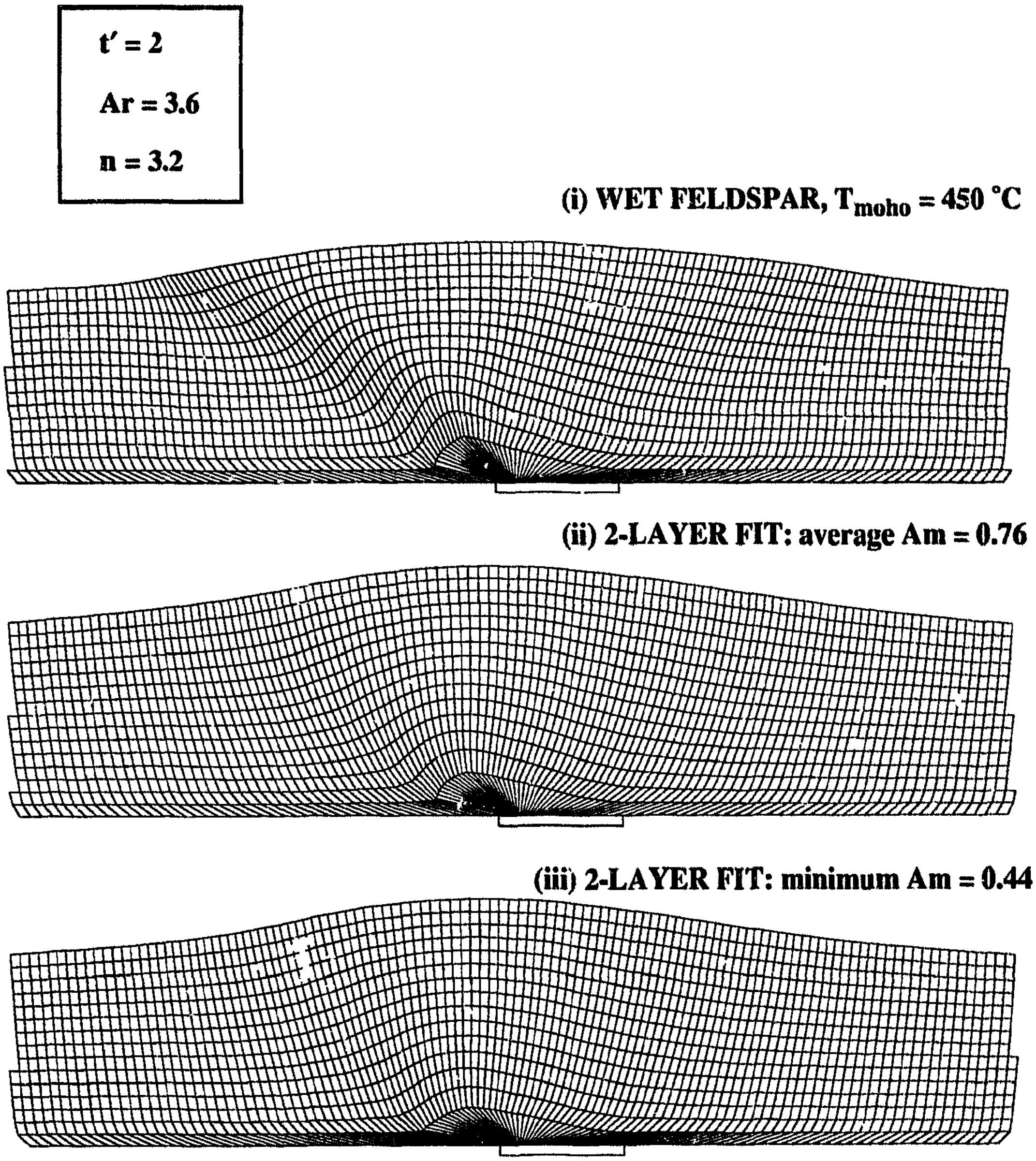
t′ = 2
Ar = 3.6
n = 3.2
(i) WET FELDSPAR, T_{moho} = 450 °C
(ii) 2-LAYER FIT: average Am = 0.76
(iii) 2-LAYER FIT: minimum Am = 0.44

Figure 16(a)

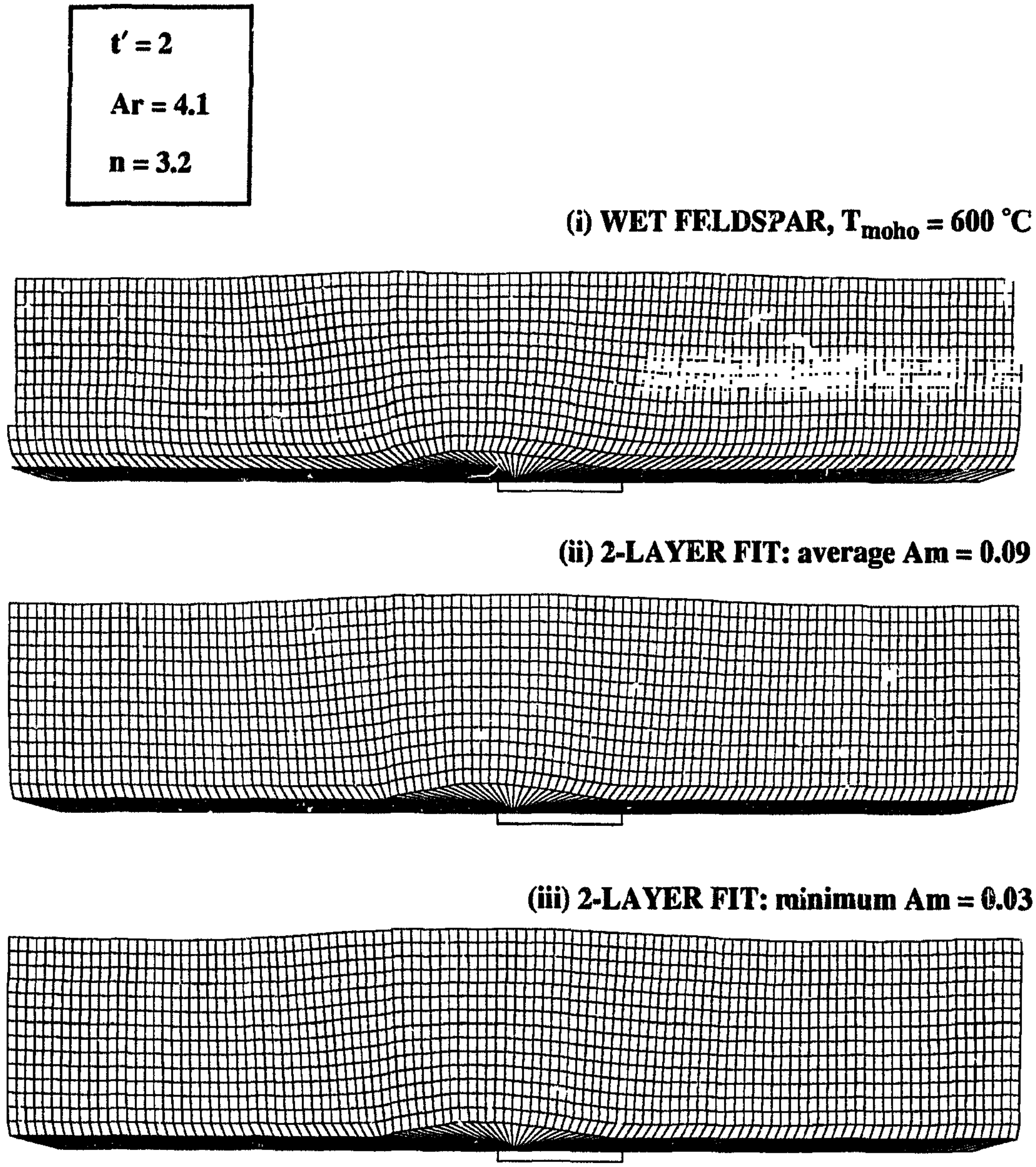
t′ = 2
Ar = 4.1
n = 3.2
(i) WET FELDSPAR, T$_{moho}$ = 600 °C
(ii) 2-LAYER FIT: average Am = 0.09
(iii) 2-LAYER FIT: minimum Am = 0.03

Figure 16(b)

Table 6: Two-layer non-linear viscous fit to representative cases

Best-fit Parameters; two-layer viscous model, n=3.2	Cold Continental Crust T_{moho} = 450 °C	Hot Continental Crust T_{moho} = 600 °C
Average differential stress $\overline{\sigma}_c$	2.6×10^8 Pa	1.6×10^8 Pa
Maximum differential stress σ_c^{max}	4.8×10^8 Pa	4.0×10^8 Pa
Basal differential stress σ_b	2.4×10^8 Pa	2.6×10^7 Pa
Average effective viscosity $\overline{\mu}_c$	1×10^{22} Pa s^{-1}	2×10^{22} Pa s^{-1}
Maximum crustal viscosity μ_c^{max}	1.6×10^{22} Pa s^{-1}	8×10^{22} Pa s^{-1}
Basal viscosity μ_b	2×10^{21} Pa s^{-1}	2.5×10^{20} Pa s^{-1}
Average crustal material parameter $\overline{B}_c$	1.8×10^{12} Pa $s^{-1/n}$	1.6×10^{12} Pa $s^{-1/n}$
Maximum crustal material parameter B_c^{max}	3.1×10^{12} Pa $s^{-1/n}$	4.5×10^{12} Pa $s^{-1/n}$
Basal material parameter B_b	1.0×10^{12} Pa $s^{-1/n}$	1.1×10^{11} Pa $s^{-1/n}$
Average strain-rate $\overline{\dot{\varepsilon}}_0$	1×10^{-14} s^{-1}	7×10^{-15} s^{-1}

Table 7: Best-fit two-layer viscous model parameters

geotherm	*stress exponent*	*thickness of lower layer*	B_c *(Pa* $s^{-1/n}$*)*	B_b *(Pa* $s^{-1/n}$*)*	*Am*
cold (T_b=450 °C)	3.2	2km	1.8×10^{12}	1.0×10^{12}	0.8±0.2
hot (T_b=600 °C)	3.2	2km	1.6×10^{12}	1.1×10^{11}	0.09±0.06

The qualitative comparisons of figure 16 suggest that the choice between average or peak layer parameters is not significant. For the boundary conditions of figure 5(a) and a crust composed of unilayered feldspar, the choice when modelling of whether to approximate layers by their strongest part (e.g. England and McKenzie, 1982), or to use average values within the layer, may therefore not be important (with regard to the style of deformation). I use the difference in the estimates of coupling (Am) predicted by using the average or peak parameter values, to give some measure of the uncertainty in determining the appropriate two-layer viscous representation (below).

Figure 17: Same as figure 16, except two-layer viscous approximation is linear viscous. (i) Fully plastic-viscous deformation for cold continental geotherm (n=3.2, and Ar=3.6); (ii) average two-layer (linear viscous) representation of (i) (n=1, and Ar=3.6); (iii) fully plastic-viscous deformation for hot continental geotherm (n=3.2, and Ar=4.1); (iv) average two-layer (linear viscous) representation of (iii) (n=1, and Ar=4.1).

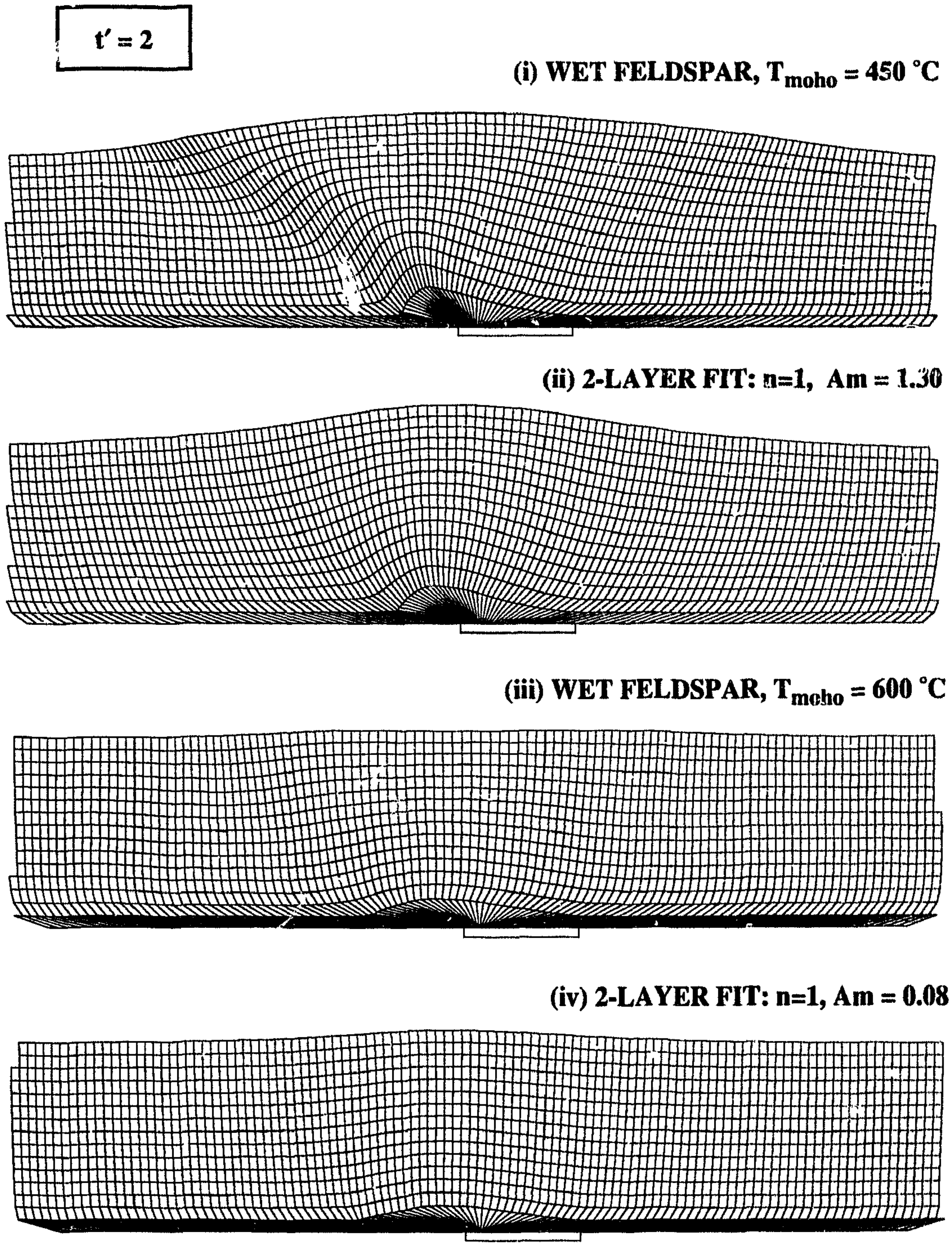
t′ = 2
(i) WET FELDSPAR, T_{moho} = 450 °C
(ii) 2-LAYER FIT: n=1, Am = 1.30
(iii) WET FELDSPAR, T_{moho} = 600 °C
(iv) 2-LAYER FIT: n=1, Am = 0.08

Figure 17

The frictional-viscous models may also be compared to equivalent thin-sheet viscous models (figure 18), where the thin simple shear layer is represented by a traction applied to the base of the remaining crust. As for the plane-strain two-layer approximation, the comparison is quite good for the hot continental case, but deteriorates for the cold geotherm case, where the simple shear component in the upper layer is significant.

The Ampferer number may be calculated for the cases discussed above using the estimates of n and B for the two layers, giving Am=0.8±0.2 for the cold continental geotherm, and Am=0.09±0.06 for the hot continental geotherm. Average parameter values have been used, and the uncertainty estimates come from the discrepancy between average and peak layer parameter predictions for Am. For oceanic crust, there is no strength minimum (figure 10), so that shear strain is an important factor throughout the crust, and Am is much greater than 1. For a range of crustal geotherms, the equivalent Ampferer numbers may be estimated in the same manner, to give the relationship between Am and the temperature at the base of the Moho. As expected, Am decreases approximately exponentially with an increasingly hot crustal geotherm (figure 19(a)).

Figure 18: Same as figure 16, except the two-layer viscous approximation is computed using a thin-sheet (one-dimensional) model. (i) Fully plastic-viscous deformation for cold continental geotherm (n=3.2, and Ar=3.6); (ii) average two-layer viscous representation of (i) (n=3.2, and Ar=3.6); (iii) fully plastic-viscous deformation for hot continental geotherm (n=3.2, and Ar=4.1); (iv) average two-layer viscous representation of (iii) (n=3.2, and Ar=4.1).

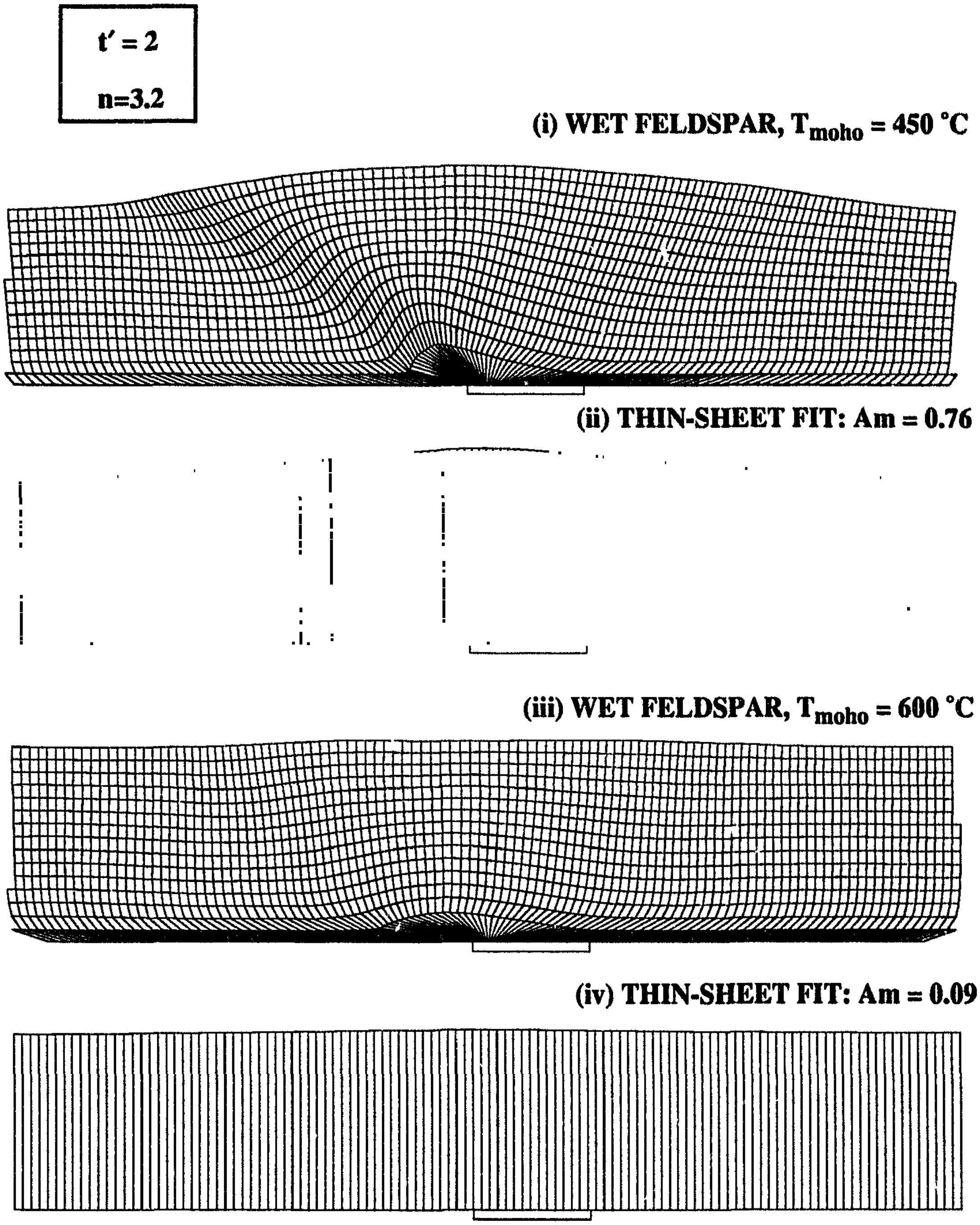

$t' = 2$
$n=3.2$
(i) WET FELDSPAR, T_{moho} = 450 °C
(ii) THIN-SHEET FIT: Am = 0.76
(iii) WET FELDSPAR, T_{moho} = 600 °C
(iv) THIN-SHEET FIT: Am = 0.09

Figure 18

For the normal range of continental crustal geotherms and 30km thick crust, the models from this section indicate that Am is between 0.01 and 1 (figure 19(a)). In regions of thickened continental crust, Am may be <0.01. The results shown in figures 16, 17 and 18, demonstrate that a (compositionally) single-layered crustal rheology can be approximated by a two-layer viscous crust, provided the base of the crust is relatively weak (i.e. Am ≤ 1). This limit is illustrated in figure 19(b), in which the normalized maximum estimate for the thickness of the basal (simple shear) layer (h_{max}) is plotted vs. Am. The smaller the value of h_{max}, the more closely a two-layer viscous rheology approximates the fully plastic-viscous model.

In summary, comparison of two-layer viscous models with strength-profiles derived from frictional-viscous models suggests that a rheologically valid range of values for the Ampferer number is between 0.01 and 1. For cases where Am >1, the two-layer viscous model is not a good representation of crustal behaviour. Am may be less than 0.01, if the crust is thicker and has a relatively steep geotherm. The results indicate that the thin-sheet model can be used to represent the geologically valid range of crustal geotherms, provided the assumptions used in this section (which represents the crustal rheology using a frictional-viscous, single compositional layer of wet feldspar) is also geologically valid.

Figure 19: (a) Dependence of basal coupling, as represented by the Ampferer number, on crustal geotherm (shown as basal temperature, in °C). Basal coupling (Am) increases as the crust cools. (b) Illustration of the increasing importance of cross-sectional shear in the crustal layer, as a function of basal coupling (Am). The error bars on Am are discrepancies between using average and peak parameter values to represent each layer. The two-layer viscous representation of the crust is best for hot (less coupled) continental crust.

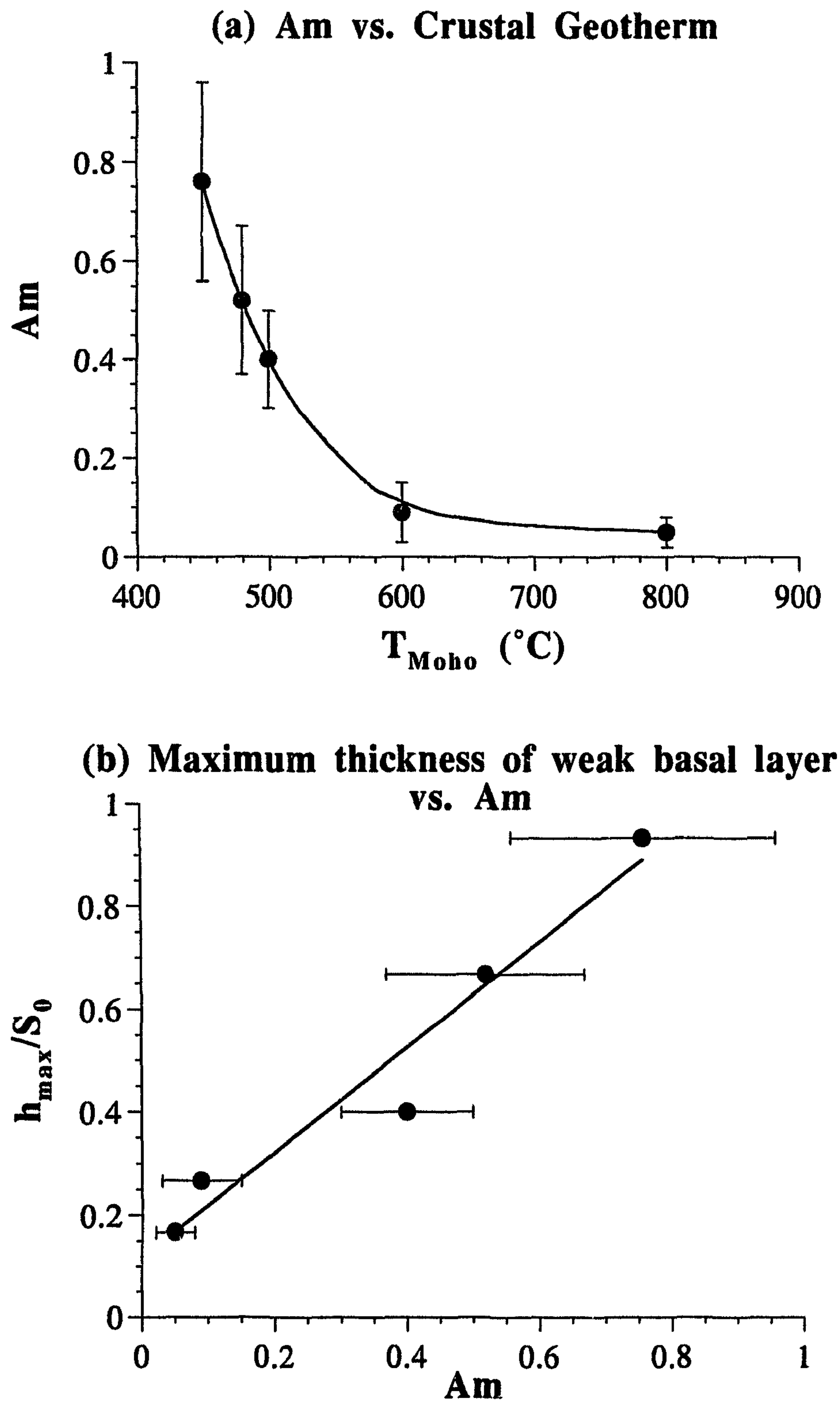
(a) Am vs. Crustal Geotherm
Am
1
0.8
0.6
0.4
0.2
0
400
500
600
700
800
900
T Moho (°C)
(b) Maximum thickness of weak basal layer vs. Am
h max /S 0
1
0.8
0.6
0.4
0.2
0
0
0.2
0.4
0.6
0.8
1
Am

Figure 19

§ 3.2 Accuracy of the Model: Comparison of Thin-Sheet with Basal Traction to Plane-Strain Models in One Dimension

Introduction

Section 3.1 has established the expected range for the Ampferer number (Am between ~0.01 and 1) for continental crust, based on rheological considerations. Results also suggest that a two-layer viscous representation of the crust is possible, provided most of the cross-sectional shear takes place within a weak layer near the Moho. Agreement between the frictional-plastic and two-layer viscous model representations of crustal deformation is fairly good for the moderate range of crustal geotherms that have been investigated.

The thin-sheet approximation places further restrictions on the range of parameter values that may be used. The effect of neglecting the vertical simple shear strain component in the crustal layer, and the application of a basal velocity boundary condition via a thin boundary layer, limit the range of parameter values for which the physical model is compatible with the thin-sheet approximation. In this section, the behaviour of the one dimensional version of the thin-sheet model (in cross-section) is compared with the equivalent vertical section two dimensional plane-strain numerical model (as described in section 3.1).

Although the model comparison is one dimensional, I argue that because the basally driven thin-sheet model is likely to be least accurate in representing cross-sectional behaviour in the direction that deformation is forced, the comparison should give a reasonable indication of general two dimensional model validity. A complete analysis will require a comparison between thin-sheet and fully three dimensional finite element calculations, which may soon be available (Braun, 1993; Braun and Beaumont, submitted).

Previous studies (Bird, 1989; Wdowinski et al., 1989) have proposed that basal traction can be included in the thin-sheet calculations with only a small loss of accuracy provided certain assumptions and conditions are met. Bird (1989) and Bird and Baumgardner (1984) applied a basal traction through a weak boundary layer (similar to this study). They argued that the traction is allowable provided that the strength of the boundary layer is relatively low, so that the coupling between crust and mantle is weak. However, no attempt was made to estimate the threshold coupling strength above which the model approximations become invalid.

Wdowinski et al. (1989) estimated thin-sheet accuracy by comparing a one dimensional lithospheric thin-sheet analytic solution with the solution for fully two dimensional flow. The basal traction was applied directly to the bottom of the model lithosphere in the form of a constant normalized periodic shear stress. For these boundary conditions the thin-sheet error can be shown to depend only on L/λ_p, where L is the thickness of the sheet, and λ_p is the periodic wavelength of the basal shear. For minimal error, the wavelength over which basal shear is applied must be several times the thickness of the sheet.

When the basal shear is applied as a velocity boundary condition which acts through a weak layer coupling the model crust to a subducting mantle, it is necessary to consider not only the effect of the basal traction length-scale, but also the relative strength of the crust and weak basal layer, and the effect of differences in crustal and mantle velocity on the region over which the crust detaches. This is accomplished by the comparison of the two numerical models (the one-dimensional thin-sheet model and the cross-sectional plane-strain model).

The comparison is made using a linear viscous rheology, and the boundary conditions described in figure 5(a) and section 3.1. A variety of basal length-scales and values for the Ampferer number are used to determine the parameter values for which the thin-sheet results are a good approximation to the full two dimensional model results. To ensure that the boundary conditions of the plane-strain and thin-sheet models are the same, the vertical velocity at the base of the model is set to zero, by considering the simple case where there is no isostatic compensation (ϕ=1). The plane-strain model includes the simple shear boundary layer at the base, whereas the thin-sheet model treats this layer implicitly via the Ampferer number.

Qualitative comparison

Figure 20 contrasts the crustal deformation predicted by the plane-strain and thin-sheet numerical models. The meshes in figure 20 show the plane-strain model solutions for a small basal detachment length-scale (λ_m<S_0) at various convergence times, and for two different values of the Ampferer number (figure 20 (a), (b)). The model crust thickens in a doubly-vergent wedge shape. The shape is initially asymmetric with a steeper 'retro' side (Willett et al., 1993) due to the differential movement of material toward the implied detachment point, but after an amount of convergence, which depends on the relative strength of the buoyancy forces, the asymmetry reverses and the 'pro' side becomes steeper. The reversal in asymmetry is caused by the competition between buoyancy forces and the basal traction. Because these forces operate on differing length-scales, with the traction length-scale approximately fixed and the response to crustal

---

Figure 20: Some qualitative comparisons of thin-sheet and plane-strain solutions for normalized convergence times t'=1, 2, 4, 8. The plane-strain crust is shown as a deformed mesh, and the thin-sheet crust is indicated by the bold line at the top of the model crustal layer. (a) Am = 0.1, model mantle detachment length-scale $\lambda_m = 0.25S_0$. Position of the mantle detachment is indicated by the symbol ⊔, and the sense of convergence is shown by the velocity vectors (not to scale) on the uppermost figure.(b) Am = 1, model mantle detachment length-scale $\lambda_m = 0.25S_0$.

Qualitative Comparison Between Thin Sheet and Plane Strain Model Results

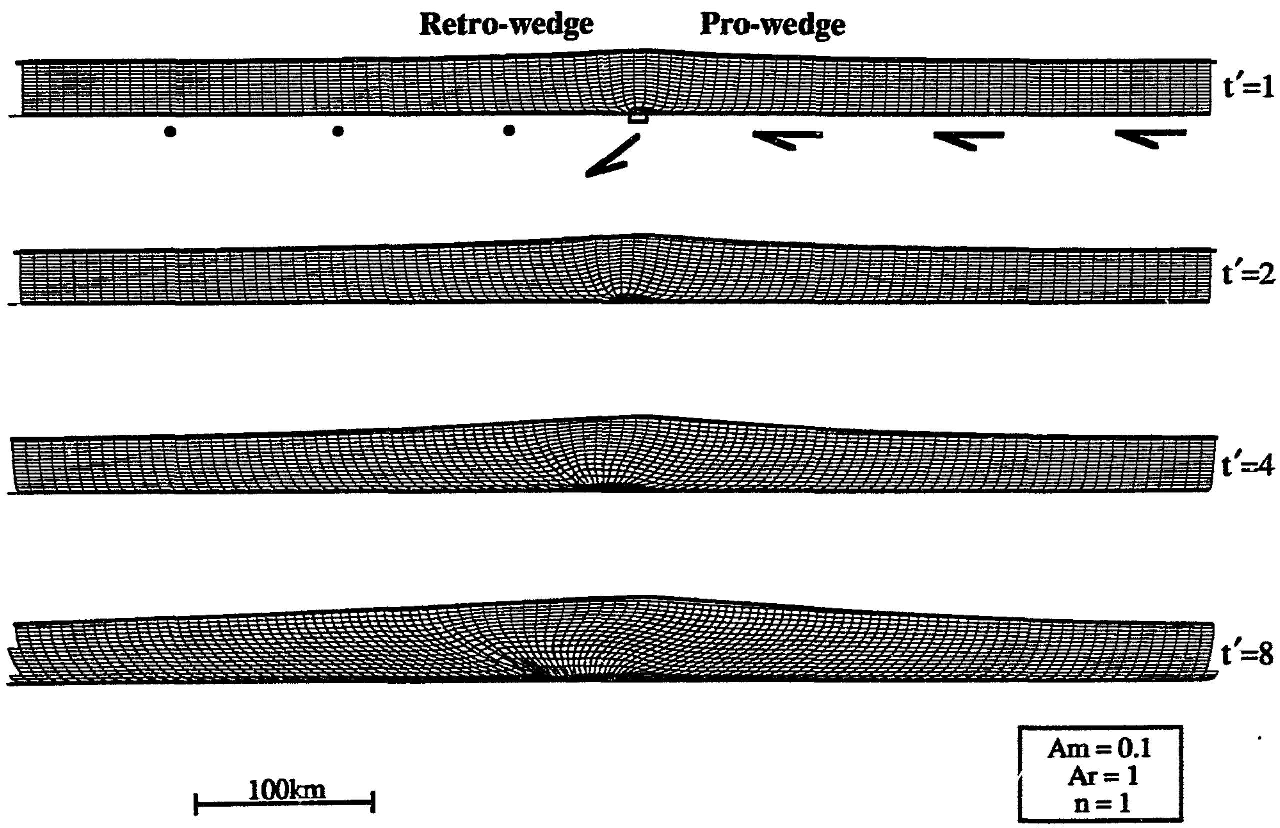

Figure 20(a)

Qualitative Comparison Between Thin Sheet and Plane Strain Model Results

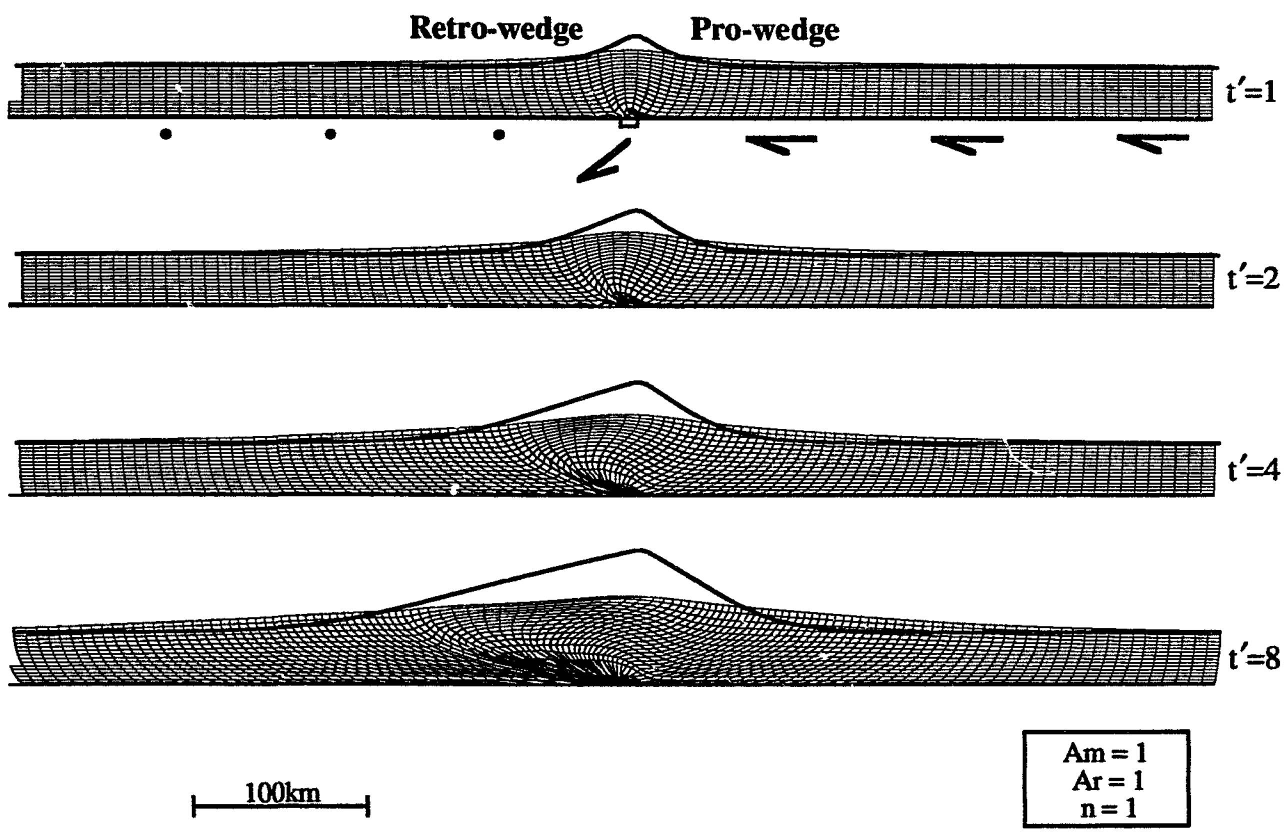

Figure 20(b)

thickness gradients increasing in length-scale, the interaction with the asymmetric transport of material leads to a reversal in slope steepness.

The equivalent set of solutions for the thin-sheet model are shown as a bold line in figure 20. At relatively low Ampferer numbers (figure 20(a)), the plane-strain and thin-sheet solutions agree quite well, but for strongly coupled problems (figure 20(b)) the thin-sheet solution overestimates the amount of thickening over the singularity. This is to be expected, for when the crust and upper mantle are strongly coupled, a significant component of simple shear exists in the crust, so that the thin-sheet model is no longer a good approximation.

The results shown in figure 20 were obtained for a small basal detachment length-scale. For equivalent cases where the imposed basal detachment length-scale λ_m is much greater than S_0, the component of simple shear strain is reduced, giving closer agreement between the plane-strain and thin-sheet model results. An interesting additional feature shown in figure 20 is the apparent surface extension of elements, with simultaneous convergence at depth, for the plane-strain viscous model. (Equivalent, vertically-averaged extension, is also present for the thin-sheet model results). Thse features are in agreement with results by Buck and Sokoutis (1994), suggesting that under certain circumstances surface extension may occur during continental convergence.

Quantitative comparison

A quantitative estimate of the difference between the thin-sheet and plane-strain models may be found by evaluating the following expressions over the deforming region, Ω:

$$\Delta M = \frac{\int_{\Omega} dM}{2M_C}$$

$$\Delta\dot{M} = \frac{\int_{\Omega} d\dot{M}}{2\dot{M}_C}$$

where $dM = (S_{PS} - S_{TS})\rho_c\,dx$, and $S_{PS}(x)$, $S_{TS}(x)$ are the crustal thicknesses for the plane-strain and thin-sheet models, respectively. M_C is the amount of mass that has entered the collision zone since the onset of convergence. $d\dot{M} = (\dot{S}_{PS} - \dot{S}_{TS})\rho_c\,dx$ is the difference in the rate of crustal thickening between the plane-strain and thin-sheet models, and $\dot{M}_C$ is the rate at which mass enters the collision zone. When the areas of thickening in the two solutions agree exactly, ΔM and $\Delta\dot{M}$ reduce to zero. The normalization factor of 2 ensures that, when the areas of thickening do not overlap at all, ΔM and $\Delta\dot{M} = 1$.

Contours of the relative discrepancy in thickening rate, $\Delta\dot{M}$, between the thin-sheet and plane-strain model results, are shown in figure 21 for t'=0. The relative error contours are plotted with axes $(\lambda_N/S_0)^2$, the ratio of horizontal crustal response length-scale to vertical scale S_0, and $(\lambda_m/S_0)^2$, the ratio of the mantle detachment length-scale to vertical scale S_0. A straight line on the plot is, therefore, Am = constant (eq. 12).

The contours show that there are two fields of behaviour, in which the error is either independent of mantle detachment length-scale λ_m (field A), or independent of crustal response length-scale λ_N (field B). A relative error of less than 5% is possible either by choosing a low basal strength so that the crustal response length-scale is sufficiently large, or by choosing mantle detachment length λ_m to be much greater than crustal thickness. To be modelled successfully using the thin-sheet approximation, a model crust must either be weakly coupled to its base, or possess a mantle detachment length-scale greater than 10 times the thickness of the model crust. The restrictive basal length-scale ratio requirement is the result of the abrupt spatial change in velocity at the bottom boundary of the model. For a more qualitative assessment of model behaviour these restrictive conditions can be reduced somewhat.

The discrepancy between the thin-sheet and plane-strain model solutions increases with normalized time. However, the increase is reduced if the effect of gravity on crustal thickness gradients, represented by the Argand number, is significant (figure 22). An additional accuracy restriction with increasing normalized time, not investigated in the model comparisons above, is due to the approximation of local isostasy. The severity of this restriction depends on the assumed elastic thickness of the mantle lithosphere. In general, for model runs with $t'>0$, Am must be sufficiently small that the length-scale of crustal deformation is at least twice the flexural wavelength (Appendix B).

The Assumption of Couette Flow in the Weak Basal Layer: is it Valid for the Thin-Sheet Model?

The thin-sheet model formulation described in chapter two uses the assumption of Couette flow within the weak basal layer, to determine the traction applied at the base of the thin-sheet. The velocity dependence for one-dimensional Couette flow can be described by the following equation:

$$u_b(z) = (\bar{u} - u_m)\frac{z}{h} + u_m$$

where $u_b(z)$ is the horizontal velocity in the thin basal layer, and z is measured vertically downwards from the bottom of the crust. Couette flow will occur, provided vertically integrated horizontal pressure gradients are negligible in comparison to the applied shear stress in the basal layer:

$$\text{i.e.} \qquad \tau_{xz} = (\bar{u} - u_m)\frac{\mu_b}{h} \qquad > \qquad \int_0^h \frac{\partial p}{\partial x} dz$$

(Turcotte and Schubert, 1982) where μ_b is the effective linear viscosity of the layer.

If horizontal pressure gradients become significant, there may be a transition from Couette to channel flow in the low viscosity layer. This possibility has been investigated by Royden (submitted), for flow within a weak lower crustal layer. She uses an analytical model of the crust, with basal velocity boundary conditions similar to those investigated in this study. For the cases described in Royden (submitted), channel flow becomes important when there is a large viscosity contrast between the upper and lower crust (> 10^6) and where the thickness of the lower ductile layer has increased by at least 100% (Royden, submitted, table 3: case 2 after 16 My convergence, and case 3 after 4 My convergence).

In her models, the upper crustal layer is taken to have a constant viscosity, and does not thicken with convergence. All crustal thickening occurs in the lower crustal layer, which therefore increases rapidly in thickness above the singularity point. Material strength in the lower crustal layer is not advected with the deformation, but instead decays exponentially with increasing depth during compensation of thickened crust.

The rapid decrease in basal viscosity for these cases (Royden, submitted, table 3) is a consequence of the exponential decay in viscosity with depth which is specified for the lower crustal layer. The models described by Royden will be valid if crustal deformation is occuring at the thermally diffusive limit, so that the base of the crust weakens rapidly as it thickens. Correspondingly, the effective Ampferer number will decrease rapidly with convergence. For instance, Royden (submitted) case 3 starts with Am ~ 1, but after 4 My convergence ($t' \sim 5$), when channel flow begins to dominate in the lower crust, the effective Am has been reduced to ~ 10^{-6}.

I believe that the transition to channel flow seen by Royden (submitted) is a direct consequence of the viscosity assumptions (i.e. the exponential decrease in μ with depth in the thickened lower layer), which effectively assume that crustal thickening takes place at a low thermal Péclet number:

$$Pe = \frac{uS}{\kappa}$$

where u is a characteristic velocity of the system, S is a characteristic length-scale (e.g. crustal thickness), and κ is the thermal diffusivity. I show in chapter six that for the cases investigated in this thesis, Pe is between 10 and 100. The results of Royden (submitted) are therefore not applicable to crustal models which operate at the thermally advective limit (model results from chapters 3-5), or those which include the thermal relaxation of the base of the crust with thickening, for Pe between 10 and 100 (chapter 6).

Throughout the rest of this thesis, I continue to assume that Couette flow is occurring in a weak basal layer, which acts as a zone of decoupling between the strong upper crust and the mantle lithosphere. The comparisons between full cross-sectional models with an assumed wet feldspar rheology, and 2-layer viscous cross-sectional and thin-sheet models, verify that for models in which advection of heat dominates the thermal behaviour, channel flow does not occur in the lower crustal layer. Other mechanisms may exist which reduce the viscosity of the lower crust in the manner assumed by Royden (submitted), but this class of models is not investigated here.

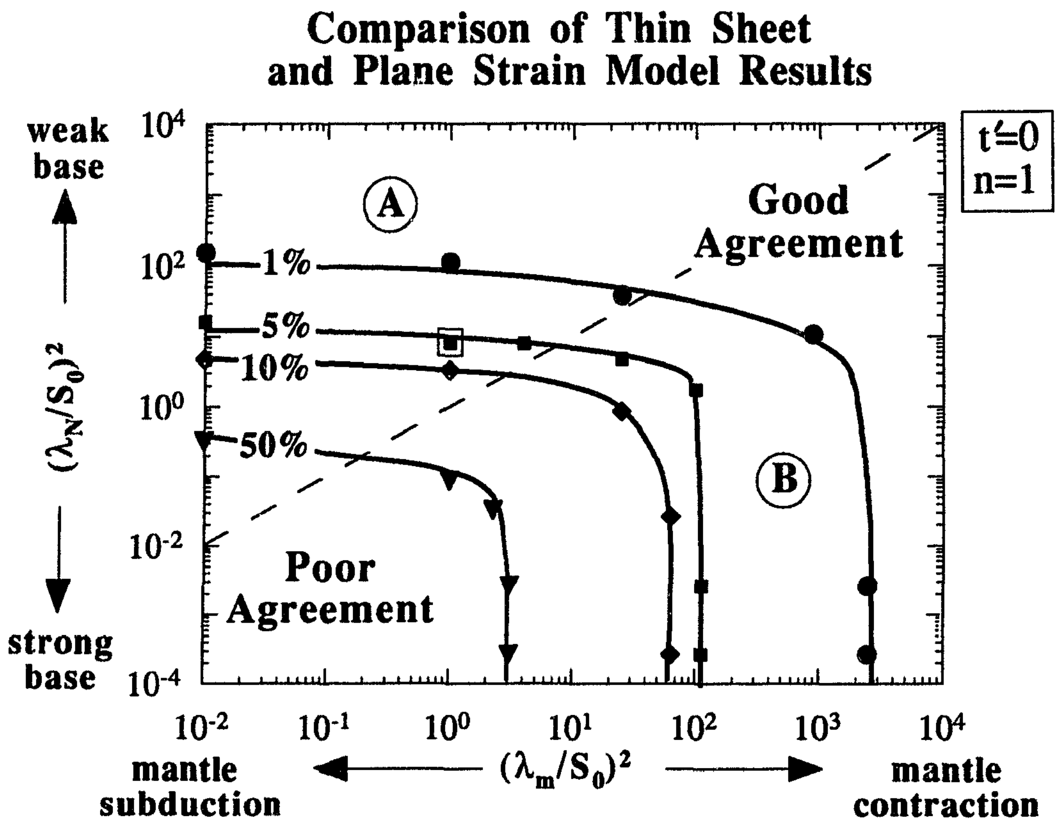

Figure 21: Contour plot of the discrepancy in thickening rates $\Delta\dot{M}$ between the thin sheet and plane-strain solutions as a function of length-scale ratios $(\lambda_m/S_0)^2$ and $(\lambda_N/S_0)^2$. The solutions were obtained using the boundary conditions shown in figure 5(a), at an early timestep (t′~0). The symbols are numerically derived values which represent the percentage discrepancy between the plane-strain and thin-sheet solutions (● = 1%, ■ = 5%, ◆ = 10%, ▼ = 50%), and the solid lines are curve fits. A straight line on the plot with a slope of 1 represents a contour of constant Ampferer number (Am = constant). The dashed line on the plot is the contour Am = 1. In region A, $\Delta\dot{M}$ depends only upon the natural response wavelength of the crust. The terms 'strong base' and 'weak base' indicate the relative strength of the crust and base. In region B, $\Delta\dot{M}$ depends only on the mantle detachment length-scale. The hollow square indicates the initial (t′=0) location of the model results shown in figure 22.

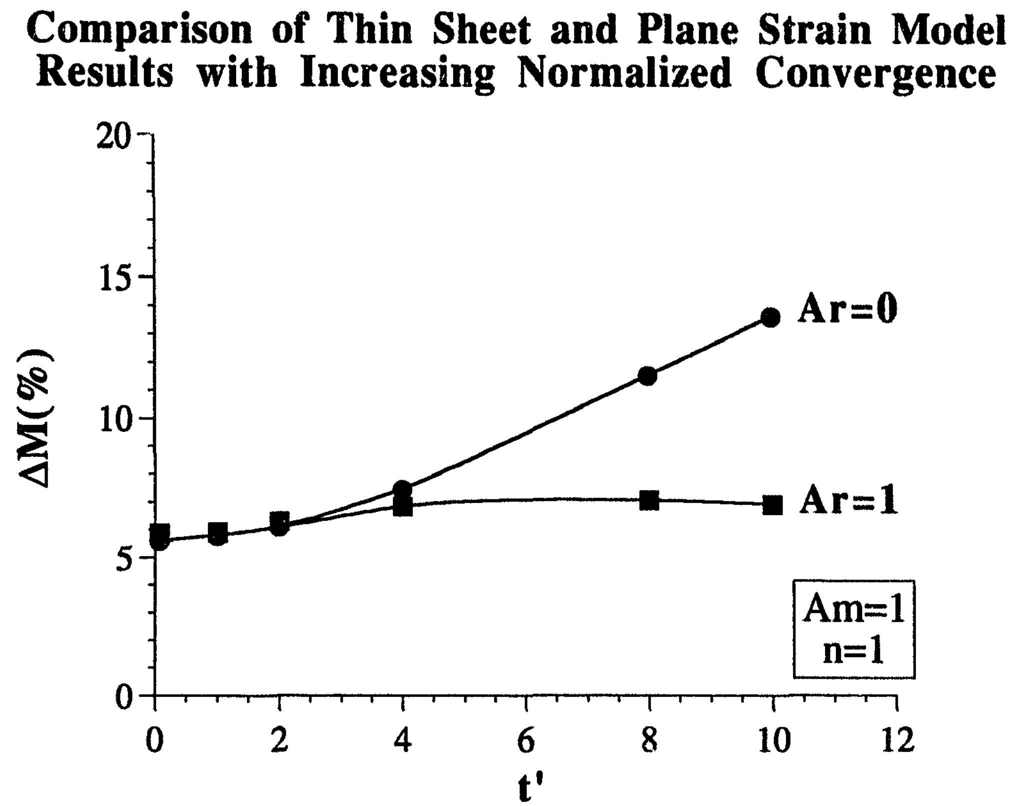

Figure 22: A plot of the discrepancy in thickening between the thin-sheet and plane strain model solutions as a function of normalized convergence time $t' = S/u_0$, and the Argand number. $Am = 1$, $\lambda_m = S_0$; symbols represent the numerically derived errors for Ar (● = 0 , ■ = 1). Solid lines are curve fits.

§ 3.3 Effect of Ar and n on Model Behaviour

Estimating the Length-Scale of Crustal Deformation

The amount of coupling between the model crust and mantle at $t'=0$ may be estimated by contrasting the maximum decrease in horizontal velocity, $\partial \bar{u}/\partial x$, which scales with u_0/λ_N, vs. the maximum slope in the basal velocity, $\partial u_m/\partial x$, which scales with u_0/λ_m. The ratio of these two quantities:

$$\left(\frac{\partial u_m}{\partial x}\right)_{max} \Big/ \left(\frac{\partial \bar{u}}{\partial x}\right)_{max}$$

defines the normalized crustal deformation length-scale, $\lambda'_N = \lambda_N/\lambda_m$.

For $t'>0$, an equivalent measure of the crustal deformation length-scale is given by:

$$\lambda'_N = \frac{M_C}{\int_{\lambda_m} dM}$$

where the integral is taken over the mantle detachment length-scale, and M_C has already been defined as the amount of convergent mass that has entered the system. When the crust passively follows the mantle, $\lambda'_N=1$ and all the convergent mass is located above the mantle detachment zone. As the crust detaches from the mantle, λ'_N increases.

The Effect of Basal Coupling and Gravity on the Crustal Deformation Length-scale

The increasing detachment of the model crust from the mantle lithosphere as a function of the Argand number is illustrated in figure 23. The figure shows contours of normalized crustal deformation length-scale, λ'_N, with non-dimensional axes representing values of Am and Ar, at $t'=1$. For the case where the Argand number is $\ll 1$, the crustal deformation length-scale will increase as coupling to the mantle (measured by Am) diminishes.

For large Ar (>1), the effect of the increased potential energy of the thickened crust causes the model crust deformation length-scale to increase (figure 23). The initial ratio between Ar and Am will determine how rapidly the defoımation spreads laterally away from the initial zone of mantle deformation, λ_m . For small Argand number, Am determines the normalized cr:ıstal length-scale, λ'_N. As the Argand number is increased, λ'_N grows at an increasing rate and in a manner that is only weakly dependent on Am. For Ar >> Am, λ'_N increases and is no longer limited by the basal coupling.

A Non-Linear Viscous Crustal Rheology

A power-law viscous rheology, as formulated in Appendix C, will have two effects on model crustal deformation: (a) the model crust will become weaker in areas of high strain-rate, thereby focusing the deformation; and (b) the coupling between the crust and base will depend locally on the relative levels of strain-rate in the two materials. Because of the interaction between these effects, the behaviour of the model is not straightforward, as shown by a contour plot (figure 24) of normalized crustal deformation length-scale, λ'_N, with axes representing the parameters n and Am, for $t'=0$. The plot shows that for small Am, the crustal deformation length-scale will initially grow, then decay, as n increases. For high values of Am, however, the deformation length-scale is comparable to the forcing length-scale, λ_m. This result will be discussed further in Chapter Four. At large n, the localization of strain by strain-rate weakening of the power-law viscous rheology dominates the behaviour.

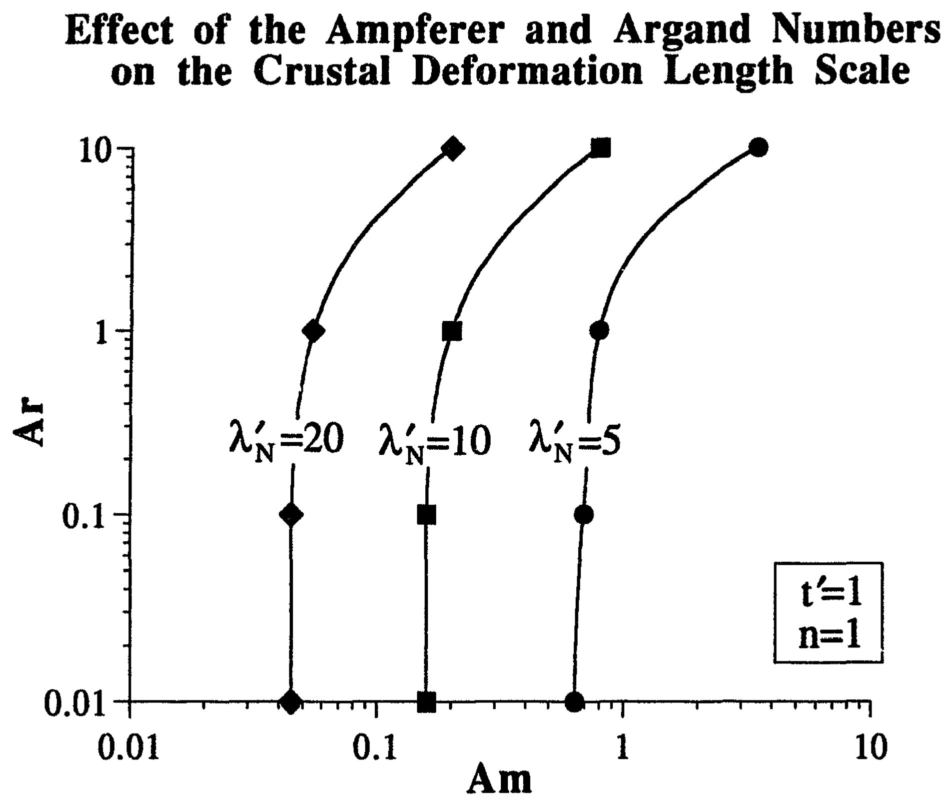

Figure 23: Effect of Am and Ar on the crustal deformation length-scale, at normalized convergence time t′=1. The symbols represent the numerically derived values of crustal deformation length-scale λ'_N (● = 5, ■ = 10, ◆ = 20). Solid lines are curve fits showing contours of λ'_N. Mantle detachment length-scale λ_m=S_0.

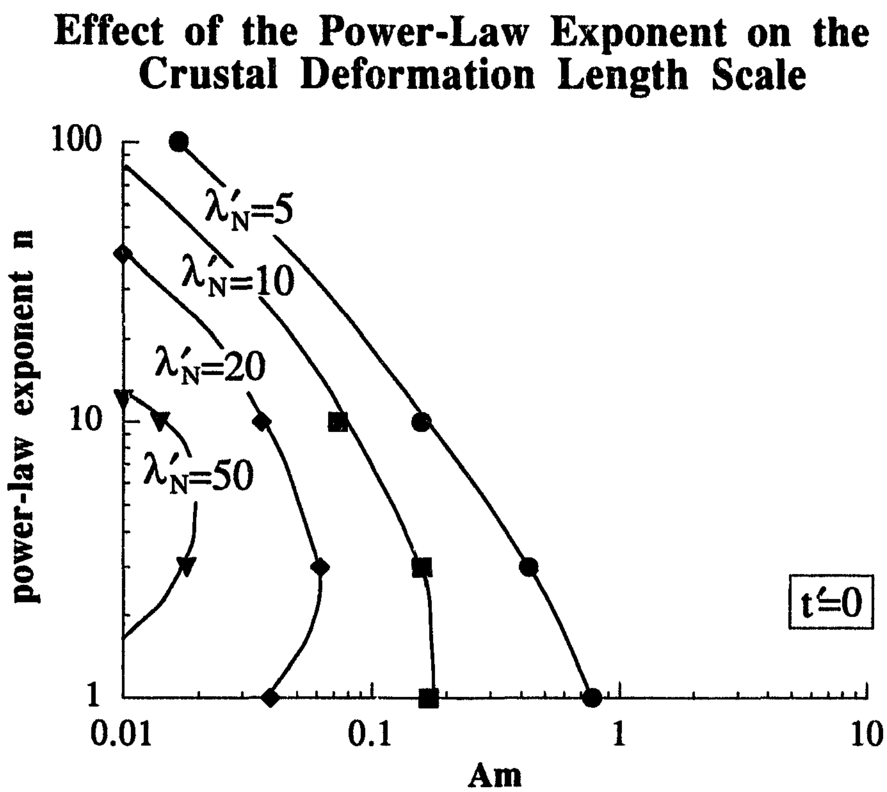

Figure 24: Effect of a non-linear viscous rheology for the crust and simple shear layer. The symbols represent the numerically derived values of crustal deformation length-scale λ'_N (● = 5, ■ = 10, ◆ = 20, ▼ = 50). Solid lines are curve fits to contours of λ'_N. Results are shown for $\lambda_m = S_0$, $t'=0$.

Chapter Four

SCALE ANALYSIS OF LITHOSPHERIC CONVERGENCE: MODEL RESULTS

§ 4.1 Introduction

The previous chapter described the one-dimensional behaviour of the tectonic model in terms of the dimensionless numbers: n, the power-law exponent; Ar, the Argand number (representing the relative importance of tectonic and gravitationally induced stresses); and the Ampferer number, Am (representing the initial coupling between the model crust and mantle lithosphere).

This chapter explores the more general problem of thin-sheet deformation under normal and obliquely convergent boundary conditions, for small and large normalized convergence time t' ($= (u_0/S_0)t$). The main objective is to determine whether the different model styles discussed in section 2.1, and illustrated in figure 25, predict different length-scales of deformation at convergent plate boundaries. For the side-driven case shown in figure 25(a), deformation is produced in response to indentation from the side of the model domain, over a horizontal length-scale, D. For convenience, I distinguish quantities predicted by the side-driven model style by the subscript 'S' as shown on the length-scale for normal convergence, λ_{NS}, in the figure. In contrast, the case shown in figure 25(b) deforms in response to basal shearing along the crust-mantle interface, with forcing length-scale λ_m. I denote the predicted normally convergent length-scale for the basally-driven model style as λ_{NB}, where the subscript 'B' indicates basal forcing. For more general cases, where deformation may be either basally or side-driven, the length-scale for the normally convergent case is written as λ_{NO}, where the subscript 'O' implies an 'observed' quantity.

Length-scale relationships for the side-driven model at small normalized convergence have already been investigated by England et al. (1985). This chapter investigates the equivalent relationships for the basally-driven model in sections 4.2 (for $t'=0$) and 4.3 (for $t'>0$), which are then compared to the side-driven results (extended to include large normalized convergence) in section 4.4. For the side-driven model, the finite length-scale of the indenter, D, enables mass to move along-strike, away from the areas of greatest thickening and deformation. Section 4.4 explores the implications of this mass transport for the growth in length-scales of deformation with time.

Figure 25: A schematic representation of two possible models for lithospheric convergence style, as previously discussed in section 2.1. (a) Whole lithosphere (side-driven) deformation, where the horizontal length-scale D (the length-scale of the boundary velocity) controls the style of deformation. The lithosphere thickens over side-driven length-scale λ_{NS}; (b) Detachment and subduction of mantle lithosphere with horizontal length-scale λ_m controlling the style of deformation; no along-strike variation in boundary velocity is shown, although such a variation may also be present. The crust thickens over basally-driven length-scale λ_{NB}.

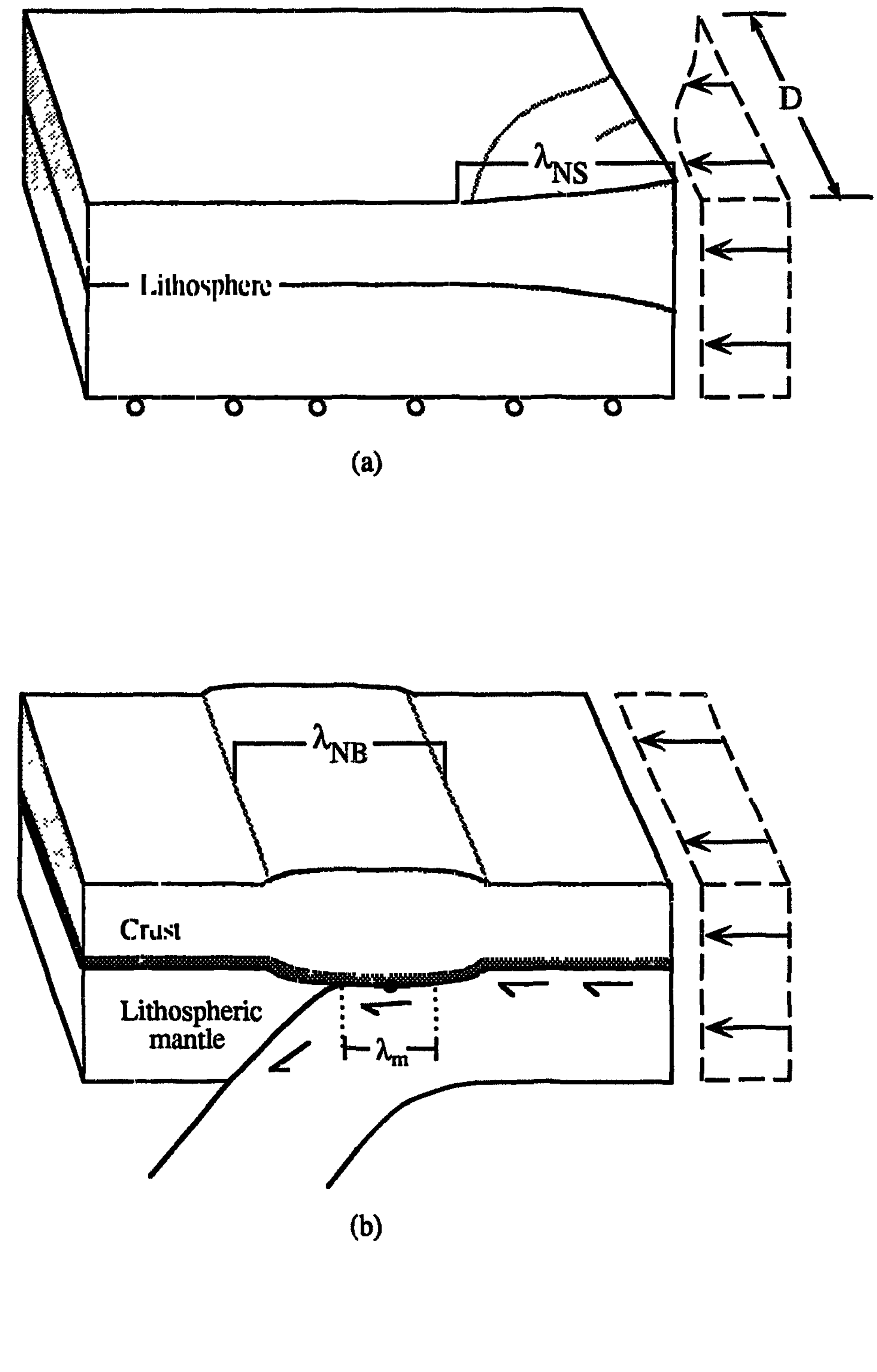
D
λ_{NS}
Lithosphere
(a)
λ_{NB}
Crust
Lithospheric mantle
λ_m
(b)

Figure 25

The partitioning of oblique convergence into normal and transcurrent movement along separate fault surfaces has been observed in numerous geological settings (e.g. England and Jackson, 1989). Although a continuum model of deformation cannot resolve individual fault structures, it can indicate whether partitioning is also likely to be present on a broad deformational scale, in terms of length-scales of normal and transcurrent deformation. The side-driven length-scale results of England et al. (1985) have been used to explain the partitioning of deformation length-scales observed during oblique convergence. I use the results from section 4.2 to determine whether these observations could also be explained by basally-driven deformation.

Aspects of the two cases illustrated in figure 25 are combined into a model with both side and basal horizontal forcing length-scales in section 4.5, in order to investigate the transition between length-scales controlled by basal forcing, to those controlled by the side-driven boundary conditions.

Measurement of the Length-Scales of Deformation for Normal Convergence

When there is no along-strike variation in the boundary condition (i.e. $D \rightarrow \infty$), the normal component of the strain-rate field, $\dot{\varepsilon}_{xx}$, provides a good measure of the across-strike length-scale of deformation and crustal thickening for small normalized convergence, because:

$$\frac{\partial S}{\partial t} \approx \dot{\varepsilon}_{zz} = -\frac{\partial \bar{u}}{\partial x}$$

where convergence is occurring in the x-directon, and the expression is written for $S \sim S_0$. However, when D is finite, neither the normal strain-rate component ($\dot{\varepsilon}_{xx}$), nor the tangential strain-rate component ($\dot{\varepsilon}_{yy}$) provide an independent measure of the length-scale for crustal thickening, because:

$$\frac{\partial S}{\partial t} \approx \dot{\varepsilon}_{zz} = -\left(\frac{\partial \overline{u}}{\partial x} + \frac{\partial \overline{v}}{\partial y}\right)$$

(for $S \sim S_0$), so that the thickening rate depends on both strain-rate components. The length-scales of the normal strain-rate component and crustal thickening rate now differ even for small convergence, because some material is transported in a direction orthogonal to the velocity of the boundary. This along-strike movement is a measure of the material 'lost' laterally by tectonic escape, which does not contribute locally to thickening of the crust.

It is important, when estimating the extent of deformation at a plate boundary, to distinguish whether length-scales of velocity components ($\overline{u}$, $\overline{v}$), horizontal strain-rates ($\dot{\varepsilon}_{xx}$, $\dot{\varepsilon}_{yy}$), or crustal thickening rates ($\dot{\varepsilon}_{zz}$), are being measured. Each of these quantities is a valid measure of some aspect of the crustal deformation. Length-scales of the integrated crustal thickening rate are often the only information we have from ancient orogens (see chapter five). The length-scales of horizontal strain-rate components may be derived using geodetic measurements of horizontal displacements for more recent cases of convergence, but these components must be combined in order to correctly predict net crustal thickening and vertical uplift rates (e.g. Walcott, 1984).

Estimates for the extent of crustal deformation in thin sheet studies have often used velocity component length-scales (e.g. England et al. (1985)). For velocity components that decrease exponentially with distance from the plate boundary, velocity length-scales and their derivatives (i.e. strain-rate component length-scales) are equivalent. Velocity length-scales may also agree with the length-scale of crustal thickening, if there are no significant variations in the kinematics along-strike. In this case, all measures of deformation length-scales are similar, and are referred to generally as 'crustal deformation length-scales'. Some of the examples investigated in this chapter can be represented in this manner, in which case a knowledge of the variation in normal and transverse velocity components with distance from the plate boundary is sufficient to estimate the extent of deformation.

For cases where the three measures of length-scale discussed above do not agree, an attempt is made in this chapter to distinguish between them. An added complexity in length-scale terminology is therefore required. The superscripts 't' for thickening, 'v' for velocity components, and 's' for horizontal strain-rate components are used. For example, the deformation length-scale for a side-driven thin sheet as measured by the normal velocity component is ${}^{v}\lambda_{NS}$, the horizontal strain-rate component is ${}^{s}\lambda_{NS}$, and crustal thickening rate is ${}^{t}\lambda_{NS}$. When length-scale differences are small, the superscript notation is dropped. As is shown later in the chapter, velocity and horizontal strain-rate length-scales are similar for the basally-driven model, and also for the side-driven model except for cases with a linear viscous rheology. Maximum length-scale differences between horizontal strain-rates and the crustal thickening rate are also attained for domains which have a linear viscous rheology (n=1), and are being indented from the side. In general, it is shown that for power-law viscous rheologies with n>1, all measures of length-scale are within 30% of the predicted length-scale from equation 22.

§ 4.2 Scale Analysis for Basally-Driven Small Normalized Convergence

When t' is close to zero (i.e. the amount of convergence is small relative to the length-scales S_0 and λ_m), crustal thickness gradients $\partial S/\partial x$ and $\partial S/\partial y$ may be neglected in the governing equation (13). This simplification allows us to explore analytical solutions to (13) for the specific cases of normal convergence (hereafter referred to as 'N') and strike-slip motion ('T') along the plate boundary.

Model Boundary Conditions

Parameter values have been chosen, on the basis of the error analysis of the previous chapter, to predict deformation with less than 5% error due to the vertical averaging of velocities. The planform geometry (figure 26) has a mantle detachment length-scale $\lambda_m = S_0$, and values of Am were chosen so that the sheet is weakly coupled to the base. The basal velocity fields are shown by arrows (figure 26). Because the incident velocity does not vary along-strike, and decreases approximately exponentially with distance from the mantle detachment zone (see below), the crustal deformation length-scale may be estimated directly from measurements of the appropriate velocity component, as discussed in section 4.1.

To determine the interaction between the normal and transverse components of the velocity field and how deformation is partitioned, numerical experiment results are shown for three boundary conditions: (1) (N) basal velocities normal to the mantle detachment zone ($\mathbf{u}_m(\infty) = (u_0, 0)$, where $\mathbf{u}_m(\infty)$ is the far-field velocity vector for the converging side of the domain); (2) (T) transverse basal velocities ($\mathbf{u}_m(\infty) = (0, v_0)$); and (3) (N+T) obliquely convergent basal velocities ($\mathbf{u}_m(\infty) = (u_0, v_0)$). Case (3) is initially explored for normal and transverse velocity boundary components (u_0, v_0) equal in magnitude, but later (figure 31) the effect of varying the relative magnitudes of velocity boundary components is demonstrated. The velocity boundary condition does not change along-strike, and extends to infinity in both directions along the plate boundary.

Figure 26: Description of the boundary conditions (a-c) applied to the thin-sheet model in sections 4.2 and 4.3. The oblique case (c) is broken down into components (a) normal to and (b) parallel to the detachment zone. Mantle velocity varies sinusoidally from (u_0, v_0) to (0, 0) across the detachment zone, which has length-scale λ_m. Lateral boundary conditions are either rollers (fig. 26(a)) or dynamically determined, as represented by the symbol ∞ in fig. 26(b, c). The nails indicate regions where the crust is stationary with respect to the underlying mantle lithosphere.

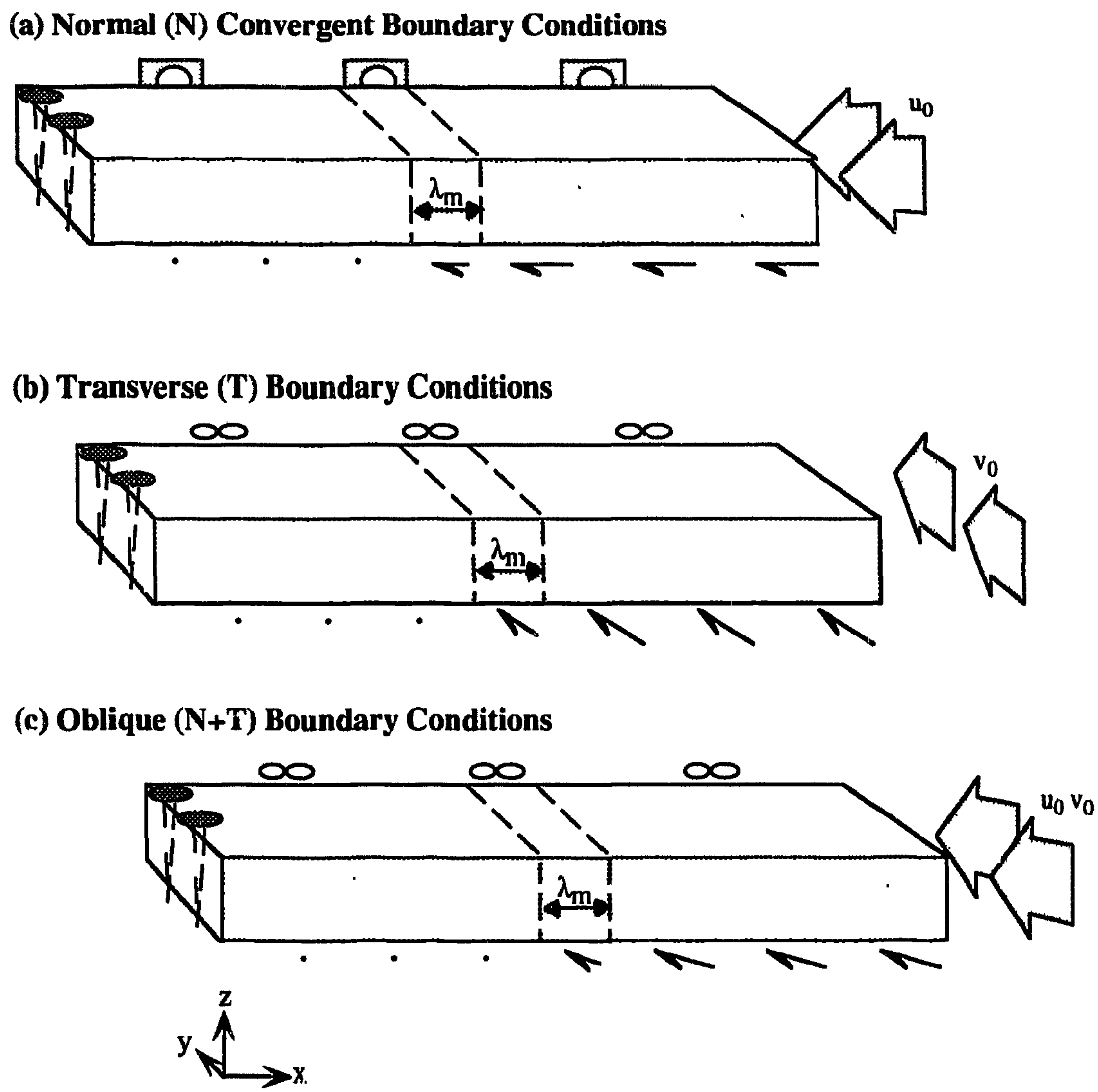
(a) Normal (N) Convergent Boundary Conditions
u_0
λ_m
(b) Transverse (T) Boundary Conditions
v_0
λ_m
(c) Oblique (N+T) Boundary Conditions
u_0 v_0
λ_m
z
y
x

Figure 26

The boundary conditions on the sides of the thin-sheet domain for normal convergence are free slip/ zero normal velocity (i.e. roller boundaries) on the lateral boundaries, and specified velocities along-strike. In the numerical experiments with a transverse basal velocity component, the roller condition on the lateral boundaries must be replaced by a dynamically determined boundary condition, in order to prevent the effect from these boundaries dominating the solution, and therefore failing to mimic an infinitely-extending boundary condition along the y-direction. The dynamical boundary velocities are determined iteratively in the following manner. Initially, the lateral boundary velocities are the same as the basal velocities, but in subsequent iterations the boundary velocities are specified to be equal to the solution velocities along the least-affected centre line (y=0) of the sheet. Velocities specified in this way converge after approximately 5-50 iterations, the exact number depending on the magnitude of basal coupling. This procedure eliminates the initial constraints of the specified velocities along these boundaries. The dynamically determined velocity condition on the lateral (x) boundaries is denoted by the symbol '∞' in figure 26 (b), (c).

Analytical Results for Linear and Non-Linear N, T Cases

The governing thin-sheet equation may be solved analytically at $t'=0$ for the boundary conditions as shown in figure 26(a) and (b), provided that the crustal response length-scale is greater than the forcing length-scale λ_m. For a linear rheology, the crustal deformation length-scales normal to the boundary can be shown (Appendix E) to be:

$$\lambda'_{NB} = \frac{4}{\sqrt{Am}} \quad \text{and} \quad \lambda'_{TB} = \frac{2}{\sqrt{Am}} \qquad \text{...(19a)}$$

where λ'_{NB} and λ'_{TB} are the full width length-scales, normalized by forcing length-scale λ_m, for separate normal (N) and transverse (T) boundary conditions. Unlike the results for the side-driven thin-sheet model, a velocity boundary condition applied along the base of the sheet with no length-scale along strike produces a finite length-scale of deformation, which depends on the relative strengths of the model crust and the weak basal layer. The ratio of length-scales for normal to transverse velocity boundary conditions is 2.

Because the Ampferer number depends on forcing length-scale λ_m, the dimensioned length-scales:

$$\lambda_{NB} = \frac{4\lambda_m}{\sqrt{Am}} = 4\sqrt{\frac{\mu_c}{\mu_b} hS_0} \quad \text{and} \quad \lambda_{TB} = \frac{2\lambda_m}{\sqrt{Am}} = 2\sqrt{\frac{\mu_c}{\mu_b} hS_0} \qquad ..(19b)$$

are independent of λ_m. Eq. (19b) describes the natural, inherent crustal response length-scales, which will be a good measure of the extent of deformation at small convergence times, provided the length-scales decribed in eq. (19b) are much larger than the forcing length-scale (λ_m).

For a non-linear viscous rheology, the normalized natural crustal response length-scales (Appendix E) are:

$$\lambda'_{NB} = 2\left(\frac{4}{n\,Am}\right)^{\frac{n}{n+1}} \qquad \text{and} \qquad \lambda'_{TB} = \left(\frac{4}{n\,Am}\right)^{\frac{n}{n+1}} \qquad ...(20a)$$

where λ'_{NB} and λ'_{TB} have been defined previously. The length-scale ratio for normal: transcurrent deformation remains at 2 for all n, provided deformation is produced by purely convergent or transcurrent boundary conditions. As for the linear case, the dimensioned length-scales:

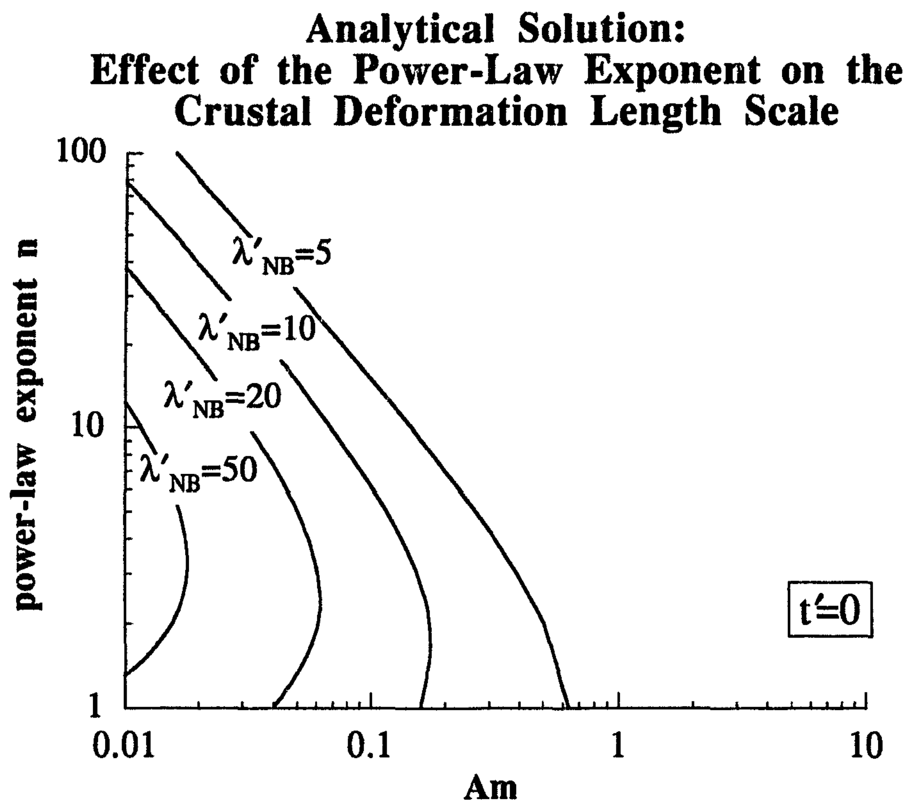

Figure 27: A contour plot of the analytical solution for basally-driven crustal deformation length-scale λ'_{NB} as a function of power-law exponent, n, and the Ampferer number, Am, for normal convergence. The analytical solution compares well with the numerical result shown in figure 24.

$$\lambda_{NB} = 2\lambda_m\left(\frac{4}{n\,Am}\right)^{\frac{n}{n+1}} = 2\left(\frac{4B_c}{nB_b}S_0\,h^{\frac{1}{n}}\right)^{\frac{n}{n+1}} \qquad \text{and}$$

$$\lambda_{TB} = \lambda_m\left(\frac{4}{n\,Am}\right)^{\frac{n}{n+1}} = \left(\frac{4B_c}{nB_b}S_0\,h^{\frac{1}{n}}\right)^{\frac{n}{n+1}} \qquad ..(20b)$$

are independent of mantle detachment length-scale λ_m.

The analytical solution for n>1 agrees well with the contour plot (figure 24, cf. figure 27) derived from numerical one-dimensional experiments in chapter 3. The normalized length-scale λ'_{NB} behaves in an interesting way with increasing power-law exponent n (figure 27). For n between 1 and 3, λ'_{NB} increases with n, but for power law exponents greater than 5, λ'_{NB} diminishes with increasing n. This behaviour is a result of the interaction between two strain-rate weakening effects: the focusing of deformation over the basal detachment zone (where strain-rates are high) as the effective viscosity of the crust decreases, in combination with decreased coupling between the base and crust away from the basal detachment zone where the effective viscosity of the model crust is higher .

Numerical Results for Linear and Non-Linear N, T Cases

Figure 28 illustrates some numerical results for the behaviour of λ'_{NB} with decreasing Ampferer number, for a linear viscous rheology. The dashed line and shaded zone represent the forcing velocity profile $u_m(x)$, and the solid curves are the resultant velocity $\bar{u}(x)$ in the crust. The half-width length-scale is measured by the e-folding width for the velocity profile, as indicated on figure 28.

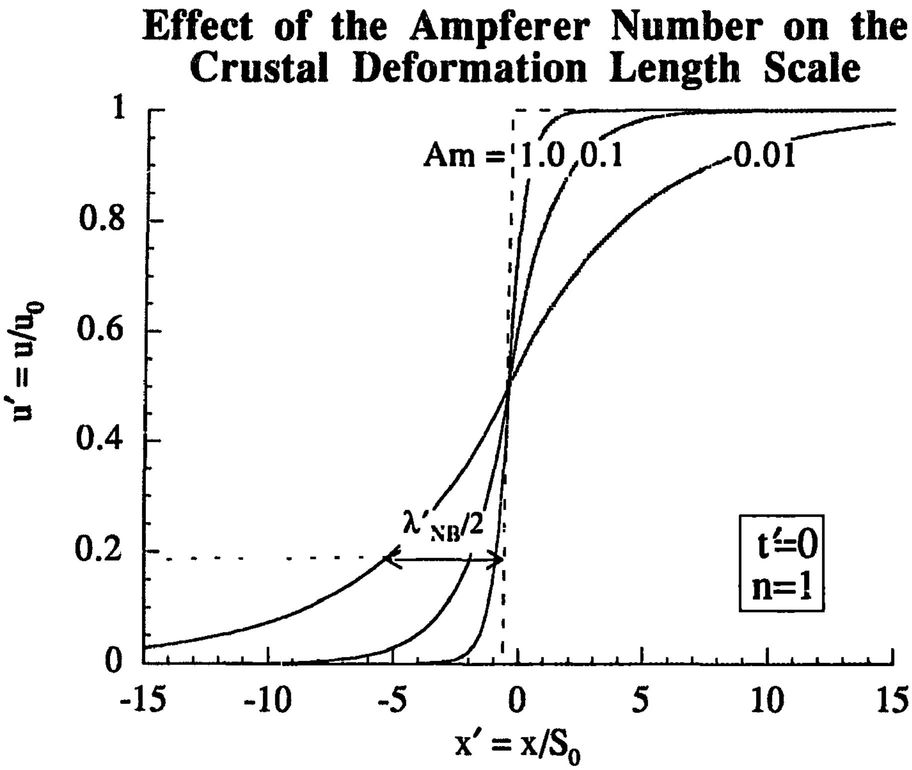

Figure 28: An illustration of the behaviour of the component of crustal velocity normal to the detachment zone ($\bar{u}$), as a function the Ampferer number Am, and normalized distance along the x-axis. The result is shown for linear rheology, n=1, and t′=0. The boundary of the shaded region (dashed line) shows the basal velocity profile. The numbers indicate the magnitude of Am. The arrowed quantity refers to the e-folding (half-width) length-scale of deformation ($\lambda'_{NB}/2$) for normal convergence.

A comparison between analytical and numerical deformation length-scales vs. Am for n=1, 3, 10 is shown in figures 29(a, b). For both normal and transverse boundary conditions, the agreement between the predicted analytical dependence of λ'_{NB} on the Ampferer number (lines), and the numerical result (symbols) is good. The lower limits on λ_{NB} and λ_{TB} are constrained by the forcing length-scale λ_m, so that as Am increases, λ'_{NB} and $\lambda'_{TB} \rightarrow 1$.

The ratio between normal and transcurrent deformation length-scales, α, also changes as λ_{NB} and λ_{TB} reach the λ_m limit (figure 29(c)). For low Ampferer numbers, $\alpha = 2$, as predicted by the analytical solution. When λ_{NB} and λ_{TB} are comparable in size to λ_m, α decreases to 1, and the solution becomes totally dominated by the basal forcing length-scale. This lower limit is reached at smaller Ampferer numbers as the power-law exponent increases, due to the stronger coupling of the crust to the base. The limit indicates that for a sufficiently strong crust-mantle coupling, crustal length-scales are likely to be determined directly from the forcing length-scale of the underlying mantle.

Figure 29: Numerical (symbols) and analytical (solid lines) crustal deformation length-scale, scaled by forcing length λ_m, as a function of n (● = 1, ■ = 3, ◆ = 10), and Am. (a) λ'_{NB} for normally convergent boundary conditions (N); (b) λ'_{TB} for transverse boundary conditions (T); (c) ratio, α, of normal:transcurrent length-scales of deformation for purely convergent (N) vs. purely transverse (T) boundary conditions. The results predict a constant normal:transcurrent ratio of 2, except when λ_{NB} and λ_{TB} approach λ_m, in which case the ratio decreases to 1.

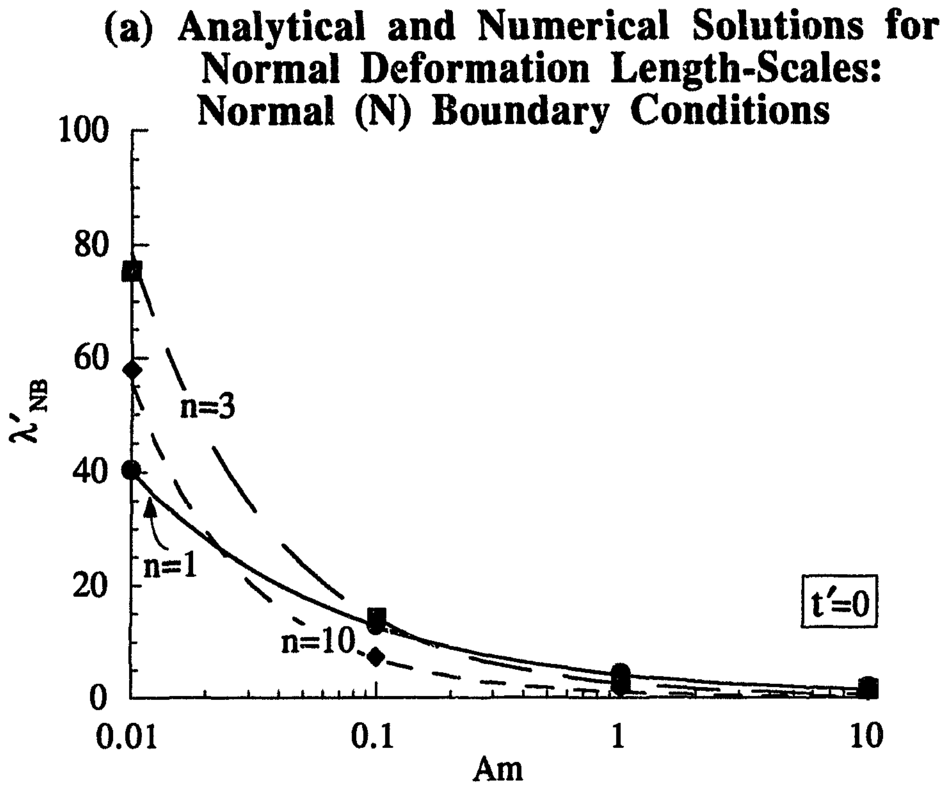
(a) Analytical and Numerical Solutions for Normal Deformation Length-Scales: Normal (N) Boundary Conditions
100
80
60
40
20
0
λ'NB
n=3
n=1
n=10
t'=0
0.01
0.1
1
10
Am

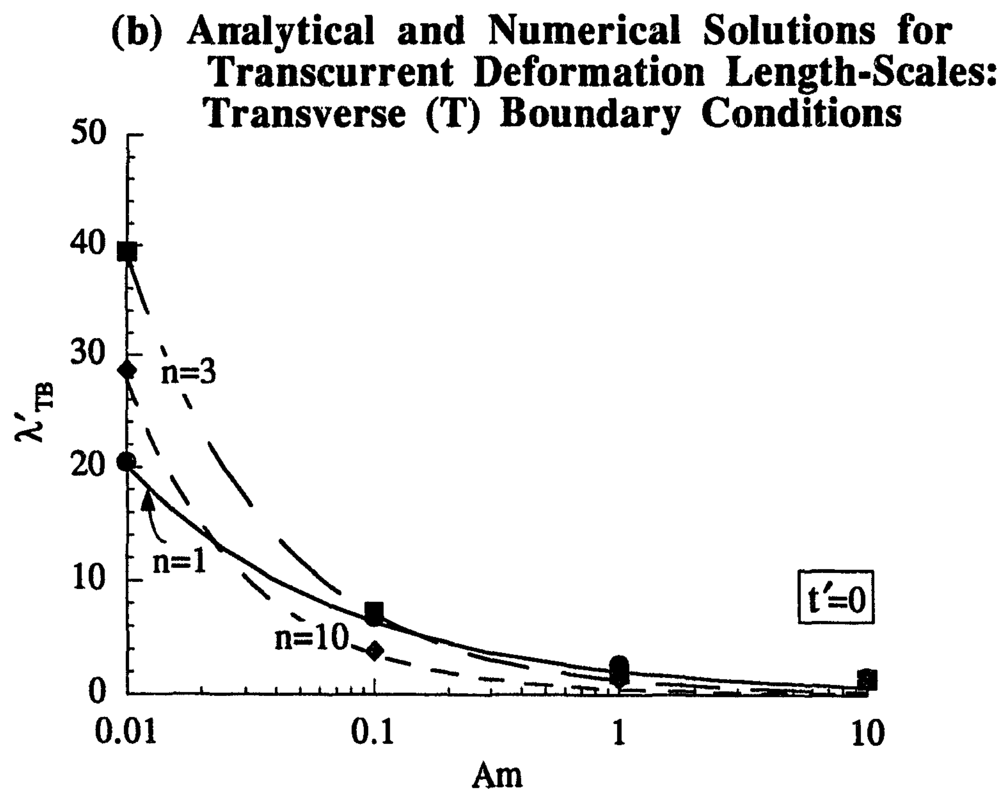
(b) Analytical and Numerical Solutions for Transcurrent Deformation Length-Scales: Transverse (T) Boundary Conditions
50
40
30
20
10
0
λ'TB
n=3
n=1
n=10
t'=0
0.01
0.1
1
10
Am

Figure 29(a,b)

(c) Ratio of Normal: Transcurrent Length-Scales, α, for N, T Boundary Conditions

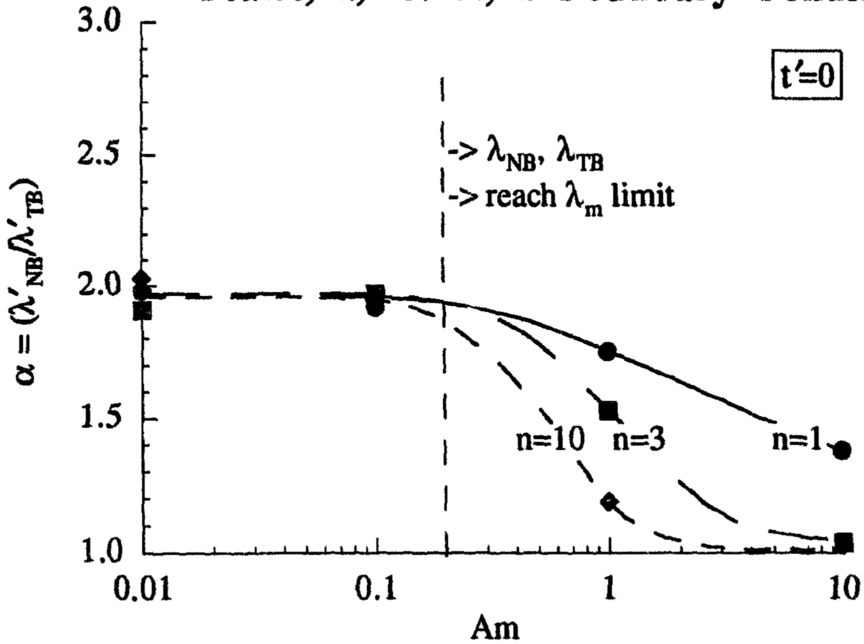

Figure 29(c)

Numerical Results for Non-Linear N+T Case

The non-linear obliquely convergent case (figure 26(c)) cannot be solved easily by analytical methods. The numerical results (figure 30(a), (b)) show the change in normalized deformation length-scales λ'_{NB} and λ'_{TB} with Am for the case when $u_0=v_0$ (note that the lines no longer represent an analytic solution). Both normal and transcurrent length-scales are reduced in comparison to the equivalent (N) and (T) results (figure 29(a),(b)), especially the normal length-scale. The reduction in length-scales is a result of the increased magnitude of strain-rate weakening caused by cross-coupling of terms in equation 13. The ratio of length-scales for normal and transcurrent components of deformation also changes with increasing power-law exponent n (figure 30(c)). For a linear viscous rheology, the ratio is the same as for the independent N and T cases. However, for n greater than 1, the effective viscosity of the crust will depend on both components of the strain-rate tensor. This cross-coupling between the components results in the length-scales taking intermediate values between those for the independent normal and transverse boundary conditions, so that α is less than 2.

Figure 30: Numerical (symbols) and analytical (solid lines) crustal deformation length-scale as a function of n (● = 1, ■ = 3, ◆ = 10), and Am. The velocity components u_0 and v_0 are equal in magnitude. (a) λ'_{NB} for oblique boundary conditions (N+T); (b) λ'_{TB} for oblique boundary conditions (N+T); (c) Ratio, α, of normal: transcurrent length-scales of deformation for the N+T case. The velocity components are equal in magnitude. As the power-law exponent increases, the normal:transcurrent length-scale ratio decreases to 1.

(a) Numerical Solutions for Normal Deformation Length-Scales: Oblique (N+T) Convergence

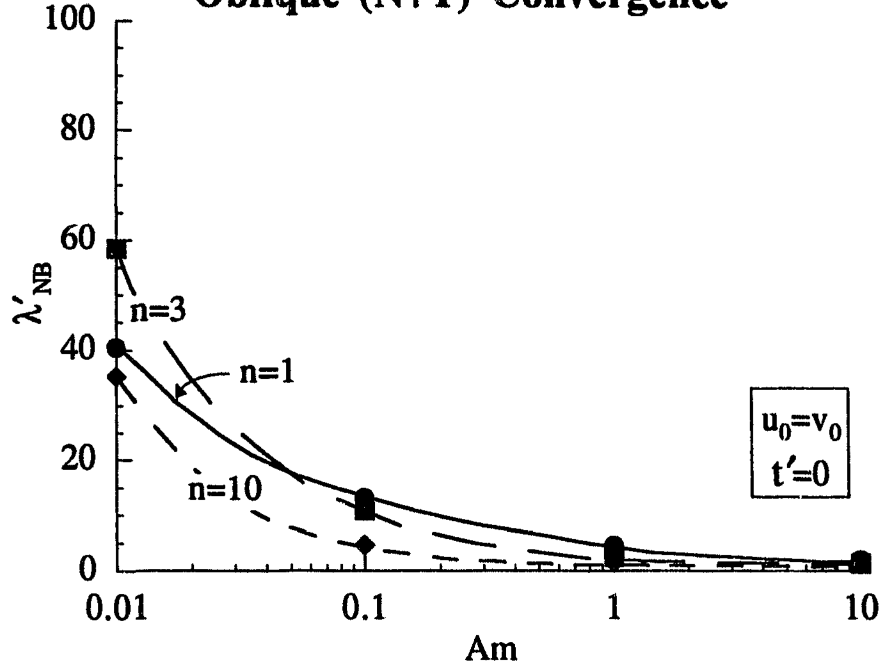

(b) Numerical Solutions for Transcurrent Deformation Length-Scales: Oblique (N+T) Convergence

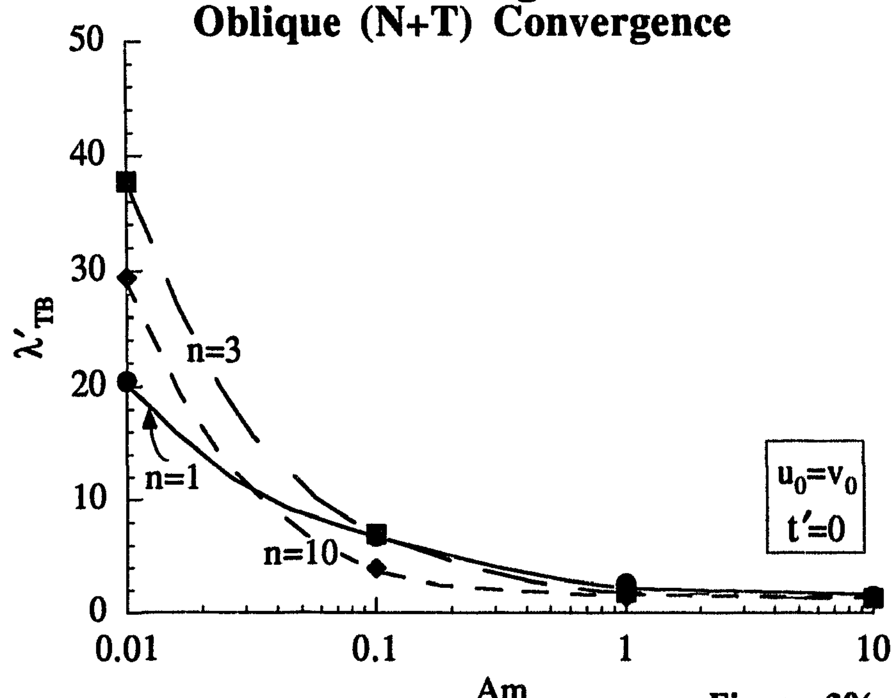

Figure 30(a,b)

(c) Ratio of Normal: Transcurrent Length-Scales, α, for Oblique (N+T) Boundary Conditions

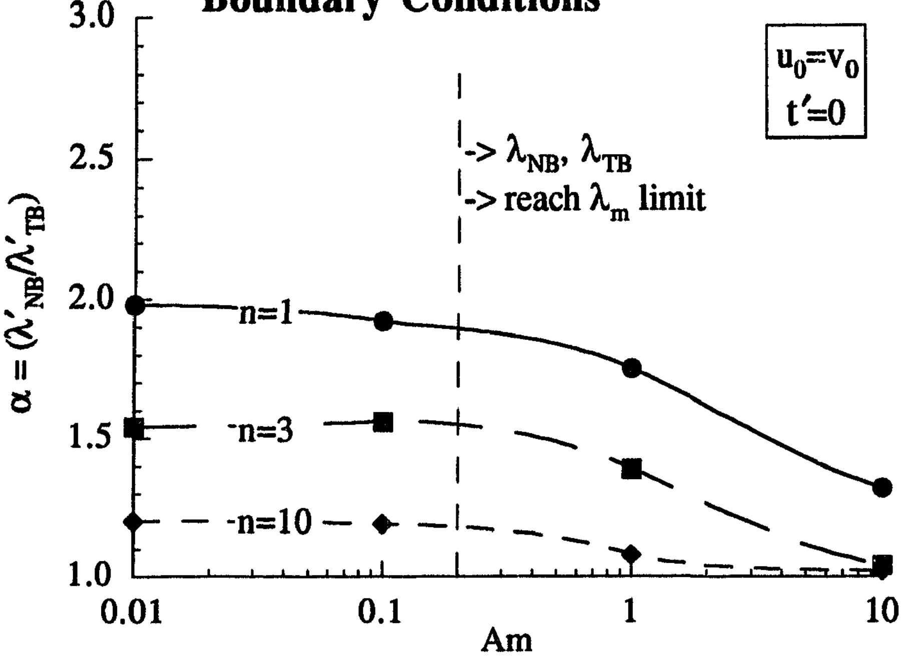

Figure 30(c)

The ratio α also depends on the relative magnitude of the normal and transverse velocity components (figure 31). For n greater than 1 but finite, α is between 2 and 1, except for cases where $v_0 \ll u_0$ or $u_0 \ll v_0$. The asymptotic behaviour of α in these cases is caused by the interaction of the non-linear rheology of the basal and crustal layers. The basal length-scale for both normal and transverse velocity components is prescribed to be λ_m. Where $v_0 \ll u_0$, the strain-rate weakening of the crust is controlled by $\partial u/\partial x$, so that weakening occurs over length-scale λ_{NB}. The resulting effective viscosity ratio creates a focusing effect which confines transcurrent deformation to a length-scale close to λ_m. The ratio of length-scales will therefore become unbounded for very small mantle detachment length-scales. Similarly, where $u_0 \ll v_0$, the crust weakens over length-scale λ_{TB} and normal deformation is confined to a length-scale close to λ_m, so that the value of the ratio α approaches zero. As n becomes very large (>100), both λ_{NB} and λ_{TB} approach the limit λ_m, and α is ~ 1 for all values of u_0 and v_0.

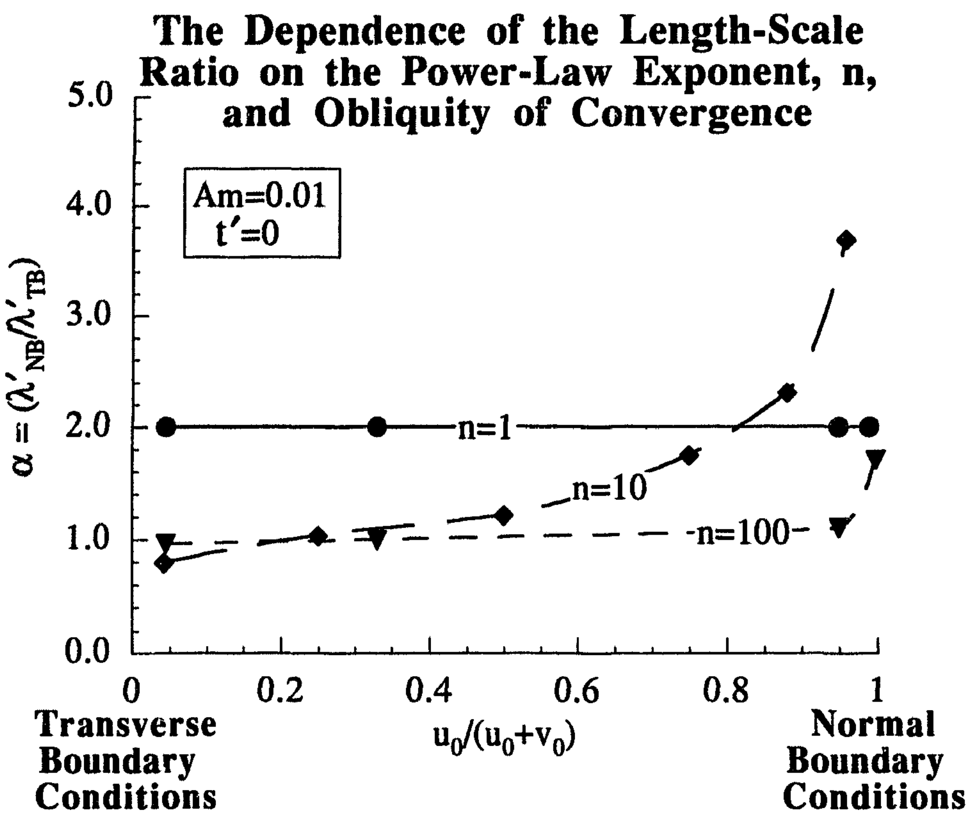

Figure 31: The dependence of the length-scale ratio, α, on the relative size of the normal and transverse velocity components. For n=1, $\alpha = 2$ for all values of (u_0, v_0). As n increases, the ratio α decreases except for the extreme cases $u_0 >> v_0$ (and $v_0 >> u_0$). For very large power-law exponents, the length-scales approach the forcing length-scale λ_m, so that α tends to 1.

§ 4.3 Scale Analysis for Basally-Driven Large Normalized Convergence

As normalized convergence time t' increases, the terms in $\partial S/\partial x$ in equation (13) may no longer be neglected for the normally incident deformation case (N). The additional dependence on crustal gradient terms represents the effect of gravity acting on crustal thickness contrasts, as well as the reduction in net basal traction (i.e. traction per unit crustal thickness) operating on each column of thickened crust. No exact analytic solution can be found for the length-scale of deformation in this case. However, for $t' > 0$ but S' still relatively close to 1, an approximate expression for the length-scale, and its dependence on the Argand number and normalized time for a linear viscous thin-sheet, may be found (Appendix E) to be:

$$\lambda'_{NB} \approx (\lambda'_{NB}|_{t'=0})\sqrt{1+\frac{Ar\,t'}{2}} \qquad \ldots.(21)$$

where $\lambda'_{NB}|_{t'=0}$ is the scaled normal deformation length-scale at $t'=0$.

This approximate analytical solution is compared to the numerical results for the increase in model length-scale in figures 32 and 33(a). Figure 32 shows contours of λ'_{NB} at normalized convergence time $t'=1$, where the symbols represent the numerical solution, and the lines are the analytical approximation. The fit is quite good, even for the cases where $Ar \gg 1$. In figure 33 (a), the change in λ'_{NB} with increasing convergence is shown for numerical (symbols) and analytical (lines) solutions, for a linear viscous thin-sheet. (The slight scatter in the initial trend of the numerical results is an artifact of the grid resolution). Results from the crustal thickness profiles (not shown) indicate that the analytical and numerical solutions diverge for crustal thickness gradients in excess of approximately 1 in 20.

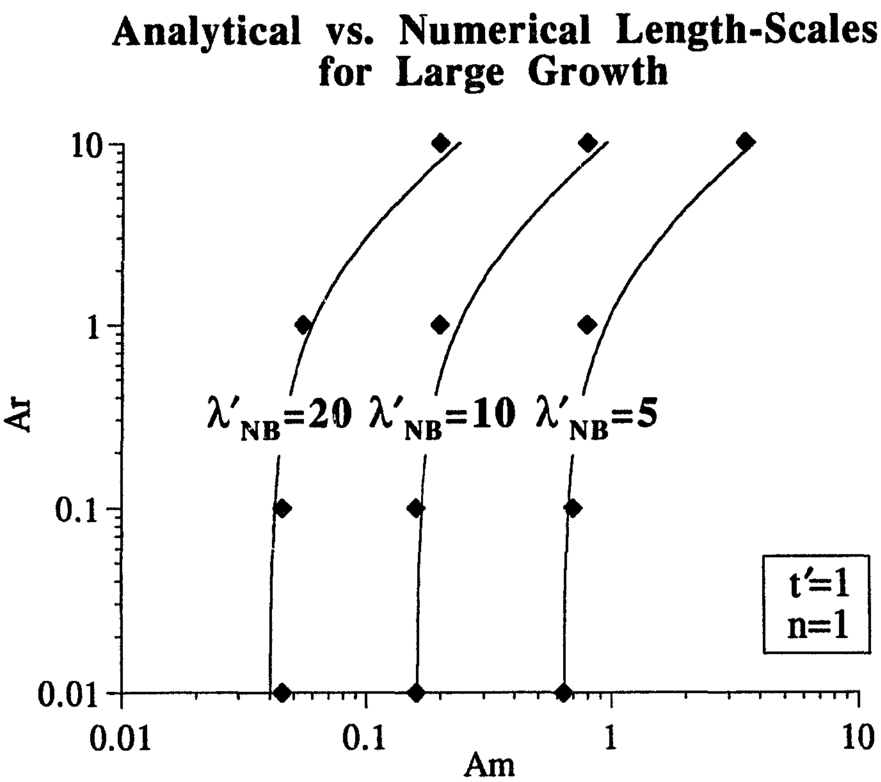

Figure 32: A comparison between numerical model results (◆) and the approximate analytical solution (solid lines) for contours of scaled normal crustal deformation length, λ'_{NB}, as a function of the dimensionless Ampferer and Argand numbers, at normalized convergence time $t'=1$.

The equivalent numerical results to figure 33(a) for a non-linear sheet (n=3) are shown in figure 33(b). No analytical result has been found for this case, but the numerical result shows that the length-scale still increases approximately linearly with $\sqrt{t'}$. The increase is initially faster than for n=1, because of the interaction between crustal thickness gradients and strain-rate wea' ;, effects in the crust and basal layers.

For purely transcurrent deformation, the crustal thickness does not change, so $\lambda'_{TB} = \lambda'_{TB}\big|_{t'=0}$ for all t'. Therefore, for the linear viscous case, the length-scale ratio $\alpha(=\lambda_{NB}/\lambda_{TB})$ increases proportionately with time by:

$$\alpha \approx \left.\frac{\lambda'_{NB}}{\lambda'_{TB}}\right|_{t'=0} \sqrt{1+\frac{Ar\,t'}{2}}$$

This relationship holds to a first approximation, and is investigated in more detail in chapter six. Crustal thickness gradients produced by oblique convergence will affect the normal length-scale much more than the transcurrent length-scale, because the buoyancy forces increase the motion away from areas of thickening. Therefore, even for oblique convergence, the length-scale ratio α will increase with t'. Figure 34 demonstrates the increase in α with t' by plotting numerical results for the length-scale ratio vs. power-law exponent n. The increase is fastest for n=10, because of the strain-rate weakening phenomenon.

Figure 33: Normal crustal deformation length-scale λ'_{NB}, vs. normalized convergence time t'. (a) n=1, Am=0.1, Ar=0.1. The approximate analytical solution is represented by the solid line; symbols (◆) are the numerical solution. Agreement is good for t' less than 10, which corresponds to crustal gradients less than about 1 in 20.(b) n=3, Am=0.1, Ar=0.1. Only the numerical solution (◆) is shown.

(a) Analytical and Numerical Length Scales vs. t′ for Large Growth Models, n=1

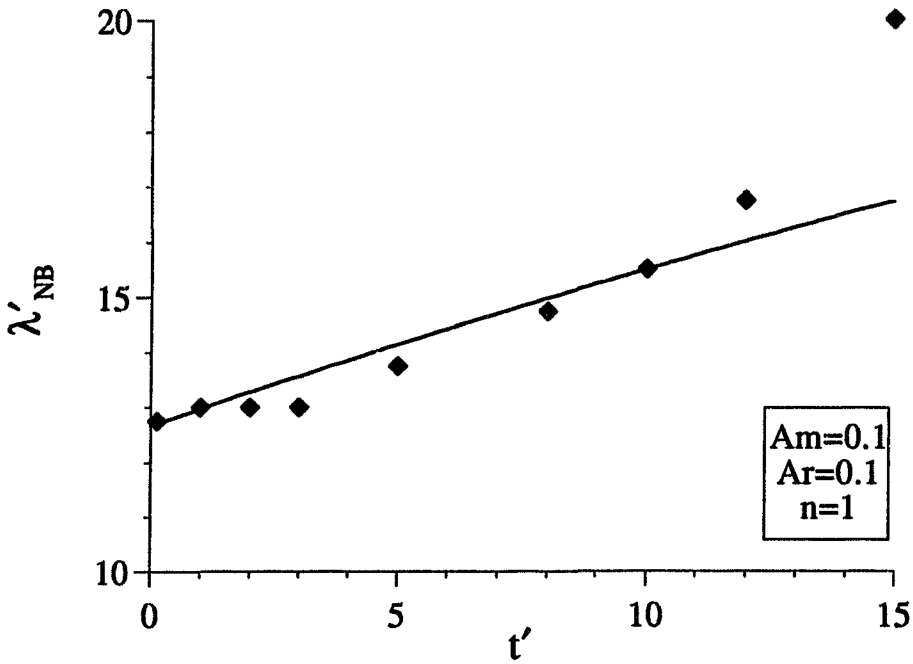

(b) Numerical Length Scale vs. t′ for Large Growth Models, n=3

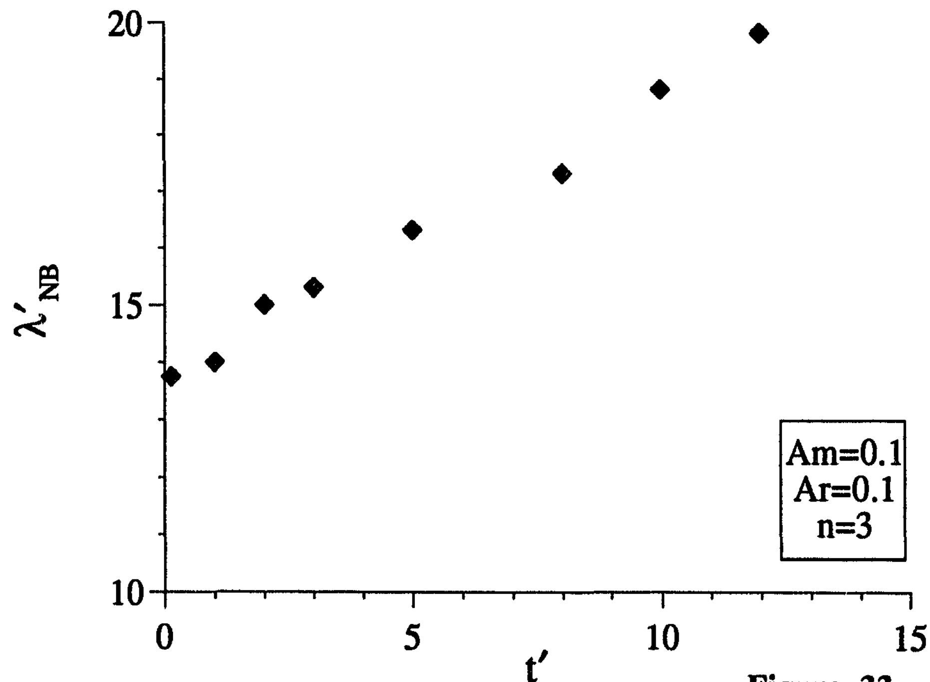

Figure 33

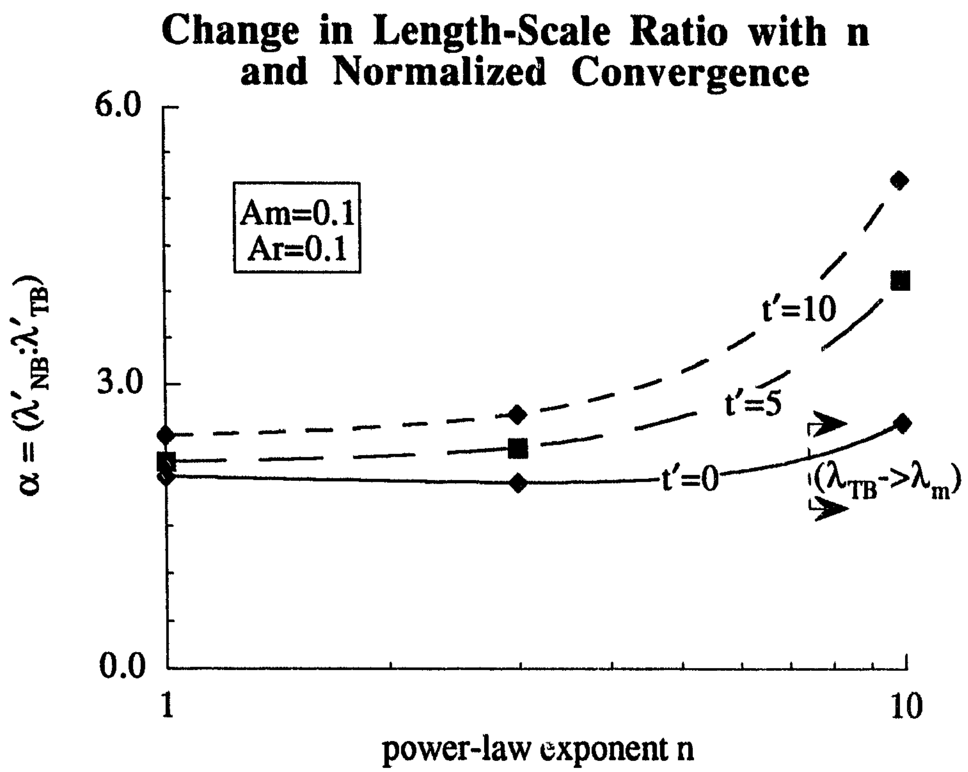

Figure 34: Length-scale ratio, α, vs. n, for convergence times t′=0, 5 and 10, and boundary conditions from figure 26(a) (=N) and 26(b) (=T). The lines represent curve fits to the numerical solutions (◆). As the crustal deformation length-scales approach the forcing length-scale limit (for t′=0), the predicted ratio of 2 and the numerical solution diverge.

§ 4.4 Comparison of Basally-Driven and Side-Driven Length-scale Predictions

Predicted Side-Driven Length-scales for Small Normalized Convergence

England et al. (1985) investigated length-scales of deformation driven by sinusoidally- varying velocity boundary conditions along the sides of the model domain (figure 35(a), (b)). By using such simple functions to describe the variation in velocity, they were able to solve analytically the behaviour of a linear viscous thin-sheet at small normalized convergence. The length-scales for side-driven normal and transcurrent velocity components are approximately related to the indenter length-scale, D (defined below), by:

$$^{v}\lambda_{NS} \cong \frac{2D}{\pi\sqrt{n}} \quad \text{and} \quad ^{v}\lambda_{TS} \cong \frac{D}{2\pi\sqrt{n}} \qquad \text{....(22)}$$

where n is the power law exponent, and the symbols $^{v}\lambda_{NS}$ and $^{v}\lambda_{TS}$ are used to indicate velocity component length-scales for a one-sided (indenter-controlled) orogen or strike-slip plate boundary. The length-scales are measured from the indenter boundary, at the along-strike position where the incident velocity attains its maximum value, horizontally out to the position where the velocity component reaches 1/e of its incident value at the side boundary. Sample results for the simple sinusoidal boundary conditions are shown in figure 36(a), (b). The plots are shown in dimensionless units, with indenter length D′=50, scaled by the initial crustal thickness S_0. The filled circles indicate the extent and along-strike location of the measured velocity length-scales.

Figure 35: The boundary conditions investigated by England et al. (1985) (a) normal convergence; (b) transcurrent deformation. As defined previously, D represents the length-scale of the indenter.

Side Forcing

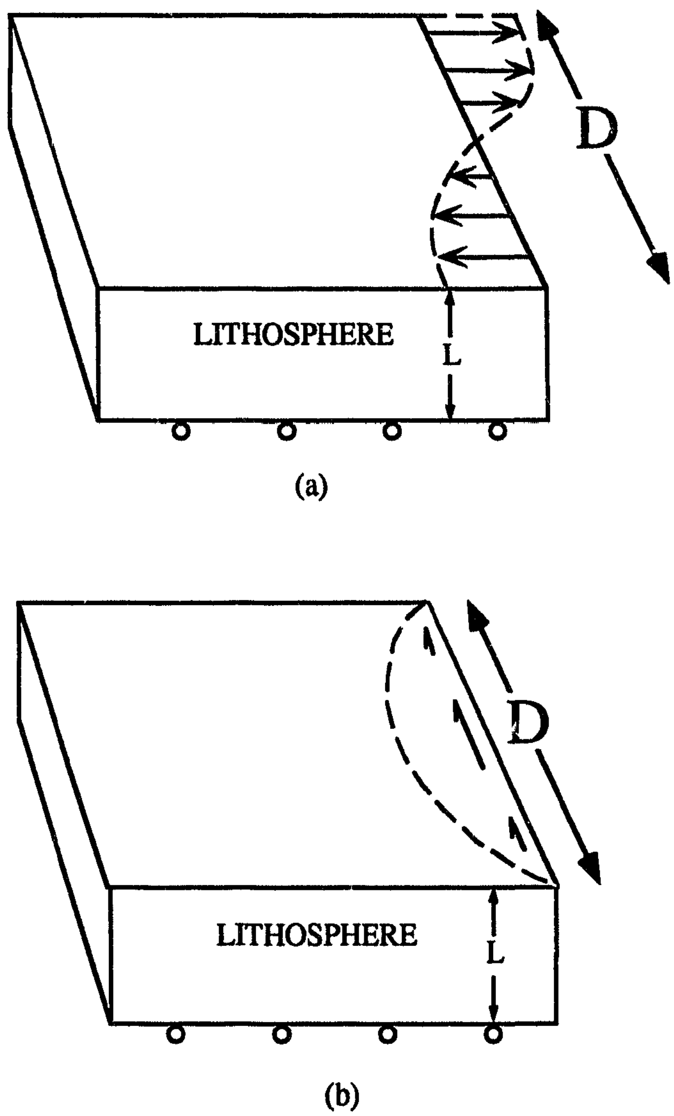

Figure 35

The parameter D (as shown in figure 25) represents the horizontal extent of the convergent (or transverse) velocity along strike, where it is assumed that convergence (or transverse motion) is between a kinematically defined indenter moving at velocity **u**(x) and a much weaker lithospheric plate. The side boundary therefore changes position with time by the amount **u**(x)t. The indenter is assumed to deform according to the specified kinematics, and is therefore not modelled physically, but is outside of the model domain. The indenter boundary does not keep the same shape with increasing convergence, because it is defined by a velocity boundary condition. Throughout this thesis, I use the term 'indenter' to indicate this kinematic form of boundary condition. The kinematic indenter is distinct from a body which indents the crust with no internal deformation, which is referred to (when used in the thesis) as a 'rigid indenter'.

The equations (22) were derived using the simple sinusoidal boundary conditions shown in figure 36(a),(b). When the shape of the indenter is changed (e.g. figure 36(c),(d)), the length-scales of velocity components will change. For example, the velocity length-scale ${}^{v}\lambda'_{NS}$ is larger by 25% for the half-sinusoid indenter shown in figure 36(c), compared to the full sinusoid (figure 36(a)). The change is related to the reduction in tectonic escape along-strike.

Figure 36: Shaded contours of vertical strain-rate, with velocity vectors superimposed, for various shaped (kinematic) indenters at small normalized convergence ($t'=0$). The bullets indicate the location and across-strike extent of the measured deformation length-scales for each case. (a) Boundary velocity $u'(x')=\cos(\pi y'/D')$, $v'(x')=0$; (b) boundary velocity $v'(x')=\sin(\pi y'/D')$, $u'(x')=0$; (c) boundary velocity $u'(x')=\cos(\pi y'/D')$, $y'<D'/2$; $u'(x')=0$, $y'>D'/2$, $v'(x')=0$; (d) boundary velocity $u'(x')=1$, $y'<D'/4$; $u'(x')=\cos^2(\pi y'/D')$, $D'/4<y'<D'/2$; $u'(x')=0$, $y'>D'/2$, $v'(x')=0$. The length-scale relations are indicated at the side of each figure.

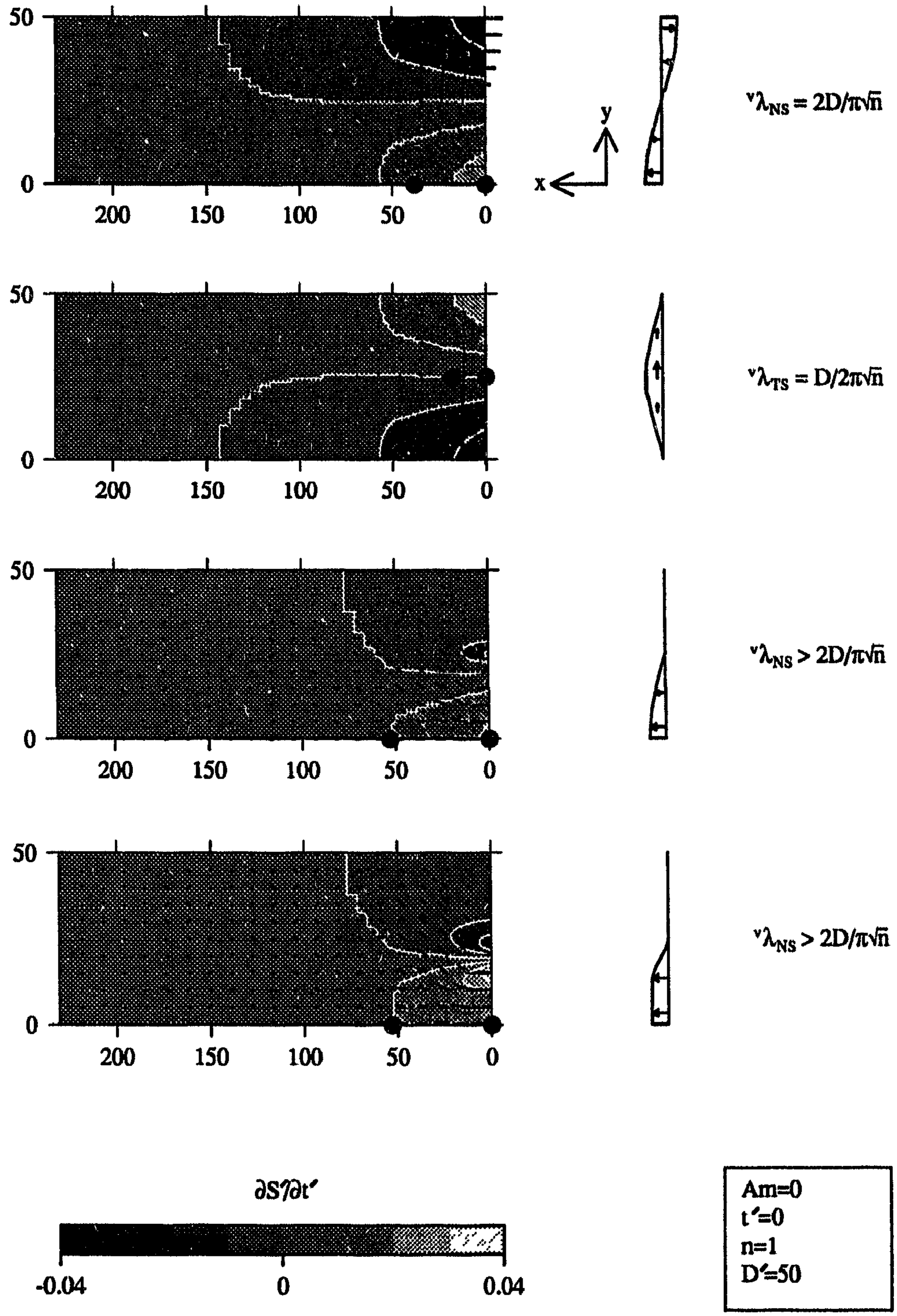
$^{v}\lambda_{NS} = 2D/\pi\sqrt{n}$
$^{v}\lambda_{TS} = D/2\pi\sqrt{n}$
$^{v}\lambda_{NS} > 2D/\pi\sqrt{n}$
$^{v}\lambda_{NS} > 2D/\pi\sqrt{n}$
$\partial S'/\partial t'$
-0.04
0
0.04
Am=0
t'=0
n=1
D'=50

Figure 36

As explained at the beginning of this chapter, the length-scale of crustal thickening for the side-driven case will not necessarily agree with the length-scale derived from the velocity components, because of the variation in the velocity boundary condition applied along-strike. This difference is illustrated in figure 37(a), which plots length-scales of velocity, horizontal strain-rate components, and crustal thickening rate, vs. along-strike length-scale D′, for n=1 and Ar=0. The length-scales are measured at the position of maximum incident indenter velocity, as for figure 36. The length-scale relation predicted from equation (22) is also shown on figure 37. The crustal thickening rate length-scale $^{t}\lambda'_{NS}$ is approximately half as big as the length-scales of the velocity and horizontal strain-rate components, which bracket the predicted relationship from eq. (22). If a linear viscous rheology can be used to represent behaviour of the lithosphere, this result suggests that measurement of the velocity or horizontal strain-rate length-scales using geodetic surveys or focal mechanisms will not provide a good estimate of the length-scale of crustal thickening. Conversely, if the only information available is the extent of thickened crust, this length-scale will not necessarily provide a good measure of the decrease in indenter velocity with distance from the plate boundary.

Figure 37: (a) A comparison of the velocity, horizontal strain-rate, crustal thickening rate, and predicted length-scales for the side-driven boundary conditions of figure 35(a), vs. normalized indenter length-scale D′. Other parameter values are t′=0, n=1, and Ar=0; (b) A comparison of the velocity, horizontal strain-rate, crustal thickening rate, and predicted length-scales for the side-driven boundary conditions of figure 35(a), vs. power-law exponent n. Other parameter values are t′=0, D′=50, and Ar=0.

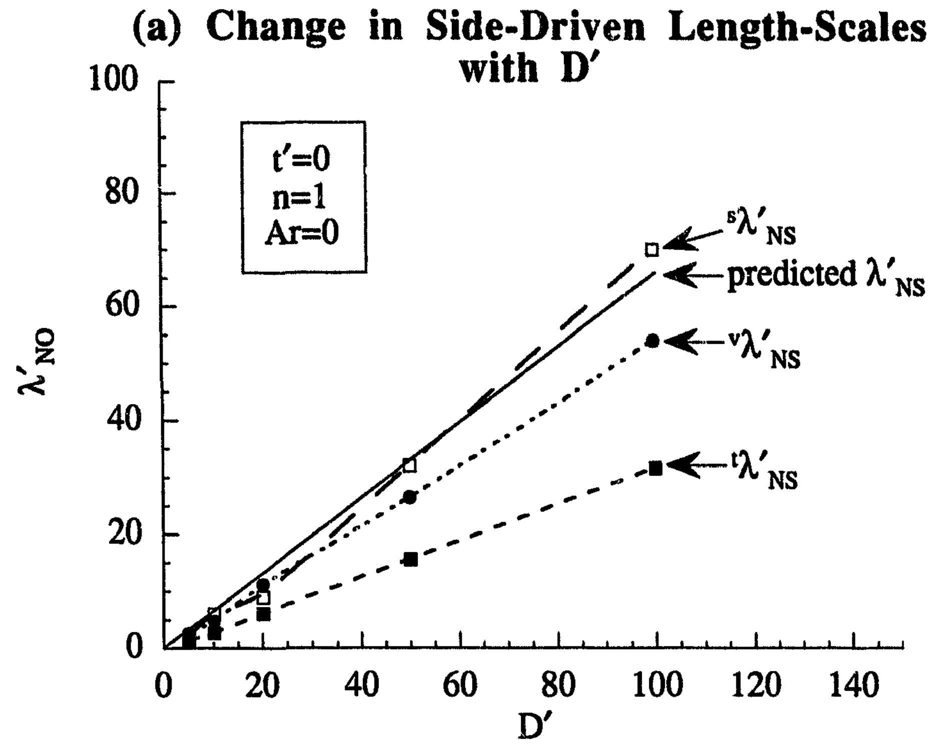
(a) Change in Side-Driven Length-Scales with D′
t′=0
n=1
Ar=0
ˢλ′NS
predicted λ′NS
ᵛλ′NS
ᵗλ′NS
λ′NO
D′
0
20
40
60
80
100
120
140

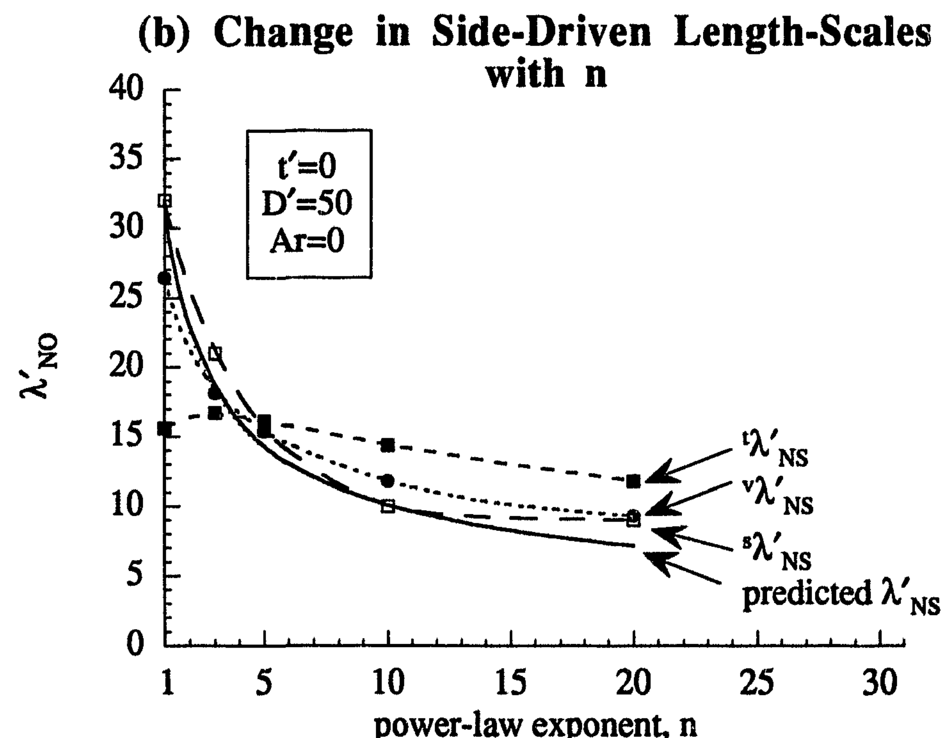
(b) Change in Side-Driven Length-Scales with n
t′=0
D′=50
Ar=0
ᵗλ′NS
ᵛλ′NS
ˢλ′NS
predicted λ′NS
λ′NO
power-law exponent, n
1
5
10
15
20
25
30

Figure 37

The difference between ${}^{v}\lambda'_{NS}$, ${}^{s}\lambda'_{NS}$, and ${}^{t}\lambda'_{NS}$ can be shown to depend on n, the power-law exponent for the deforming layer. Figure 37(b) illustrates this dependence for the side-driven case, with D′=50 and Ar=0. The solid line is the predicted relationship based on equation (22). The difference between thickening rate and velocity component length-scales decreases substantially for n>1, and all the length-scale measures are within 30% of each other for power-law viscous rheologies. This result indicates that tectonic escape of mass along-strike becomes much less important for n>1, a result of the increased coupling of the model lithosphere to the indenter boundary conditions.

Comparison with Basally-Driven Results for Small Normalized Convergence

(i) Length-Scales

The results from section 4.2 demonstrate that length-scale relationships for small amounts of crustal convergence driven by the detachment of underlying mantle lithosphere (λ'_{NB}, λ'_{TB}, eq. 20b), differ from those derived from the side-driven indenter model (λ'_{NS}, λ'_{TS}, eq. 22). In particular, the side-driven model predicts that deformation length-scales will extend further and further from the plate boundary as $D \rightarrow \infty$, whereas the basally-driven model predicts length-scales for this case which are independent of the side boundary conditions.

(ii) Ratio of Length-Scales for Separate Normal and Transverse Boundary Conditions

The side-driven results summarized in eq. (22) show that for linear and power-law viscous rheologies, the length-scale of the normal velocity component across-strike extends approximately 4 times further away from the boundary than the corresponding transcurrent velocity component, provided the normal and transverse boundary conditions are applied separately. The discrepancy between the length-scale ratio of 4 for the side-driven model, and 2 for the basally-driven model, suggests that a potential test to distinguish between the two styles of deformation is to estimate velocity length-scale ratios for convergent, vs. strike-slip, active plate boundaries.

(iii) Length-Scale Ratios for Oblique Convergence

England et al. (1985) and Sonder et al. (1986) did not investigate the equivalent side-driven results for oblique convergence (N+T), but only for the separate normal (N) and transcurrent (T) responses. There are no published results that show how the side-driven velocity length-scale ratio of 4 will be modified for the obliquely convergent case. Using the boundary conditions of figure 38(a), I conducted a simple test, for increasing values of power-law exponent and an incident velocity vector with equal normal and tranverse components ($u_0=v_0$). The results, summarized in a plot of the length-scale ratio (α) vs. power-law exponent (n) (figure 38(b)), show that the velocity length-scale ratio for a side-driven thin-sheet model decreases with n in a similar manner to the basally-driven thin-sheet. As for the basally-driven case, the cross-coupling between normal and transverse velocity components through strain-rate weakening tends to reduce differences between the length-scales. Therefore, although results imply that for separate normal and transcurrent boundary conditions, measurement of velocity length-scale ratios may be useful in distinguishing different deformation styles, length-scale ratio tests for *oblique* convergence may not be so useful, since for both the side-driven and basally-driven models, the ratio tends to 1. This conclusion is based on the assumption that an average power-law rheology with n>1 can be used to represent the deforming layer.

Figure 38: (a) Shaded contours of vertical strain-rate, with velocity vectors superimposed, for oblique side-driven convergence. Velocity boundary conditions are: $u'(x')=\sin(\pi y'/D')$, $v'(x')=\sin(\pi y'/D')$, and results are shown for n=1 and n=3; (b) A plot of the length-scale ratio, α, vs. n, for the cases shown in (a).

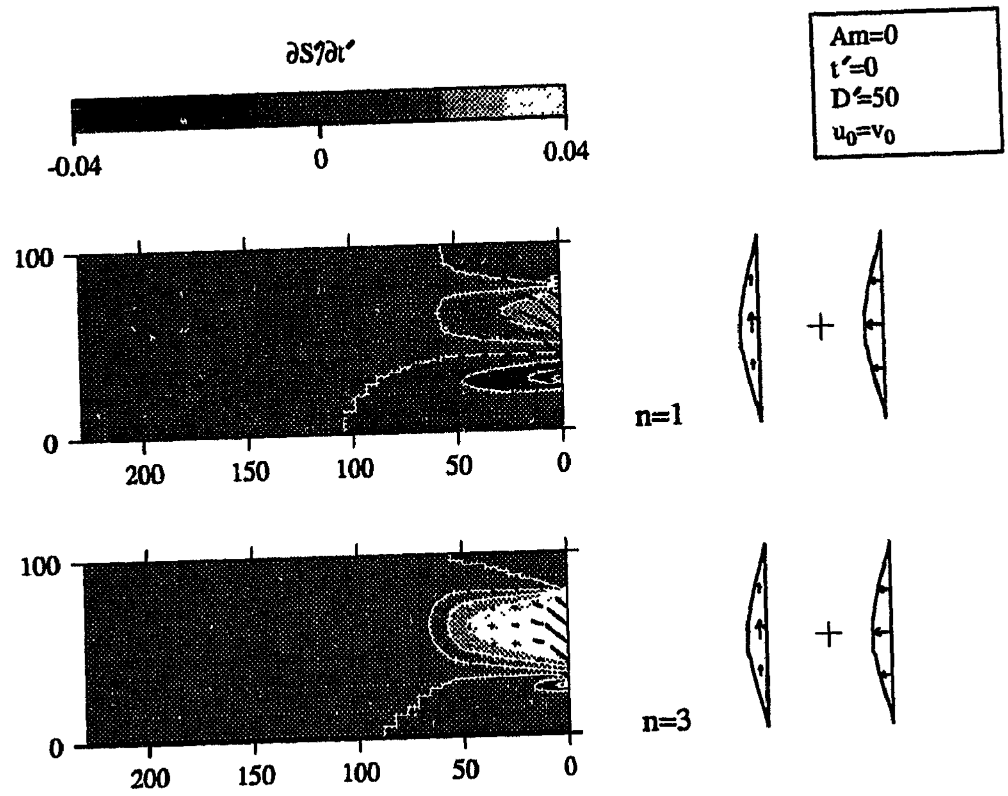
∂S'/∂t'
-0.04
0
0.04
Am=0
t'=0
D'=50
u_0=v_0
100
0
200
150
100
50
0
n=1
n=3

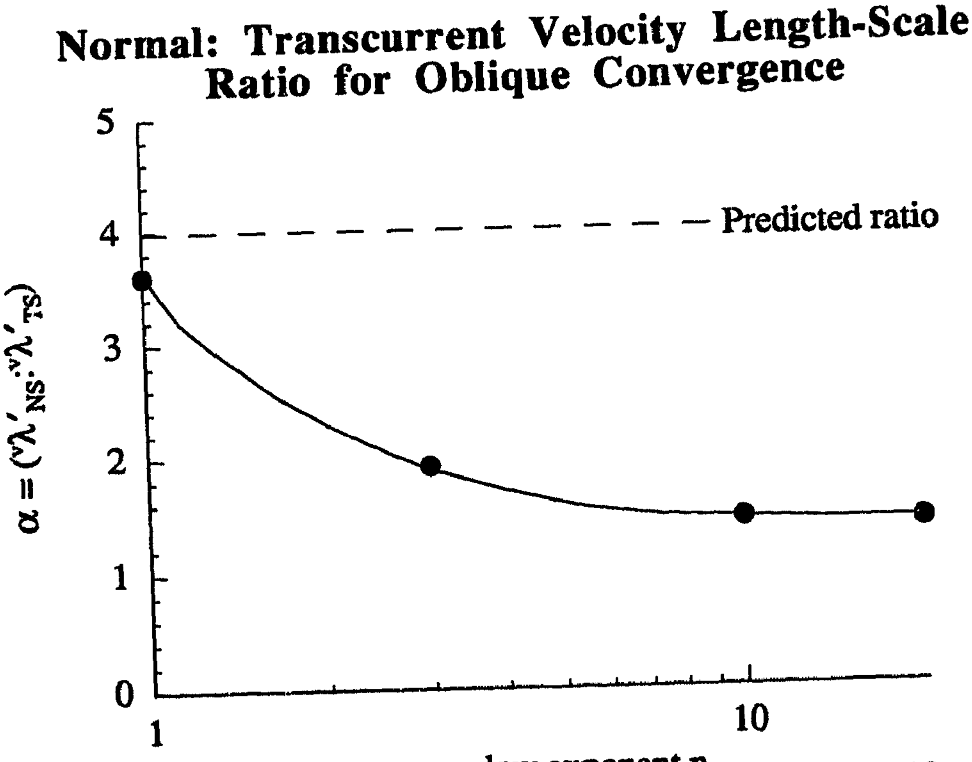
Normal: Transcurrent Velocity Length-Scale Ratio for Oblique Convergence
Predicted ratio
$\alpha = ({}^{v}\lambda'_{NS} : {}^{v}\lambda'_{TS})$
power-law exponent n
5
4
3
2
1
0
1
10

Figure 38

Predicted Side-Driven Length-scales for Large Normalized Convergence

The increase in the normal deformation length-scale with t' for basally-driven deformation was discussed in section 4.3. No similar length-scale analysis exists for the side-driven thin-sheet model, although many numerical studies have been done (England and McKenzie, 1983; Houseman and England, 1986).

When there is no basal traction exerted on the thin-sheet, the length-scales of deformation are determined by the competition between crustal thickening due to indentation at the boundary, the effect of buoyancy forces on crustal thickness gradients, and the tectonic escape of mass along-strike, which is a function of the applied length-scale, D. Figure 39 shows an example of the change in crustal thickness, thickening rates, and length-scales with normalized convergence, for the boundary conditions of figure 35(a). Normalized distance x' is measured from the indenter position at the bottom right-hand corner of the domain ($y'=0$). The right hand boundary ($x'=0$) moves with the indenter velocity into the domain, and the length-scales of $u(x,y)$ and S' are measured from this indenting boundary. Figure 39(a) demonstrates that crustal thickness grows

---

Figure 39: (a) Excess crustal thickness (S'-1), and (b) vertical strain-rates ($\partial S'/\partial t'$), for the indenter case with an along-strike variation in velocity. Results (lines) are shown for normalized convergence times t'=2, 8, and 10; (c) The integrated vertical strain-rate along section A-A′, Σ, vs t', for the side-driven indenter case with no basal traction (Am=0, D'=50, Ar=1, n=1); (d) Length-scales of deformation, as measured by the normal velocity component (${}^{v}\lambda'_{NS}$), horizontal strain-rate component (${}^{s}\lambda'_{NS}$), and crustal thickening (${}^{t}\lambda'_{NS}$), for the side-driven case. The decrease in integrated strain-rate along the section, and the levelling off of the growth in length-scales with time, indicates that steady state will eventually be attained.

(a) Excess Crustal Thickness for Side Forcing
Am=0, Ar=1, D′=50

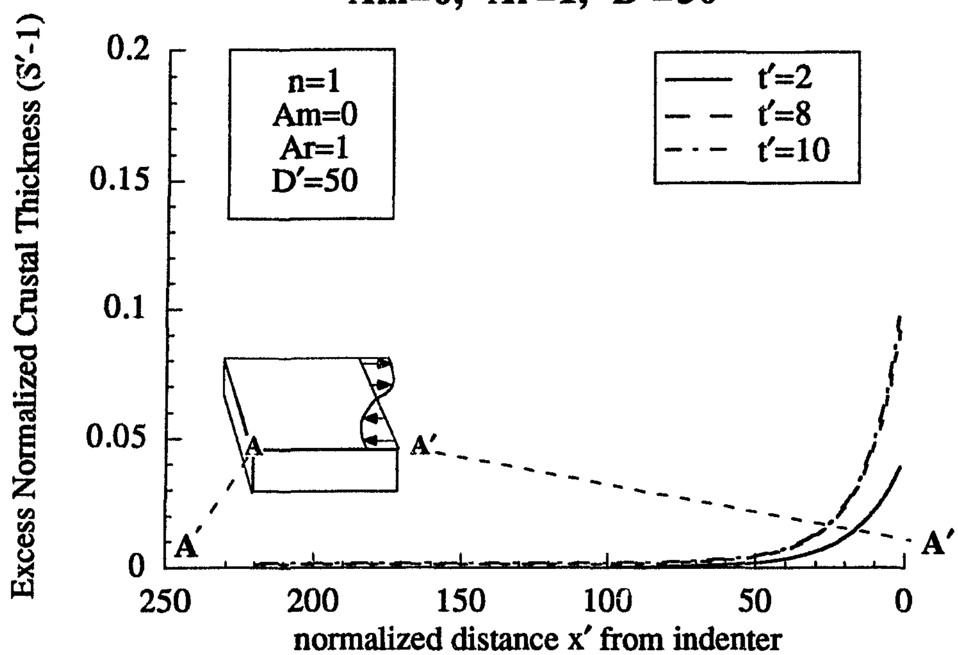

(b) Vertical Strain-Rate for Side Forcing
Am=0, Ar=1, D′=50

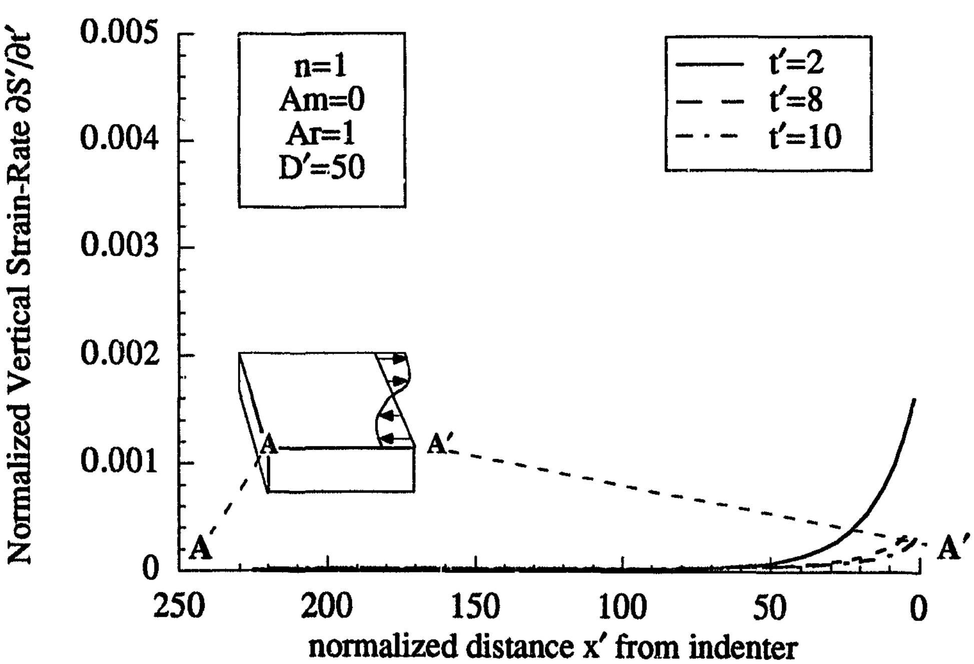

Figure 39(a,b)

(c) Change in Crustal Thickening Integrated Across-Strike: Side Forcing

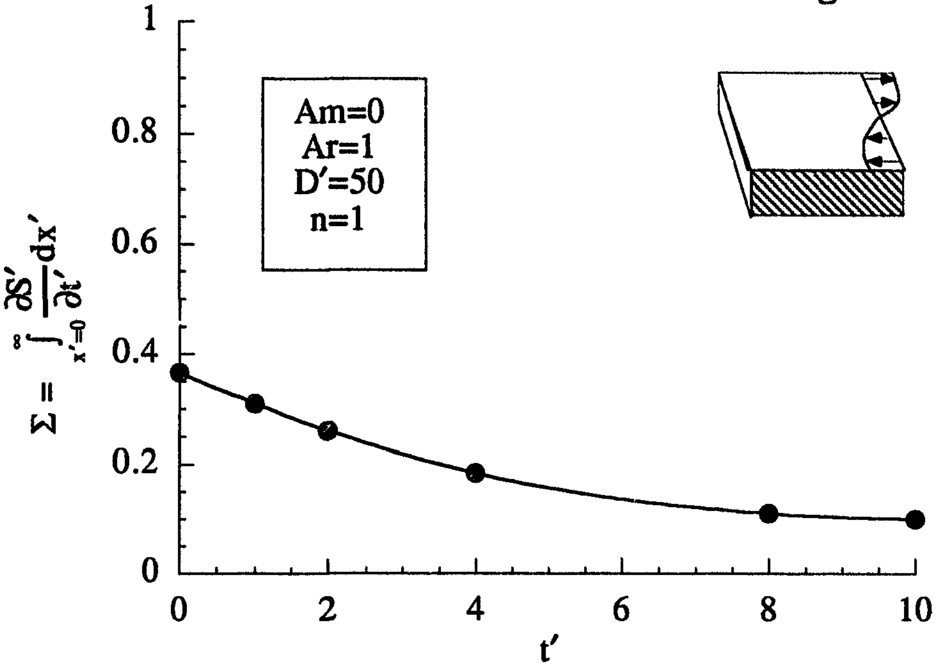

(d) Normalized Length-Scales vs. t′: Side Forcing

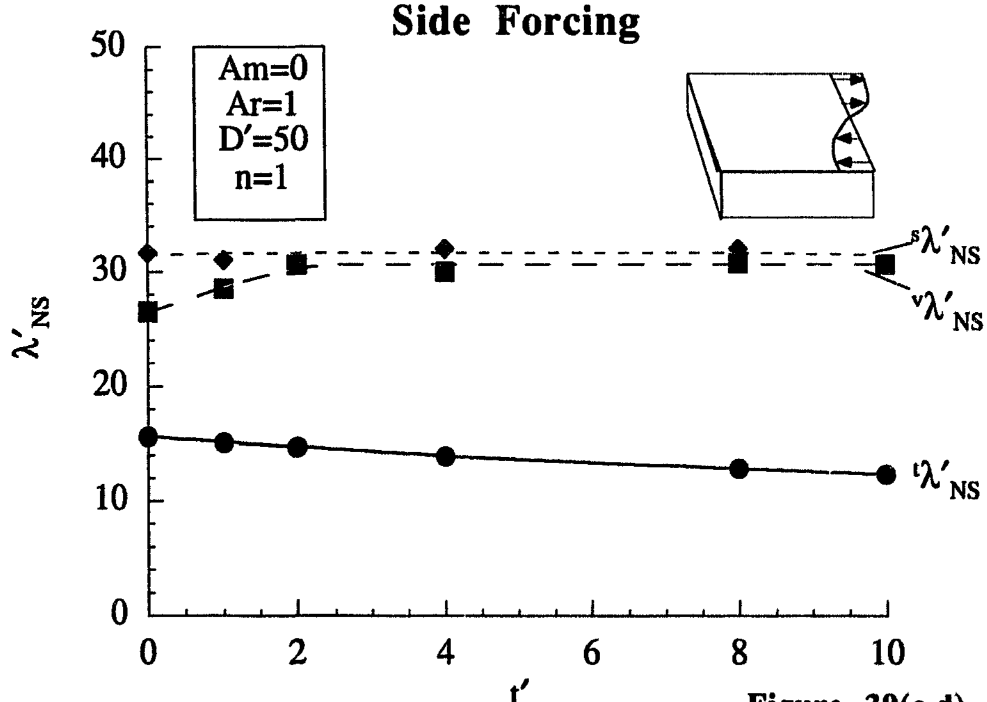

Figure 39(c,d)

exponentially from the boundary. The unrealistic topography created by an indenter has already been discussed by Koons (1990), and illustrates a major problem with the concept of a one-sided orogen.

As the crust thickens, the effect of the buoyancy term adds to the lateral tectonic escape component, and the vertical strain-rate diminishes all along section A-A′ (figure 39(b), curve for $t' \rightarrow 10$). An estimate of the change in the integrated sectional thickening rate can be found by computing the quantity:

$$\Sigma = \int_{x'=0}^{\infty} \frac{\partial S'}{\partial t'} dx'$$

at each normalized convergence time along section A-A′ (i.e. at $y'=0$). If $\Sigma=1$, all of the mass displaced by the indenter for a small convergence increment stays within the cross-section. If $\Sigma<1$, as in figure 39(c), some of the displaced mass moves out of the cross-section along-strike. Figure 39(c) shows a decrease in Σ with increasing t', which indicates that tectonic escape along-strike increases with normalized convergence. This relationship is caused by the growing importance of the Argand number as crustal gradients increase with time. As the effect of gravity on crustal thickness contrasts increases, the thickened crust spreads out along-strike, increasing the deformation length-scale, and laterally by tectonic escape. Eventually, the quantity Σ tends to a con.tant limit. Once the limit is reached, the section A-A′ may be considered to have reached a local steady state, where the thickening of the layer in the cross-section (from movement of the indenting boundary) is balanced by the movement of mass out of the cross-section along-strike. Note that this does not imply that the domain as a whole has reached a steady state, but it does mean that the deformation length-scale will reach a limiting value, beyond which the orogen ceases to grow outwards along section A-A′, but instead grows laterally by tectonic escape.

The change in the normal strain-rate component, velocity component and crustal thickening length-scales with increasing t' is shown in figure 39(d). For n=1, the thickening length-scale is approximately one-half of the velocity length-scale, because of the tectonic escape term. The velocity and horizontal strain-rate length-scales agree for $t'>2$. The 'bump' in the velocity length-scale plot for small t' appears to be an effect of material moving down-slope, caused by gravity acting on crustal gradients. For $t'\sim0$, extra mass moving down-slope due to gravity initially acts next to the boundary, and so is constrained to move in a direction normal to the plate boundary, increasing the velocity length-scale. After more convergence, slopes steepen further away from the boundary, and excess mass escapes along-strike, causing the velocity profile to steepen again, so that the velocity length-scale slowly decreases. This effect is more noticable for the velocity length-scale than its spatial derivative, ${}^{s}\lambda'_{NS}$, because over most of the cross-section the slope of the velocity field is unchanged by this process.

Figure 40: (a) The integrated vertical strain-rate along section A-A′, Σ, vs t', for the side-driven indenter case with a high Argand number and no basal traction (Am=0, D'=50, Ar=5, n=1). The decrease in the integrated thickening rate is faster than for figure 39(c), because of the increased importance of buoyancy forces to the tectonic escape term; (b) Length-scales of deformation, as measured by the normal velocity component (${}^{v}\lambda'_{NS}$), horizontal strain-rate component (${}^{s}\lambda'_{NS}$), and crustal thickening (${}^{t}\lambda'_{NS}$), for the side-driven case with Ar=5; (c) same as (a) but for a non-linear rheology and Am=0, D'=50, Ar=1, n=3. Buoyancy forces are insufficient to cause the movement of mass away from the boundary, so that the integrated thickening rate does not decrease with time; (d) same as (b) but for a non-linear rheology and Am=0, D'=50, Ar=1, n=3. Length-scales decrease with increasing convergence, as all mass becomes concentrated at the side boundary.

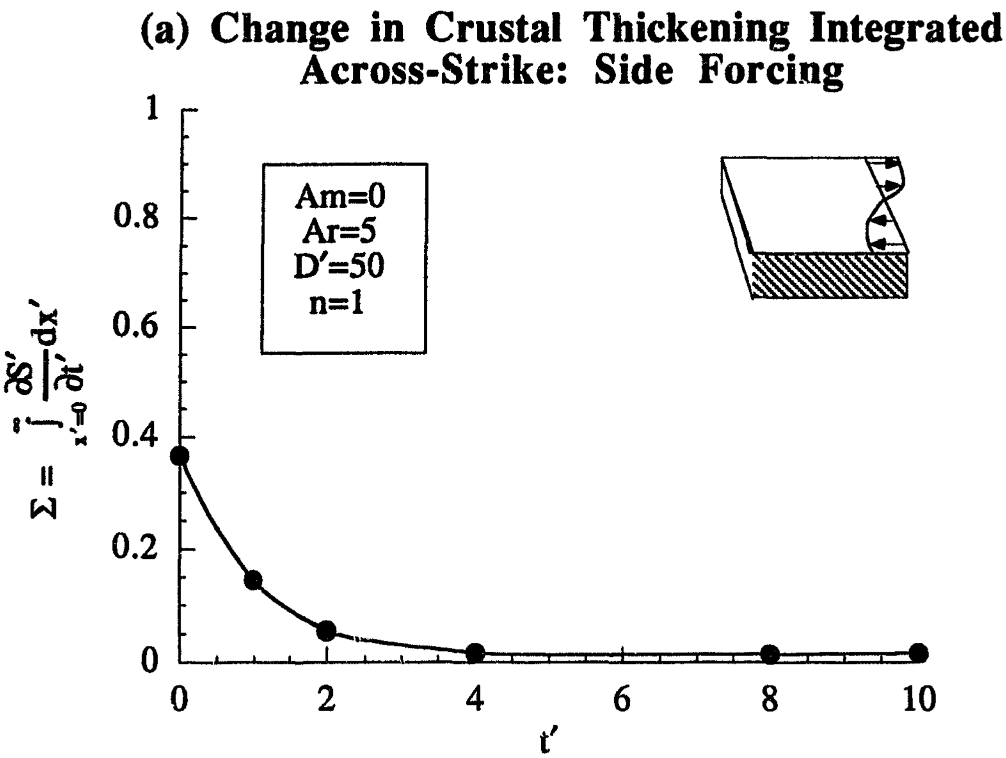
(a) Change in Crustal Thickening Integrated Across-Strike: Side Forcing
Am=0
Ar=5
D′=50
n=1
$\Sigma = \int_{x'=0}^{\infty} \frac{\partial S'}{\partial t'} dx'$
t′

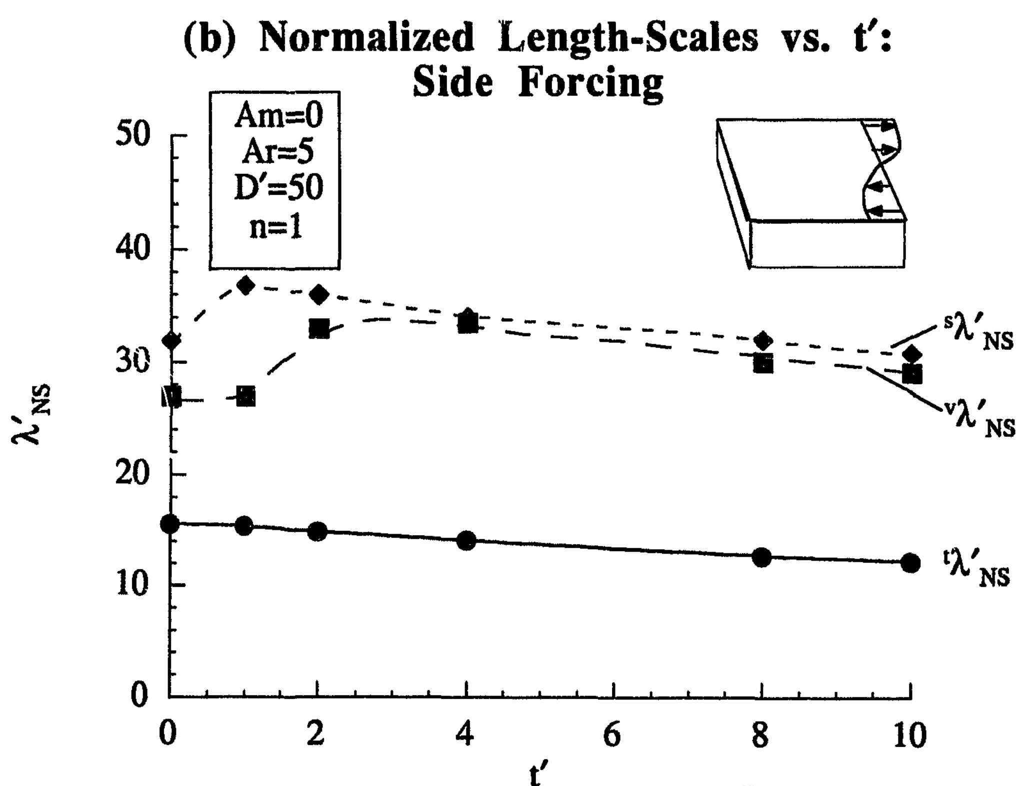
(b) Normalized Length-Scales vs. t′: Side Forcing
Am=0
Ar=5
D′=50
n=1
λ'_{NS}
${}^{s}\lambda'_{NS}$
${}^{v}\lambda'_{NS}$
${}^{t}\lambda'_{NS}$
t′

Figure 40(a,b)

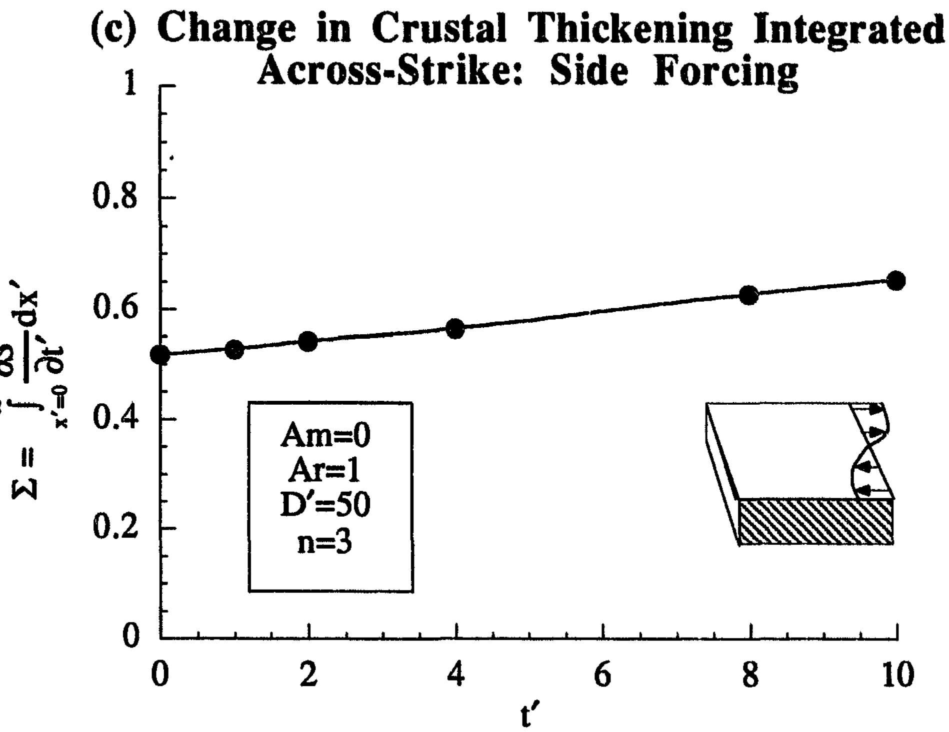
(c) Change in Crustal Thickening Integrated Across-Strike: Side Forcing
$\Sigma = \int_{x'=0}^{\infty} \frac{\partial S'}{\partial t'} dx'$
Am=0
Ar=1
D′=50
n=3
t′

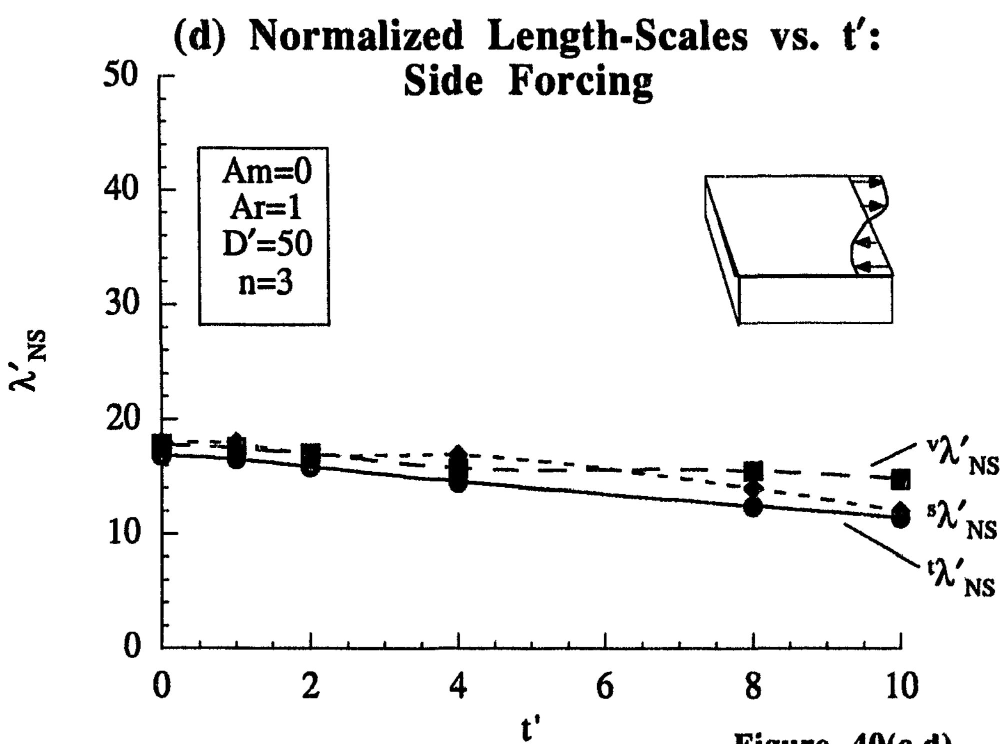
(d) Normalized Length-Scales vs. t′: Side Forcing
λ'_{NS}
Am=0
Ar=1
D′=50
n=3
$^{v}\lambda'_{NS}$
$^{s}\lambda'_{NS}$
$^{t}\lambda'_{NS}$
t'

Figure 40(c,d)

The time taken to reach steady state depends on the relative magnitudes of Ar and D′. When Ar is increased (figure 40(a,b)), steady state is achieved sooner in the development of topography. Figure 40(a) shows the integrated cross-sectional thickening decreasing to zero, which indicates that when steady-state is attained, all of the mass entering the cross-section is transported laterally by tectonic escape, so that the thickened section propagates forward at the indenter velocity, with a constant shape. The bump in the velocity length-scale with increasing t′ is even more noticable than for Ar=1 (figure 40(b)), as the effect of gravity on crustal thickness gradients is more important.

The differences between length-scales are much less for n=3 (figure 40(d)), suggesting that tectonic escape is less important in this case. In fact, the amount of mass moving out of the cross-section decreases slightly with increasing normalized convergence (figure 40(c)). This effect is due to the focusing of compression next to the indenting boundary with increasing t′, causing the deformation length-scales to decrease. The strain-rate weakening of a non-linear rheology changes the balance between compression, buoyancy forces, and lateral tectonic escape, so that the indentation of the side boundary dominates the model behaviour. Excess material cannot move away fast enough either along or across-strike, and becomes concentrated just in front of the indenter boundary.

The results shown in figures 39 and 40 may be understood more easily by considering some limiting cases. If Ar→∞, crustal thickness gradients cannot develop, and model behaviour corresponds to a two-dimensional (planform) plane-strain solution (as noted by England and Jackson, 1989). Because crustal thickening is not possible, all mass advected into the model domain with the indenter must escape laterally. The example shown in figure 40(a,b) is approaching this limit. Although crustal thickening does occur in section A-A′, a critical state is reached beyond which all the mass advected in front of the indenter escapes laterally, and the thickened crust propagates forward as a viscous wedge with a constant concave shape.

For the limiting case where Ar = 0, no buoyancy forces operate, and the amount of mass escaping laterally is constant or decreasing (because the shape of the boundary changes with convergence). As the boundary indents the domain, the length-scale of crustal thickening will become very small, so that all the excess (indented) mass is concentrated at the boundary. The example shown in figure 40(c,d) is approaching this limit. The non-linear rheology tends to accentuate the concentration of thickening at the boundary, by strain-rate weakening. Because Ar > 0 for the case shown in figure 40(c,d), the length-scale decrease will eventually level off when slopes become very steep.

Comparison Between the Basally-Driven and Side-Driven Length-Scales for Large Normalized Convergence- A Summary

(i) Length-Scales

The results from this section indicate some fundamental differences between styles of thickening for the basally and side-driven models. When normal convergence is controlled by the detachment and subduction of mantle lithosphere, crustal deformation length-scales increase with normalized convergence. The increase is similar for all measures of deformation (velocity and strain-rate components), and is initially proportional to $\sqrt{t'}$. For whole-lithosphere side-driven convergence, length-scales of the normal velocity and strain-rate components do not necessarily agree. Length-scales may increase, decrease, or stay constant with t', depending on the relative effects of gravity acting on crustal thickness gradients, compression from the indenting boundary, strain-rate weakening for a power-law rheology, and tectonic escape of mass along-strike.

(ii) Length-Scale Ratios

Velocity length-scale ratios for basally-driven convergence (${}^v\lambda_{NB}/{}^v\lambda_{TB}$) will increase with t', whereas the length-scale ratios for side-driven convergence (${}^v\lambda_{NS}/{}^v\lambda_{TS}$)

may grow or diminish, depending on the relative importance of the effects noted in (i).

(iii) The Development of Plateaus

A plateau is a finite zone of thickened crust for which topographic slopes are much smaller than the slopes at the boundary between deformed and undeformed crust. At large normal convergence times, the topography for the basally-driven case discussed in section 4.3 continues to grow outwards from the detachment zone with time, with the maximum topography located over the detachment zone. A plateau does not develop, although topographic slopes may be quite small (e.g. figure 20). Additional factors, such as a change in the strength of the shear zone between the crust and mantle as a consequence of thickening, must be invoked in order to produce a plateau (e.g. Willett et al., 1993).

In contrast to the basally-driven model, the side-driven thin-sheet may in certain cases develop a plateau over part of the thickened region. The formation of a plateau seems to depend on the shape of the velocity boundary condition at the side of the model domain, and the value of the Argand number. For instance, no plateau has developed at $y'=0$ for the sinusoidal indenting boundary conditions of figure 36, with $t'=1$ and $Ar=1$. The maximum thickening for this case occurs adjacent to the side boundary (figure 39(a)). However, Houseman and England (1986) demonstrate that a plateau may be formed by a more complicated indenter shape, where indenter velocity decreases to zero over a relatively small distance (causing a 'syntaxis' to develop). Figure 4(c,f,i) of Houseman and England (1986) shows crustal thicknesses for such a case, where maximum crustal thickness along a direction normal to the plate boundary is not always at the boundary, and a broad region of approximately constant thickness has developed in front of the indenter. Formation of a plateau is also facilitated by a large Argand number (Houseman and England 1986, figure 5).

§ 4.5 Length-Scales of Deformation for Mixed Side-Driven and Basally-Driven Boundary Conditions: Small Normalized Convergence

This section investigates crustal deformation styles for a mixed case, which combines indenter mechanics with subduction of the mantle lithosphere. The boundary conditions thus include variations in the along-strike incident velocity at the model plate boundary, as well as detachment of the model mantle lithosphere.

The side-driven model discussed in the previous section makes two major assumptions about the behaviour of continental lithosphere under convergence. The first assumption, which has already been discussed in chapter two, is that crust and mantle lithosphere deform together ('whole lithosphere deformation') with no shear between them. The second assumption is that the plate boundary separates two regions of lithosphere with very different average strengths, so that one side of the plate boundary acts as a rigid (or kinematically prescribed) indenter into the weaker, deforming side. The strong lithospheric region is not modelled in the side-driven thin sheet model, but is specified kinematically.

An example where the assumption about different strengths on either side of the plate boundary may be valid is at an advancing subduction zone, where the oceanic lithosphere is much stronger, and is moving towards the continental interior at trench velocity, V_S. Contrasts in strength are also possible during continent-continent collision, if convergence occurs along a zone that was previously the site of active oceanic subduction. Continental lithosphere adjacent to a zone of oceanic subduction is likely to be hotter and weaker than continental lithosphere adjacent to a passive margin, because of the additional volcanic heat flux from the subducting oceanic lithosphere, and accretion of micro-terranes to the active margin. If two continental lithospheric plates of differing origins (active and passive margins) collide, a difference in average lithospheric strength across the plate boundary is expected, and may cause the stronger side to act as an indenter into the weaker, hotter lithospheric plate.

In contrast to the indenter assumption, the basally-driven model has been investigated for the case where there is no significant change in lithospheric strength across the plate boundary (e.g. section 4.2). As discussed above, this will not always be a good representation of convergent plate interactions. A third deformation style is therefore required (figure 41(a)), to model cases where mantle lithosphere detaches and subducts, as in the basally-driven model, but where there are significant changes in

---

Figure 41: Schematic diagram of the physical problem which the 'mixed' boundary conditions represent. (a) Normally convergent case. An indenter, which may be regarded as strong crust with a cold geotherm, well coupled to the underlying mantle, is indenting less coupled, weaker crust. At the plate boundary, the mantle lithosphere of the weaker side detaches and subducts, so that the velocity boundary condition at the base of the crust is reduced from the indenter velocity to zero over forcing length-scale, λ_m. The problem thus has two horizontal forcing length-scales: the indenter velocity length-scale, D, and the basal detachment length-scale. (b) Transverse motion at the plate boundary. The stronger (indenter) lithospheric plate moves away from the observer, with a velocity varying over length-scale D. The mantle lithosphere is separated by a weak shear zone at the plate boundary. The sense of dip of this shear zone is arbitrary, and will depend on the along-strike setting and previous history of the boundary zone. The velocity boundary condition at the base of the crust is reduced from the indenter velocity to zero over forcing length-scale, λ_m.

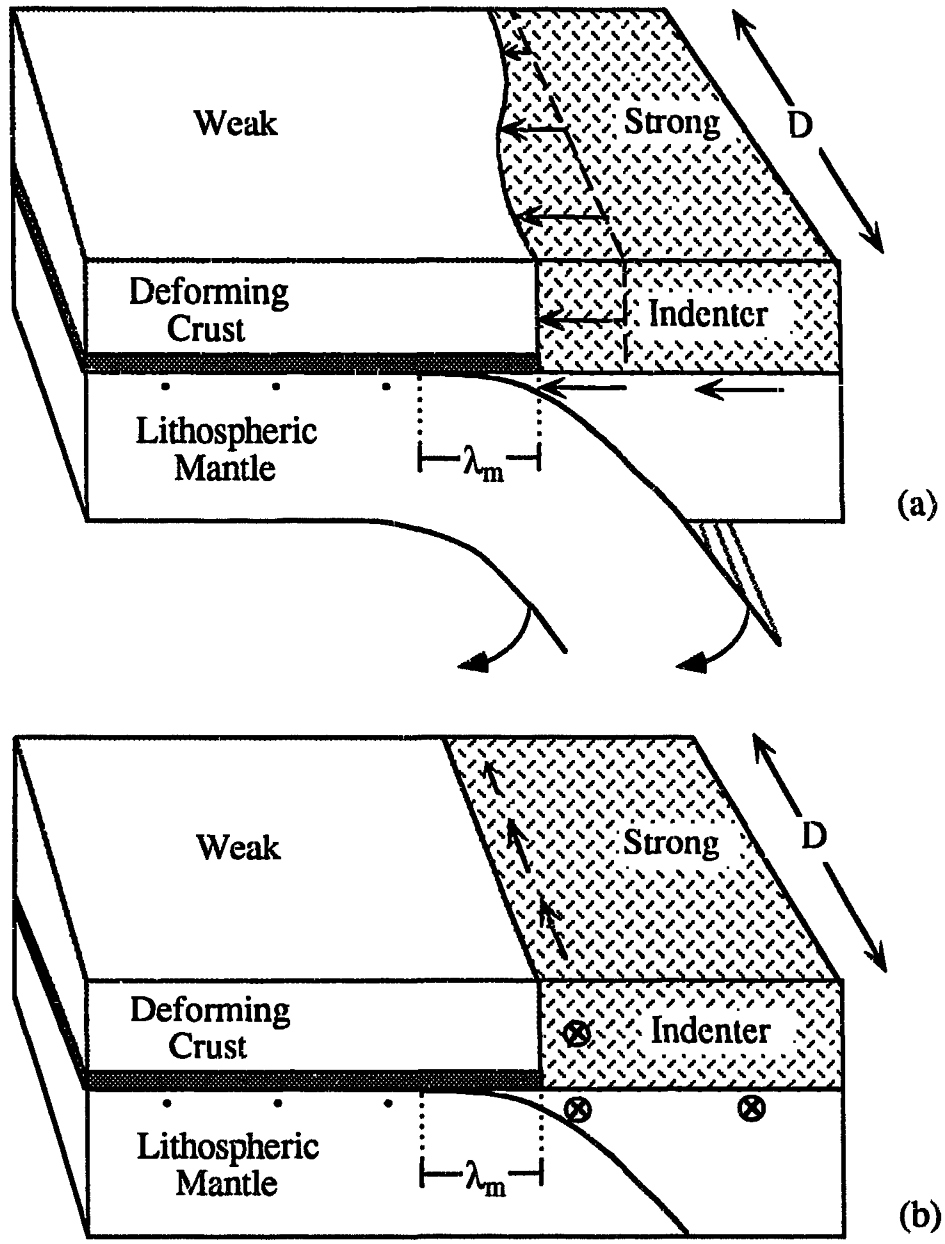
Weak
Strong
D
Deforming Crust
Indenter
Lithospheric Mantle
λ_m
(a)
Weak
Strong
D
Deforming Crust
Indenter
Lithospheric Mantle
λ_m
(b)

Figure 41

strength at the plate boundary. This model combines some of the aspects of the side-driven and basally-driven models, and is therefore referred to as the 'mixed' model. Deforming crust on the weak side of the plate boundary is simultaneously indented by the much stronger lithospheric plate, and forced at its base by a detaching and subducting mantle lithosphere.

The mixed case may also provide a possible model for some strike-slip settings (figure 41(b)). The mantle lithosphere in this case is assumed to decouple strike-slip motion along a fixed, small length-scale λ_m, representing the plate boundary within the lower lithosphere. For continental transform boundaries which developed from a previously convergent setting (e.g. the San Andreas and Western U.S.), it is likely that average lithospheric strength will change across the plate boundary zone, so that in the limiting case the stronger plate may be specified as a rigid (or kinematically prescribed) strike-slip boundary condition at the side of the domain.

The mixed model is used to determine when length-scales of deformation in the weaker plate are controlled by crust-mantle interactions (basal forcing), vs. indentation of the crust from the plate boundary (side forcing). In particular, when $Am \rightarrow 0$, deformation on the weak side of the plate boundary zone does not depend on the basal forcing. For this case it is likely that deformation length-scales will be controlled by the side indentation length-scale, in a manner similar to the results from section 4.4, although for the crustal layer only, since the mantle lithosphere is still assumed to detach and subduct. Conversely, when the indenter length-scale, D, becomes very large, it is expected that deformation length-scales in the crust will be controlled by basal forcing rather than indenter mechanics.

Figure 42: The 'mixed' boundary conditions used in sections 4.5 and 4.6. (a) normal incidence; (b) transverse incidence.

Side and Basal Forcing

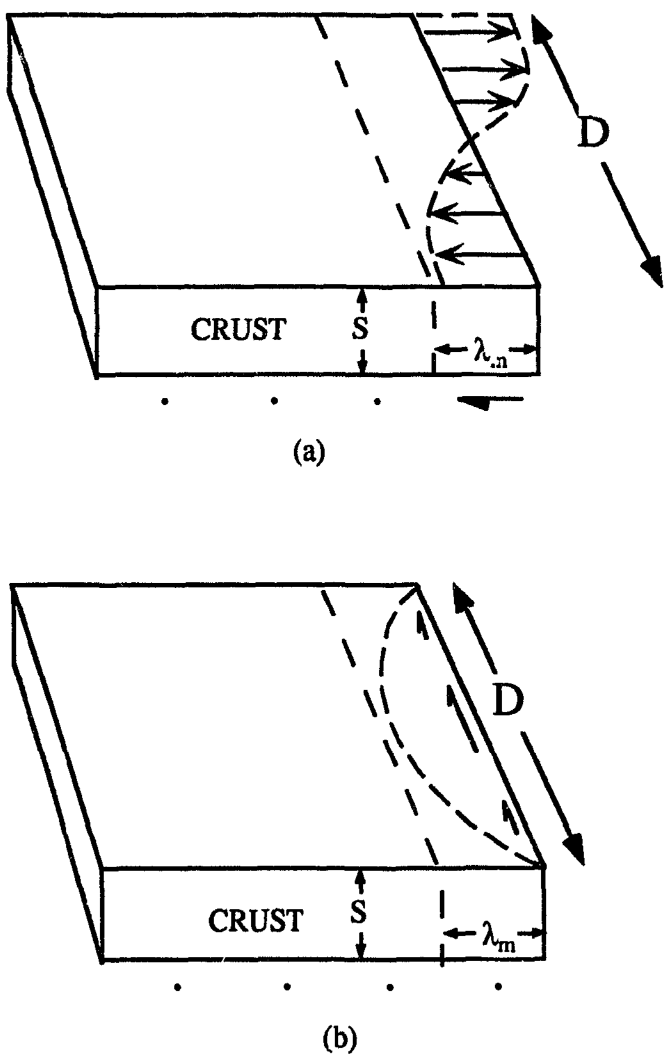

Figure 42

The mantle lithosphere is assumed to detach on the weak side of the plate boundary, and the detachment zone moves with the velocity of the indenter into the deforming domain. The mantle detachment length-scale, λ_m, remains constant with normalized convergence time, and represents the zone over which basal velocities decrease from those of the indenter mantle lithosphere to zero. The sense of subduction of mantle lithosphere is shown on figure 41 as dipping towards the strong side of the plate boundary. The physical rationale for this orientation is discussed in chapter six. For the simple velocity boundary conditions used in this thesis, the choice of subduction direction for the mantle lithosphere does not affect the velocity boundary condition imposed at the base of the crust.

Model Boundary Conditions

The side-driven boundary conditions of England et al. (1985) are combined with the basal drag boundary conditions of section 4.2, by taking the detachment zone at the side rather than the middle of the modelled zone (figure 42(a), (b)). In accordance with the assumption of detachment and subduction of the mantle lithosphere, the model domain is taken to be over the crust only. The side boundary conditions are sinusoidal functions of normal (N) and transverse (T) velocity. The boundary velocities $u_0(y)$ and $v_0(y)$ are applied at the side and base of the model, and are reduced along the base to zero, over detachment length-scale λ_m. The length-scales of deformation are measured from the boundary, as for the previous section.

Figure 43: Velocity vectors and vertical strain-rates for (a) n=1, t′=0, Am=0.001 and D′=50; (b) n=1, t′=0, Am=0.1 and D′=50. ${}^v\lambda'_{NO}$= normal velocity length-scale for the boundary conditions of figure 42(a); ${}^v\lambda'_{TO}$= transcurrent velocity length-scale for the boundary conditions shown in figure 42(b); length-scales are measured at the along-strike positions indicated on the figures.

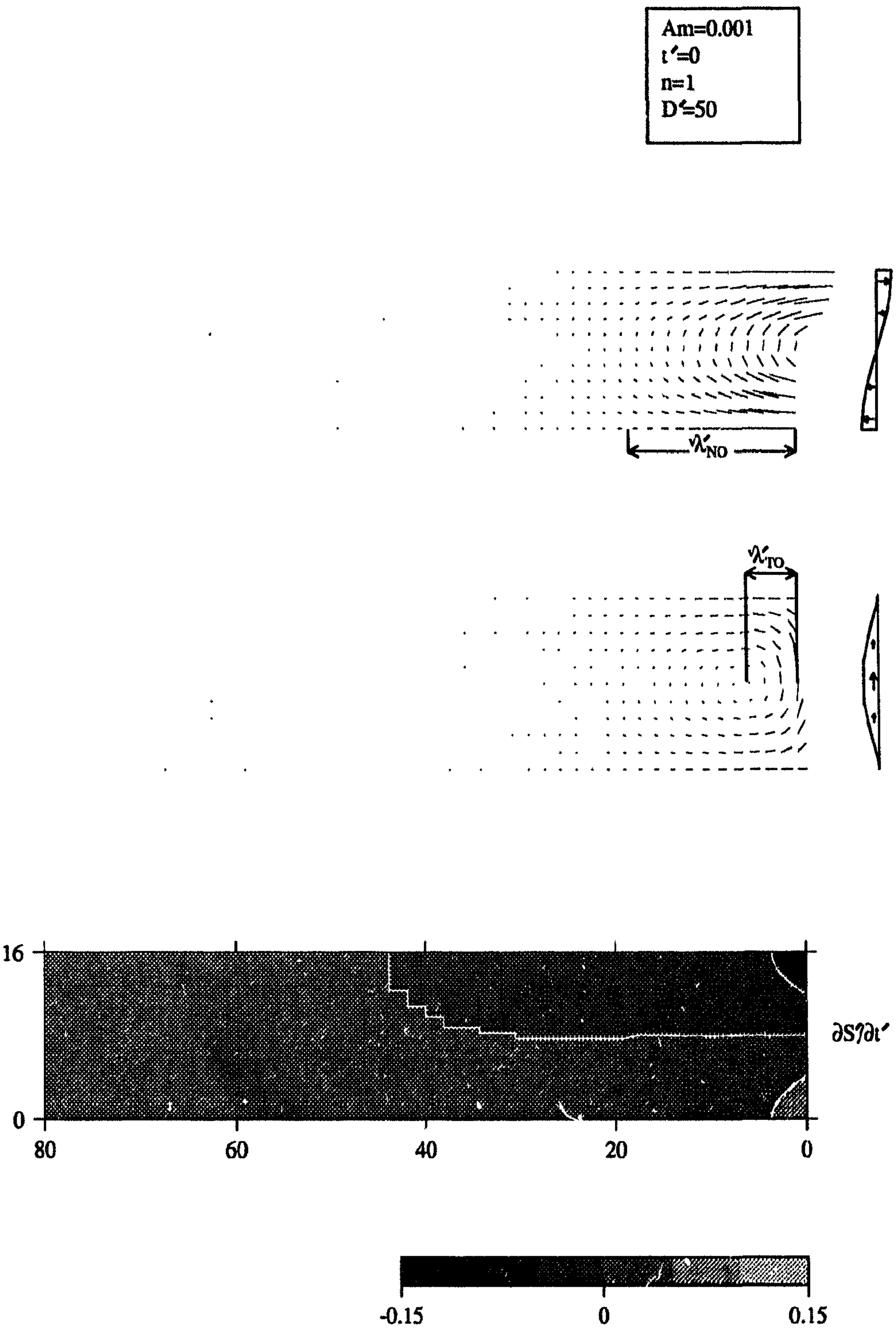
Am=0.001
t′=0
n=1
D′=50
λ'_{NO}
λ'_{TO}
16
0
80
60
40
20
0
∂S′/∂t′
-0.15
0
0.15

Figure 43(a)

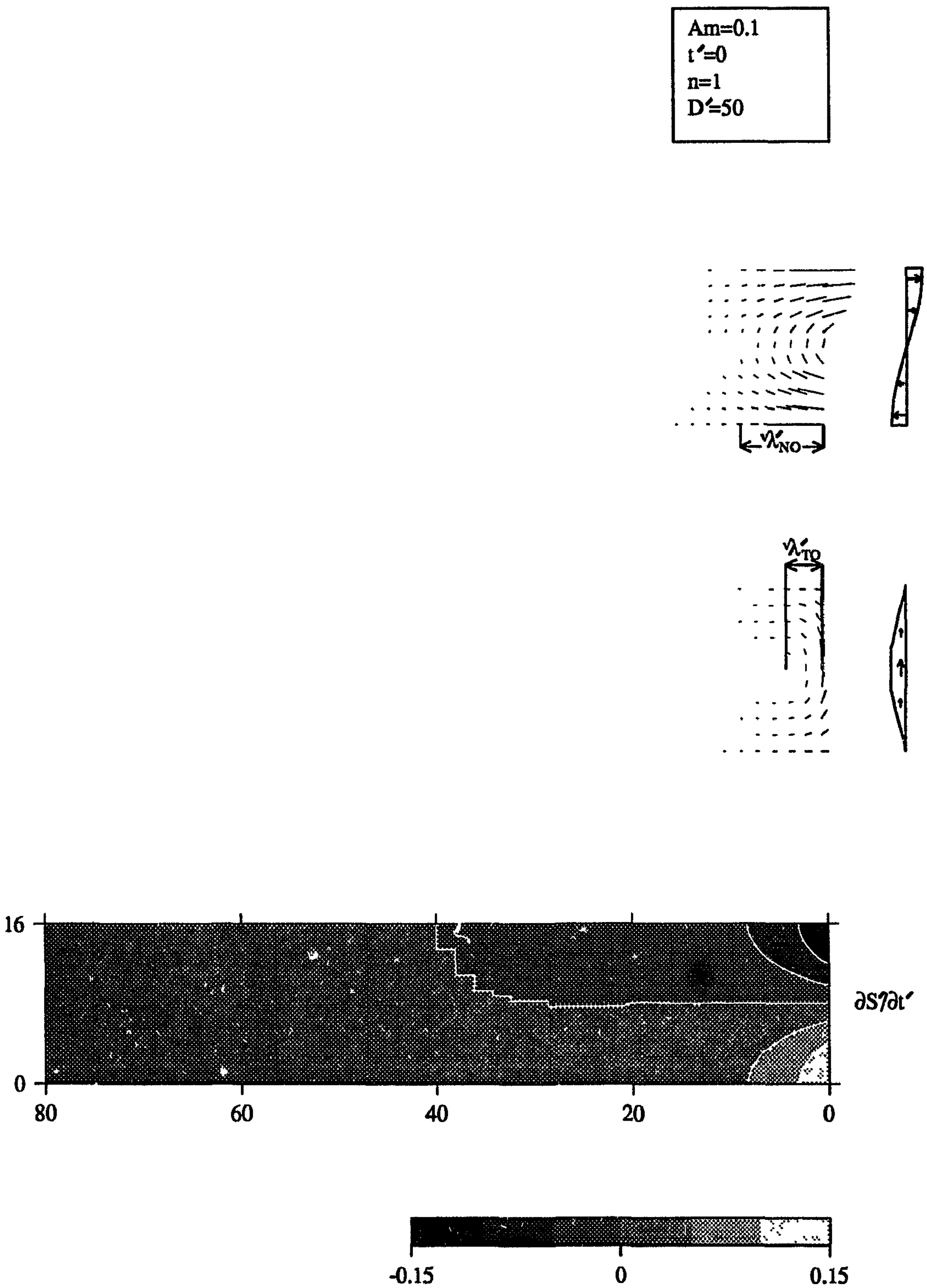
Am=0.1
t′=0
n=1
D′=50
$\sqrt{\lambda'_{NO}}$
$\sqrt{\lambda'_{TO}}$
16
0
80
60
40
20
0
∂S′/∂t′
-0.15
0
0.15

Figure 43(b)

Results for Linear and Non-Linear Viscous Rheologies at t′=0

Examples of the velocity fields and crustal thickening rates for a linear thin-sheet are displayed in figure 43, for the sinusoidal side boundary conditions N (figure 43(a)) and T (figure 43(b)). The [illegible]ide detachment length-scale, λ_m, is equal to the initial crustal thickness. The maximum observed deformation length-scales, λ'_{NO} and λ'_{TO}, are measured as shown on the figure, at the along-strike position where the incident velocity is a maximum. The plots are shown in dimensionless units, with scaled indenter length-scale D′=50, for two values of the Ampferer number: (a) Am=0.001 (figure 43(a)); (b) Am=0.1 (figure 43(b)). The velocity fields show that for Am=0.001, the deformation (as measured by λ'_{NO} and λ'_{TO}) spreads out far from the side boundary. As Am increases to 0.1, the length-scale dependence on basal drag becomes stronger, and deformation is restricted to an area close to the side boundary. Crustal thickening rate contours for the N case are also shown.

To determine under what conditions the indenter length-scale (D′) controls the crustal deformation length-scales (λ'_{NO} and λ'_{TO}), I compare the numerical results, measured for the mixed case with the boundary conditions of figures 42(a) and (b), with the predicted velocity length-scales for basal and side-driven forcing (equations 19 and 22). The predicted length-scales if deformation were caused only by the traction at the base of the crust, are $\lambda'_{NB}/2$ and $\lambda'_{TB}/2$ (where λ'_{NB}, λ'_{TB} are defined in equation 19, and are valid for length-scale measures of velocity, horizontal strain-rate, or thickening components). The division by two is necessary because model mantle subduction takes place at the boundary of the domain, so that these are half-width measures of deformation compared to the analysis in section 4.2. The predicted side-driven velocity length-scales are ${}^{v}\lambda'_{NS}$ and ${}^{v}\lambda'_{TS}$ (where ${}^{v}\lambda'_{NS}$, ${}^{v}\lambda'_{TS}$ are defined in equation 22). Although these length-scale predictions were derived for a whole lithosphere indenter, the following results will show that they are equally applicable for crustal deformation, in the limit where the horizontal shear traction between the crust and mantle lithosphere becomes negligible.

Figure 44 plots the numerical results (solid lines) for the variation in velocity length-scales vs. Am under the mixed boundary conditions, with: (a) normally incident velocity (N); and (b) transverse incident velocity (T). Predicted basal and side-driven velocity length-scale solutions are indicated by the dashed lines. $(\lambda'_{NB}/2)$ and $(\lambda'_{TB}/2)$ are the analytical solutions for basally-driven deformation (eq. 19), and ${}^{v}\lambda'_{NS}$ and ${}^{v}\lambda'_{TS}$ are the analytical solutions for side-driven deformation (eq. 22), and are shown for two different values of D′, the side-boundary length-scale.

The numerical results (figure 44) show that, for weak basal coupling (Am→0), the deformation style will be determined by the side (indenting) boundary condition (i.e. ${}^{v}\lambda'_{NO} \rightarrow {}^{v}\lambda'_{NS}$ and ${}^{v}\lambda'_{TO} \rightarrow {}^{v}\lambda'_{TS}$), as expected . Correspondingly, as Am increases (stronger basal coupling), the deformation style will be determined by the basal boundary condition (${}^{v}\lambda'_{NO} \rightarrow (\lambda'_{NB}/2)$ and ${}^{v}\lambda'_{TO} \rightarrow (\lambda'_{TB}/2)$). The length-scale at which the transition from side-driven to basally-driven deformation occurs depends on the relative

---

Figure 44: (a) Numerical results (symbols, with solid lines as curve fits) for mixed boundary conditions, and the normal velocity length-scale ${}^{v}\lambda'_{NO}$, vs. Am. Results are shown for two values of indenter length-scale, D′=16, and D′=50. Also shown are the predicted deformation length-scales of purely side-driven (${}^{v}\lambda'_{NS}$) vs. basally-driven $(\lambda'_{NB}/2)$ models (dashed lines). Figure 44(b) is the same as 44(a) but for transcurrent velocity, ${}^{v}\lambda'_{TO}$.

(a) Velocity Length-Scale for Normal Convergence

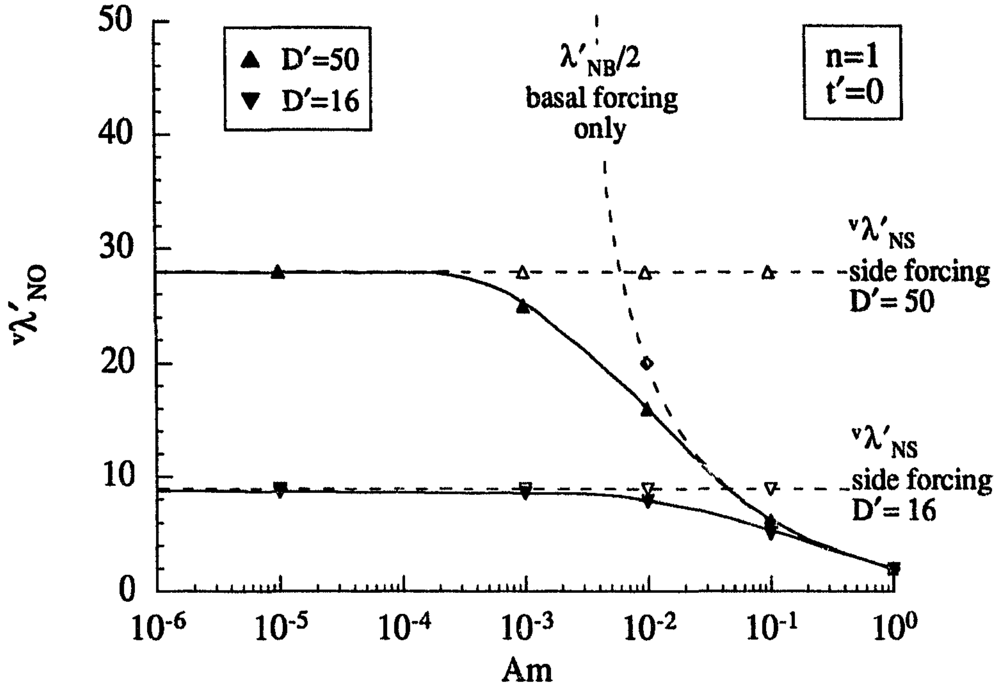

(b) Velocity Length-Scale for Transcurrent Motion

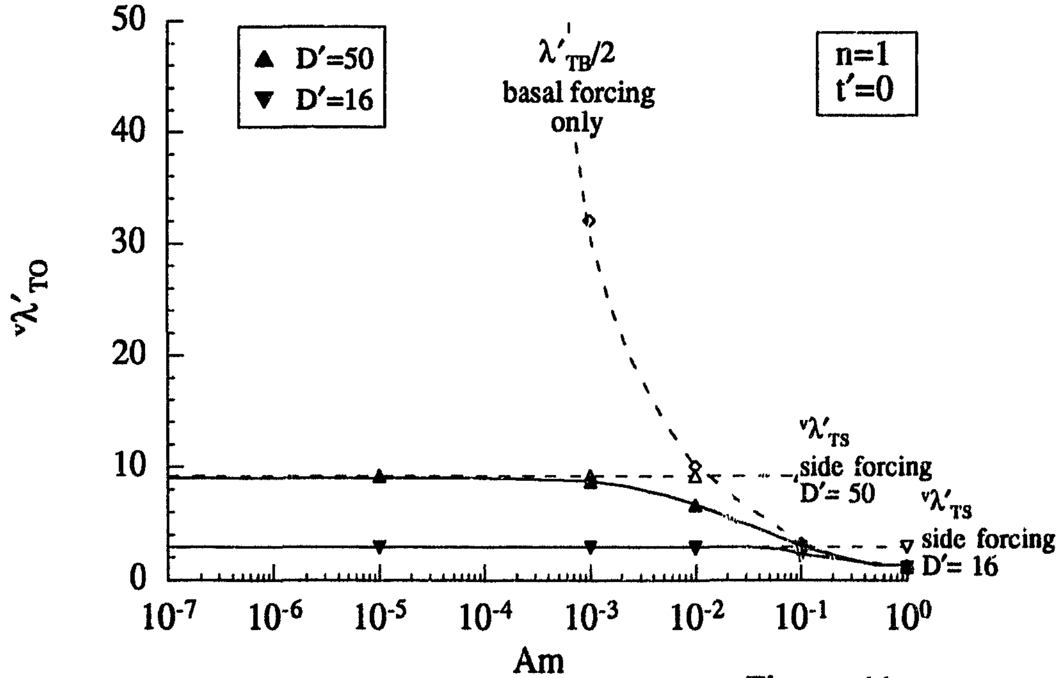

Figure 44

size of the two predicted length-scales. For instance, when D=50′ and Am=0.1, the side-driven normal convergence velocity length-scale (from eq. 22) is:

$$^{v}\lambda'_{NS} \cong \frac{2D'}{\pi} = 32$$

The equivalent length-scale predicted by the basal boundary conditions (from eq. 19) is:

$$\frac{\lambda'_{NB}}{2} \cong \frac{2}{\sqrt{Am}} = 6.3$$

Because $^{v}\lambda'_{NS} >> (\lambda'_{NB}/2)$ for these values of Am and D′, the velocity length-scale will be mostly determined by the basal boundary condition. In fact, the measured velocity length-scale in this case closely corresponds to the basally-driven prediction . When D′=50 and Am=10^{-5}, the predicted analytical length-scales are $^{v}\lambda'_{NS} = 32$ and $(\lambda'_{NB}/2) = 632$, and the measured length-scale is 28, so the length-scale depends primarily on the side boundary forcing. The slight discrepancy between the predicted and measured length-scales in the side-driven limit (Am→0) is caused by the approximate nature of equation 22. For examples with a linear rheology, such as the case illustrated in figure 44, an exact expression for the length-scale exists (England et al., 1985), and predicts that $^{v}\lambda'_{NS}$=28, in agreement with the measured result.

Figure 45: Velocity profiles u/u_0 and v/v_0 vs. normalized distance along the x-axis, for the boundary conditions of figure 42(a) and (b), and: (a) Am=0.001; (b) Am=0.1. The profiles are taken at the same along-strike positions as shown on figure 43. The dashed line indicates the e-folding velocities $u=u_0/e$, $v=v_0/e$; the intersection of the profiles with this line therefore provides a measure of half-width velocity length-scales.

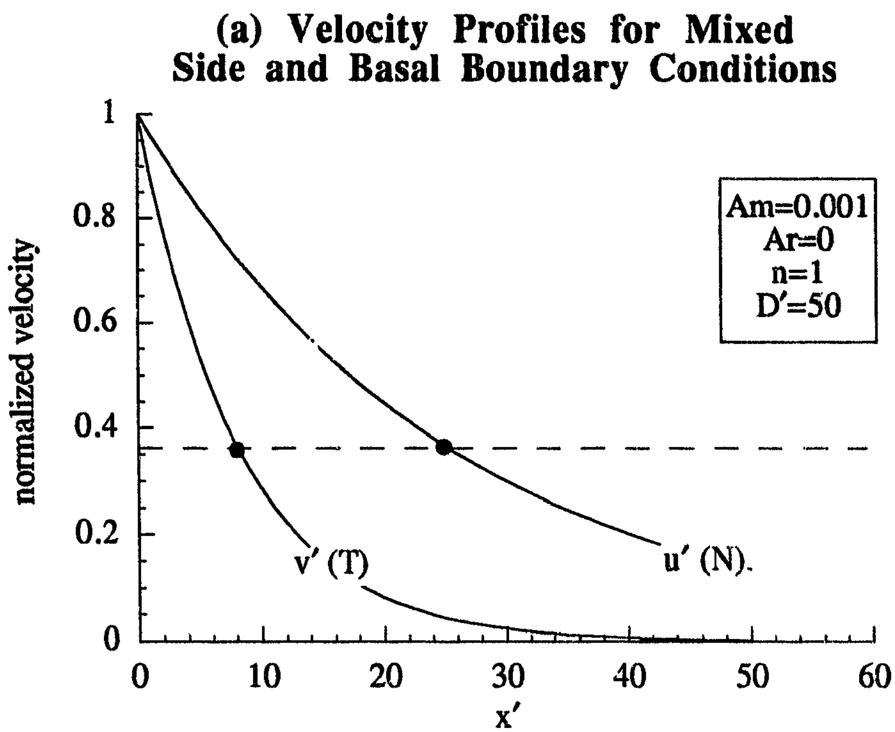
(a) Velocity Profiles for Mixed
Side and Basal Boundary Conditions
normalized velocity
x′
Am=0.001
Ar=0
n=1
D′=50
v′ (T)
u′ (N).
0
0.2
0.4
0.6
0.8
1
0
10
20
30
40
50
60

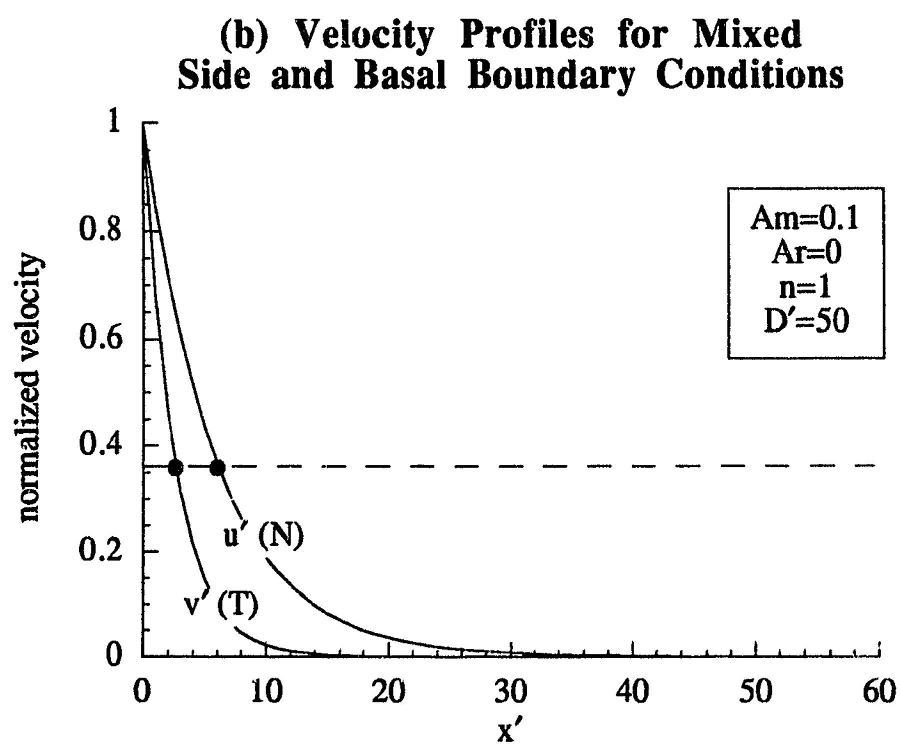
(b) Velocity Profiles for Mixed
Side and Basal Boundary Conditions
normalized velocity
x′
Am=0.1
Ar=0
n=1
D′=50
u′ (N)
v′ (T)
0
0.2
0.4
0.6
0.8
1
0
10
20
30
40
50
60

Figure 45

These results have interesting implications for the effects of strain partitioning on deformation length-scales. For a linear rheology, the ratio between normal and transcurrent velocity length-scales will change from 4 to 2 as deformation becomes controlled by the underlying mantle detachment, rather than the length-scale of the indenter. This change is demonstrated in figure 45, which shows the normalized velocity profiles for normal convergence (N) and transverse motion (T) for relatively strong and weak values of Am. For Am=0.001, the ratio of length-scales N:T at the e-folding width is approximately 4. For the stronger basally coupled case Am=0.1, the ratio reduces to 2.

The equivalent results to figure 44 for D′=50, and a non-linear rheology, are shown in figure 46. Although the length-scales predicted by the side and basal boundary conditions are different in magnitude compared to the linear cases, the same transition criterion between them applies. As for the linear case, the length-scale follows the minimum of the predicted basal and side-driven solutions.

Figure 46: The dependence of velocity length-scales on side and basal forcing for a non-linear viscous crust. Normal length-scale (${}^{v}\lambda'_{NO}$) vs. Am for (a) n=3; (b) n=10; transcurrent length-scale (${}^{v}\lambda'_{TO}$) vs. Am for (c) n=3; (d) n=10.

(a) Velocity Length-Scale for Normal Convergence, n=3

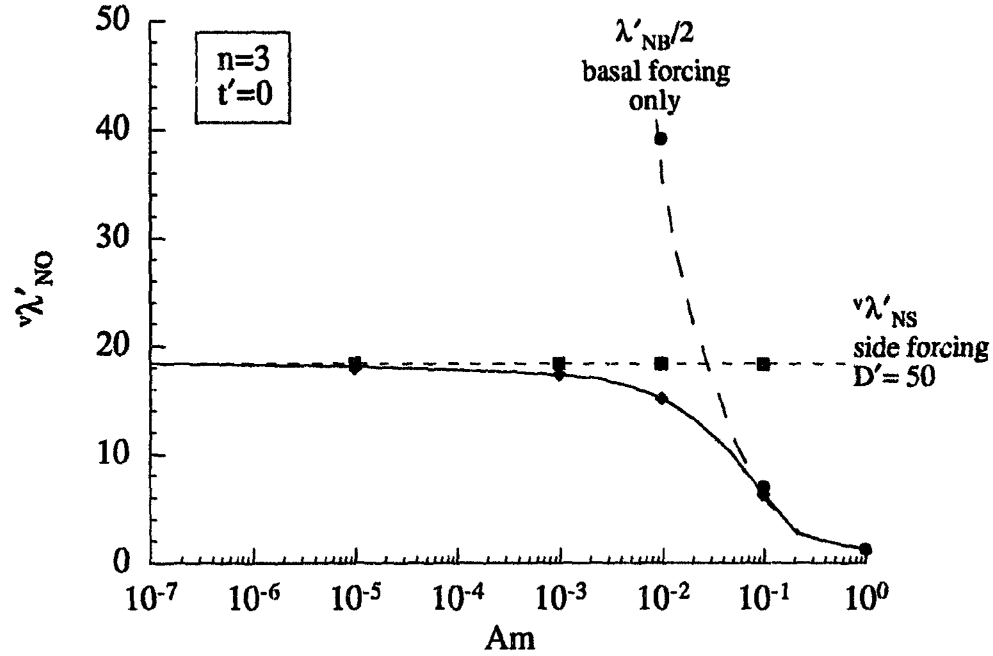

(b) Velocity Length-Scale for Normal Convergence, n=10

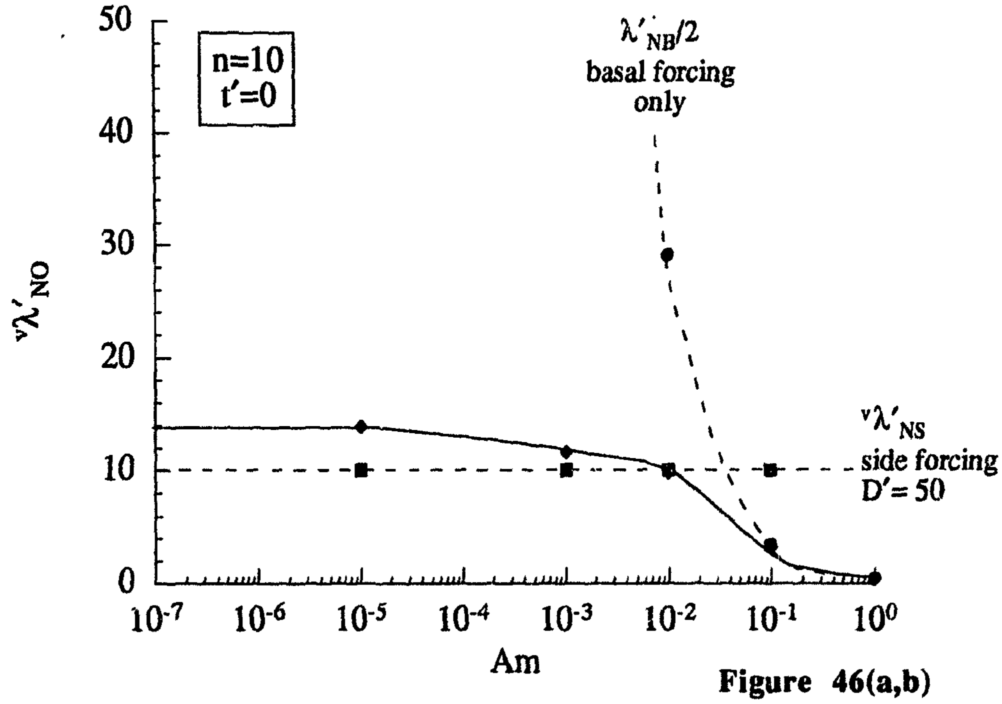

Figure 46(a,b)

(c) Velocity Length-Scale for Transcurrent Motion, n=3

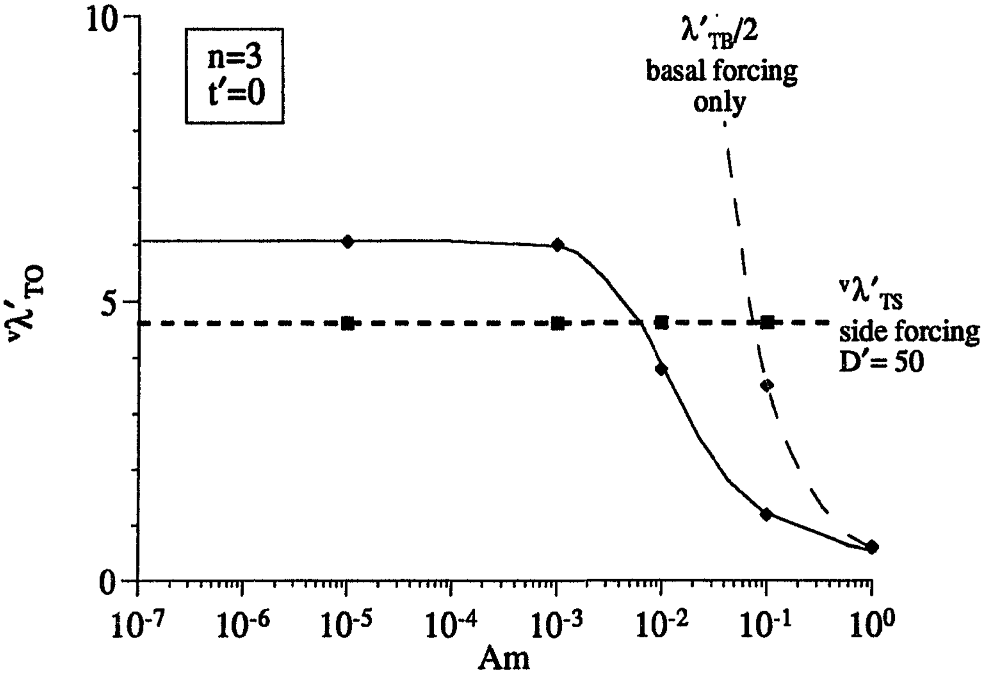

(d) Velocity Length-Scale for Transcurrent Motion, n=10

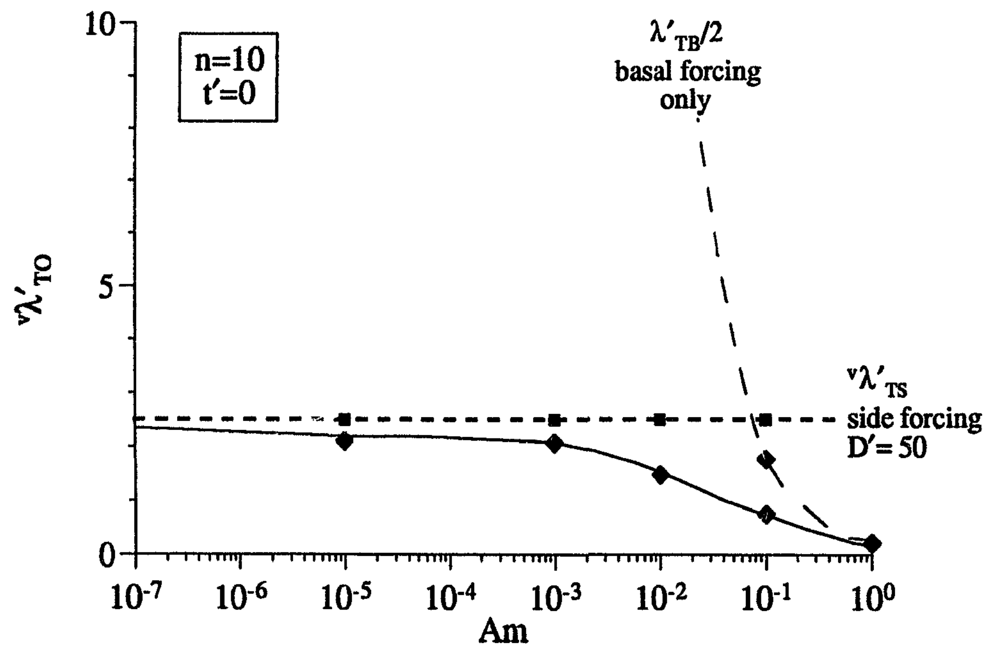

Figure 46(c,d)

In the previous section, the importance of the difference between deformation length-scales measured by the velocity components, and by the crustal thickening rate was noted, for n=1. Figure 47 demonstrates that the length-scale criteria for mixed boundary conditions is true for either measure of length-scale, even when they are different. Figure 47(a) shows numerical results for velocity and thickening length-scales (symbols and solid/ light, dashed lines) compared to the predictions for side-driven and basally-driven deformation, respectively. The same result for a non-linear rheology (n=3) is shown in figure 47(b), where there is little discrepancy between the length-scale measures.

Figure 47: Observed normal deformation length-scale, λ'_{NO}, vs. Am, showing the difference between measuring the length-scale using the normal velocity component (${}^{v}\lambda'_{NO}$, shown using a thin dashed line), and the crustal thickening (${}^{t}\lambda'_{NO}$, shown using a solid line). For the parameter values in (a) (n=1, Ar=0, D′=50 and t′=0), the two length-scale measures are the same for limiting basally-driven deformation case ($\lambda'_{NB}/2$), but the velocity deformation length-scale for side-driven deformation limit ${}^{v}\lambda'_{NS}$ is approximately twice the length-scale measured by crustal thickness, indicating substantial movement of mass along-strike. For the parameter values in (b) (n=3, Ar=0, D′=50 and t′=0), the two length-scale measures closely agree, indicating very little along-strike mass movement.

(a) Velocity and Thickening Length-Scales vs. Am at t′=0

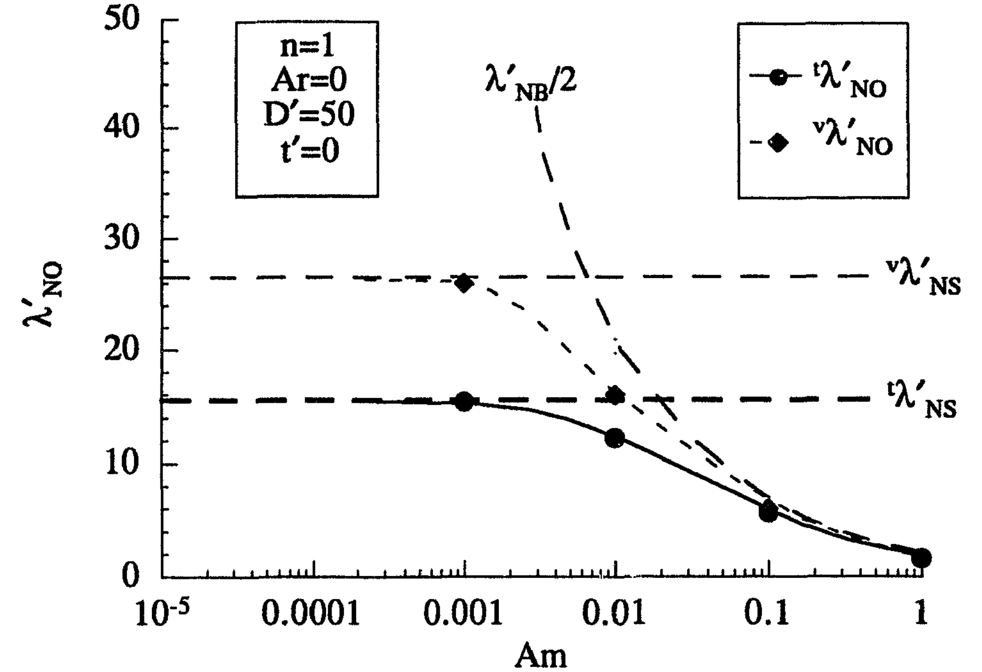

(b) Velocity and Thickening Length-Scales vs. Am at t′=0

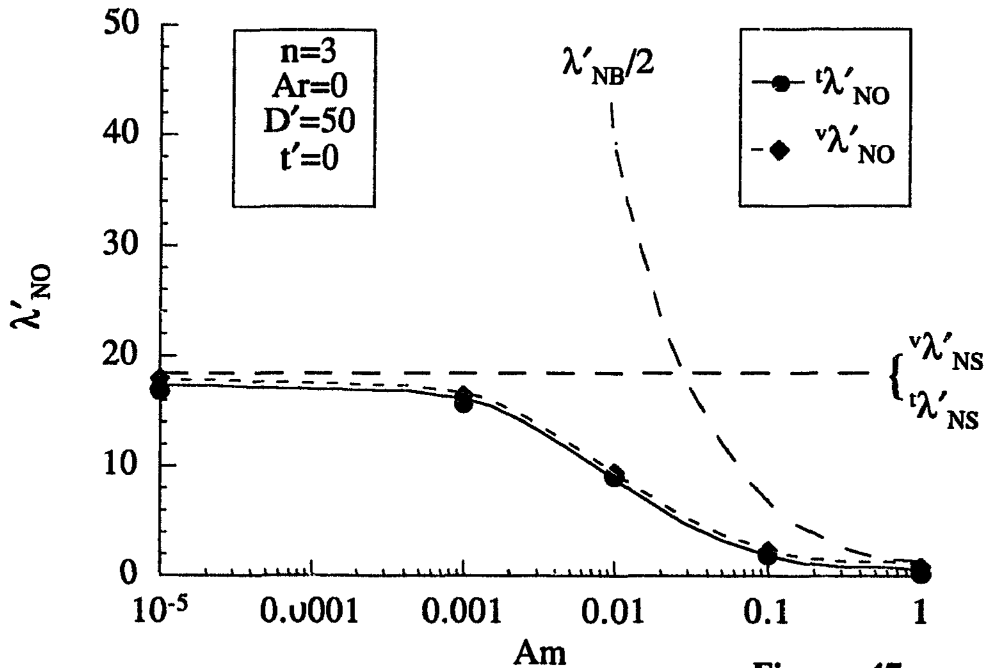

Figure 47

§ 4.6 Length-scales of Deformation for Mixed Side-Driven and Basally-Driven Boundary Conditions: Large Normalized Convergence

This section investigates the behaviour of the mixed case at large normalized convergence times. Only the normally incident case (figure 42(a)) is discussed, because it is assumed that the transcurrent length-scale does not change significantly with increasing normalized convergence. The investigation of thin-sheet behaviour under mixed boundary conditions is conducted initially for the case when the length-scale of the indenter at the side of the domain, D, is infinitely large. Behaviour may be compared with equivalent results from section 4.3, in order to determine the effect that advecting the detachment zone into the domain (with the indenter) has on the basally-controlled length-scale of deformation. Subsequently, the length-scale dependences of the mixed case are investigated for a finite variation in the indenter length-scale, D.

Large Normalized Convergence With no Along-Strike Variation in Velocity

When $D' \rightarrow \infty$ and $Am > 0$, the problem is similar to the case investigated in section 4.3. The deformation is determined by the competition between crustal thickening (on a length-scale determined by Am), and buoyancy forces due to crustal thickness gradients (on a length-scale determined by Ar). An important difference between this analysis and section 4.3, is that movement of crustal material through the zone of mantle detachment is no longer a free parameter, as it was for the two-sided case, but is constrained by the incident velocity $u_0(x)$.

The absence of tectonic escape along-strike produces greater amounts of crustal thickening with time (figure 48(a)) compared to the side-driven case investigated in section 4.4. The rate of crustal thickening integrated across-strike is approximately constant (figure 48(c)) (the slight increase is a numerical effect), although the spatial distribution of thickening changes with time as the effect of buoyancy forces on crustal thickness gradients increases (figure 48(b)). The length-scales, as measured by the normal velocity component and the thickening distribution, both increase with t' (figure 48(d)), but diverge because of the indentation of the side boundary. Note that these length-scales would agree for the two-sided case investigated in section 4.3.

Figure 48(d) also demonstrates that when $D \rightarrow \infty$, the mixed case does not reach a steady state with increasing convergence time; therefore, deformation will propagate forward indefinitely, provided Ar is sufficient to ensure that the mass involved in thickening does not become concentrated along the side boundary.

Figure 48: (a) Excess crustal thickness (S'-1), and (b) vertical strain-rate ($\partial S'/\partial t'$), for the mixed case, where mantle detachment occurs at the side of the model domain, and Am=0.01, $D \rightarrow \infty$, Ar=1, n=1. Results (lines) are shown for normalized convergence times t'=2, 8, and 10; (c) The integrated vertical strain-rate along section A-A$'$, Σ, vs t', for basal forcing where mantle detachment occurs at the side of the model domain, and Am=0.01, $D \rightarrow \infty$, Ar=1, n=1; (d) Length-scales of deformation, as measured by the normal velocity component (${}^{v}\lambda'_{NO}$) and crustal thickening (${}^{t}\lambda'_{NO}$), for the mixed boundary conditions. Note that there is no decrease in integrated strain-rate along the section with time, and that the length-scales continue to grow.

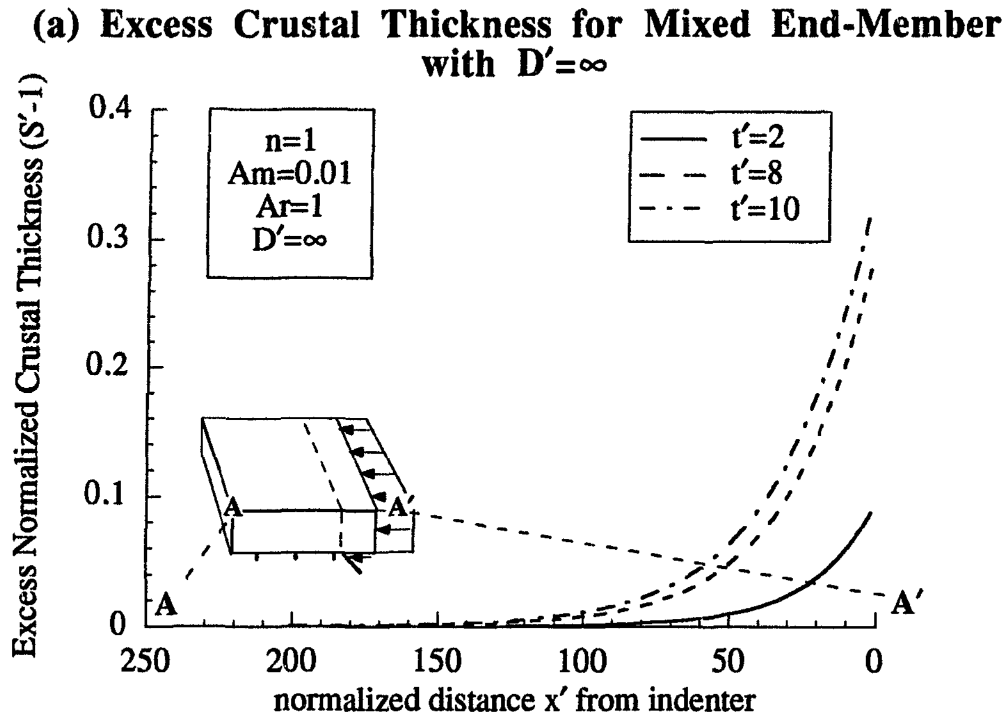
(a) Excess Crustal Thickness for Mixed End-Member with D′=∞
n=1
Am=0.01
Ar=1
D′=∞
t′=2
t′=8
t′=10
Excess Normalized Crustal Thickness (S′-1)
0.4
0.3
0.2
0.1
0
A
A′
250
200
150
100
50
0
normalized distance x′ from indenter

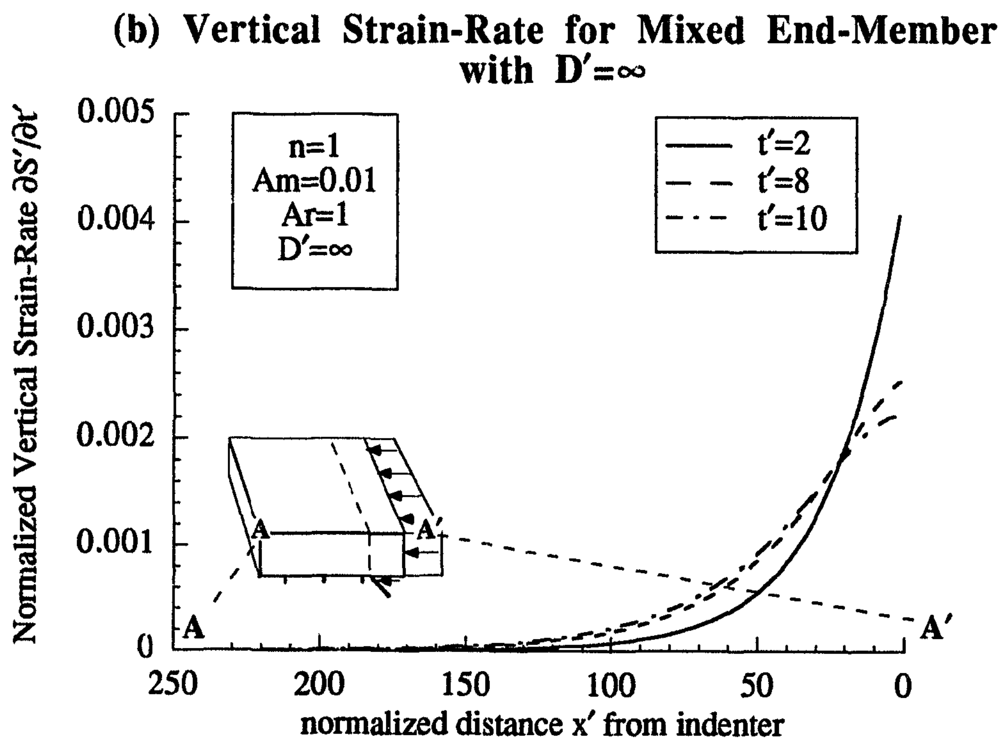
(b) Vertical Strain-Rate for Mixed End-Member with D′=∞
n=1
Am=0.01
Ar=1
D′=∞
t′=2
t′=8
t′=10
Normalized Vertical Strain-Rate ∂S′/∂t′
0.005
0.004
0.003
0.002
0.001
0
A
A′
250
200
150
100
50
0
normalized distance x′ from indenter

Figure 48(a,b)

(c) Change in Crustal Thickening Integrated Across-Strike: Mixed End-Member with D′=∞

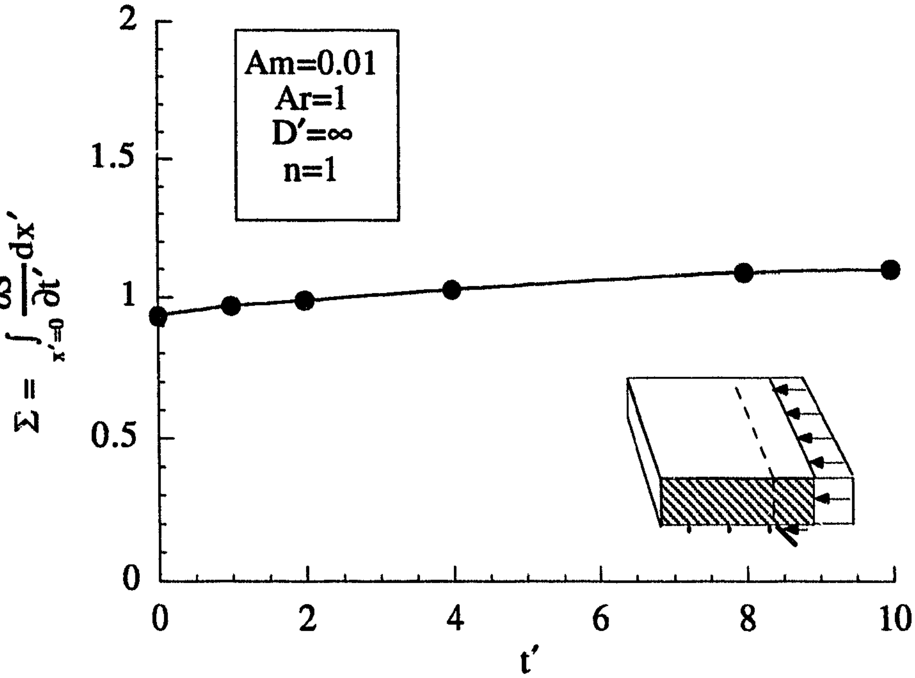

(d) Normalized Length-Scales vs. t′: Mixed End-Member with D′=∞

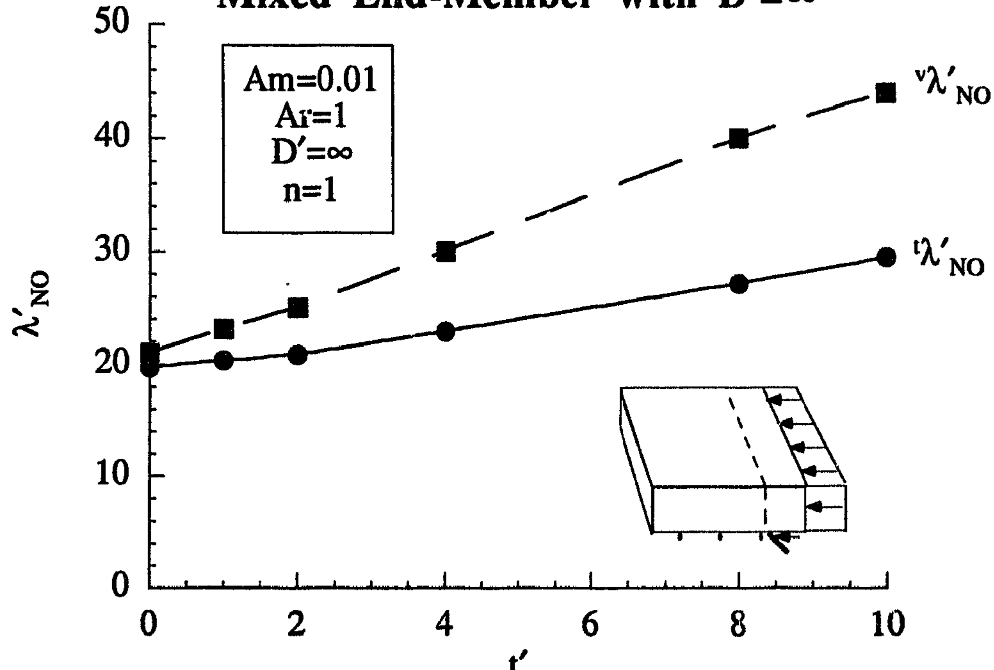

Figure 48(c,d)

Large Normalized Convergence With an Along-Strike Variation in Velocity

Figure 49(a,b) shows the change in crustal thickness and vertical strain-rate with normalized convergence for the mixed case, with the boundary conditions as shown in figure 42(a), and with parameter values Am=0.01, Ar=1, and D′=50. The size of the deformation length-scale depends upon the competition between basal coupling, indentation of the boundary, buoyancy forces, and tectonic escape. Crustal thickening is maximum at the side boundary, and is intermediate in magnitude compared to the whole-lithosphere side-driven case (figure 39(a)), and to the mixed case results which had no along-strike variation in D (figure 48(a)). As for the side-driven case, it is now possible for the loss of mass from tectonic escape along-strike to balance mass entering the cross-section, so that a steady state may be achieved. The trend towards this steady state is shown in figure 49(c).

Figure 49: (a) Excess crustal thickness (S'-1), and (b) vertical strain-rate ($\partial S'/\partial t'$), for the mixed case, where mantle detachment occurs along a boundary which is indenting the model domain, and Am=0.01, D′=50, Ar=1, n=1. Results (lines) are shown for normalized convergence times t′=2, 8, and 10; (c) The integrated vertical strain-rate along section A-A′, Σ, vs t′, for basal forcing where mantle detachment occurs at the side of the model domain, and Am=0.01, D=50, Ar=1, n=1; (d) Length-scales of deformation, as measured by the normal velocity component (${}^{v}\lambda'_{NO}$) and crustal thickening (${}^{t}\lambda'_{NO}$), for the mixed boundary conditions. The decrease in integrated strain-rate along the section, and the levelling off of the growth in length-scales with time, indicates that steady state will eventually be attained.

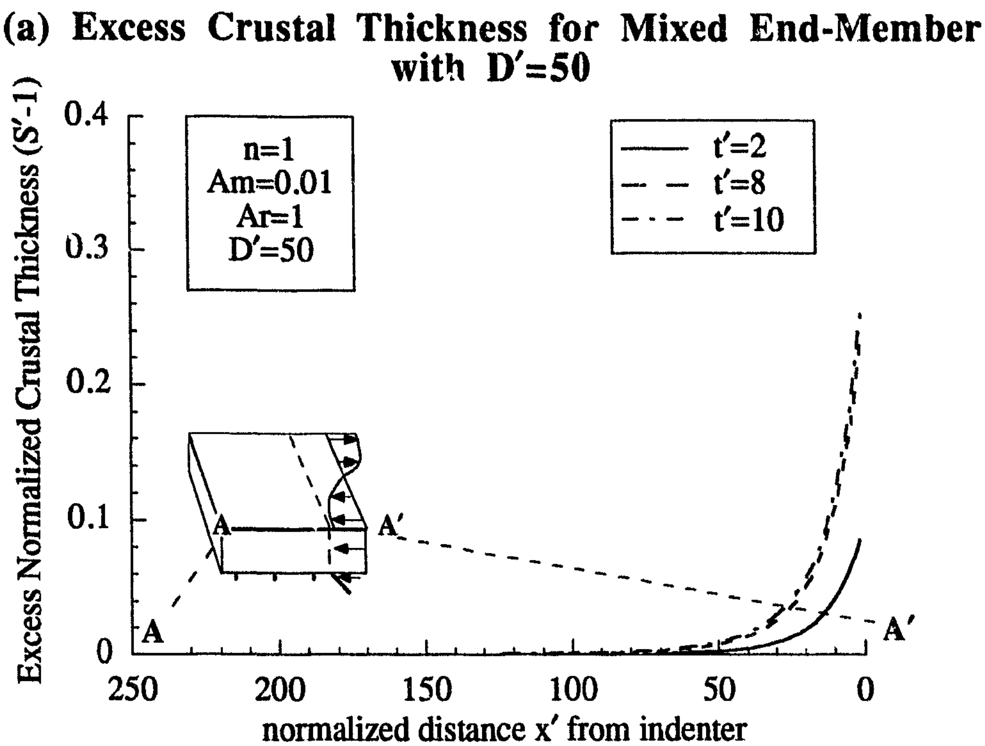
(a) Excess Crustal Thickness for Mixed End-Member with D′=50
Excess Normalized Crustal Thickness (S′-1)
0.4
0.3
0.2
0.1
0
n=1
Am=0.01
Ar=1
D′=50
t′=2
t′=8
t′=10
A
A′
250
200
150
100
50
0
normalized distance x′ from indenter

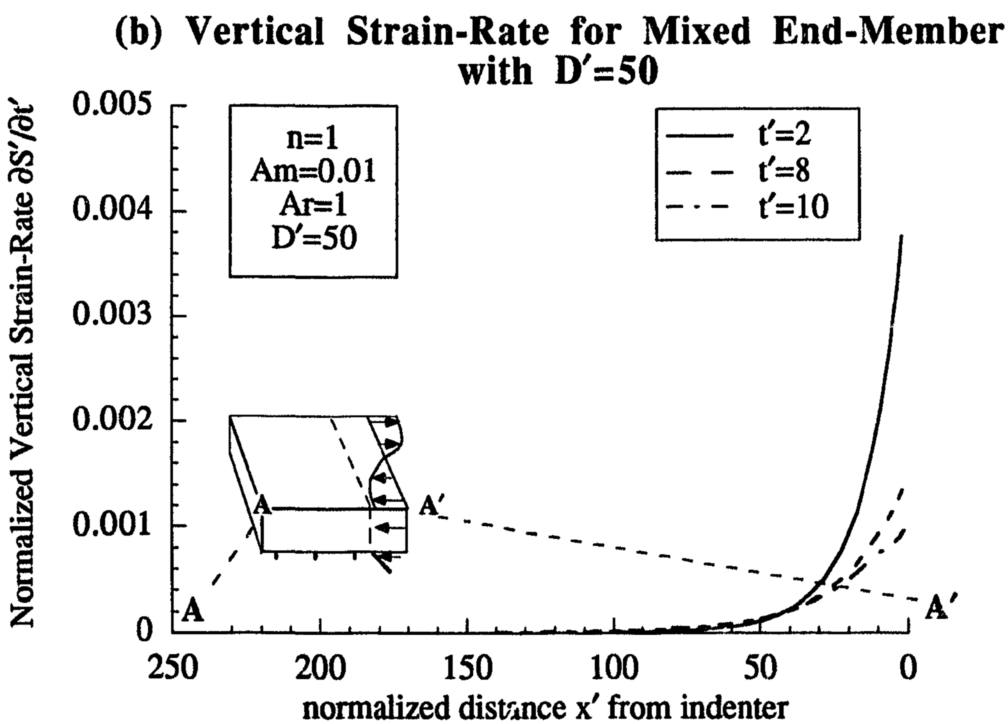
(b) Vertical Strain-Rate for Mixed End-Member with D′=50
Normalized Vertical Strain-Rate ∂S′/∂t′
0.005
0.004
0.003
0.002
0.001
0
n=1
Am=0.01
Ar=1
D′=50
t′=2
t′=8
t′=10
A
A′
250
200
150
100
50
0
normalized distance x′ from indenter

Figure 49(a,b)

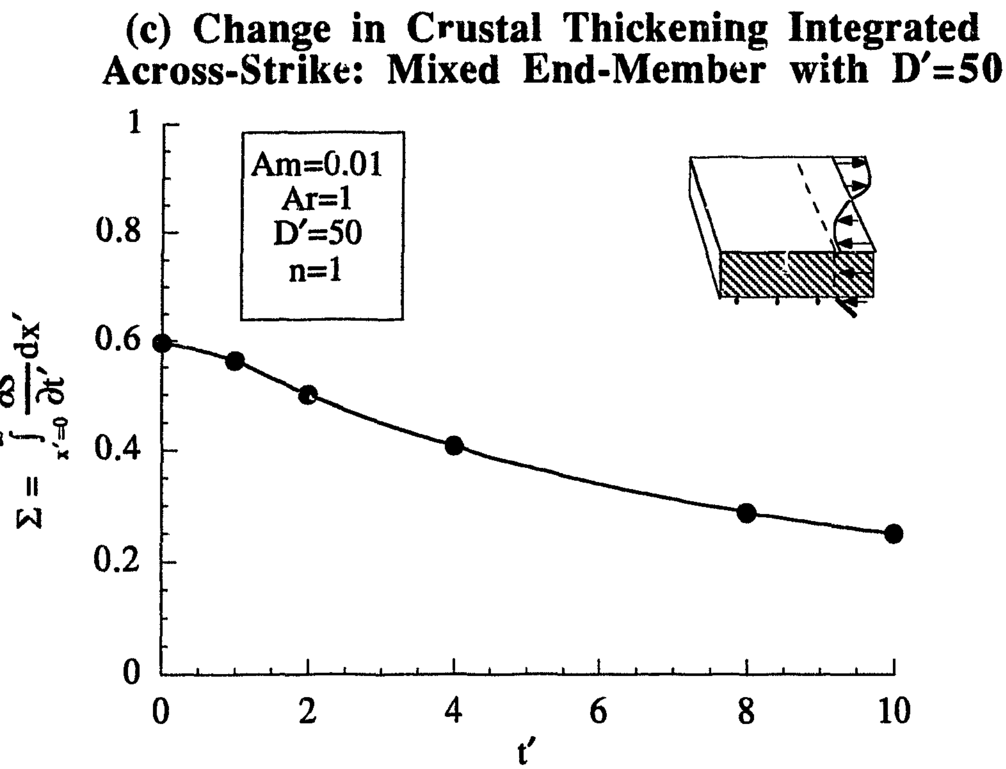

(c) Change in Crustal Thickening Integrated Across-Strike: Mixed End-Member with D′=50
Am=0.01
Ar=1
D′=50
n=1
$\Sigma = \int_{x'=0}^{\infty} \frac{\partial S'}{\partial t'} dx'$
1
0.8
0.6
0.4
0.2
0
0
2
4
6
8
10
t′

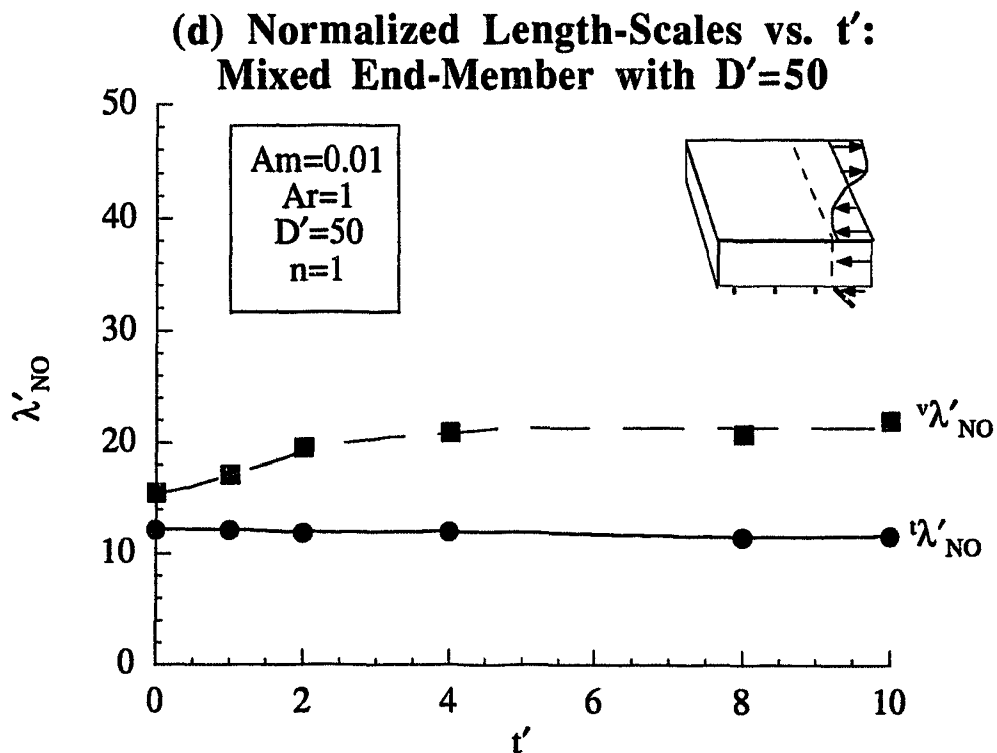

(d) Normalized Length-Scales vs. t′: Mixed End-Member with D′=50
Am=0.01
Ar=1
D′=50
n=1
λ'_{NO}
50
40
30
20
10
0
0
2
4
6
8
10
t′
$^{v}\lambda'_{NO}$
$^{t}\lambda'_{NO}$

Figure 49(c,d)

The $t'=0$ results from section 4.5 showed that the velocity length-scale for mixed boundary conditions is determined by the minimum of the predicted side and basally-driven length-scales (figure 50(a)). This is also true for large normalized convergence ($t' > 0$) (e.g. figure 50(b)). However, the predicted side and basally-driven length-scales change with time. For example, the basally-controlled length-scale increases with t', whereas the side-driven length-scale may reach a steady state where the forward movement of mass normal to the boundary is balanced by tectonic escape. The shift in limiting length-scales (indicated by the arrows in figure 50(b)) will change the location of the transition region between basally and side-controlled deformation as t' increases. The magnitude and direction of the shift depends on n, Ar and D'.

Figure 50: Normal velocity length-scale ${}^{v}\lambda'_{NO}$ for crustal thickness, vs. Am, for mixed boundary conditions (Am=0.01, D'=50, Ar=1, n=1), at: (a) t'=0; (b) t'=10. The limiting basally- and side-driven cases are indicated by the dashed lines. Note the change in the limiting length-scales with increasing normalized convergence, shown by the open arrows.

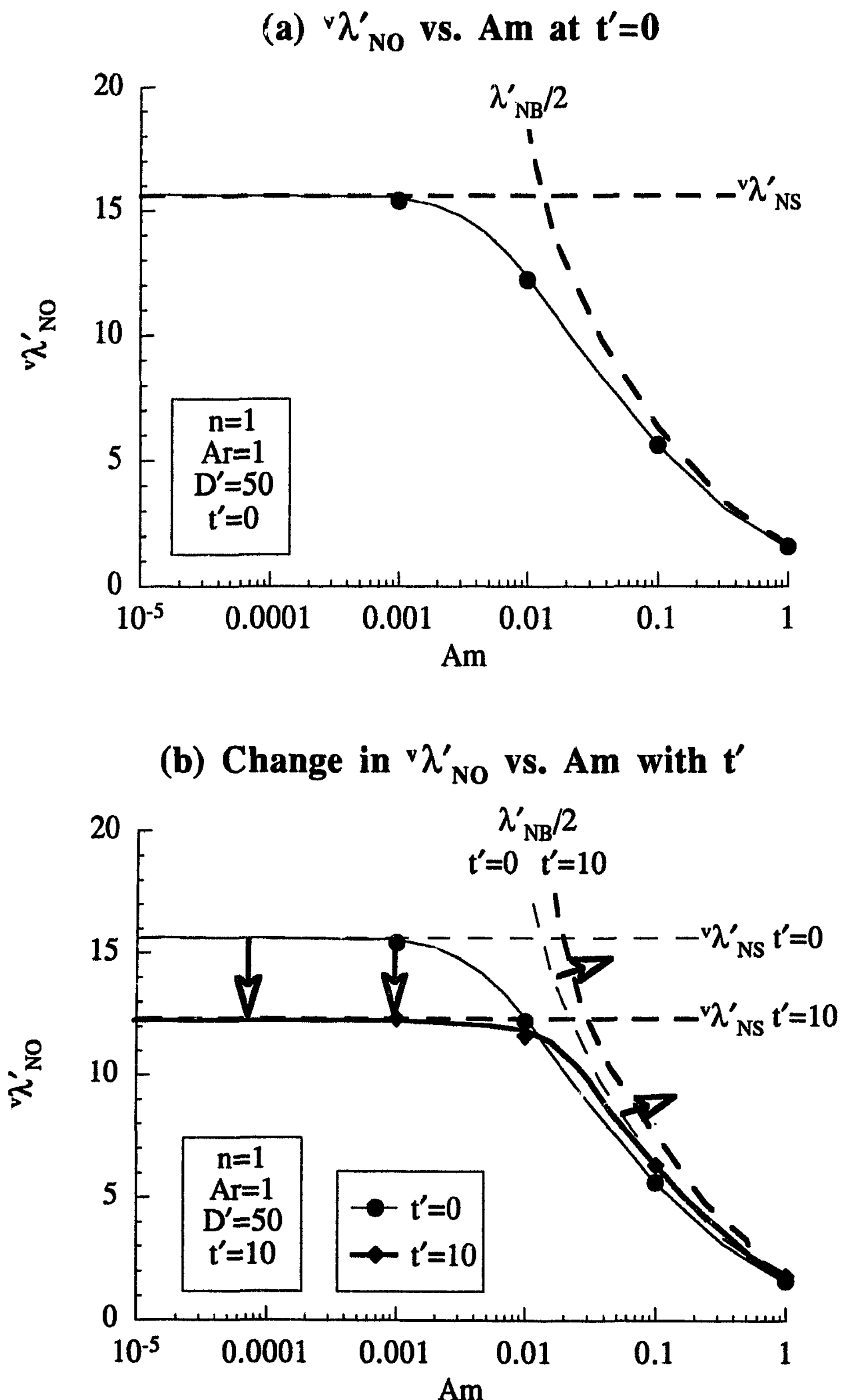
(a) ${}^{v}\lambda'_{NO}$ vs. Am at t′=0
20
15
10
5
0
${}^{v}\lambda'_{NO}$
$\lambda'_{NB}/2$
${}^{v}\lambda'_{NS}$
n=1
Ar=1
D′=50
t′=0
10^{-5}
0.0001
0.001
0.01
0.1
1
Am
(b) Change in ${}^{v}\lambda'_{NO}$ vs. Am with t′
20
15
10
5
0
${}^{v}\lambda'_{NO}$
$\lambda'_{NB}/2$
t′=0 t′=10
${}^{v}\lambda'_{NS}$ t′=0
${}^{v}\lambda'_{NS}$ t′=10
n=1
Ar=1
D′=50
t′=10
t′=0
t′=10
10^{-5}
0.0001
0.001
0.01
0.1
1
Am

Figure 50

§ 4.7 Summary

The results from this chapter indicate that there are some predictable differences between the deformation resulting from basally-driven and side-driven convergence. Length-scales of basally-driven deformation are determined by the values of n, Ar, t', and the Ampferer number, Am. Length-scales of side-driven deformation are determined by n, Ar, t', and the horizontal extent of the indenting boundary condition, D'. For a combination of indenter mechanics and basal forcing, deformation length-scales are determined by the minimum of the predicted length-scales from the side-driven and basally-driven cases.

For both side and basal forcing, the model results suggest that normally convergent velocities will extend further from the plate boundary than will velocities for predominantly strike-slip boundary conditions, if all other parameters controlling deformation are the same. The basally-driven model predicts that the length-scales for these cases will have a ratio of 2, for all values of n, at small normalized convergence times. In contrast, the side-driven model predicts that this ratio will be 4, for all values of n, at small normalized convergence times. In the case of oblique convergence, assuming a non-linear viscous rheology for the crust, both models predict that the length-scale ratio will tend to 1, so that no appreciable partitioning of normal and transcurrent velocity fields will be observed.

When determining deformation length-scales for the (kinematic) indenter model, it is important to specify what is being measured. The length-scale over which the normal velocity component dies away from the boundary is, in general, greater than the length-scale over which crustal thickening occurs, because of the likelihood of movement of mass along-strike, and the forced deformation of the indenting boundary.

As the crust thickens with increasing normalized convergence times, some changes in the length-scale of deformation normal to the plate boundary , as measured by the crustal thickness, are likely to occur. If the thickening is controlled by basal forcing, the length-scale for normal deformation, λ'_{NB}, will increase, the magnitude of the increase depending on the values of Ar, n, Am, and t'. However, if thickening is controlled by side forcing, the deformation length-scale will not necessarily increase with t'. For cases where buoyancy forces are insufficient to redistribute mass away from the indenting boundary, the normal deformation length-scale will decrease with t'. Even if buoyancy forces are significant, the movement of mass along-strike (tectonic escape) may prevent the deformation length-scale from growing indefinitely with time. Eventually a local steady state may be reached, where the thickening from indentation of the boundary is balanced by tectonic escape of mass along-strike.

A plateau may develop for the side-driven case, given a suitably shaped (kinematic) indenter, as discussed in section 4.4. However, when there is no along-strike variation in velocity, the basally-driven thin-sheet will not form a plateau, even after considerable amounts of convergence, unless the value of the controlling parameters Am, Ar and n are locally changed. Such a change may occur as a consequence of crustal thickening. For example, the value of Am may locally decrease if thickening of the crust leads to an increase in Moho temperature (see Chapter Six). Similarly, an increased crustal thickness will change the thermal and pressure regimes, and perhaps alter the predominant creep mechanism, therefore changing n. A decrease in the strength of the crust may also affect the local value of the Argand number (England and Houseman, 1989).

When both side and basal forcing are present (e.g. indentation and simultaneous mantle detachment), the length-scales of deformation at all normalized convergence times will be dictated by the *minimum* of the predicted length-scales for the basally- and side-driven cases.

Chapter Five

SCALE ANALYSIS OF LITHOSPHERIC CONVERGENCE: GEOLOGICAL APPLICATIONS

§ 5.1 Introduction

The previous chapter made a number of predictions concerning the different behaviour of crust subjected to convergence by a 'side-driven' indenter, vs. crust which is controlled by 'basally-driven' tractions due to the detachment and subduction of underlying mantle lithosphere. Can these predictions be used to determine whether the basally-driven (mantle detachment) model, or the side-driven (indenter) model, better represent deformation of the earth's crust in convergent settings? In this chapter, I develop a series of tests, based on the deformation styles investigated in the previous chapter, to try to distinguish between primarily basal and side-driven forcing (Table 8). The first two tests compare length-scale measures from natural orogenic settings to the predictions of crustal deformation length-scales for side and basal forcing. The third test compares the ratios between observed normal and transcurrent crustal deformation length-scales, λ_{NO} and λ_{TO}, to the side and basal predictions, for purely convergent vs. strike-slip settings. Lastly, test four compares observed and predicted length-scale ratios for cases with oblique convergence.

The model predictions on which Table 8 is based are summarized in figures 51 and 52. Figure 51 illustrates the basic behaviour of the side-driven model, in which the whole lithosphere deforms over a length-scale which depends on the wavelength of forcing at the indenting side boundary (D), vs. the basally-driven model, where

Table 8: Testing Length-Scale Relations from Chapter Four

Model Prediction	**Test Method**
Aspect Ratio Test One Length-scales for normal deformation at small normalized convergence times will be the minimum of: $\lambda_{NS} \approx \frac{2D}{\pi\sqrt{n}}$ $\lambda_{NB} \approx 2\left(\frac{4}{nAm}\right)^{\frac{n}{n+1}} S_0$	Plot D vs. λ_{NO} for orogens which have not experienced significant normalized convergence All points should fall *on*, or *below*, the line which has slope $2/\pi\sqrt{3}$ If points are significantly below this line, it indicates the orogen may be basally-driven.
Aspect Ratio Test Two Length-scales for transcurrent deformation will be the minimum of: $\lambda_{TS} \approx \frac{D}{2\pi\sqrt{n}}$ $\lambda_{TB} \approx \left(\frac{4}{nAm}\right)^{\frac{n}{n+1}} S_0$	Plot D vs. λ_{TO} All points should fall *on*, or *below*, the line which has slope $1/2\pi\sqrt{3}$ If points are significantly below this line, it indicates the orogen may be basally-driven.

Aspect Ratio Test Three The ratio of purely normal: purely transcurrent length-scales of deformation will be between 2:1 (basally controlled) and 4:1 (side-driven)	Find cases where the direction of plate motion changes along-strike from predominantly normal to strike-slip. Estimate $\lambda_{NO}:\lambda_{TO}$ ratio.
Aspect Ratio Test Four Oblique Convergence: Assuming n>1, for both side and basally-driven cases, normal and transcurrent deformation length-scales will tend to 1.	Estimate the ratio $\lambda_{NO}:\lambda_{TO}$ for obliquely convergent systems.

Figure 51: Summary of the deformation styles investigated in chapter four. (a) The side-driven model. where crust and mantle lithosphere deform as one layer, with no shear between them. Deformation length-scales in the crust are a function of the wavelength of the applied velocity boundary condition, D, at the plate boundary. Purely compressive deformation extends four times as far from the boundary as purely transcurrent deformation. This ratio is reduced somewhat for obliquely convergent settings. (b) The basally-driven case, where subduction of the mantle lithosphere at the plate boundary produces deformation in the overlying crust, on a length-scale determined by the crust-mantle coupling (Am). Purely compressive deformation extends twice as far from the initial detachment zone as does purely transcurrent deformation. This ratio is also reduced for obliquely convergent settings.

Figure 51

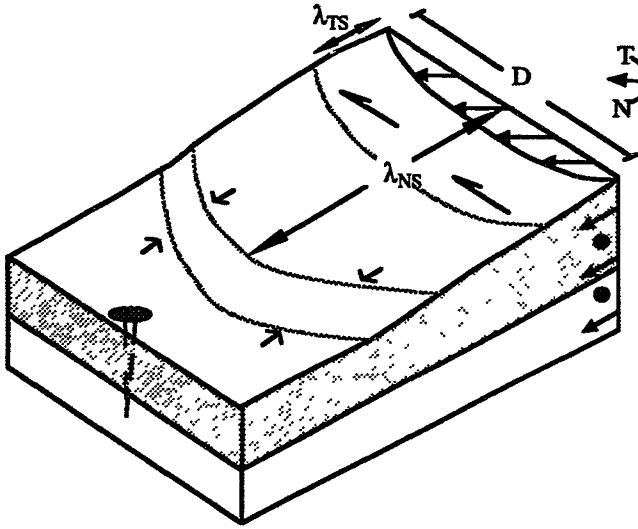

(a) Pure Shear Whole Lithosphere Deformation

1. **Forcing from side boundaries**
2. **Whole lithosphere deforms; no relative shear between crust and mantle**
3. **Length scale of deformation depends on length scale of applied velocity at boundary, D, and power law exponent, n**

$$\lambda_{NS} \sim \frac{2D}{\pi\sqrt{n}} \qquad \lambda_{TS} \sim \frac{D}{2\pi\sqrt{n}}$$

$$\lambda_{NS} : \lambda_{TS} \sim 4$$

$$\lambda_{NS} : \lambda_{TS} < 4 \quad \text{(oblique)}$$

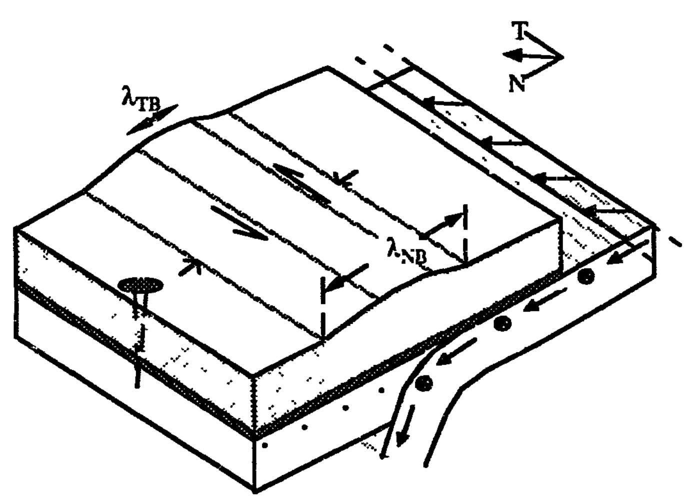

(b) Subduction of Mantle Lithosphere Beneath Crust

1. **Forcing by basal traction from mantle lithosphere**
2. **Crustal deformation; shear between crust and mantle through weak basal layer**
3. **Length scale of deformation depends on crust-base coupling**

$$\lambda_{NB} \sim 2\left(\frac{4}{n\,Am}\right)^{\frac{n}{n+1}} S_0 \qquad \lambda_{TB} \sim \left(\frac{4}{n\,Am}\right)^{\frac{n}{n+1}} S_0$$

$$\lambda_{NB} : \lambda_{TB} \sim 2$$

$$\lambda_{NB} : \lambda_{TB} < 2 \quad \text{(oblique)}$$

deformation in the crust is a result of the detachment and subduction of underlying mantle lithosphere, and the length-scale of deformation depends on the strength of the coupling at the detachment interface. The predicted ratios for normal and transverse incidence are summarized underneath each schematic illustration, as well as the ratio for the oblique case, where both normal and transverse components act simultaneously at the plate boundary.

The real behaviour of the lithosphere at convergent plate boundaries may be a combination of the cases shown in figure 51. Results from chapter four showed that for a possible intermediate case, as illustrated in figure 52, the crust will deform over a length-scale which is the minimum of the side-driven and basally-driven predicted length-scales. For instance, if the crust is only weakly coupled to the mantle lithosphere, its behaviour will depend on the applied indenter length-scale at the plate boundary, and will be independent of the basal boundary condition. If the crust is strongly coupled to the mantle lithosphere, or the side length-scale D is very large, the crust will deform in response to the basal boundary condition. Although the tests in Table 8 are formulated for the separate basal and side-driven cases, they are also applicable to the mixed case, if it is assumed that the final deformation 'state' of an orogen is either determined by the side or basal forcing, depending on the transition criterion discussed above. (Recall that in chapter four, the mixed case was demonstrated to have a deformation length-scale which

---

Figure 52: Application of the model styles illustrated in figure 51 to intermediate cases, where there is a combination of basal forcing or drag, and indenter mechanics. The deformation length-scales for the intermediate case (indicated by λ_{NM} and λ_{TM} on the figure) will be the minimum of the predicted side-driven and basally-driven length-scales, as shown in the previous chapter.

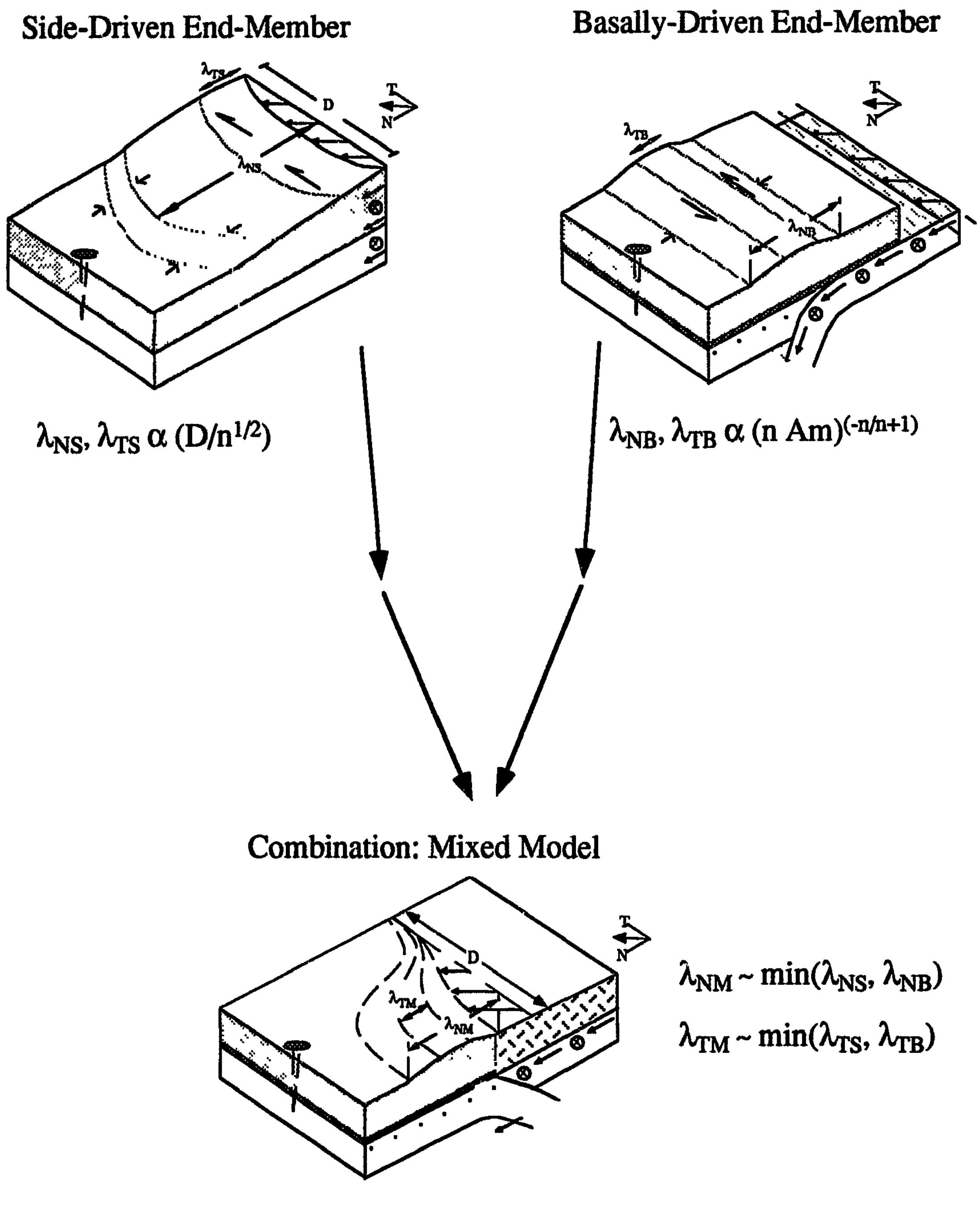
Side-Driven End-Member
Basally-Driven End-Member
$\lambda_{NS}, \lambda_{TS} \alpha (D/n^{1/2})$
$\lambda_{NB}, \lambda_{TB} \alpha (n\ Am)^{(-n/n+1)}$
Combination: Mixed Model
$\lambda_{NM} \sim \min(\lambda_{NS}, \lambda_{NB})$
$\lambda_{TM} \sim \min(\lambda_{TS}, \lambda_{TB})$

Figure 52

depended on the *minimum* of the length-scales due to the indenter (side) boundary condition, and basal traction from detachment and subduction of underlying mantle lithosphere.)

The aspect ratio tests require estimates for the length-scales of deformation for natural convergent and strike-slip settings, λ_{NO} and λ_{TO}, where the '$_O$' indicates 'observed', as well as the along-strike length-scale of variations in the relative velocity at the plate boundary, D. The natural examples to be used in the tests must meet a number of requirements, which are discussed in section 5.2. The geographical locations of the selected examples are illustrated in figures 53 and 54, for recent (fig. 53) and more ancient (fig. 54) convergent settings.

Figure 53: Summary of the plate boundary settings for modern examples described in Appendix F. Map figure modified from Bott (1982). Small figures modified from authors indicated in brackets: (a) European Alps (Royden, 1993a); (b) Northern and Eastern Anatolian faults, and the Levant fault with associated convergent deformation at the Lebanon (LEB) Mts (Hempton, 1987); (c) Andes (Dewey and Lamb, 1992); (d) Banda Arc (Johnston and Bowin, 1981; Karig et al., 1987); (e) Chaman Fault, with the associated Zhob and Makran foldbelts (Lawrence et al., 1981); (f) Tibetan Plateau (Peltzer and Tapponnier, 1988); (g) New Zealand Southern Alps and Alpine Fault (Beaumont et al., submitted); (h) New Guinea (Smith, 1990); (i) Pyrenees (Muñoz, 1992; Alonso and Teixell, 1992); (j) Taiwan (Lu and Malavieille, 1994); (k) San Andreas fault (Irwin, 1990); (l) Zagros (Hempton, 1987; Jackson, 1992). Symbols on figures: filled sawtooth indicates continental thrust; unfilled sawtooth indicates oceanic subduction; strike-slip faults denoted by shear arrows. Areas above sea-level shown by dotted pattern; approximate extent of deformed area indicated by shaded pattern. Arrows with unfilled heads represent directions of plate motion. The aspect ratio measurement for each orogen is indicated by the dashed polygon.

(a) Eastern, Western, and Southern Alps

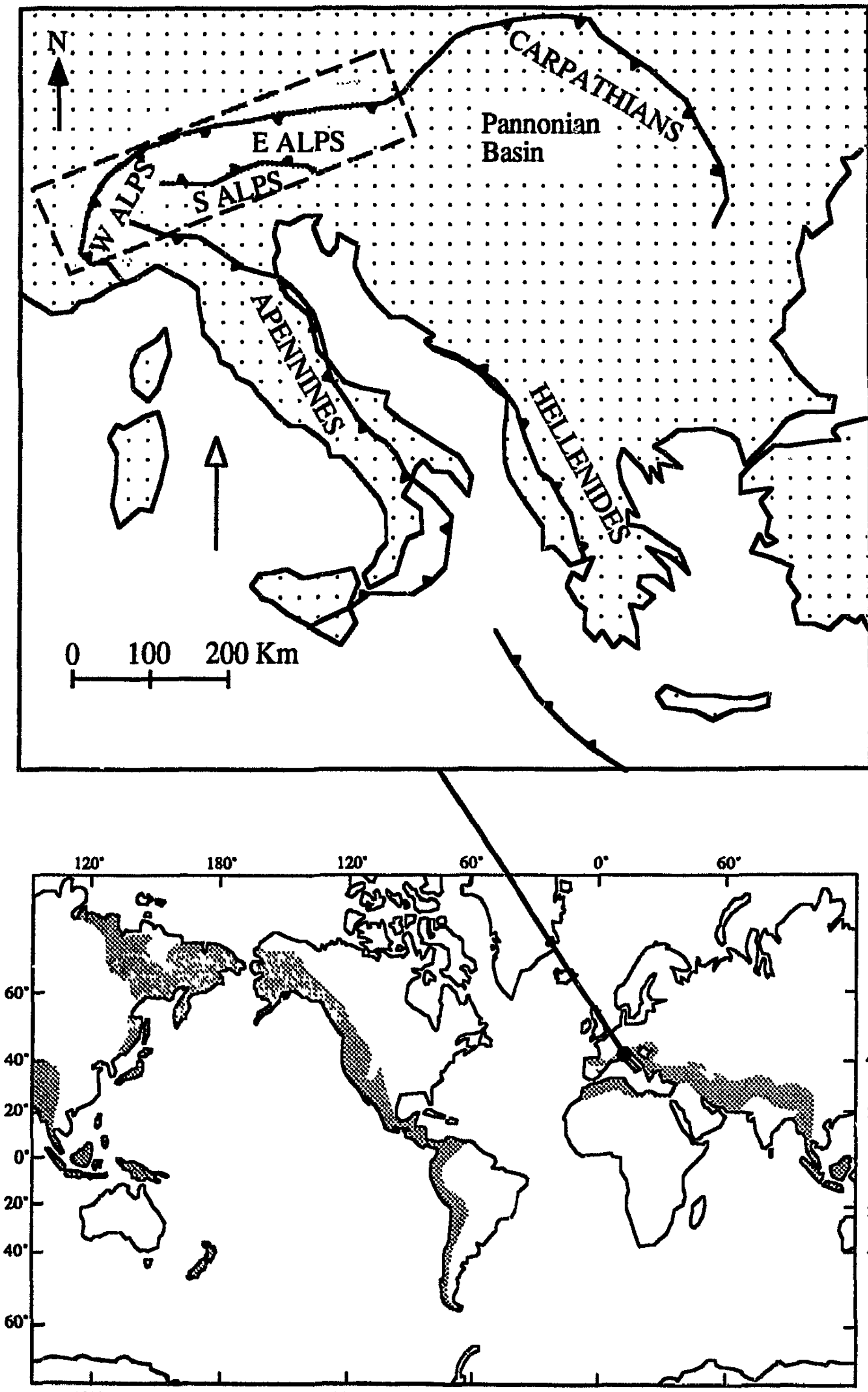

Figure 53(a)

(b) Eastern and Northern Anatolian Faults, Levant Fault, and Lebanon Mts

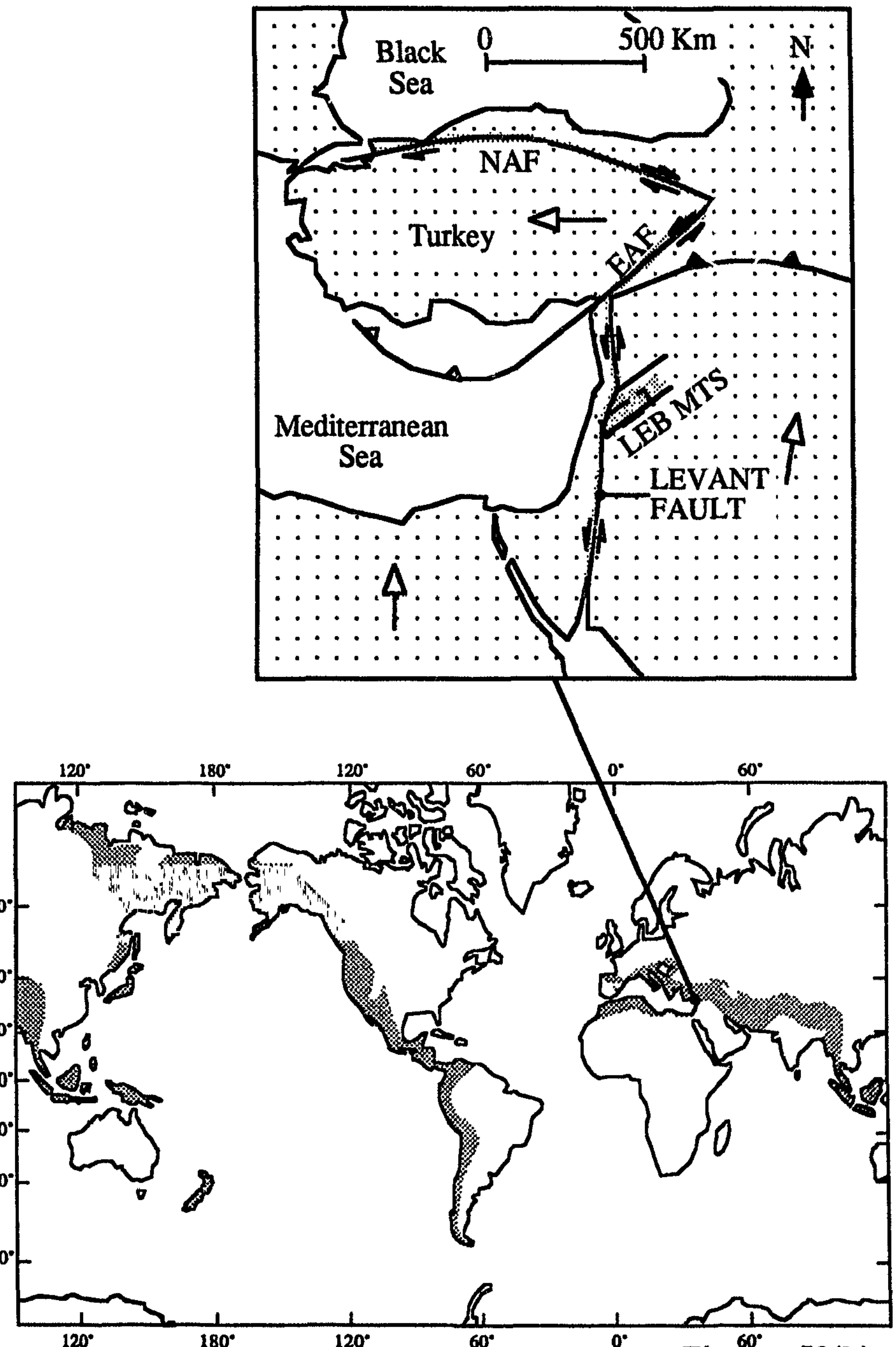

Figure 53(b)

(c) Andes

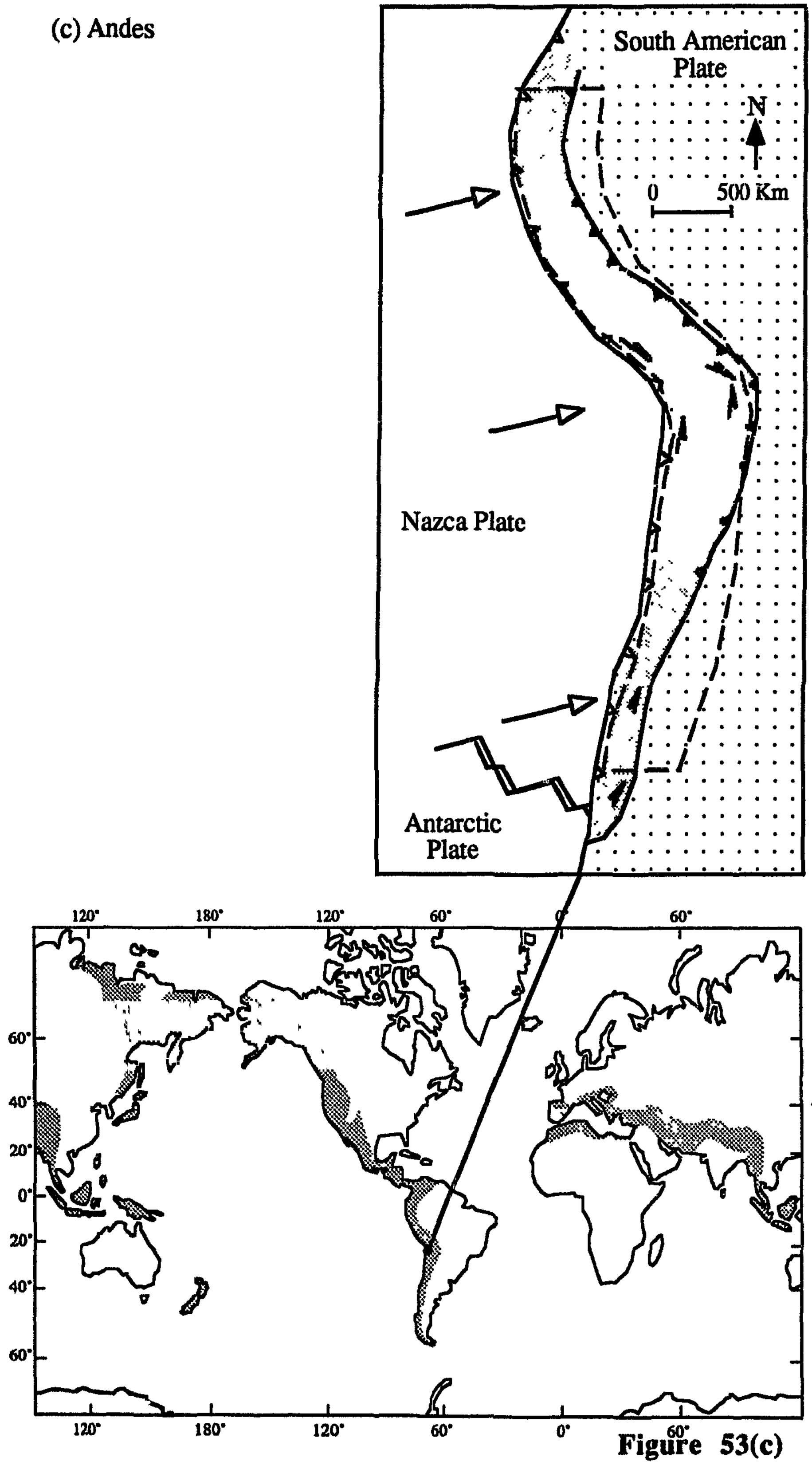

Figure 53(c)

(d) Banda Arc

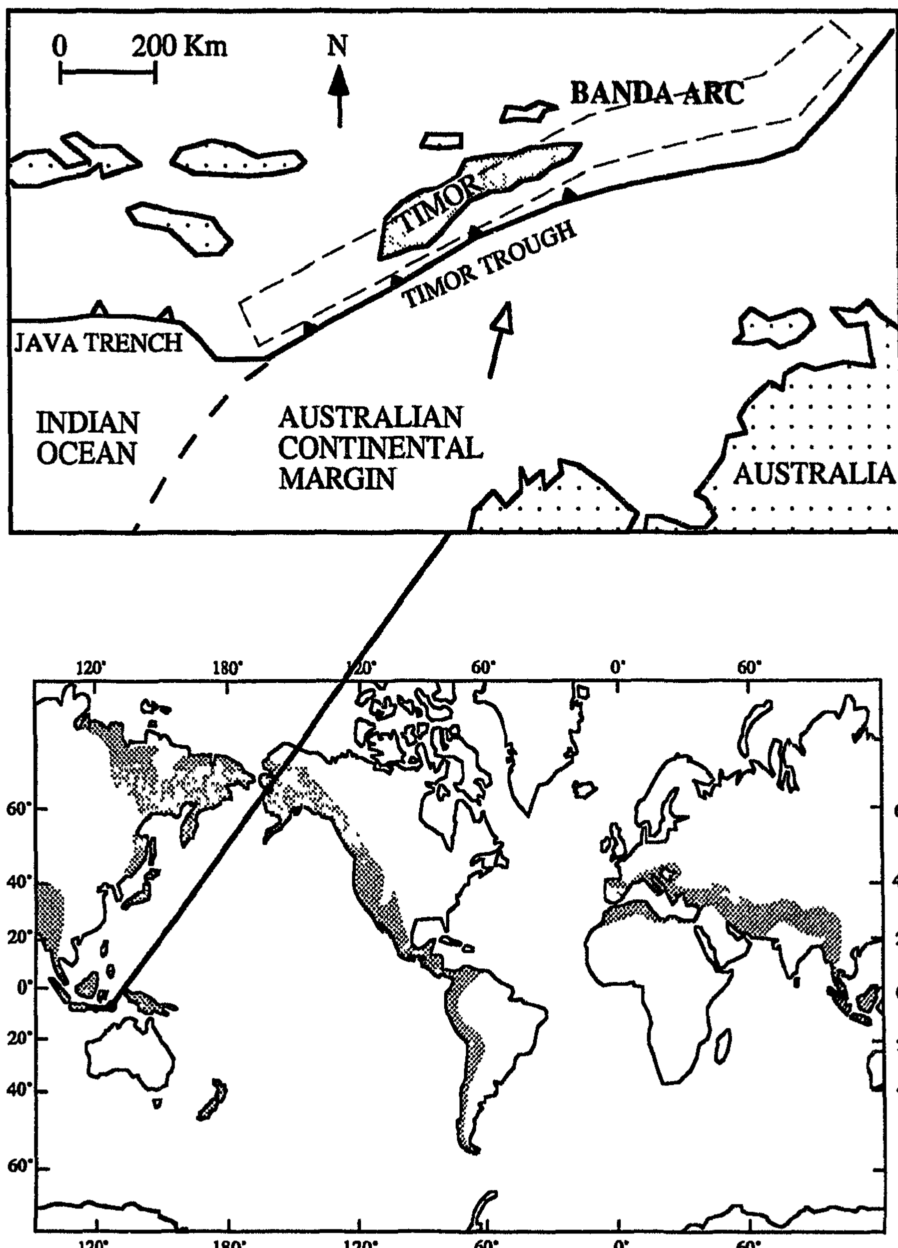

Figure 53(d)

(e) Chaman Fault, Zhob Convergent Zone, Makran Foldbelt

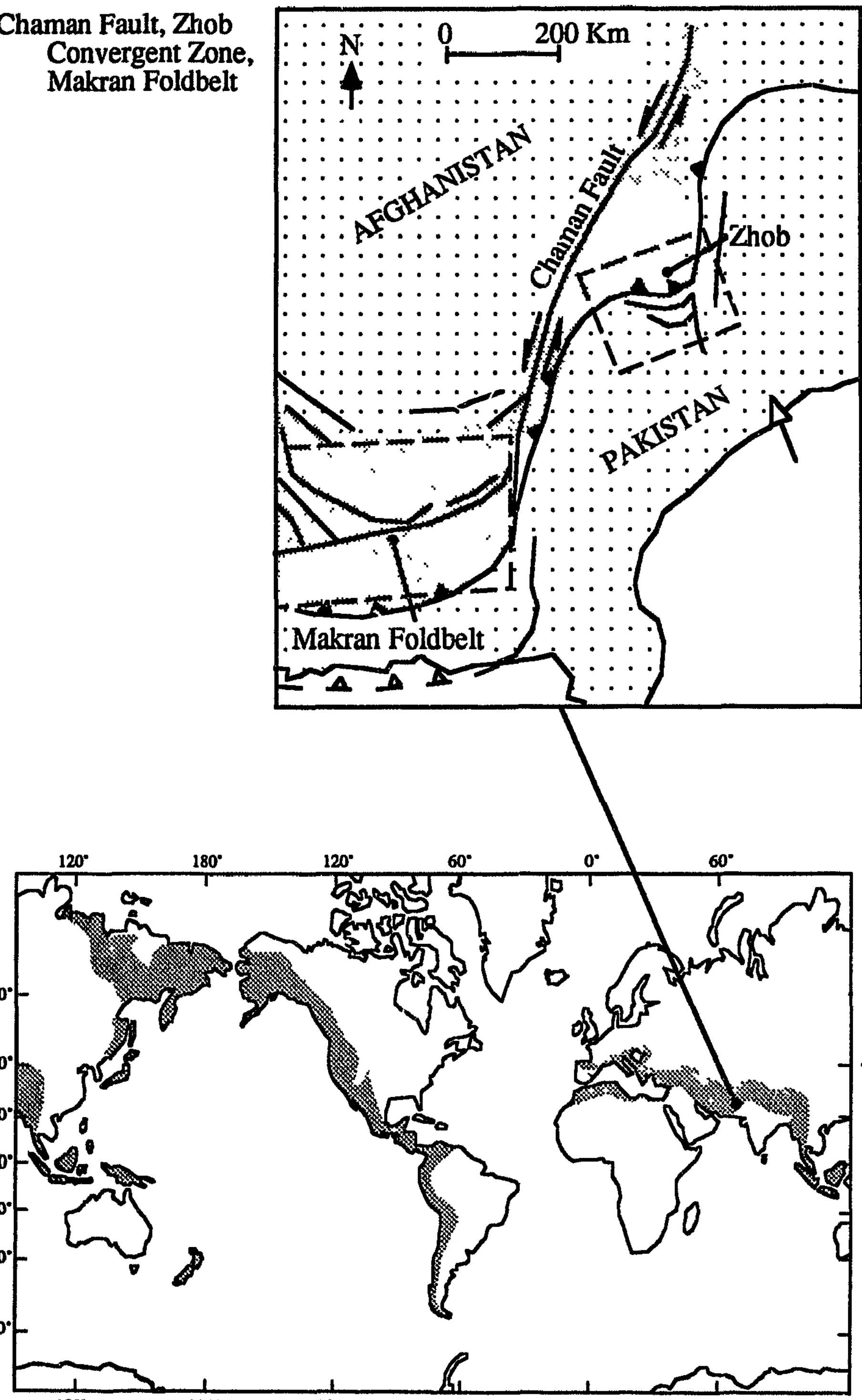

Figure 53(e)

(f) Tibetan Plateau

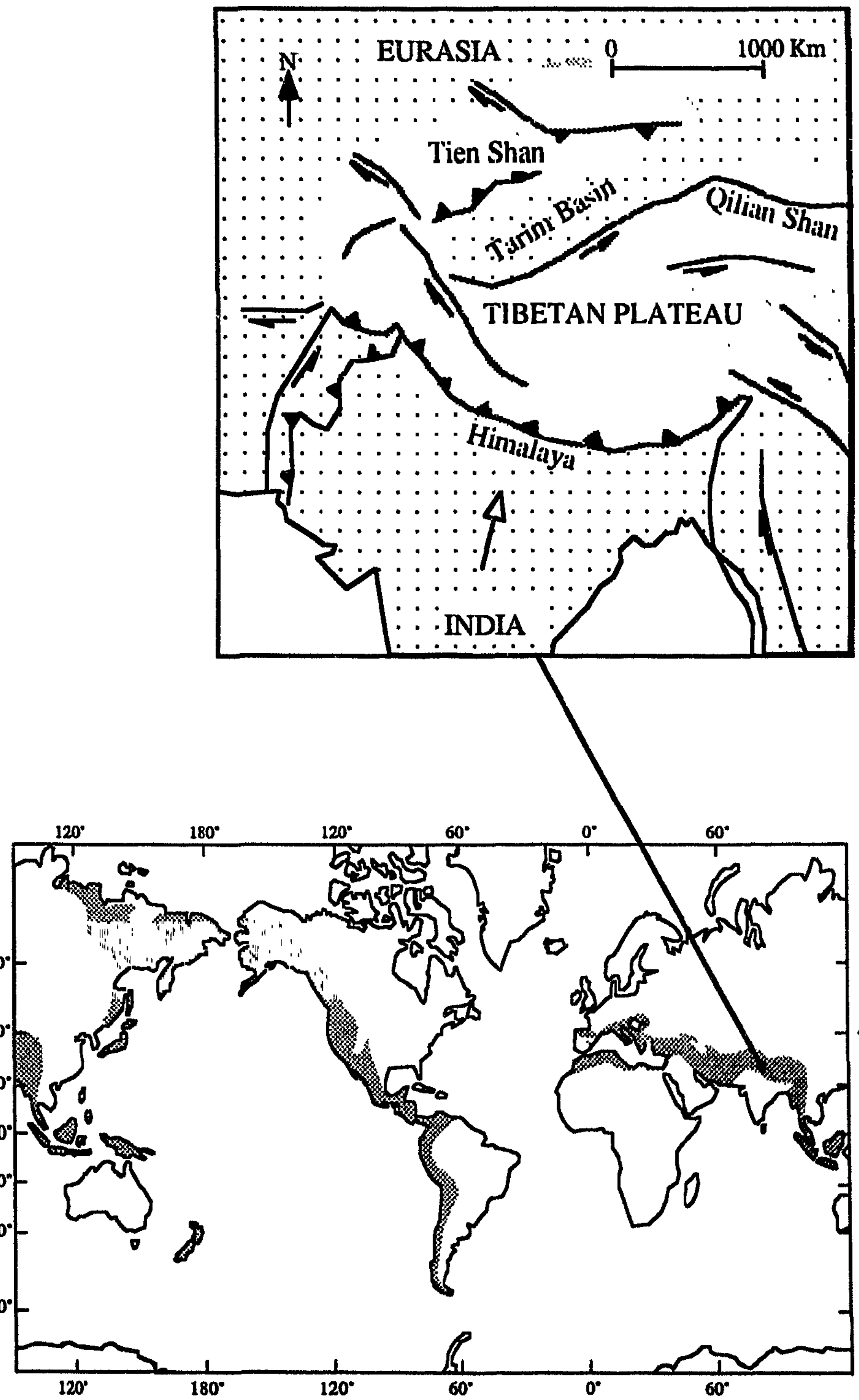

Figure 53(f)

(g) New Zealand Southern Alps and the Alpine Fault

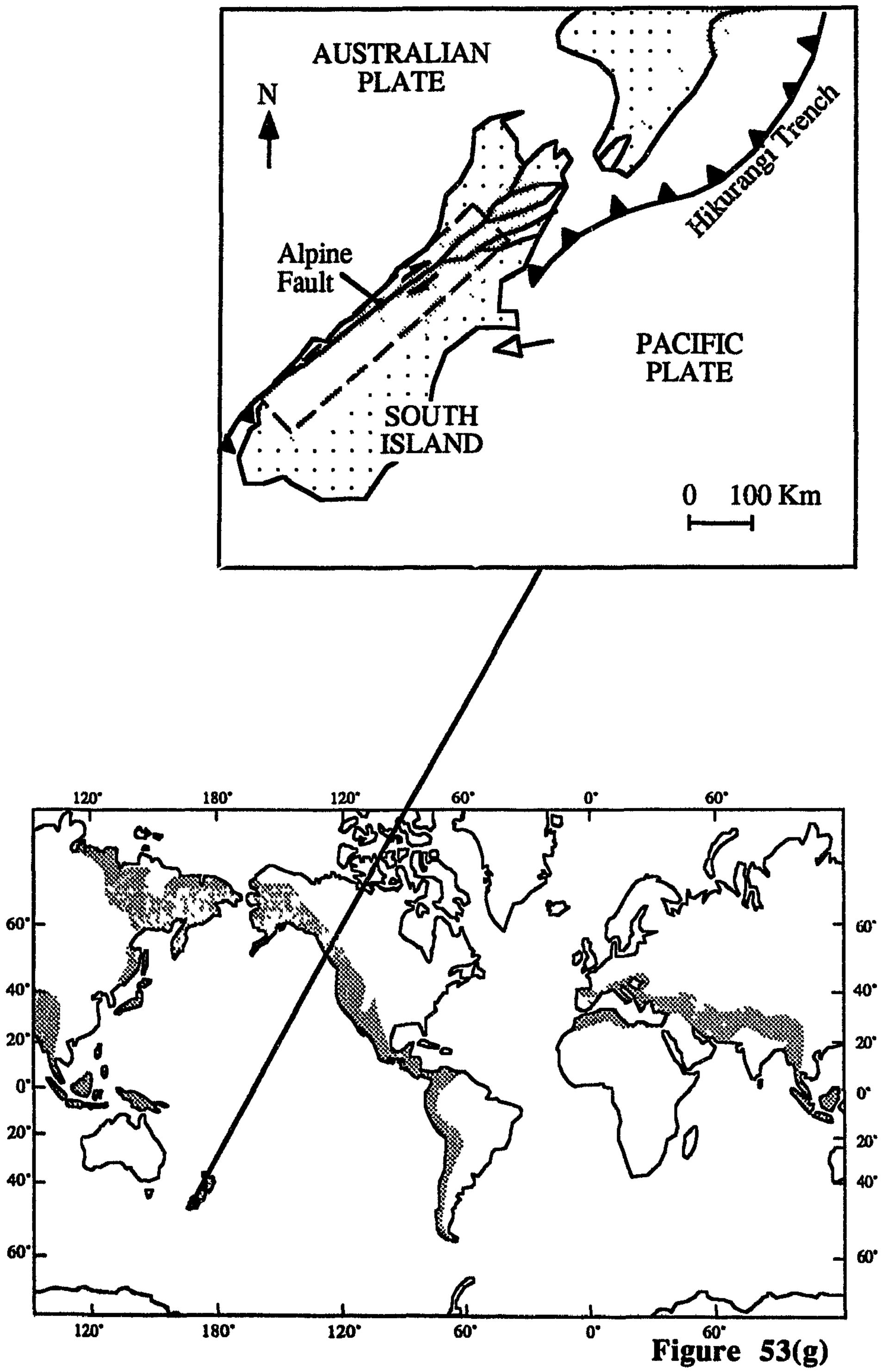

Figure 53(g)

(h) New Guinea

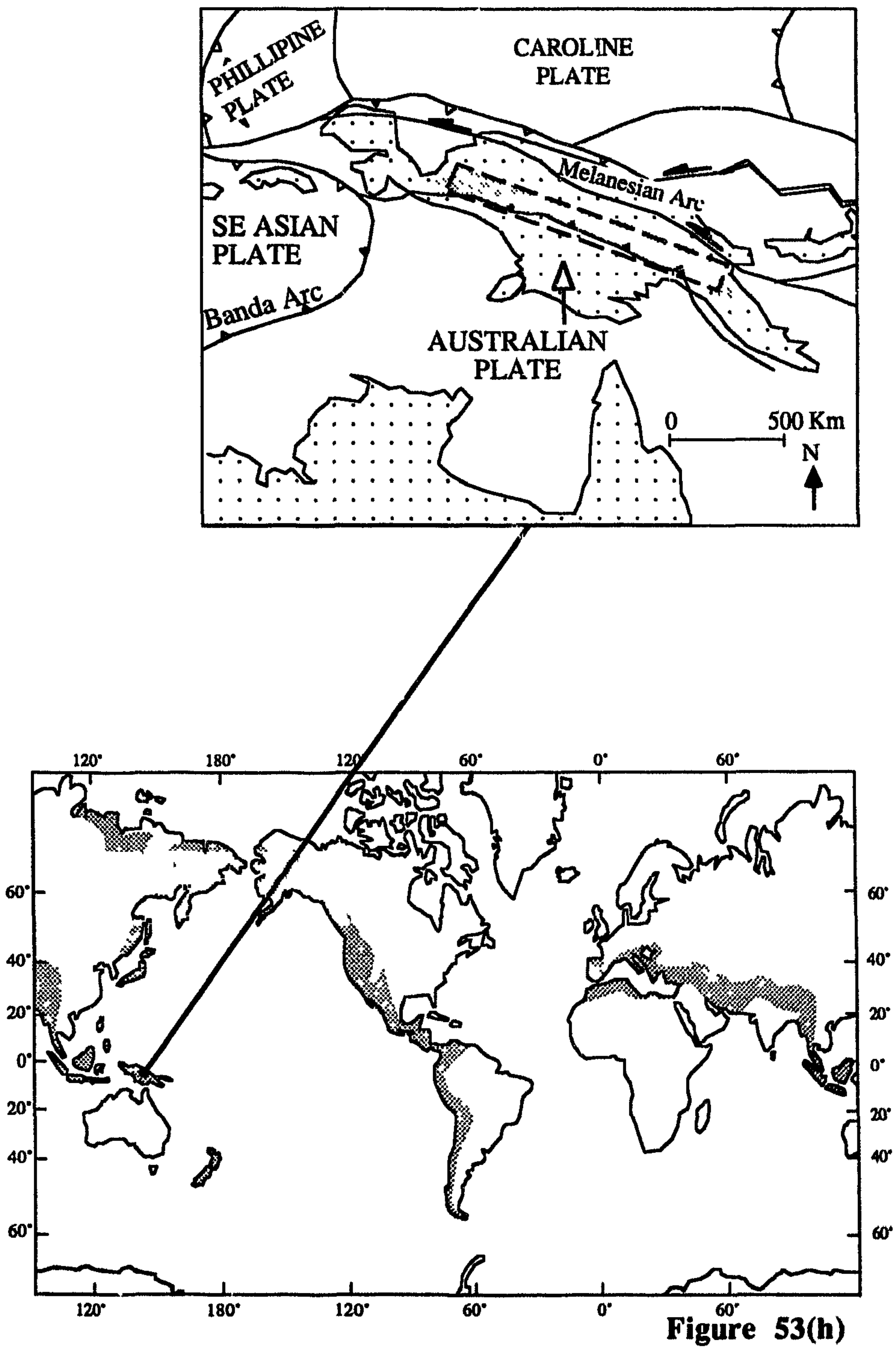

Figure 53(h)

(i) Pyrenees

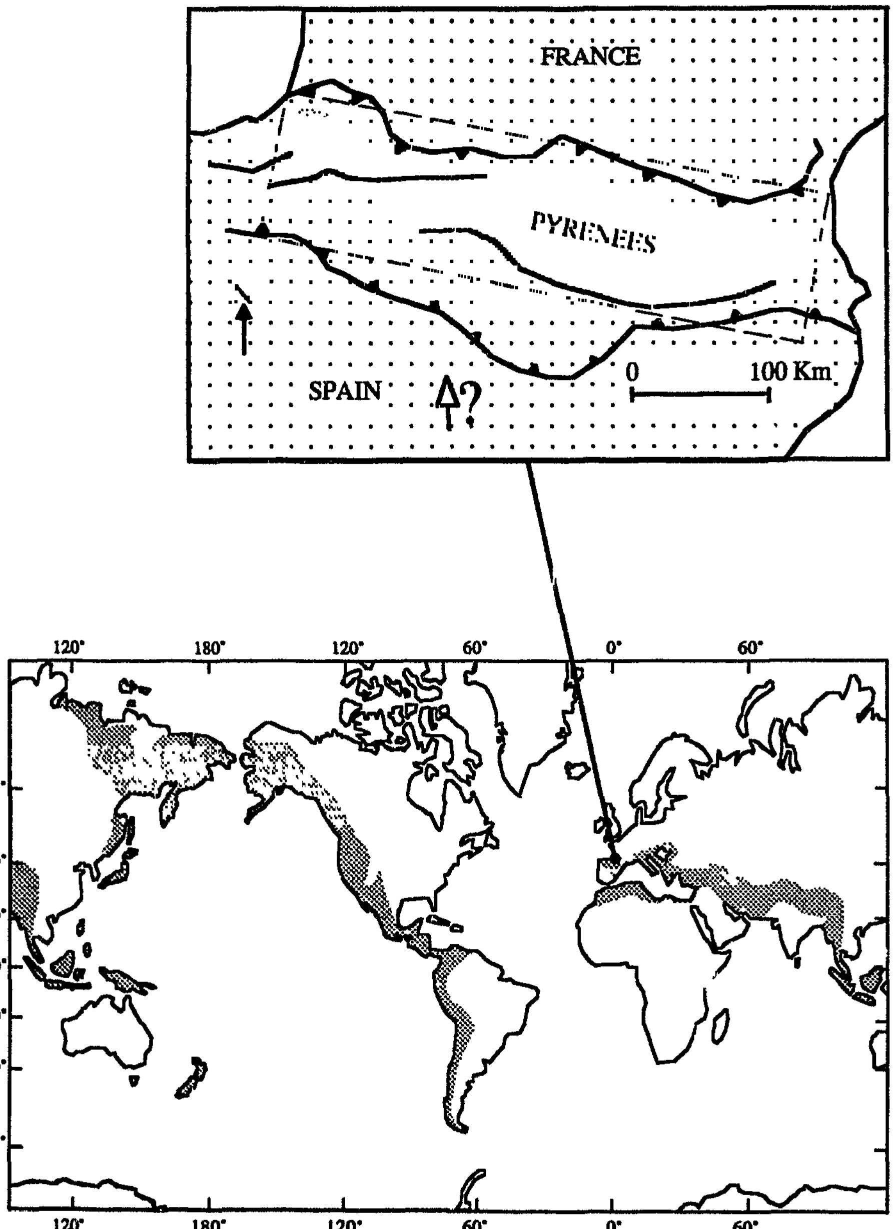

Figure 53(i)

(j) Taiwan

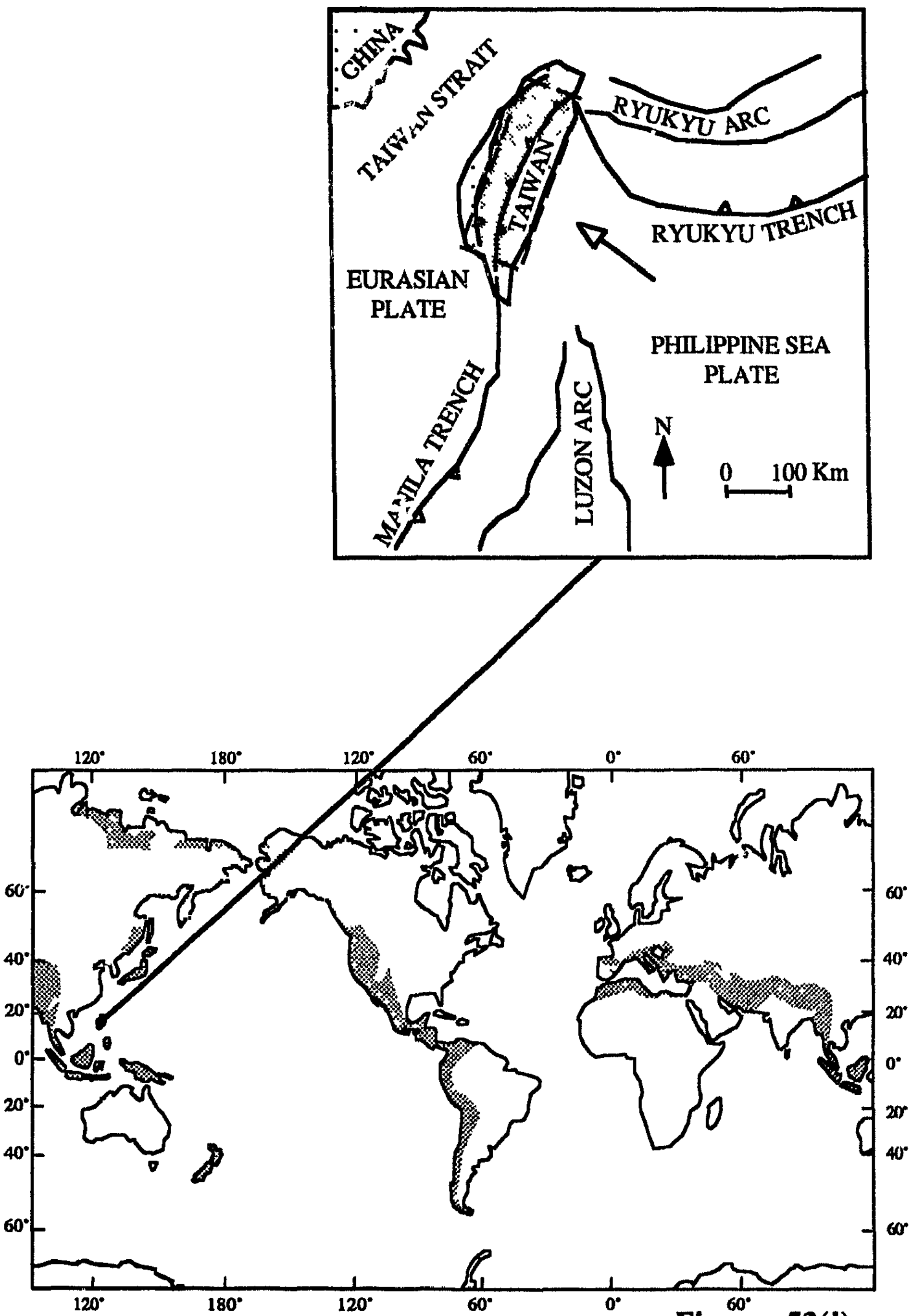

Figure 53(j)

(k) San Andreas Fault

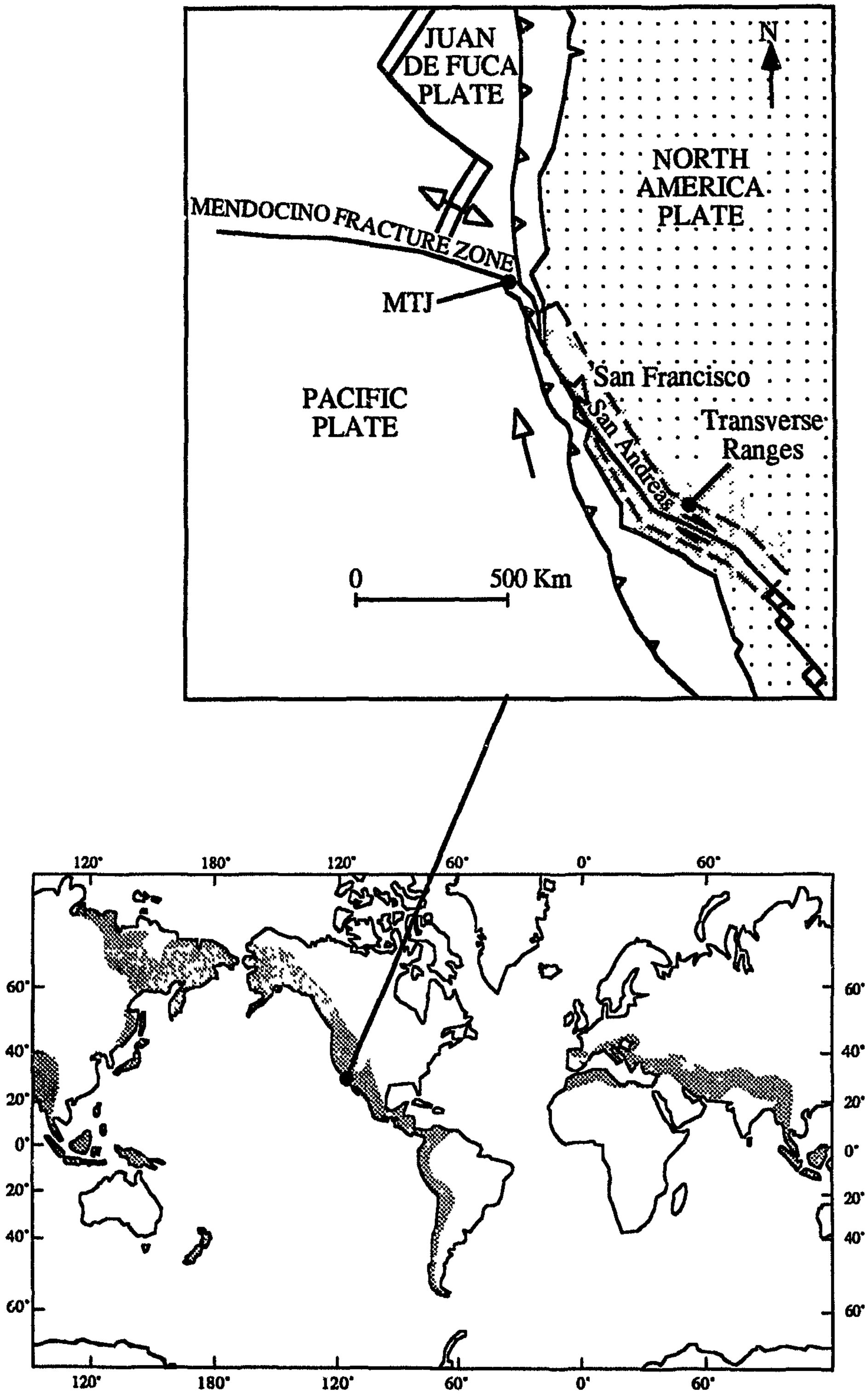

Figure 53(k)

(l) Zagros

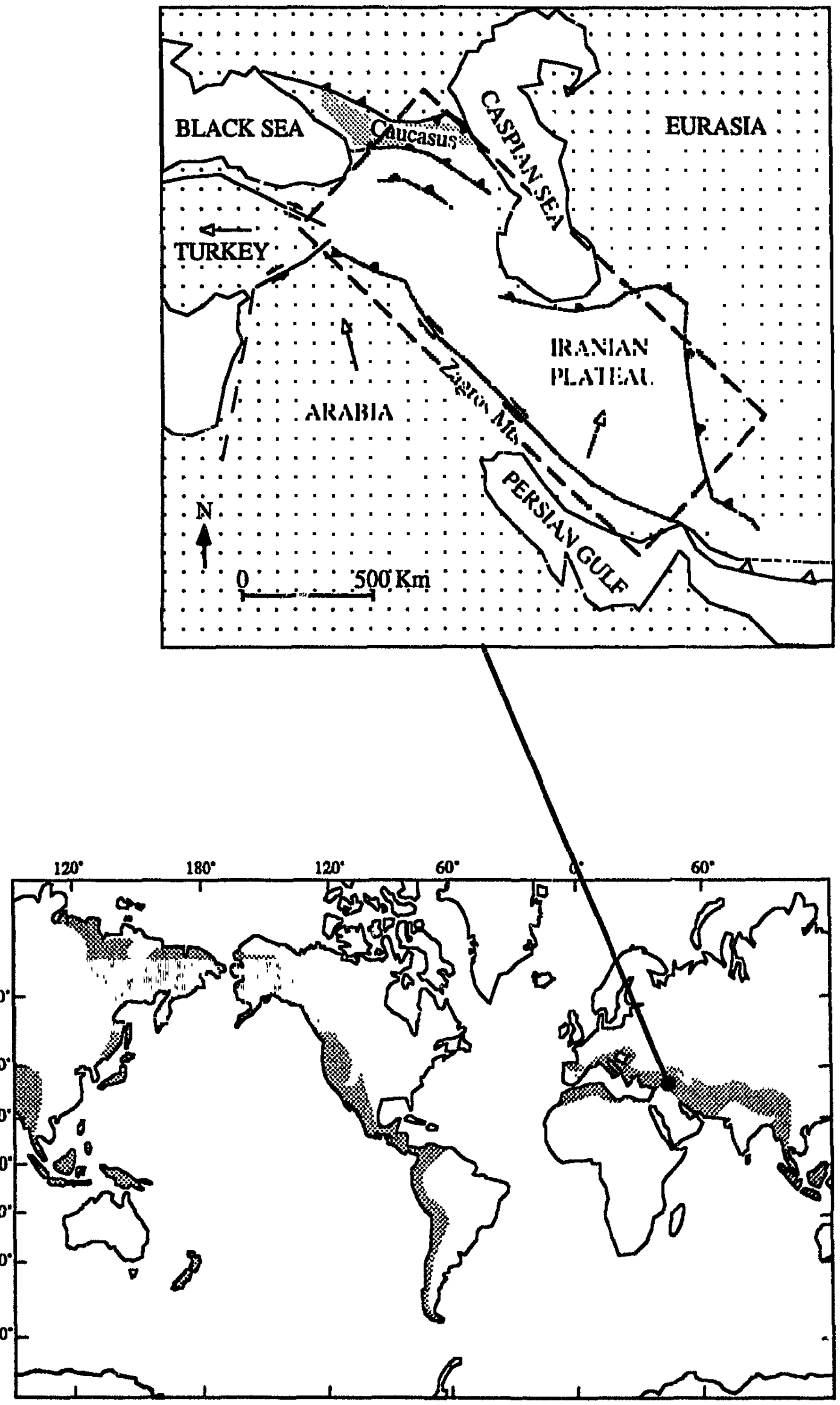

Figure 53(l)

Figure 54: Summary of the plate boundary settings for (a) Early Proterozoic amalgamation of Laurentia, showing New Quebec, Thelon, Torngat, and Trans-Hudson orogens, and the Great Slave Lake shear zone (GSLsz) (simplified from Hoffman, 1989); (b) Mid-Proterozoic proto-Gondwana, showing Albany-Fraser, Kibaran, and Capricorn orogens (simplified from Unrug, 1992); (c) Late Proterozoic Gondwana, showing Damaran, Paterson, and Brasilian orogens, and Najd shear zone (simplified from Unrug, 1992); and (d) Pangea, showing Alleghanian, Uralian, and Variscan orogens (redrawn from Ziegler, 1993). Solid sawteeth indicate continental thrusts. Present-day land positions indicated by dotted pattern; other contemporaneous orogens (not used in this study) shaded light grey, studied orogens shaded dark grey. Aspect ratio measurements are shown by the dashed boxes. Names of cratons mentioned in Appendix F shown by outlined boxes. Question marks are placed wherever reconstructions are very uncertain. In figure 54(a), the overprinting of Early Proterozoic orogens by later events is shown by including names of later orogenic events in brackets.

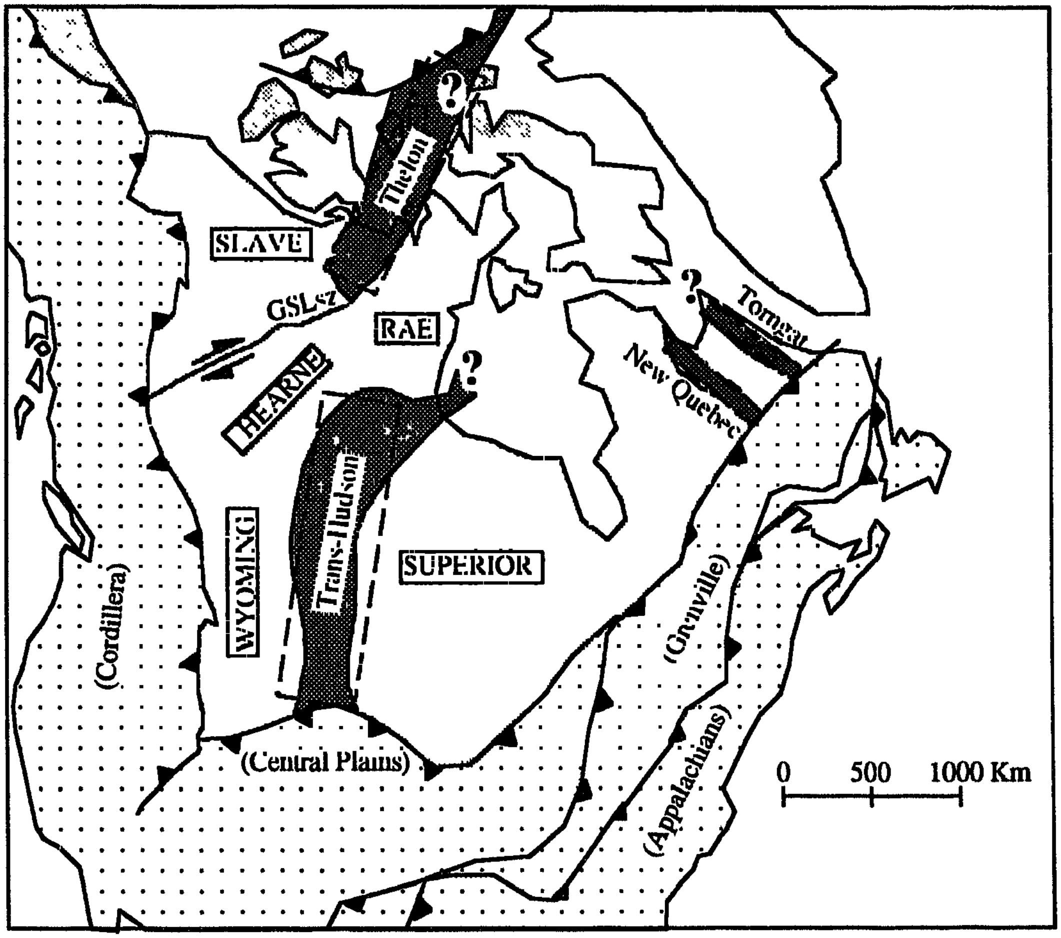

(a) PROTEROZOIC OROGENS OF NORTH AMERICA

Figure 54(a)

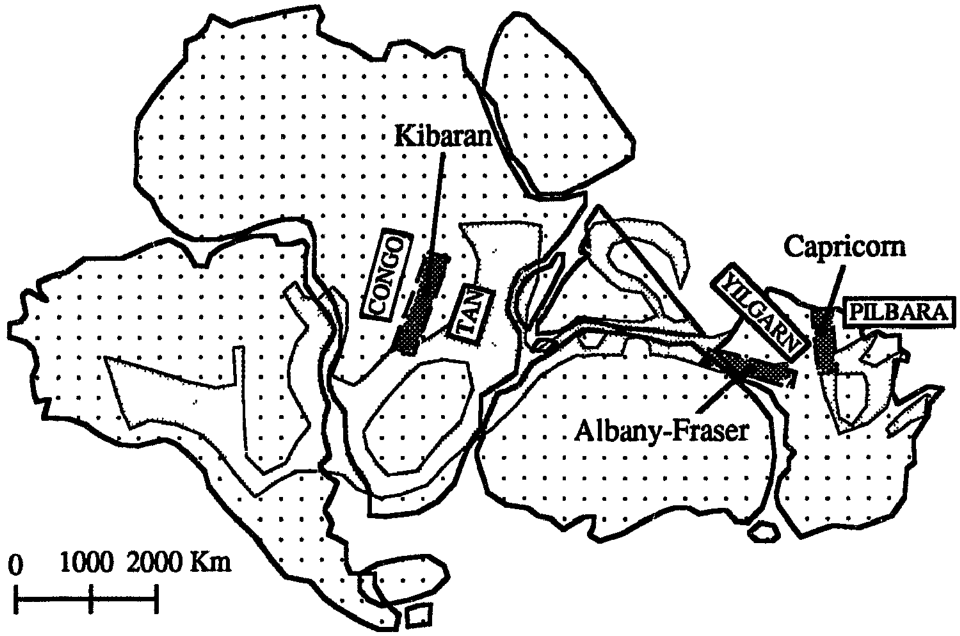

(b) GONDWANA - MID-PROTEROZOIC (1700-900 MA)

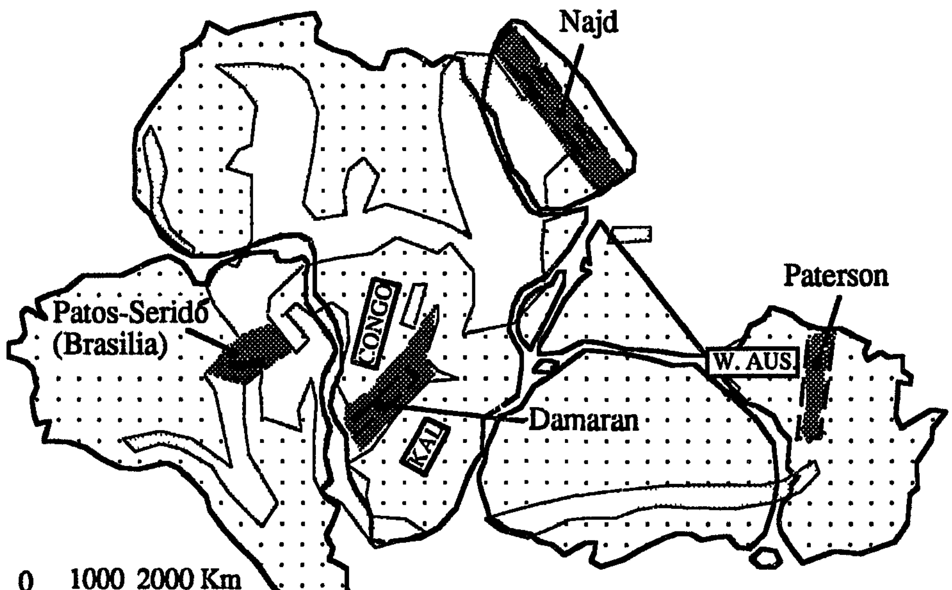

(c) GONDWANA - LATE-PROTEROZOIC (900-600 MA)

Figure 54(b,c)

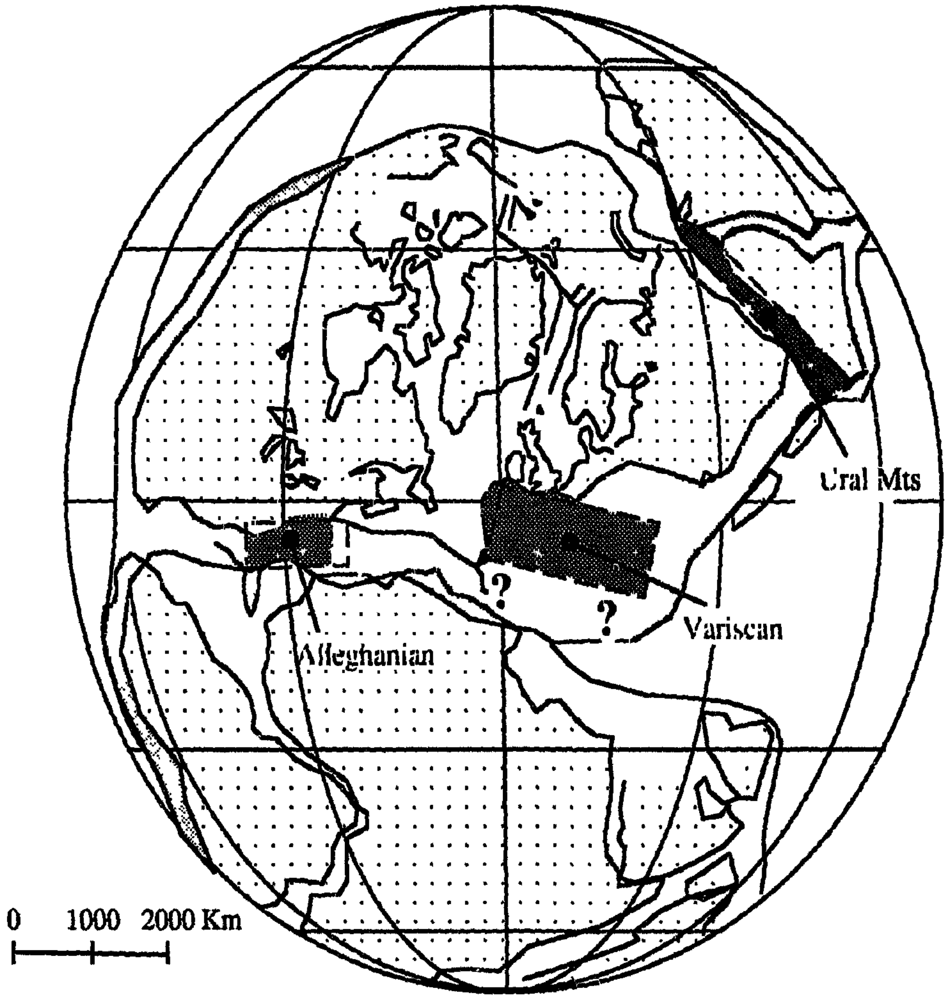

(d) PANGEA 310 MA

Figure 54(d)

In order to conduct the tests specified in Table 8, it is necessary to assume an average power-law exponent for the stress-strain rate relationship in the crust or lithosphere. I make the assumption that the average power-law exponent is 3 for the deforming layer (i.e. n=3 for the crust, if deformation is driven by detachment of underlying mantle lithosphere, or for the lithosphere, if deformation is driven by indentation from the side). This is in rough agreement with the ductile behaviour of wet feldspar (see chapter 3). A more general analysis could be undertaken for a complete range of possible values for the power-law exponent, but would prevent the tests from being useful, as any data point could then be fitted by an appropriate choice for n. Note that the use of n=3 is in agreement with previous comparisons between aspect ratios and the side-driven thin sheet predictions (e.g. England and Molnar, 1991, and England and Jackson, 1989). In these cases, a best-fit value of ~3 was interpreted to represent the average power-law exponent for the entire lithosphere, implying that olivine or wet feldspar (with viscous creep power-law exponents of ~3) would be appropriate controlling mineral phases for the lithosphere.

The assumption that n=3 for the crust or lithosphere also allows the use of velocity, horizontal strain-rate, and thickening rate length-scales interchangably when estimating the across-strike extent of crustal deformation. (The equivalence between velocity and thickening rate length-scales for n>1 was demonstrated in chapter four). These length-scale measures are therefore not distinguished in chapter five. Most of the length-scale estimates of normal deformation for orogens are based on thickening length-scales, whereas transcurrent length-scale estimates are made using geodetic results, focal mechanisms, and the extent of strike-slip faults.

Previous Geological Applications of Length-scale Analyses

Scale analysis results from the side-driven thin sheet models have already been compared to several geological examples of normal, strike-slip and extensional settings (for a summary, see England and Jackson 1989). For small normalized convergence and selected examples, a good fit is observed between model length-scales of strain and rotation rates, and observed deformation. Examples from Southern California, the Aegean, and Tibet, have been fitted by using a viscous rheology with a power-law exponent of 3 (England and Houseman, 1986; Sonder et al., 1986; England et al., 1985). England and Jackson (1989) also argue that the ratio between length-scales of purely normal vs. strike-slip deformation qualitatively agree with the predicted side-driven ratio of 4. However, there are no comprehensive quantitative demonstrations of the 4:1 ratio, so that it is unclear whether these results could be equally well fitted by assumptions of basally-driven deformation.

Strain partitioning phenomena, during oblique convergence, and the associated difference in normal vs. transverse deformation length-scales, were first noted by Fitch (1972), who gave a simple force analysis to explain why strike-slip movement will likely partition itself from thrust movement at oblique subduction zones. Other cases of partitioning and length-scale differences at oblique subduction zones have been documented by Walcott (1978) and Beck (1983), who argued that partitioning followed the principle of minimum energy dissipation. McKenzie and Jackson (1983) used a kinematic argument to explain strain partitioning in terms of finite deformation, and McCaffrey (1992) showed that the minimum energy argument of Beck (1983) could be generalized to a force balance analysis. Using a strain model of transpression, Tikoff and Teyssier (1994) investigated displacement-field partitioning. Braun and Beaumont (submitted) used a three-dimensional numerical model to predict strain partitioning and length-scale differences for cases where the incident plate boundary velocity is significantly oblique. In all these analyses, differences between normal and transverse deformation length-scales were predicted for cases where the incident transverse velocity component is significantly greater than the normal velocity component. In contrast, the results from the basally-driven thin sheet study (chapter four) predict differences in normal and transverse length-scales to be more likely when the strike-slip velocity is much less than the normally incident velocity (figure 31). Test four will attempt to discriminate which of the model predictions best fits observed length-scales of deformation at obliquely convergent plate boundaries.

§ 5.2 Selection Criteria for Scale Analyses

Aspect ratios from a wide selection of currently active, as well as ancient, orogens, are used to test the side and basally-driven predictions. Selection criteria for these examples are either based on knowledge of the orogen dimensions and thickening style, or on the limitations of the models. In this section I outline in a point-wise fashion, and then review in detail, a number of the primary restrictions which determine the selection criteria that are used.

Selection Criteria

The following is a summary of the criteria that must be met for an orogen to be included in the aspect ratio list:

(i) Across-strike length-scales of deformation which are comparable in scale to the crustal thickness (i.e. $\lambda \leq 3\ S_0$) are included, but cannot be directly compared to model predictions;

(ii) Deformation and thickening cannot be primarily due to magmatic intrusions;

(iii) Deformation and thickening cannot be a result of accretion by numerous micro-terranes which cannot be distinguished individually, although subsequent deformation of the accreted mass by a coherent collision event is testable;

(iv) Deformation due to convergence cannot be dominated by extensional features (e.g. retreating subduction boundaries);

(v) Plate reconstructions must be well-constrained; if orogen components have become widely scattered by subsequent dispersion of terranes, they must be traceable by: (a) inversion of sea-floor spreading (last 180 Ma), or (b) significant paleobiogeographic and paleoclimatic proof of correlations (Proterozoic and Archean examples). If fragmentation has affected only a part of the along-strike extent of the orogen, a minimum estimate for D may be used as a lower bound;

(vi) Post-collisional along-strike displacements must be well-constrained and allow palinspastic restoration of orogen dimensions;

(vii) The deformation must not be significantly overprinted by subsequent deformation events;

(viii) Orogens which have experienced significant normalized convergence may be included in the list, but their deformation length-scales should be regarded as maximum length-scales only, because of the effect of gravity acting on crustal thickness contrasts.

Discussion of Selection Criteria

Because the predictions are based on models which use the thin-sheet approximation with local isostatic compensation, orogens with observed deformation length-scales λ_{NO} and λ_{TO} of less than approximately 3 times the crustal thickness (for 5% error) cannot be directly compared to the models (restriction (i)). This precludes direct comparisons with data from the New Zealand oblique continental collision, for instance, because deformation in this case is concentrated along the Alpine Fault (Norris et al., 1990). Similarly, the arc-continent collision in Taiwan is too narrow to be compared to model predictions. Despite this restriction, I have included narrow orogens in the selection in order to indicate the trends in the data.

The type of convergent boundary may restrict the choice of orogens for the aspect ratio test. The examples are drawn primarily from cases of continent-continent collision, but some island-arc/ continent collision cases are also used, provided it can be shown that deformation is mostly a result of thickening due to the collision, rather than originating from island-arc magmatism (restriction (ii)), or the accretion of numerous small, thin terranes (restriction (iii)). This last restriction does not exclude cases where minor deformation due to accretion of small terranes has preceded the main, discrete collisional event. Examples with oceanic-continental convergence, such as the Neogene Andes, may also be included in the aspect ratio list, provided continental deformation in these cases can be related to the advancing subduction of oceanic lithosphere (restriction (iv)).

The aspect ratios for Mesozoic and Cenozoic orogens can often be determined by plate reconstructions based on sea-floor magnetic anomaly patterns, even when the orogen has become fragmented subsequent to the deformation event. However, plate reconstructions for orogens older than ~200 Ma, where no constraints are available from magnetic anomaly patterns, are often poorly determined in comparison to the more recent examples (restriction (v)). For example, suggested plate configurations which locate the Grenvillian orogen as a suture between the continents of Laurentia and Baltica are still conjectural (Hoffman, 1991, Condie and Rosen, 1994). Parts of the Grenvillian lithosphere have become widely distributed on different continents due to the subsequent break-up of the supercontinent in the Palaeozoic, and so the extent and sequence of orogenic events is poorly known.

Large, unquantifiable strike-slip movement of terranes along an orogenic belt may also present difficulties, especially if such movements make the estimation of across-strike deformation length-scales dubious (restriction (vi)). An example is the Cordillera of western North America, for which paleomagnetic data indicate relative along-strike movements of many hundreds of kilometres for principal terranes (Oldow et al., 1989), whereas geological evidence suggests little relative strike-slip movement (see Cowan, 1994 for a summary of this debate) . The Cordillera also illustrate another problem, the overprinting of an orogen by subsequent deformation events (restriction (vii)). A cratonic suture is quite likely to be the site of more than one episode of deformation, due to inherited weaknesses. Many ancient orogenic events are therefore overprinted by more recent deformation cycles.

Preservation potential may introduce a bias into the dimensions of selected examples. Orogens which have undergone large amounts of convergence (i.e. $t' >> 10$) are well-represented in the aspect ratio list, due to their greater chance of preservation than smaller-scale examples with time. The tests in this section ignore the growth in deformation length-scales with increased convergence. Therefore, the observed length-scales for these cases should be regarded as maximum length-scales (restriction viii).

Using the criteria discussed above, a list of plate boundary examples has been assembled in Appendix F, with their relevant dimensions summarized in Tables 9 to 12. The list is by no means an exhaustive survey of orogenic belts and strike-slip faults, but includes cases from the three recognised super-continent cycles, as well as a large assortment of modern-day examples. The geographic locations, as mentioned previously, are illustrated in figures 53 and 54.

Table 9: Length-Scales for Normal Deformation

Orogen	Primary References	D	λ_{NO}	Total Convergence[8]; Maximum Crustal Thickness[9]
Albany-Fraser Orogen (Australia)	Myers, 1990	>1500 km	250±50 km	significant; significant
Alleghanian Orogen (eastern N. America)	Ziegler, 1988 LeFort, 1989	1600±300 km	950±350 km	~ 400±200 km; significant
E., W., and S. Alps (Europe)	Royden, 1993a	600±100 km	150±50 km	300±200 km; 50±20 km
Andes (western S. America)	Dewey & Lamb, 1992 Isacks, 1988 Jordan et al., 1983 Wdowinski et al., 1989	4500±500 km	600±200 km	250±100 km; 60±10 km
Banda Arc (Indonesia)	Johnston and Bowin, 1981	1500±200 km	150±50 km	150±50 km; 35±5 km
Capricorn Orogen (Australia)	Myers, 1990 Tyler and Thorne, 1990	>1100 km	280±50 km	significant; significant

Damaran Orogen (Africa)	Kukla and Stanistreet, 1991	800±200 km	120±50 km	100±30 km; 50±20 km
Kibaran Orogen (Africa)	Pohl, 1987	1500±300 km	300±50 km	unknown; unknown
Lebanon Mts (Middle East)	Walley, 1988 Salel and Séguret, 1994	150±30 km	80±30 km	small; 30±5 km
Makran Fold Belt (Iran, Pakistan)	Lawrence et al., 1981	900±100 km	300±100 km	100-200 km; small
New Guinea	Smith, 1990 McCaffrey and Abers, 1991	1500±200 km	200±50 km	60±20 km; 55±10 km
New Quebec (N. America)	Van Kranendonk et al., 1993	> 800 km	100±30 km	small; small
New Zealand	Walcott, 1984 Kamp, 1986	500±100 km	50±20 km	50±10 km; 35±5 km
Paterson Orogen (Australia)	Myers, 1990	1300±300 km	250±100 km	significant; significant
Pyrenees (Europe)	Muñoz, 1992	400±100 km	120±20 km	125±25 km; 50±10 km

Taiwan (Asia)	Suppe, 1987 Lu and Malavieille, 1994	200±50 km	100±50 km	150±50 km; 40±5 km
Thelon Orogen (NWT, N. America)	Hoffman, 1988, 1989	>1500 km	300±100 km	significant; significant
Tibetan Plateau (Eurasia)	England & Houseman, 1986 Many others	3000±500 km	2200±500 km	2000±500 km; 70±10 km
Torngat Orogen (Labrador, N. America)	Van Kranendonk et al., 1993; Mengel and Rivers 1991; Hoffman, 1988	>600 km	100±30 km	small; small
Trans- Hudson Orogen (N. America)	Hoffman, 1988, 1989	>1500 km	400±100 km	significant; significant
Urals (Eurasia)	Dymkin & Puchkov, 1984	2500±500 km	300±100 km	significant; >55 km
Variscan Orogen (Eurasia)	Ziegler, 1988	2000±500 km	1000±500 km	~ 400±200 km; significant
Zagros (Iran)	Hempton, 1987 England & Jackson, 1989	1900±200 km	1000±200 km	500±100 km; 50±5 km

Zhob Convergent Zone (Sulaiman Fold Belt) (Pakistan)	Lawrence et al., 1981	220±50 km	220±50 km	10-50 km; small

[8]"small" = less than 100 km; "significant" ≈ 300 km

[9]"small" = less than 1.5 S_0; "significant" > 1.5 S_0

Table 10: Length-Scales for Transcurrent Deformation

Strike-slip area	**Primary References**	**D**	λ_{TO}	**Amount of displacement; approximate r value**[10]
E. Anatolian Fault (Turkey)	Kiratzi, 1993 Jackson & McKenzie, 1984 Westaway, 1994	500±50 km	30±20 km	30-100 km; $r \sim 0.13$
N. Anatolian Fault (Turkey)	Kiratzi, 1993 Jackson & McKenzie, 1984 Westaway, 1994	1000±100 km	30±20 km	30-100 km; $r \sim 0$
Chaman Fault Zone (Pakistan)	Lawrence et al., 1981 Kazmi, 1979	800±100 km	120±80 km	> 200 km; $r \sim 0$

Great Slave Lake Shear Zone (N. Canada)	Hoffman, 1987	1300±200 km	80±40 km	300-700 km; r ~ 0 - 0.3
Levant Fault (Dead Sea Transform) (Middle East)	Garfunkel, 1981 Garfunkel et al., 1981 Westaway, 1994	1000±100 km	20±10 km	>105 km; r ~ 0
Najd Shear Zone (Arabia)	Sultan et al., 1988 Stern, 1985	2000±500 km	300±100 km	240-300 km; r > 0.5? Extensional
New Zealand Alpine Fault	Walcott, 1984 Kamp, 1986 Braun and Beaumont, submitted	500±100 km	50±20 km	> 480 km; r ~ 0.10
San Andreas (western N. America)	Sonder et al., 1986 Furlong and Hugo, 1989 Walcott, 1993 Wallace, 1990	1200±100 km	100±50 km	850 km; r ~ 0.18
Taiwan (Asia)	Suppe, 1987 Lu and Malavieille, 1994	200±50 km	50±20 km	360±50 km; r ~ 0.5

[10]r-value indicates obliquity of convergence, $r = u_0/(u_0+v_0)$

Table 11: Length-Scales for Normal/Transcurrent Deformation

Convergent / Strike-slip area	**Primary References**	D_N D_T	λ_{NO} λ_{TO}	r_N r_T
Lebanon Mts/ Levant Fault (Middle East)	Walley, 1988 Salel and Séguret, 1994	D_N = 150±30 km; D_T = 1000±100 km	λ_{NO} = 80±30 km; λ_{TO} = 20±10 km	$r_N \sim 0.3$ $r_T \sim 0$
Makran Convergent Zone / Chaman Fault Zone (Iran, Pakistan)	Lawrence et al., 1981 Kazmi, 1979	D_N = 900±100 km; D_T = 800±100 km	λ_{NO} = 300±100 km; λ_{TO} = 120±80 km	$r_N \sim 0.8$-0.9 $r_T \sim 0$
Patos-Seridó System (S. America)	Corsini et al., 1991	D_N > 300 km; D_T = 400±100 km	λ_{NO} = 100±50 km; λ_{TO} = 30±10 km	$r_N \sim 0.8$ $r_T \sim 0$
Zhob Convergent Zone / Chaman Fault Zone (Sulaiman Fold Belt) (Pakistan)	Lawrence et al., 1981 Kazmi, 1979	D_N = 220±50 km; D_T = 800±100 km	λ_{NO} = 220±50 km; λ_{TO} = 120±80 km	$r_N \sim 0.9$ $r_T \sim 0$

Table 12: Length-Scales for Oblique Deformation

Transpress-ive Area	**Primary References**	**D**	λ_{NO} λ_{TO}	**Obliquity, r**
E. Anatolian Fault (Turkey)	Kiratzi, 1993 Jackson & McKenzie, 1984 Westaway, 1994	500±50 km	λ_{NO} = 50±20 km; λ_{TO} = 30±20 km	r ~ 0.13
Levant: Lebanon Bend (Middle East)	Walley, 1988 Salel and Séguret, 1994	150±30 km	λ_{NO} = 80±30 km; λ_{TO} = 50±30 km	r ~ 0.3
New Zealand Alpine Fault	Walcott, 1984 Kamp, 1986 Braun and Beaumont, submitted	500±100 km	λ_{NO} = 50±20 km; λ_{TO} = 50±20 km	r ~ 0.10
San Andreas (N. America)	Sonder et al., 1986 Furlong and Hugo, 1989 Walcott, 1993 Wallace, 1990	1200±100 km	λ_{NO} = 200±50 km; λ_{TO} = 100±50 km	r ~ 0.18
Taiwan (Asia)	Suppe, 1987 Lu and Malavielle, 1994	200±50 km	λ_{NO} = 100±50 km; λ_{TO} = 50±20 km	r ~ 0.5

Measurement of Length-Scales and Convergence

Throughout the selection process and accompanying tests, it is assumed that on a large enough scale the lithosphere can be treated as a continuum. Therefore, the observed normal and transcurrent deformation length-scales (λ_{NO} and λ_{TO}) are determined from regional deformation patterns rather than individual faults and structures. The extent of deformation is estimated from the presence of structural features such as shear zones and faults, combined with the history of uplift and displacement of a region, when available. An effort is made to distinguish crustal-scale deformation features from thin-skinned tectonics (e.g. detachment and folding of a thin surface layer along a weak decollement). Geodetic measurements are used to check estimates, but in general there are not enough data, over a sufficient time period, to base length-scale estimates on these techniques. Uncertainty estimates for deformation length-scales are based on the individual circumstances of each case; in general, the magnitude of uncertainty increases with age of the deformation event.

The along-strike extent of each plate boundary regime, D, must also be measured. In present-day examples, it is relatively easy to determine D by examining the variation of relative plate motion vectors along a plate boundary (e.g. DeMets et al., 1990). For cases from previous super-continent cycles, estimates for D are less certain, and may be a minimum if a part of the along-strike boundary has been removed by subsequent deformational events. Where this is suspected, the error bound on D is taken as a positive interval of 300 km.

Many orogens are deformed on plate boundaries which have some curvature (e.g. the Andes, the European Alps, etc.). In these cases, across-strike length-scales are estimated from the plate boundary at various positions along-strike, and the average value is used. Along-strike length-scale D is measured taking the curvature into account, but uncertainty estimates for D are increased correspondingly.

The total thickening and convergence may have an important influence on the interpretation of test results. Chapter four results indicated that deformation length-scales for convergent orogens may increase with normalized time, due to the effect of gravity on crustal thickness contrasts, represented in the models by the Argand number. Although mass may be lost from the system due to erosion and along-strike transport, estimates of convergence are quoted as a first-order indication of how important Ar is in determining the resultant deformation length-scale. A more accurate measure would be the total added mass to the deformed region; however, this quantity is not well constrained, especially for ancient orogens, and relies on conjectured modes of thickening, whereas convergence estimates may often be estimated independently using plate reconstructions. Where amounts of convergence and crustal thickening are not known, estimates are made ('small convergence' 0-100 km; 'significant convergence' 100-500 km, 'large convergence' >500 km; 'small thickening' $S <\sim 1.5S_0$), based on plate reconstructions.

An important factor in determining deformation length-scales is the degree of obliquity of convergence, measured by r, where $r = (u_0/u_0+v_0)$, and u_0, v_0 are the components of normal and transverse velocity at the plate boundary. Table 9 summarizes length-scales for orogens from Appendix F which have undergone primarily normally convergent thickening (i.e. $r \geq 0.5$), which are used in test one. Aspect ratios for transcurrent shear zones (Table 10), which have undergone predominantly strike-slip motion (i.e. $r \leq 0.5$), are used in test two.

The third test requires estimates of the length-scales of predominantly strike-slip and predominantly convergent boundaries, which must be closely related so that the degree of basal coupling for the two cases can be assumed to be similar (i.e. it can be assumed that Am does not vary significantly). This requirement may be attained by cases which have regions with mainly normal convergence, and adjoining regions which are predominantly strike-slip. For example, the Chaman Fault has strike-slip boundary conditions for most of its length, but has a ~ 90° jog at the Zhob convergent zone (also known as the Sulaiman fold belt) in Pakistan. The strike-slip boundary length D is measured for the whole length of the Chaman fault, because the scale of the jog is small. It is assumed that the coupling between crust and mantle lithosphere is similar in the convergent and adjoining strike-slip regions. Table 11 summarizes the dimensions for this case, and some similar examples from other settings where a change in the relative velocity of convergence occurs without a significant change in lithosphere rheology.

Table 12 describes the dimensions for transpressive examples which have significant obliquity (i.e. r is between 0.1 and 0.9) and may be used for test four. Uncertainty in determining the obliquity of convergence, r, is a result of poorly determined relative velocity components at a plate boundary, or due to a change in r along-strike for long plate boundaries (e.g. the South Island of New Zealand).

§ 5.3 Scale Analysis of Convergent Margins

Test One: Aspect Ratios for Normal Convergence

The length-scale estimates from Table 9 can be viewed in a plot of across-strike length-scale, λ_{NO}, vs. along-strike dimension, D (figure 55(a)-(d)). The shaded region of figure 55(a) indicates points which fall in the length-scale range for which the thin sheet is not valid. The solid line represents the predicted relationship for the side-driven case, using n=3, as predicted by Sonder et al. (1986). Uncertainty estimates λ_{NO} and D are shown as error bars in 55(a). For cases where the along-strike extent of D is believed to be a minimum (i.e. where overprinting or fragmentation are thought to have reduced D), error bars are only drawn on the positive side of the estimate for D, with an arbitrarily large uncertainty increment of 300 km. For clarity, error bars are not shown for the subsequent plots (55(b)-(d)).

Several features are evident from figure 55. Firstly, most of the data points plot below the line for the side-driven relation. The three points that do not are the Tibetan Plateau (HT), the Zhob convergent zone (ZH), and the Zagros/Iranian Plateau (ZA)

Figure 55: Width of deformation, λ_{NO}, where the 'O' represents 'observed', vs. along-strike length-scale, D, for normally incident velocities at a plate boundary. Data points are taken from Table 9. (a) Points shown with estimated error bars, and compared to the side-driven prediction (solid line) which is labelled λ_{NS}. The length-scale limit below which the thin sheet models cannot be compared to the data is shown by dotted pattern. (b) The same quantities, with circles representing the relative amount of convergence since thickening began. Note the general trend towards higher observed length-scale λ_{NO} with increasing normalized convergence. (c) and (d) key to the figure, showing names of the orogen represented by each data point. Shaded region indicates area of correspondence between plots. AF=Albany-Fraser Orogen, AL=Alleghanian Orogen, AN=Andes, AP=Alps, BA=Banda Arc, CA=Capricorn Orogen, DA=Damaran Orogen, HT=Himalayas-Tibetan Plateau, KI=Kibaran Orogen, LB=Lebanon Mts, MA=Makran Fold Belt, NG=New Guinea, NQ=New Quebec Orogen, NZ=New Zealand Southern Alps, PA=Paterson Orogen, PY=Pyrenees, TA=Taiwan, TH=Trans-Hudson Orogen, TL=Thelon Orogen, TO=Torngat Orogen, UR=Urals, VA=Variscan Orogen, ZA=Zagros, ZH=Zhob Convergent Zone.

Comparison between λ_{NO} and λ_{NS}
(a) error bars

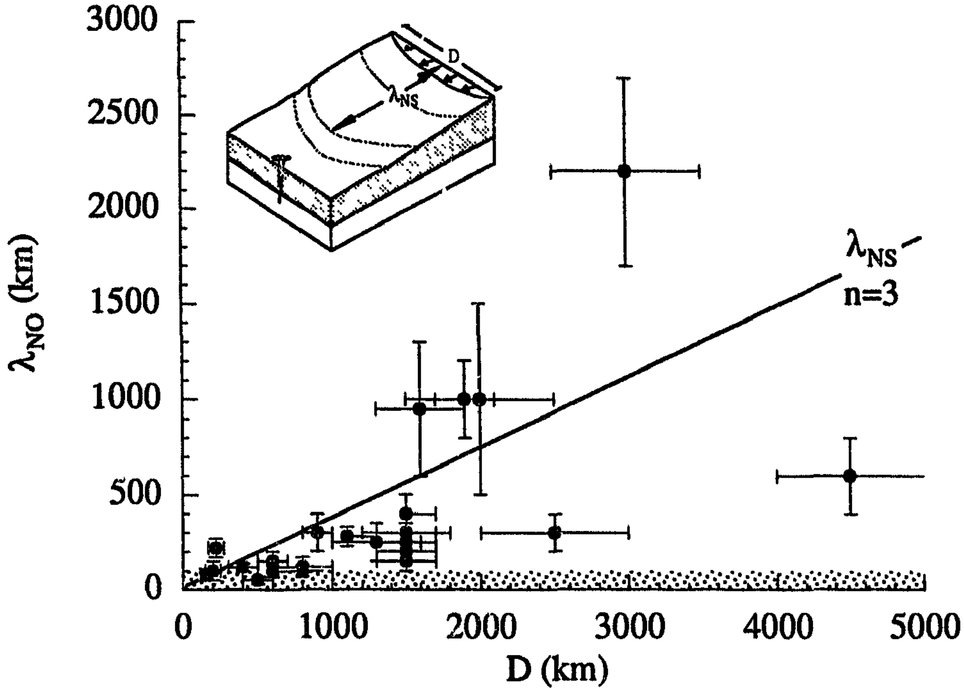

Comparison between λ_{NO} and λ_{NS}
(b) convergence estimates

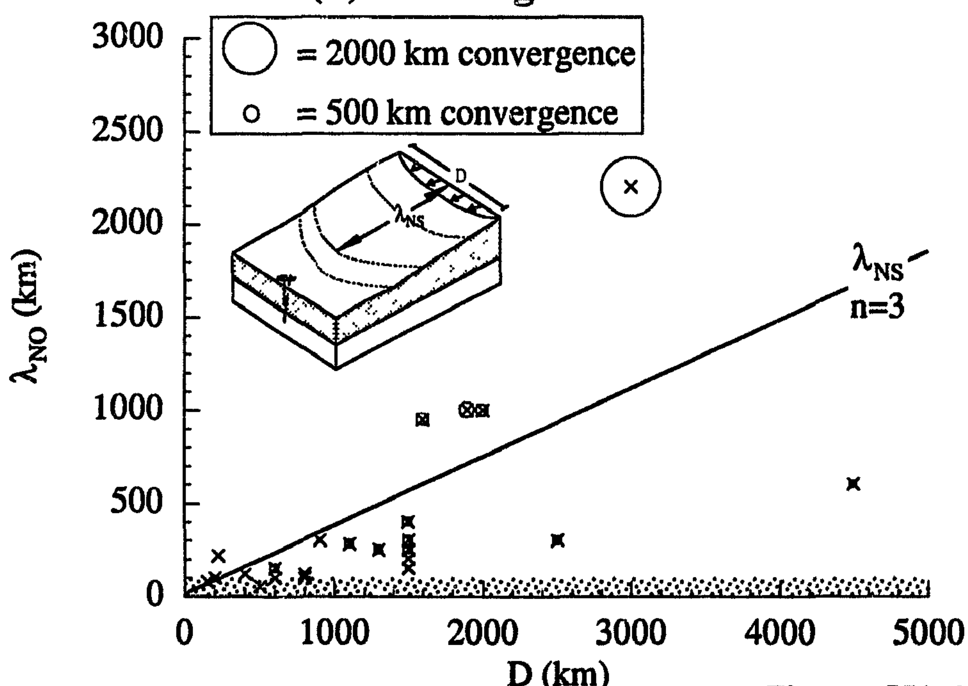

Figure 55(a,b)

Comparison between λ_{NO} and λ_{NS}
(c) key to data points, large scale

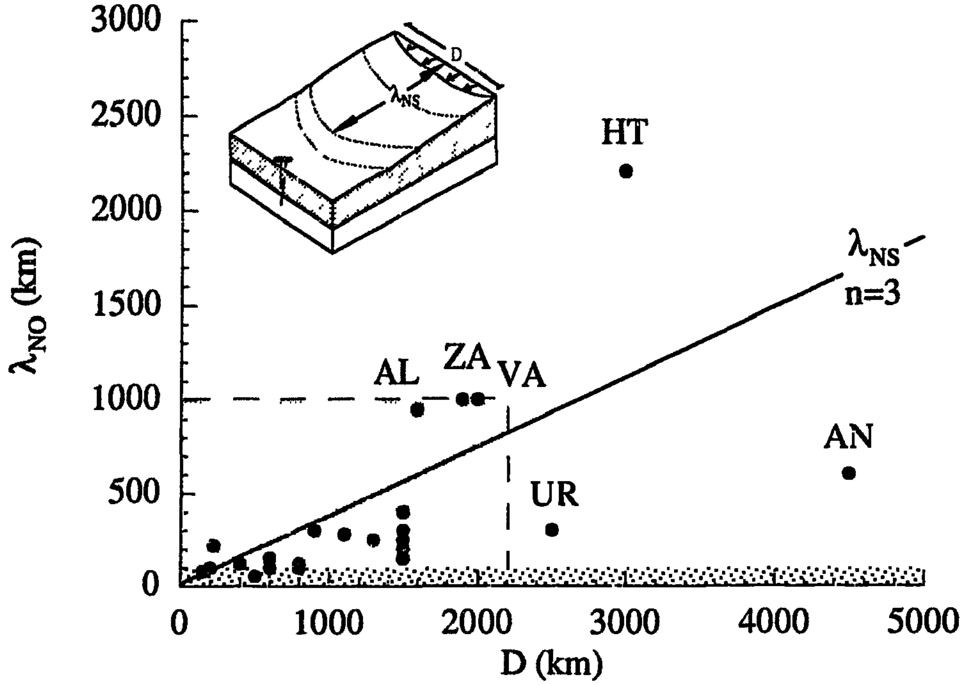

Comparison between λ_{NO} and λ_{NS}
(d) key to data points, small scale

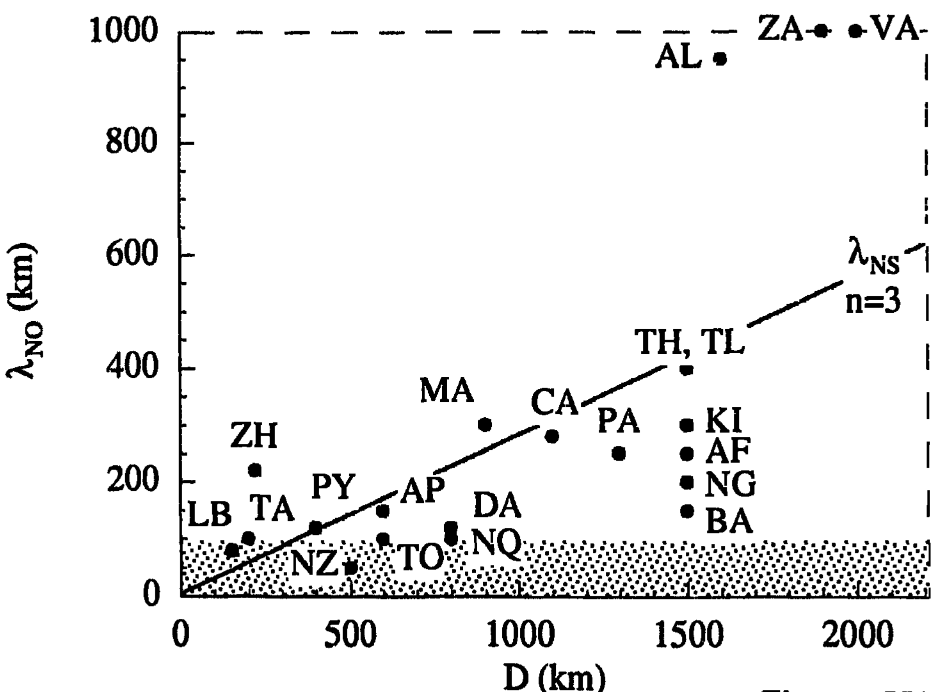

Figure 55(c,d)

(figure 55(c)). Apart from these points, the data seem to agree with the test one prediction made in Table 8; that is, orogen length-scales are less than or equal to the predicted indenter length-scale $\lambda_{NS} = 2D/\pi\sqrt{3}$. In agreement with the result illustrated in figure 52, length-scales may be considerably less than the side-driven prediction if coupling between the crust and underlying detached layer (as measured by Am) is significant, indicating that the orogen is wholly or partially basally-controlled. The aspect ratios for many of the points illustrated in figure 55 are well below the predicted side-driven aspect ratio (e.g. the Ural mountains and the Andes). I suggest that these orogens developed in a mechanical setting primarily controlled by basal fcrcing.

The solid line representing the side-driven length-scale prediction is for small convergence times, before significant thickening. The results from chapter four showed that for large normalized convergence times (t'), provided the effect of gravity acting on thickened regions is relatively large (as measured by the Argand number) and $n>1$, the across-strike length-scale will increase significantly. Some of the anomalous aspect ratios may result from this effect. In figure 55(b), the circles around the data points are proportional in size to the total amount of convergence in each case. For the Zagros/Iranian Plateau (convergence of 500±100 km), and especially for the Tibetan Plateau (convergence of 2000±500 km), the side-driven aspect ratio prediction is likely to be an underestimate, as the effects of gravity on the crustal thickening will increase the across-strike length-scale.

Figure 55(b) suggests a general trend for increasing across-strike length-scale with increased convergence. I investigate this further by plotting across-strike length-scale λ_{NO} vs. estimated convergence since the start of thickening (figure 56(a)-(c)). Figure 56(a) shows the orogen estimates with their associated uncertainties. The lower limit with which data may be compared to the thin-sheet model results is shaded. Figure 56(a) appears to show a relationship between increasing deformation length-scale and convergence, the implications of which are discussed in more detail in chapter six.

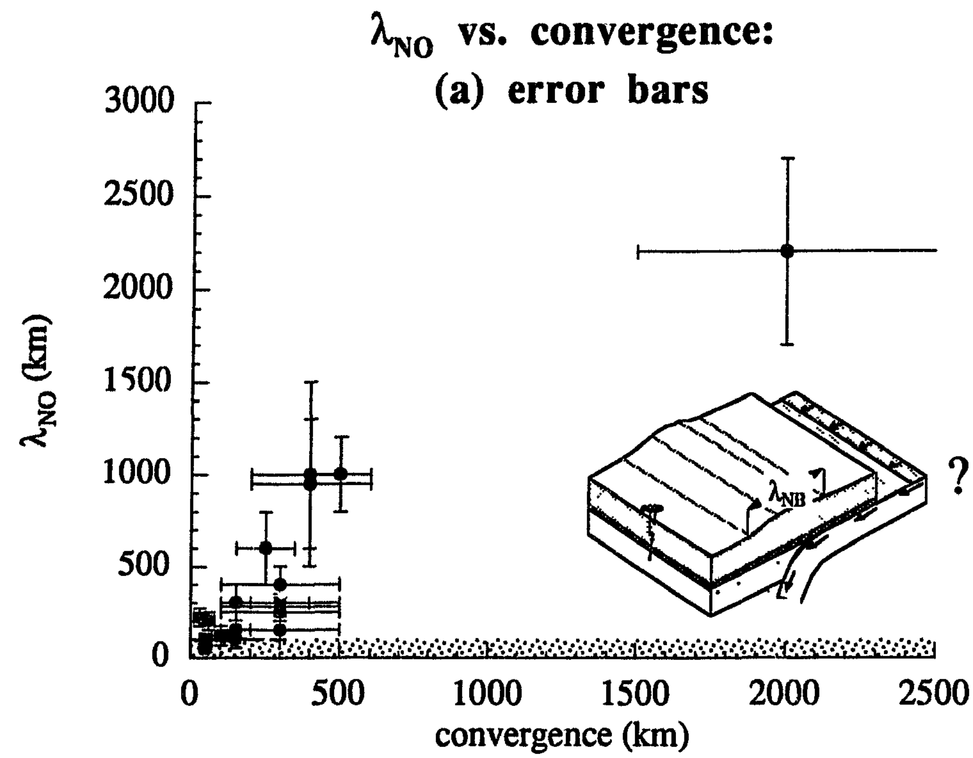

Figure 56(a)

Figure 56: Width of deformation, λ_{NO}, vs. amount of convergence in km. (a) Data points shown with error bars. Dotted pattern on portion of plot represents the lower limit which cannot be compared to model predictions. The inset schematic of basally-driven model is shown with a question-mark, indicating that this may be a possible explanation for the trend in the figure. (b) and (c) key to the figure. Letter symbols are the same as for figure 55.

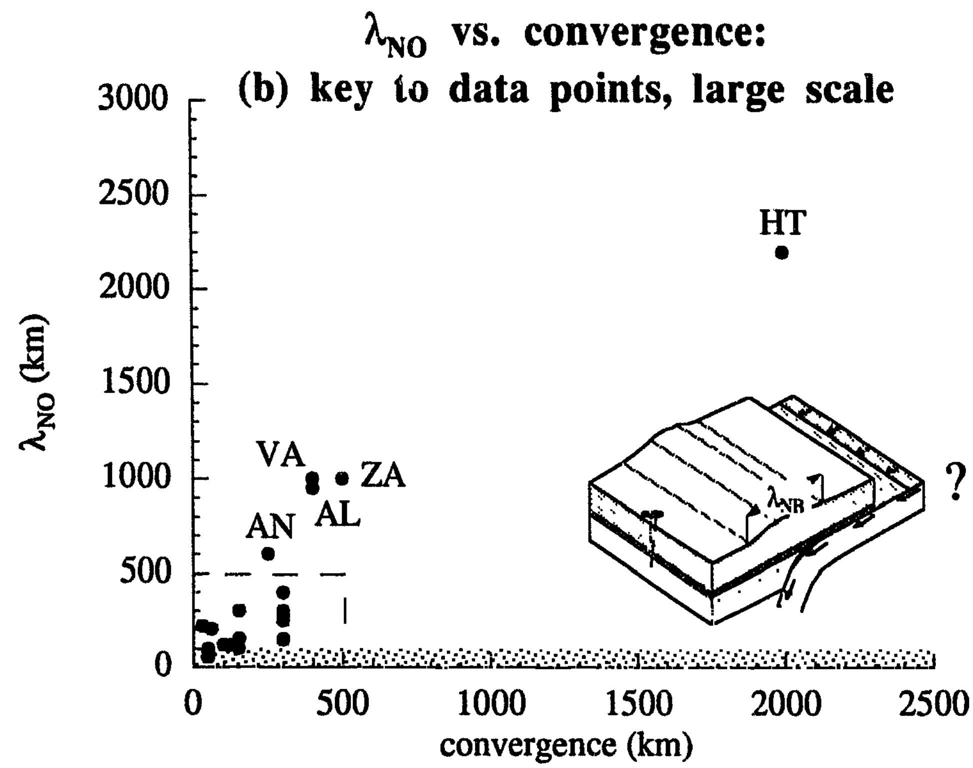

λ_{NO} vs. convergence:
(b) key to data points, large scale
λ_{NO} (km)
3000
2500
2000
1500
1000
500
0
HT
VA
ZA
AL
AN
?
λ_{NB}
0
500
1000
1500
2000
2500
convergence (km)

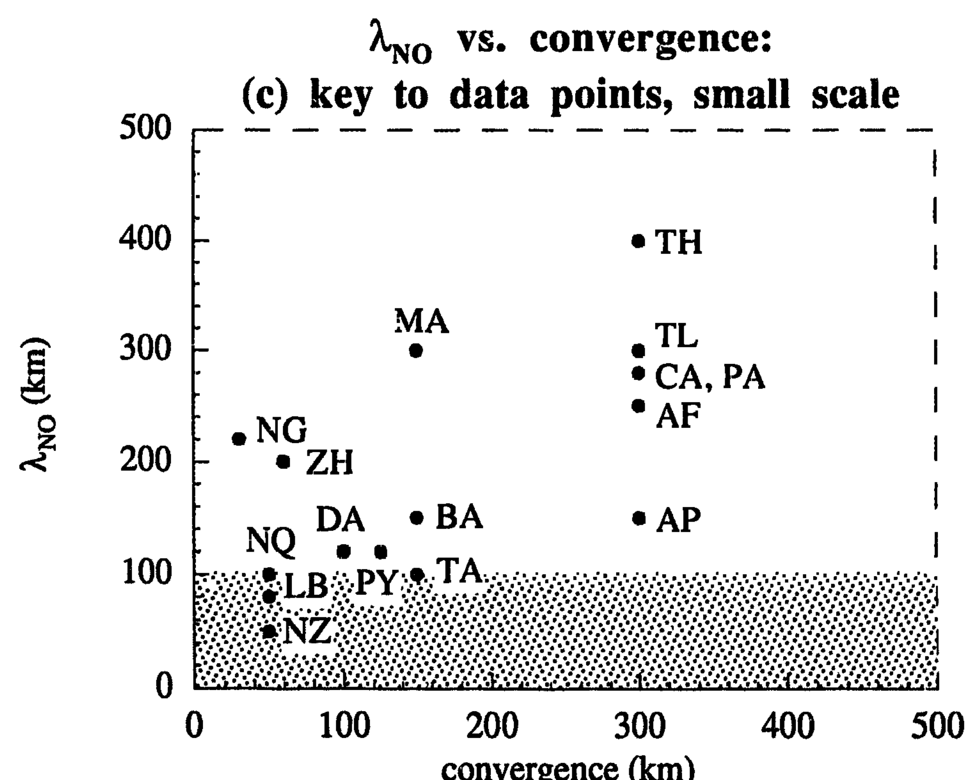

λ_{NO} vs. convergence:
(c) key to data points, small scale
λ_{NO} (km)
500
400
300
200
100
0
TH
MA
TL
CA, PA
AF
NG
ZH
DA
BA
AP
NQ
LB
PY
TA
NZ
0
100
200
300
400
500
convergence (km)

Figure 56(b,c)

Test Two: Aspect Ratios for Transcurrent Deformation

Where plate boundary kinematics are predominantly along-strike, the length-scale of transcurrent deformation, λ_{TO}, may be estimated on a regional scale by finding the width over which most of the shearing takes place (Table 10). A plot of aspect ratios for these examples (figure 57(a)-(c)) may be compared to the predicted side-driven relation of Sonder et al. (1986). Unfortunately, most of the length-scales are below the limit at which the thin sheet model approximations become valid (lack of validity is indicated by the shaded region, figure 57(a)), and so a direct comparison cannot be made. However, two elements should be noted from figure 57: (i) Apart from the uppermost point, the Najd Shear Zone, there does not appear to be a very systematic trend to the aspect ratios; and (ii) There is no obvious relationship between obliquity of convergence, as indicated by the circles around points in figure 57(b), and aspect ratios. In general, I conclude that the transcurrent shear zones do not show any systematic trends in length-scale λ_{TO} which may be used to infer a driving mechanism, and that many more examples will be needed to test these ideas further.

Figure 57: Width of deformation, λ_{TO}, where the 'O' represents 'observed', vs. along-strike length-scale, D, for transverse velocities at a plate boundary. Data points are taken from Table 10. (a) Points shown with estimated error bars, and compared to the side-driven prediction (solid line) which is labelled λ_{TS}. The length-scale limit below which the thin sheet models cannot be compared to the data is shaded. (b) The same quantities, with circles representing the obliqueness of collision, as measured by the ratio $r=u_0/(u_0+v_0)$. No general trend with r is evident from the data points. (c) key to the figure, showing names of the orogen represented by each data point. CH=Chaman Fault Zone, EA=East Anatolian Fault, GS=Great Slave Lake shear zone, LE=Levant Fault Zone, NA=North Anatolian Fault, NJ=Najd Shear Zone, NZ=New Zealand Alpine Fault, SA=San Andreas Fault, TA=Taiwan.

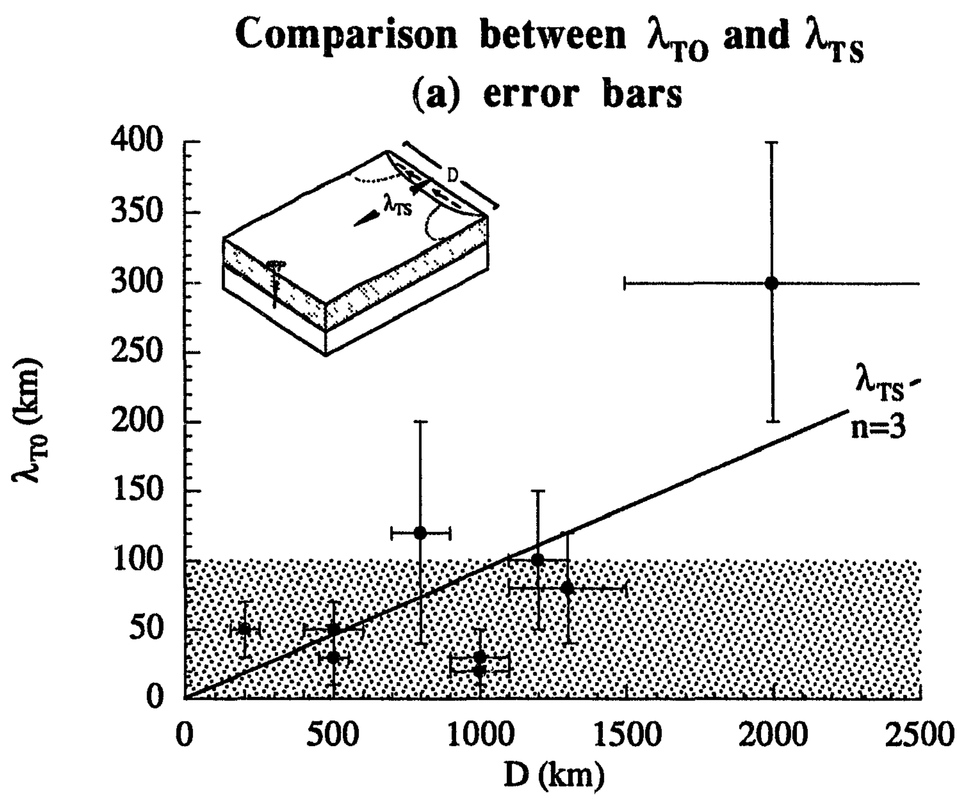
Comparison between λ_{TO} and λ_{TS}
(a) error bars
λ_{TO} (km)
D (km)
λ_{TS}-
n=3
D
λ_{TS}
0
50
100
150
200
250
300
350
400
0
500
1000
1500
2000
2500

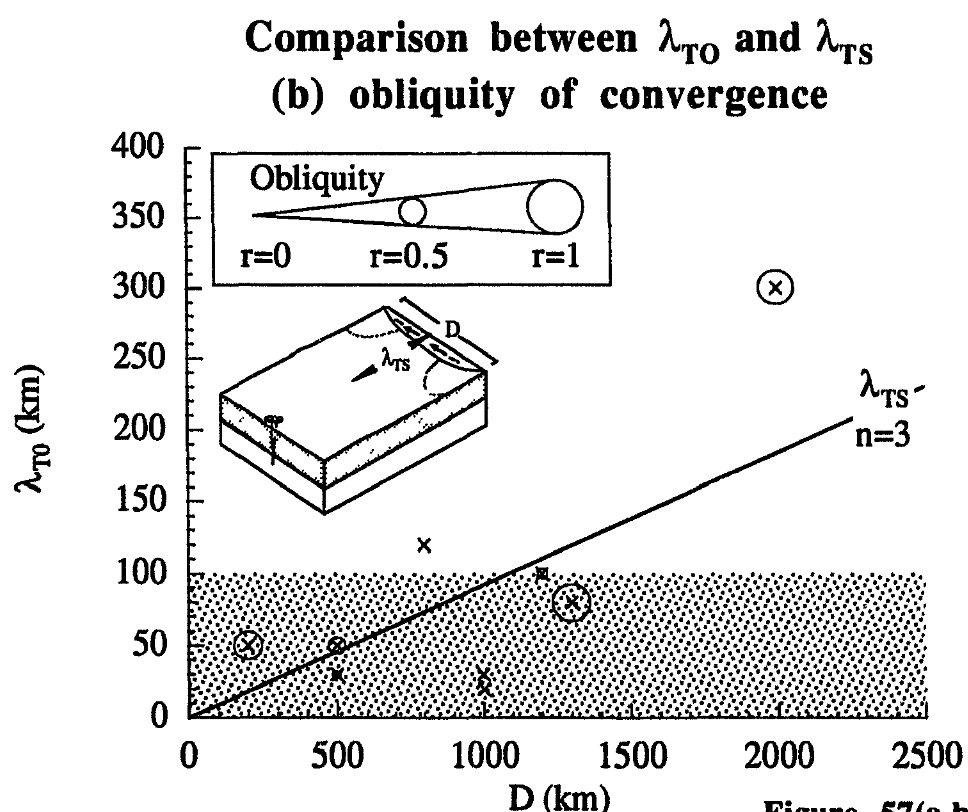
Comparison between λ_{TO} and λ_{TS}
(b) obliquity of convergence
Obliquity
r=0
r=0.5
r=1
λ_{TO} (km)
D (km)
λ_{TS}-
n=3
D
λ_{TS}
0
50
100
150
200
250
300
350
400
0
500
1000
1500
2000
2500

Figure 57(a,b)

Comparison between λ_{TO} and λ_{TS}
(c) key to data points

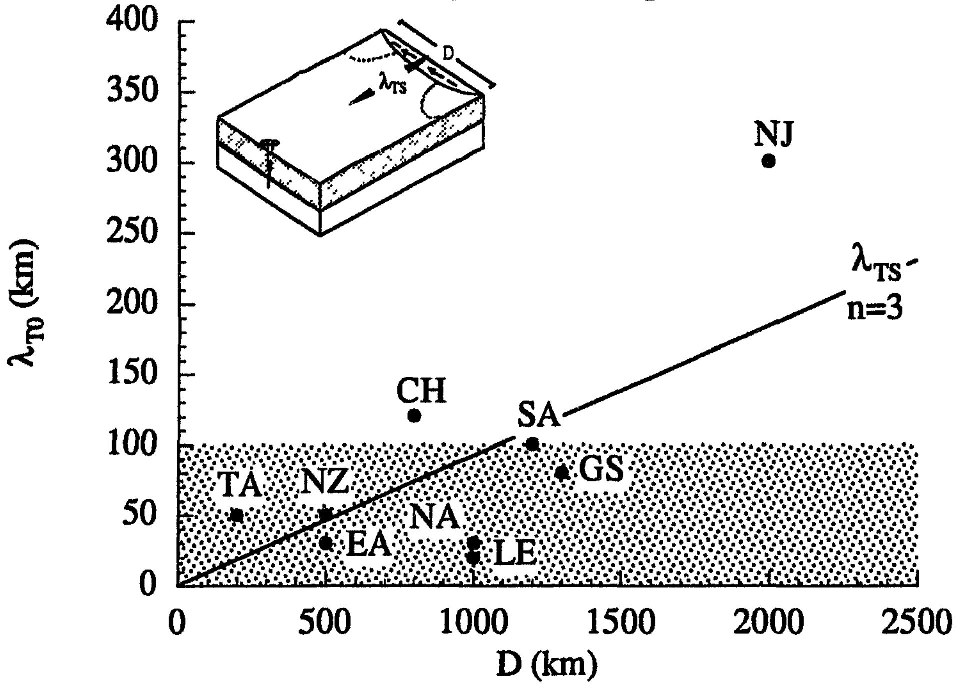

Figure 57(c)

Test Three: Ratio of Purely Normal to Purely Transcurrent Deformation

In some instances the incident velocity acting at a plate boundary may change along-strike from purely normal to purely strike-slip incidence, due to a change in the orientation of the plate boundary, or in relative plate configurations. There are a few field settings where this change from normal to strike-slip motion can be used to estimate the length-scale ratio $\lambda_{NO}:\lambda_{TO}$, provided some assumptions are made. Firstly, it must be assumed that the mechanics of stress transfer do not change significantly between the two cases. Secondly, if the change in strike is not fully 90°, it must be assumed that, provided the orientation change is from predominantly strike-slip to predominantly normal convergence, the length-scales can be taken to represent 'pure' normal and transcurrent length-scales. These criteria reduce the subset of examples that may be used to 4 points, so it must be cautioned that any trends in the data are suggestive only, and cannot be used as a rigorous test.

Figure 58 shows the resultant ratios of normal:transcurrent deformation. In figure 58(a), the normal and transcurrent length-scales are shown, normalized by their respective along-strike boundary condition length-scales, D_N and D_T. The predicted side-driven values for these quantities, assuming n=3, are:

$$\frac{\lambda_{NS}}{D_N} = \frac{2}{\pi\sqrt{3}}$$

and

$$\frac{\lambda_{TS}}{D_T} = \frac{1}{2\pi\sqrt{3}}$$

Therefore, if the data points obey the side-driven thin sheet predictions, they should plot on or near the point $(1/2\pi\sqrt{3}, 2/\pi\sqrt{3})$, which is shown as a shaded square in figure 58(a).

Alternatively, if the plate interaction is basally controlled, there should be no dependence on the along-strike length-scales D_N and D_T, and the normal and transcurrent deformation length-scales should plot along a line representing the length-scale ratio. Figure 58(b) compares the data to the predicted basally-driven relationship $\lambda_{TB}/\lambda_{NB}=1/2$, shown by the solid line on the plot. The shaded region represents the thin sheet accuracy limit.

Figure 58 demonstrates that even for these few points, the real ratios (and accompanying uncertainties) are roughly in agreement with either the side-driven or basally-driven predictions; one exception is the Zhob-Chaman fold-belt, which does not seem to agree with the side-driven prediction of figure 58(a). In general, however, the measurements cannot be used to distinguish between the two driving mechanisms, given the limited data set available.

Figure 58: (a) Transcurrent deformation length-scale for purely transverse incident velocity, vs. normal deformation length-scale for purely convergent incident velocity. Each length-scale is normalized by the relevant side boundary condition, D_T for transcurrent parts of the plate boundary, and D_N for the normally incident section, as shown in Table 11. The predicted value if deformation is controlled by indenter mechanics is represented by the shaded square on the figure, which lies at the intersection of the predicted normal and transcurrent length-scale relations (dashed lines). The distance of each data point from the shaded square therefore represents the discrepancy between the data and the side-driven prediction. (b) Transcurrent deformation length-scale vs. normal deformation length-scale, for the same data set as shown in (a). The solid line is the predicted ratio from the basally-driven model. The shaded region is the length-scale limit, below which the model approximations are not valid. LB=Lebanon bend vs. Levant Fault; MA= Makran Convergent Zone vs. Chaman Fault; PS=Patos-Seridó Shear System; ZH=Zhob Convergent Zone vs. Chaman Fault.

(a) Length-scale ratio cf. side-driven predictions

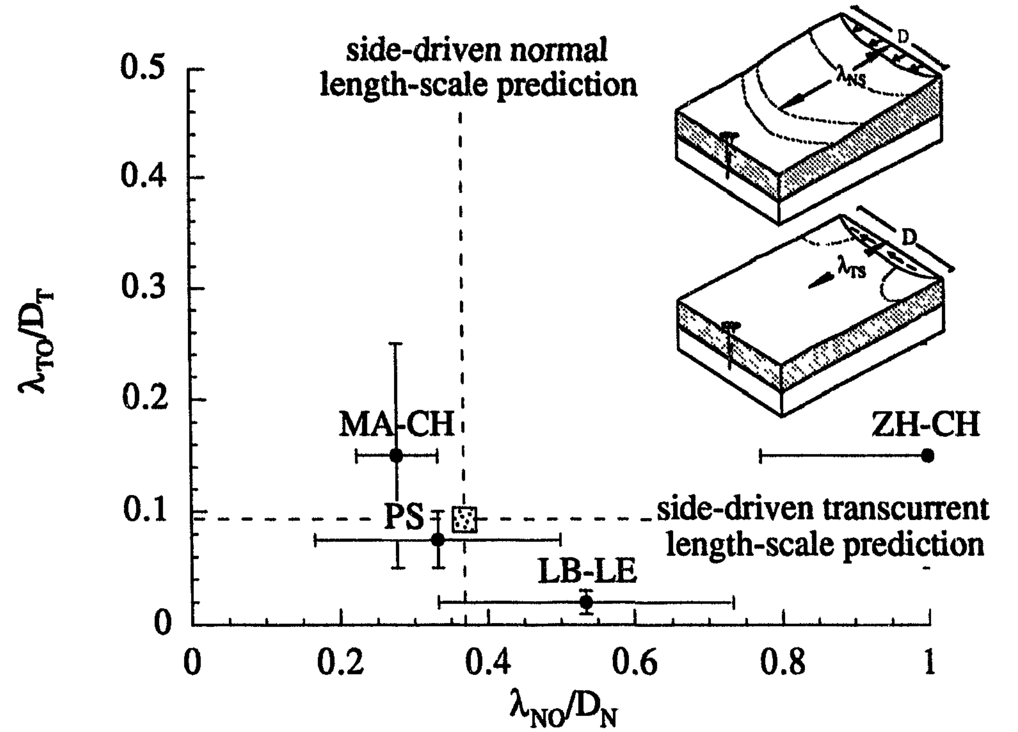

(b) Length-scale ratio cf. basally-driven predictions

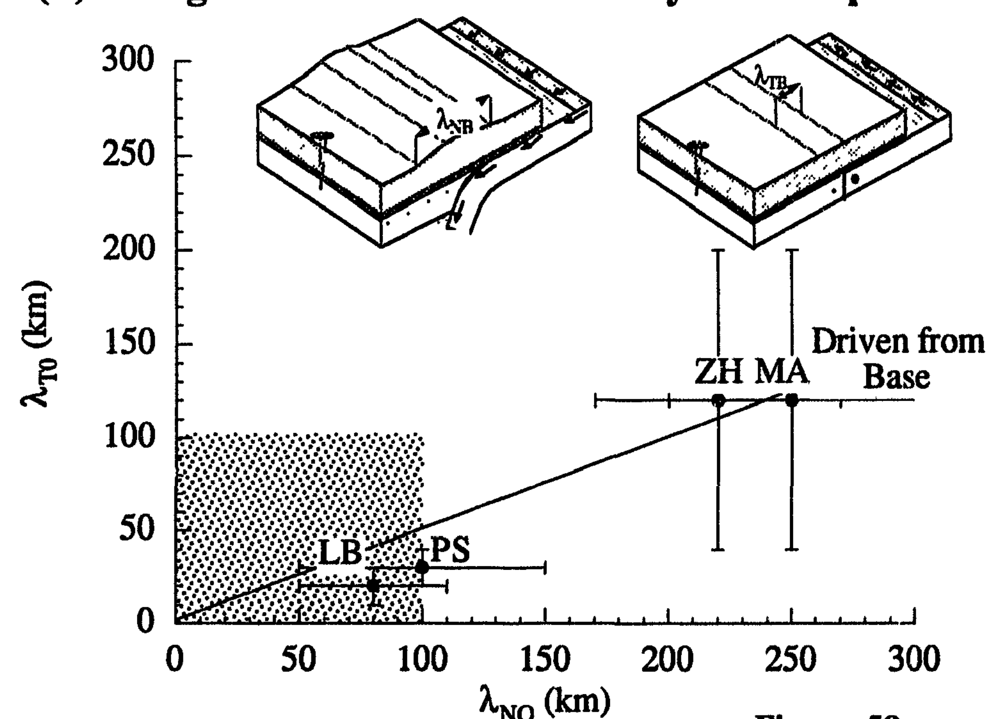

Figure 58

Test four: Oblique Convergence

Transpressive examples are used to test whether significant obliquity in convergence reduces the ratio of strain partitioning. Figure 59 plots the estimated obliquity, r, vs. the length-scale ratio, α, for these cases. As for the previous plot, the uncertainties in determining length-scale ratios precludes interpretation of any trends in the data; the most that can be gleaned from the plot is that all of the data points have a ratio somewhere between 4 and 1.

Discussion of Test Results: a Cautionary Note

The lack of clear trends and relationships in measured aspect ratios and length-scales for the natural examples may be due to: (a) lack of suitable examples; (b) difficulties in measurement of length-scales; (c) transient effects on length-scales, which destroy the validity of comparison with the simple models investigated here; and/or (d) additional effects on length-scales not predicted by the models. This sub-section dicusses some of the problems with estimating length-scales for the examples in Appendix F, as well as additional factors which may render the comparison with simple, steady-state models invalid.

(a) Problems with finding suitable natural examples

One of the major difficulties with data-model comparisons is that almost half of the examples used have small length-scales (< 200 km), and so are at the limit of validity for comparison with thin-sheet models. This is the case for ~ 11 out of 24 of the normally convergent examples in Appendix F. The problem is even more apparent for examples of transcurrent deformation, such as the East Anatolian fault, for which deformation seems to be restricted to within a few kilometres of the plate boundary. The aspect ratio tests require a large range of length-scales and aspect ratios in order to be rigorous, and the clustering of data points at small-scales inhibits the interpretation of any trends in the data.

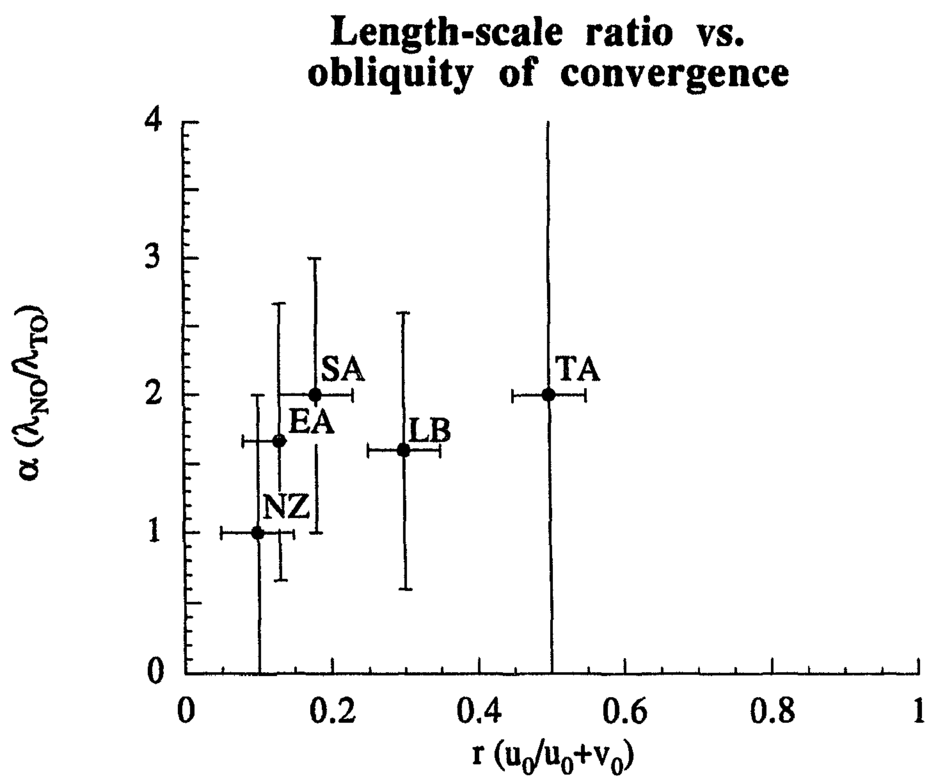

Figure 59: Length-scale ratio, α, vs. obliquity of convergence, as measured by the ratio r. Letter symbols as for figures 57 and 58.

(b) Problems in estimating length-scales

Measurement of the along-strike length of the convergent (or strike-slip) plate boundary (D) is often uncertain, especially for the more ancient examples. Overprinting at either end of the orogen may cause D to be under-estimated (e.g. the Albany-Fraser and Capricorn orogens in Australia (Myers, 1990)). For pre-Mesozoic examples, the best method for estimating D is to take the along-strike length of the two cratons involved in the collision, where known (e.g. the Alleghanian Orogen is limited by the length of African craton which was in contact with North America). But this method is strongly influenced by potential errors in plate reconstructions.

Some of the natural examples exhibit large variations in orientation along-strike. For example, the European Alpine system (the Eastern, Western and Southern Alps) has a marked concavity towards the south. Although the results from the previous chapter indicate that it is the length-scale of the convergent velocity that determines D (rather than the initial shape of the plate boundary), if curvature is large, the components of normal and transverse incident velocity will change along-strike, and this could affect length-scales of deformation. The curvature problem has not been addressed in this analysis. An associated problem is the effect of rotation (during deformation) of the plate boundary, which may change the velocity boundary condition with time.

The models assume that collision occurs synchroneously along-strike, but this will not often be the case. Although for large-scale examples (e.g. the India-Eurasia collision) this is not likely to affect resultant length-scales, for many of the smaller-scale cases with less convergence, asynchroneity may dominate the deformation style of the orogen. For example, the Chaman fault zone at the western side of the India-Eurasia collision has an along-strike length which must have grown with time, as India ploughed northwards into Eurasia. The growth in D with time for this case would be roughly 2000 km in 40 My. If the side-driven indenter model is valid, the deformation would thus have spread outwards across-strike with time, an effect not explored in the models. Another example where a growth in D with time is probable is Taiwan. (Continental collision in Taiwan is just beginning at the southernmost end, but has been occurring for ~ 4 Ma in northern Taiwan (Suppe, 1987)). The San Andreas fault has also grown in along-strike extent over the past 25 Ma (Furlong, 1993).

Plate reconstructions for many of the ancient examples are still dubious, and various alternatives are debated by the geological community. Dimensions and timing for the three Proterozoic orogens from western Australia used in the scale analysis (the Albany-Fraser, Capricorn, and Paterson orogens) are taken from a recent interpretation by Myers (1990). However, many alternative interpretations, including some which dispute plate tectonics as a cause of west Australian Proterozoic deformation, exist (e.g. Etheridge et al., 1987). Uncertainties in plate reconstructions may influence estimates for along-strike length D, and in addition, if two sides of an orogen have been subsequently separated by sea-floor spreading, estimates for deformation length-scales based on one side of the orogen only will probably be an under-estimate.

Estimating the total amounts of convergence for an orogen (e.g. figure 56) requires a good knowledge of shortening history. This is often a poorly known quantity, especially for ancient orogens. In many instances palinspastic reconstructions are not valid, because of along-strike mass movement subsequent to orogenesis, or lack of sufficient constraining data.

(c) The effect of transient episodes and inherited weaknesses on length-scales

Many of the larger-scale orogens will have undergone several transient episodes of convergence and/or strike-slip motion, completely precluding comparison with simple, steady-state models. For some of the ancient cases, we do not have a good enough dating resolution to identify structures associated with a particular transient deformation episode. For instance, there is some evidence that the Damaran orogen in Africa was multiply deformed (Kukla and Stanistreet, 1991), but knowledge about this Late Proterozoic orogen is so sparse that individual episodes cannot be resolved. The Variscan orogeny almost certainly involved many different episodes of deformation, which may have occurred in different locations at different times. The aspect ratio tests are conducted assuming that most deformation occurred during one major phase of orogenic activity. Some of the scatter in the length-scale analyses may result from natural examples for which this assumption is not correct.

(d) The effect of additional parameters

Some of the misfit between data and model predictions may be caused by additional parameters which influence deformation length-scales, but which have not been included in the models. For example, the scale analysis has assumed an average power-law exponent n=3 for all cases; the average value of n may, however, change with amount of thickening, and the thermal condition of the continental lithosphere before deformation begins. The effect of a changing power-law exponent is discussed in section 5.4. Figure 56 suggests that the amount of convergence experienced by an orogen also influences length-scales, and this effect is investigated further in chapter six.

Erosion of mass from an orogen may reduce deformation length-scales, an effect which may be important for the New Zealand Southern Alps (Beaumont et al., 1992). Inherited weaknesses may also control the style of deformation, by changing the location of detachment layers in the crust. In some cases, detachment may occur preferentially at mid-crustal levels, rather than at the Moho, as assumed in the basally-driven model. This is the conjectured style for the Pyrenees according to Muñoz (1992), and may lead to different coupling characteristics (and hence deformation style) than those investigated in the simple basally-driven model presented here.

Some of the natural examples used in the analyses are cases of active oceanic subduction. The assumption has been made that styles of continental deformation for advancing subduction cases are similar to the continental collision examples (see chapter two). For instance, this assumption is used for the Neogene Andes, which are situated next to an active subduction margin. However, there are some problems with the advancing subduction/collision equivalence assumed for the Andes. The relative importance of the addition of magma to the crust, vs. crustal shortening, in controlling deformation style is not clear. Also, the effect of the downgoing oceanic lithosphere on mantle dynamics may be significant. In particular, it has been suggested that the extent of deformation at the plate boundary is related to the dip of the oceanic slab (Isacks, 1988).

In conclusion, there are many difficulties inherent in the scale analysis attempted in this section. The difficulties may completely obscure some aspects of a comparison with the simple model styles, and indicate that length-scale analyses should be interpreted with great caution. Any tentative conclusions drawn from such analyses should be augmented by geophysical studies of the deep structure of the crust.

§ 5.4 Summary of Scale Analysis

The analysis of the preceding section indicates that it is very difficult to estimate length-scale measurements sufficiently accurately to be useful in the aspect ratio tests. Despite this difficulty, test one suggests that aspect ratios for convergent orogens are in rough agreement with a model in which there is both side and basal forcing, with the indenter length-scale providing a limit to the width of deformation that may be attained at small convergence times.

Many of the normally convergent examples have an across-strike width much below that predicted from a side-driven thin sheet model, assuming $n=3$. It is tempting to claim that this is attributable to detachment and drag between the crust and mantle lithosphere, as shown in chapter four. However, figure 60(a) suggests an alternative explanation that is equally plausible. Most of the examples which have experienced only minor amounts of convergence plot roughly near a side-driven relation with a power-law exponent $n=10$. An average value of $n\sim10$, for unthickened lithosphere subjected to typical values of compressional stress in convergent zones, was suggested by Sonder and England (1986). It is possible that the average rheology of the lithosphere changes with increasing convergence, due to the increased thickness and corresponding increase in average lithospheric temperature. This may reduce the power-law exponent from a high value ($n\geq10$), which corresponds to a fairly cool, brittle crust overlying a strong mantle, to a lower value ($n=3$ to $n=1$) where the crust and mantle deform predominantly by ductile viscous creep (England and Jackson, 1989). Results from chapter four (figure 37) showed that the predicted side-driven length-scale for crustal thickening at $n=1$ is roughly the same as for $n=3$, because of the tectonic escape term, but length-scales for $n=10$ are

---

Figure 60: Two possible explanations for the trends in the data shown in figures 55 and 56. Explanation (a): Deformation is controlled by indenter length-scale, D, but the average power-law exponent for the lithosphere decreases as total convergence increases (and the lithosphere thickens and heats up), increasing the slope of the length-scale relationship. If this interpretation is correct, most small-scale orogens can be modelled as a thin viscous sheet having an average crustal power-law exponent of 10; this exponent decreases to 1-3 for extreme cases of convergence (e.g. the India-Asia collision, with over 2000 km convergence). Explanation (b): Deformation is controlled by detachment of mantle lithosphere. With increasing convergence, the width of deformation increases in the manner shown in chapter four. It is likely that as the crust thickens and heats up, crust-mantle coupling (and the Ampferer number) will reduce. The plot shows the increase in across-strike length-scale as a function of convergence, for two values of Am, and Ar=1, and for small normalized convergence.

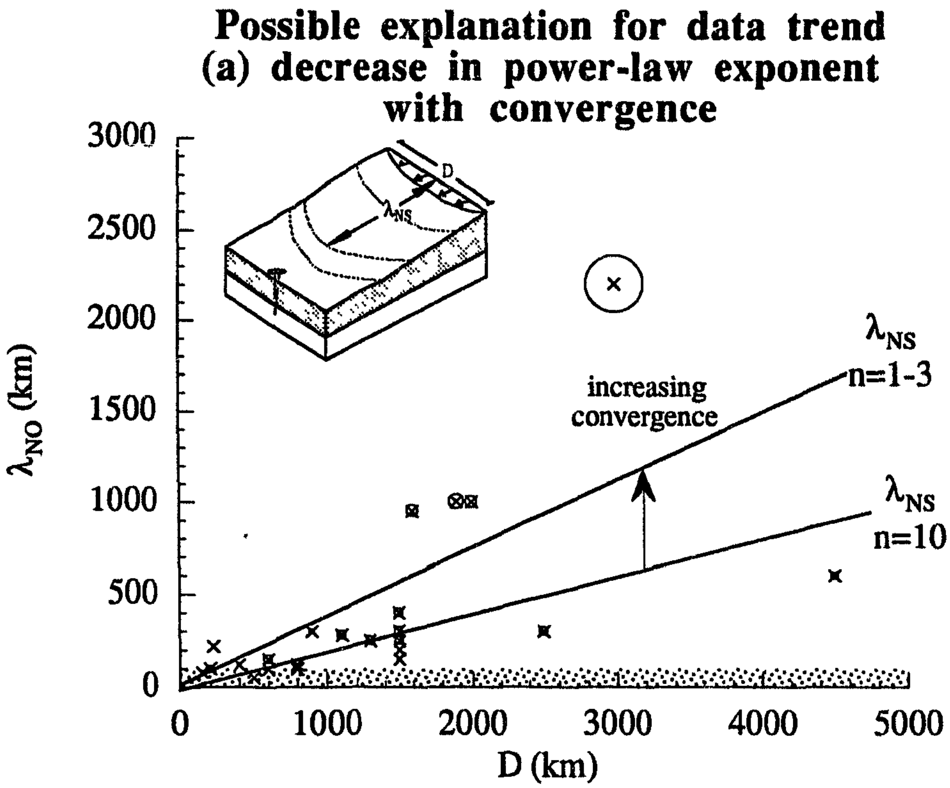

Possible explanation for data trend
(a) decrease in power-law exponent
with convergence
3000
2500
2000
1500
1000
500
0
λ_{NO} (km)
D
λ_{NS}
λ_{NS}
n=1-3
increasing
convergence
λ_{NS}
n=10
0
1000
2000
3000
4000
5000
D (km)

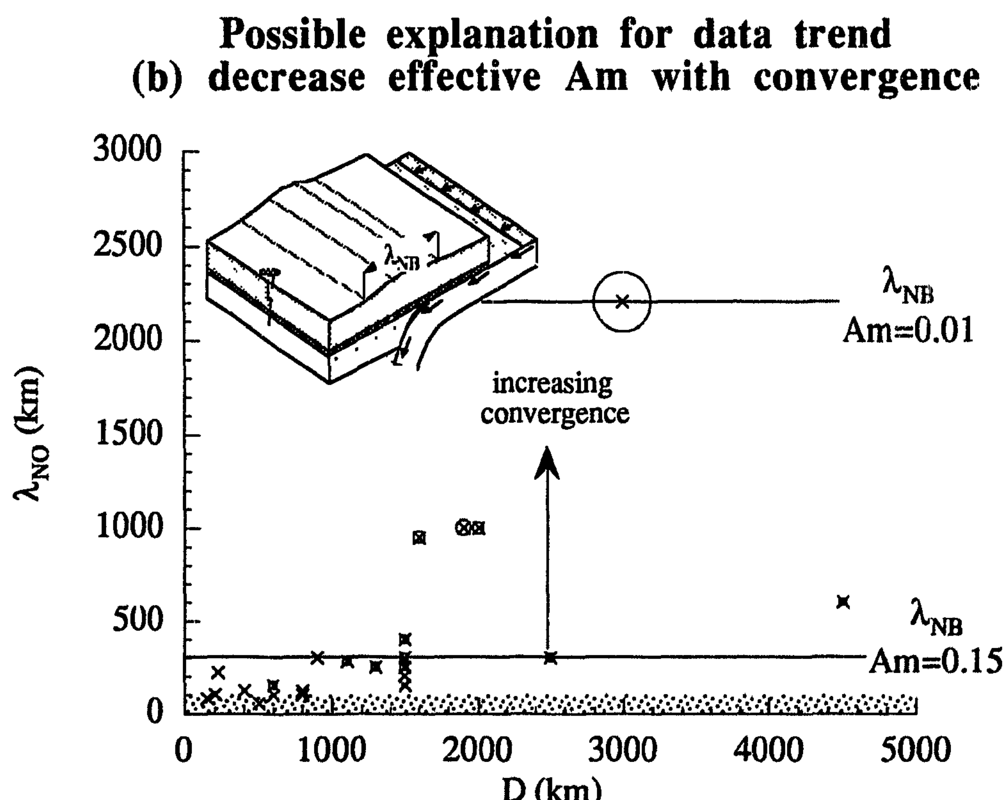

Possible explanation for data trend
(b) decrease effective Am with convergence
3000
2500
2000
1500
1000
500
0
λ_{NO} (km)
λ_{NB}
λ_{NB}
Am=0.01
increasing
convergence
λ_{NB}
Am=0.15
0
1000
2000
3000
4000
5000
D (km)

Figure 60

higher. In combination with an increase in length-scales due to the effect of gravity on crustal thickness contrasts, the scatter in the trend of the data may therefore be explained by lithosphere which is responding to indentation from the side (figure 60(a)).

The opposite explanation, where crustal deformation is controlled primarily by basal detachment and drag, is equally possible. Figure 60(b) is similar to figure 60(a), but compares the data to theoretical predictions from the basally-driven model. Most of the data have an across-width length-scale of 300±100km, which corresponds to an Ampferer number of about 0.15±0.1 (for n=3). The arrows on the figure show the trend in the normal deformation length-scale with increasing convergence. This trend is likely not only because of the relationship between length-scale and normalized convergence, due to effects of gravity on crustal thickness contrasts, investigated in figure 33, but also because thickening of the crust is likely to reduce crust-mantle coupling, and lower Am in the deforming region. A decrease in crust-mantle coupling, combined with the diffusional effects of gravity acting on crustal thickness contrasts, may therefore be an equally valid explanation of the change in across-strike deformation with increasing convergence. This possibility is investigated further in chapter six.

Do Length-Scales Provide Useful Constraints on Deformation Style?

The ambiguity of the results for test one, and the lack of significant controls on length-scale estimates for the remaining tests, indicate that it may not be possible to distinguish between the likely driving mechanisms for convergent and strike-slip deformation using measurements of aspect ratios. This result may seem disappointing, but I believe it is important, because it indicates that many of the claims made by various authors about the relationship between surface deformation and underlying processes, may not be quantitatively provable. The results indicate that length-scale tests by themselves are unlikely to conclusively determine deformation styles in convergent orogens, and must be augmented by empirical measurements of the deep crustal and lithospheric structure, in order to determine predominant driving mechanisms for crustal deformation.

Chapter Six

DEVELOPMENT AND RECAPITULATION

§ 6.1 Introduction

In chapter four it was predicted, on the basis of the two conjectured styles of forcing at plate boundaries, that side-driven and basally-driven deformation will possess different length-scale dependences. Examples from convergent and strike-slip plate boundaries were used in chapter five to try to determine which deformation style has the closest agreement with real lithospheric behaviour, for small amounts of convergence. The results were inconclusive, in that the quantitative tests could not be used to distinguish unequivocally between the different possibilities. Neither the basally-driven, nor the side-driven model styles (or a combination of them), could be disproved as the most likely candidate for forcing at convergent boundaries.

The purpose of this chapter is to broaden the discussion of controls on deformation length-scales. Firstly, the length-scale analysis of the previous chapters, which was based on mathematical analysis of the force balance equation for constant controlling parameters Am, Ar, n, and D, is expanded and developed in section 6.2 in order to compare the predicted increase in model deformation length-scales with convergence, to the trend in the data for natural (convergent orogen) examples. In addition to the effect of gravity acting on crustal gradients, the thermal weakening of crust-mantle coupling as the crust thickens, causes the basally-driven deformation length-scale to increase. The thermal analysis is performed with the use of a partially coupled thermo-mechanical model of the lithosphere. The simple analysis demonstrates that the combined effects of gravity acting on crustal thickness contrasts, and the weakening of the detachment layer on the retro-side of an orogen, may explain the length-scale trend with convergence.

In section 6.3, the model predictions concerning an increase in length-scales with convergence are compared to the development of the India-Eurasia collision, the largest scale orogenic system that is currently active. The comparison suggests that the mixed model, with aspects of both the side-driven (indenter) and basally-driven models, may provide the best representation for the large-scale orogen.

In the recapitulation (section 6.4), the conceptual physical models behind the model assumptions are summarized in terms of two major controls: the presence, or lack, of a weak layer between the crust and mantle lithosphere, and the relative strengths of the lithosphere on either side of the plate boundary. The discussion moves beyond the simple cases investigated in this thesis to speculate on the controls of deformation style and symmetry. It is suggested that if two continental lithospheric plates converge and one continent is much stronger than the other, basal detachment may occur preferentially on the weak side. The polarity of mantle lithosphere subduction for the mixed model may therefore be controlled by the strength difference across the plate boundary.

§ 6.2 A General Model for the Growth of Basally Controlled Orogens

The Role of Convergence

This section investigates whether the basally-driven model may be used to explain the length-scale trend found in chapter five for the growth in deformation length-scales with convergence, which is re-illustrated in figure 61. Basally-driven length-scales have already been shown to increase initially by an amount proportional to $\sqrt{Ar\, t'}$, where t' is normalized convergence. The behaviour for large amounts of convergence may be investigated using the numerical model. The effect on length-scales is compared to the data from figure 61 in the first part of this section.

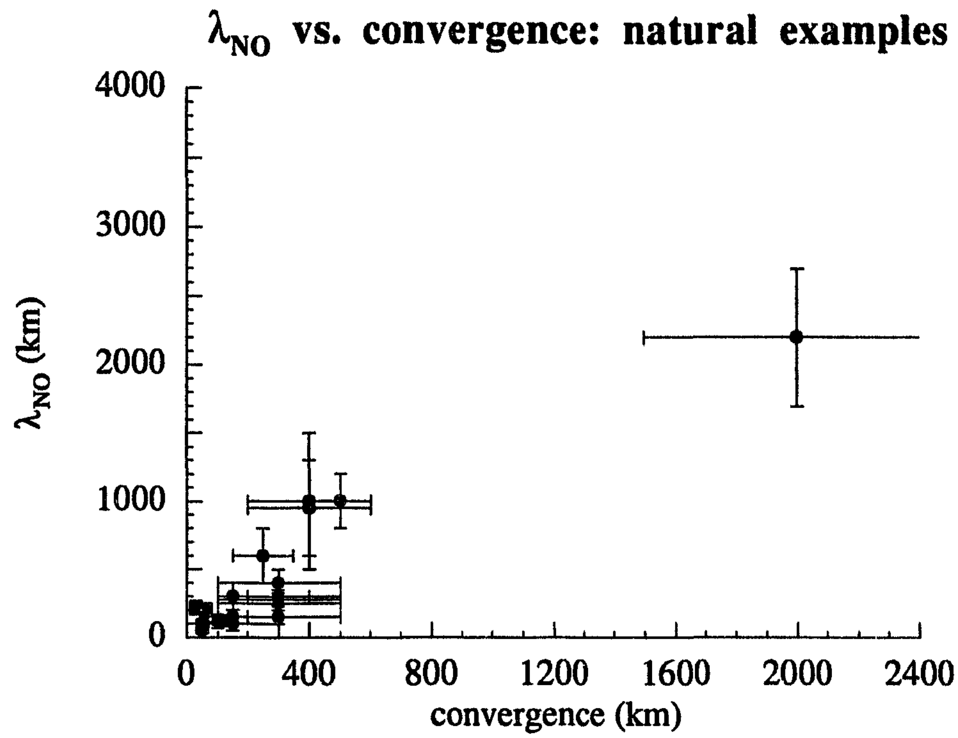

Figure 61: The increase in deformation length-scale with convergence for the natural examples from chapter 5 (redrawn from figure 56).

In addition to the effect of the Ar parameter on basally-driven length-scales discussed above, for large amounts of convergence the parameter Am may also change, because of the effect of crustal thickening on the average strength of the crust and weak detachment layer. By substituting simple approximations for the relationship between the temperature at the Moho and the parameter Am into the numerical model, I can investigate what the effect of changes in this parameter will be on the increase of length-scales with convergence for the basally-driven case.

Throughout this section, the model crust with which the natural length-scale measurements are compared is assumed to start out with a uniform thickness of 30 km. The initial crustal geotherm is taken to be 15 °C/km, giving a temperature at the Moho of 450 °C. This temperature is used to estimate an initial Ampferer number of 0.75, from the calibration plot (chapter three, figure 19(a)) for T_{moho} vs. Am. All of the length-scale analyses for which results are shown assume this initial, uniform value for Am. Other choices for an initial (pre-deformation) Am would give a slightly different set of results. The following results should therefore be viewed as indicators of the trends in length-scales only. A more rigorous comparison between model results and natural examples would require better knowledge of the initial conditions in each convergent zone.

Effect of Gravity on the Basally-Driven Deformation Length-Scale

For a given value of Am, the normal length-scale for the basally-driven model has been shown to increase with normalized convergence (λ_{NB} vs. t') at small t' according to the approximate relation (equation 21):

$$\lambda'_{NB} \approx \lambda'_{NB}\big|_{t'=0}\sqrt{1+\frac{Ar\,t'}{2}}$$

For large amounts of convergence ($t'>>1$), the length-scale relation diverges from this simple approximation. In this analysis, the length-scale increase is computed numerically.

As discussed above, the value for Am for initial stages of collision is estimated to be 0.75. In this sub-section, Am is taken to be constant throughout the convergence. Length-scale increases are computed for three values of Ar (Ar=1, 5, and 25). In chapter three of this thesis, the best estimates for Ar for a cross-sectional model of the crust composed of wet feldspar were between 1 and 5. This agrees with the study by England and Houseman (1986), which found that a value for Ar between 1 and 3 best fitted a comparison between the side-driven thin sheet model and the development of the Tibetan Plateau.

The predicted length-scale increase, using results from the numerical model, is shown in figure 62(a), and compared to the natural length-scale data in figure 62(b). As well as the numerical results (solid curves), the predicted length-scale changes using the approximate analytical relation (eq. 21) are shown by the dotted lines. The deformation length-scale, measured using the numerical model, changes its dependence on Ar from $(1+Ar\ t'/2)^{1/2}$ to $(Ar\ t')^{1/2}$ with increasing convergence. The analytical solution for small t' described above therefore predicts an increasingly different length-scale solution compared to the numerical results with increasing t'.

Figure 62: (a) Predicted deformation length-scales for the basally-driven case, for Ar=1, 5, and 25. Dotted lines are the analytical prediction; solid lines are the numerical results for the basally-driven model. (b) Observed deformation length-scales, λ_{NO}, vs. convergence, for the natural examples from chapter five, contrasted with the predicted numerical (solid lines) length-scale relations for the basally-driven model, for Ar=1, 5, and 25. All calculations assume a constant crustal geotherm, with a Moho temperature of 450°C (Am=0.75), and n=3.

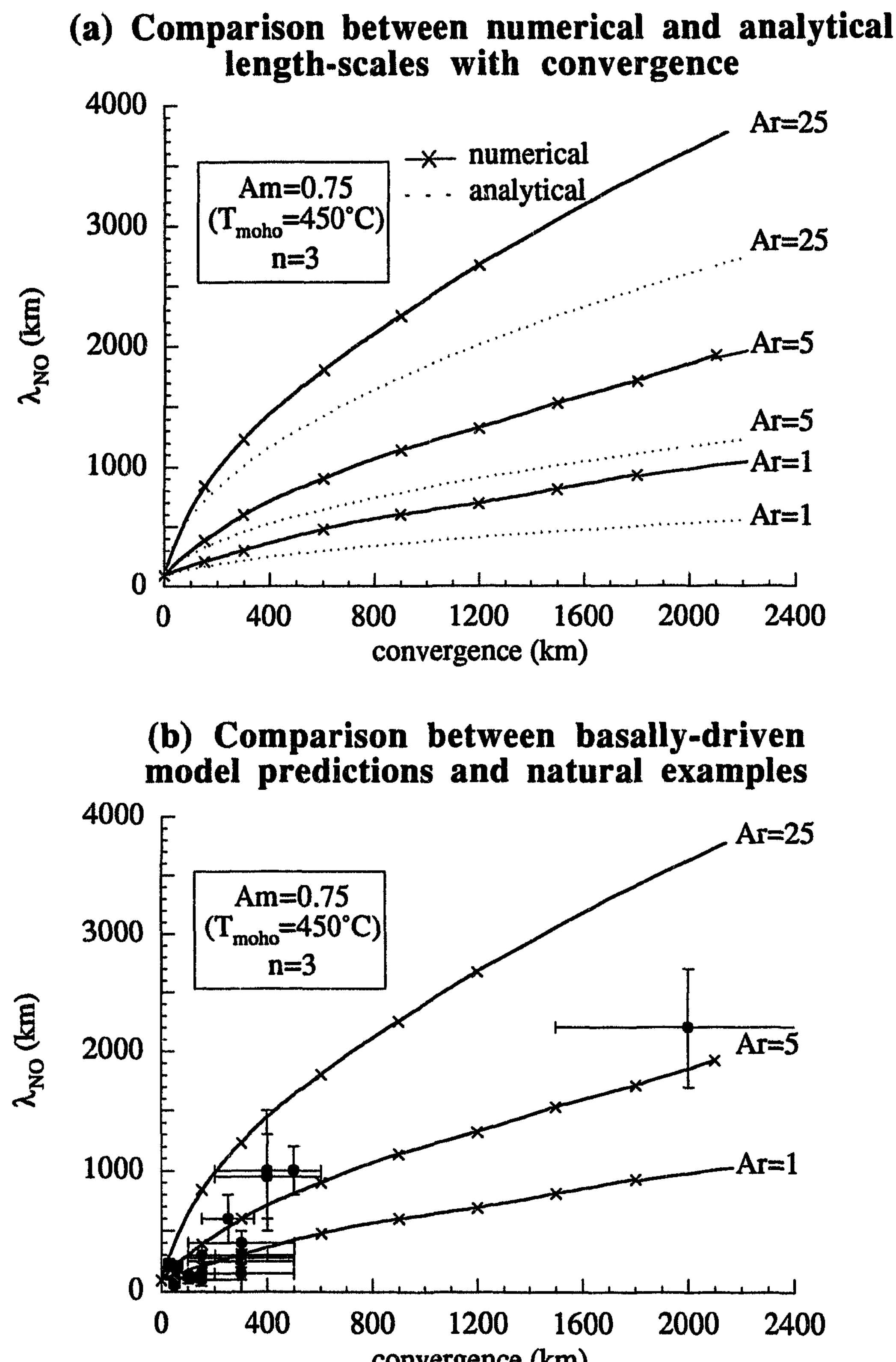
(a) Comparison between numerical and analytical length-scales with convergence
Am=0.75
(Tmoho=450°C)
n=3
numerical
analytical
Ar=25
Ar=25
Ar=5
Ar=5
Ar=1
Ar=1
λNO (km)
convergence (km)
0
1000
2000
3000
4000
0
400
800
1200
1600
2000
2400
(b) Comparison between basally-driven model predictions and natural examples
Am=0.75
(Tmoho=450°C)
n=3
Ar=25
Ar=5
Ar=1
λNO (km)
convergence (km)
0
1000
2000
3000
4000
0
400
800
1200
1600
2000
2400

Figure 62

Comparison between the numerical results and the data indicates that, given the error in estimates for convergence and length-scales of deformation for the natural examples, a basally-driven model with Ar = 5 could provide a possible explanation for the length-scale trend in the data. Given that the best-fitting values for Am and Ar seem geologically reasonable (as discussed above), this provides encouraging evidence for some amount of basal detachment between crust and mantle lithosphere during convergent deformation.

The Effect of Thickening on Crustal Geotherms and the Deformation Length-Scale

In addition to the Ar effect, the crustal and Moho temperatures are expected to rise for cases which have experienced considerable convergence, which will locally (i.e. depending on spatial coordinates) change the Ampferer number. The change in Am with t' may alter the length-scale relationships shown in figure 62, in the manner demonstrated below. The effects are first described in terms of scaling relationships, and then more accurate numerical results are presented.

(i) Scaling Relationships for the Effect of Thickening on Am and Ar

Thickening of the crust by convergent processes will cause a perturbation in the initial, steady-state crustal geotherm, which will relax with time due to the diffusion of heat (Carslaw and Jaeger, 1959). The relative rates of the advective process which causes the perturbation, and the diffusive relaxation towards a steady-state crustal geotherm, can be estimated by the non-dimensional Péclet number:

$$Pe = \frac{uS}{\kappa}$$

where S is the length-scale of the perturbation (the crustal thickness for this case), u is the advective velocity, and κ is the diffusivity, for which an average crustal value is

10^{-6} m^2s^{-1}. The Péclet number for an orogenic setting, with typical convergent velocities of between 1 and 5 cm/yr, and a crustal thickness between 30 and 60 km, is ~10-100, indicating that the initial thickening of the crust in a convergent system generally occurs at the advective limit.

Maximum crustal thicknesses in convergent settings seldom exceed twice the initial crustal thickness. Convergence at 1 cm/yr at a deformation length-scale of 90 km will double the crustal thickness in ~ 10 My, assuming negligible removal of mass by erosion; faster convergence rates will require less time. Assuming the pure-shear thickening takes place at the advective limit, for the reasons discussed above, the geotherm after doubling the crustal thickness will be:

$$T(z,t) = \frac{1}{2}\left(\frac{\partial T}{\partial z}\right)_0 z$$

where $(\partial T/\partial z)_0$ is the crustal geotherm at t=0, before any thickening has taken place, as illustrated in figure 63(a). The crust and mantle lithosphere are heated from below by the

---

Figure 63: The effect of doubling the crustal thickness on the geotherm. Initially (a), the crust (shaded area) has a geotherm of 15 °C/km, so that the Moho is at a temperature of 450 °C when the crust has initial thickness S_0=30 km. After doubling the crustal thickness at the advective limit (b), the geotherm will initially be stretched to an average value of 7.5 °C/km, so that the Moho temperature remains at 450 °C. Diffusive heating in the crust will eventually cause the geotherm to increase to its pre-thickening value, heating the Moho to a temperature of >800 °C. The geotherm at various times after instantaneous thickening are shown by the boxed figures on the lower plot of figure 63(b), in millions of years. A thermal diffusivity of 10^{-6} m^2s^{-1} is assumed for the crust. The simple model ignores the effects of crustal radiogenic heat production.

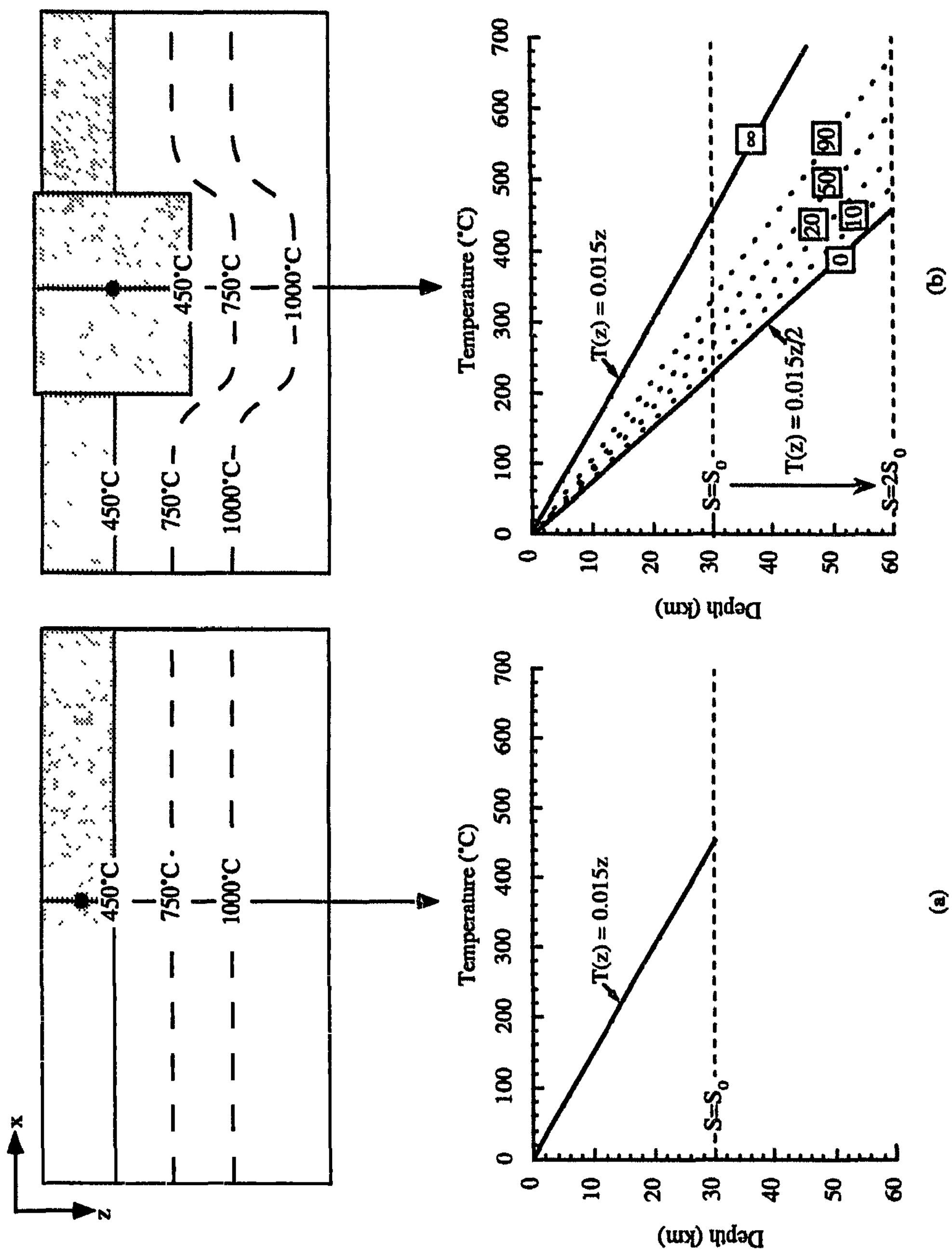
x
z
450°C
750°C
1000°C
Temperature (°C)
Depth (km)
T(z) = 0.015z
T(z) = 0.015z/2
S=S$_0$
S=2S$_0$
∞
90
50
20
10
0
(a)
(b)

Figure 63

mantle asthenosphere. Doubling the crustal thickness will double the amount of radiogenic heat production in a crustal column, but in the following (approximate) analysis I neglect heat production in the crust, and assume a linear geotherm throughout the crust and mantle. If radiogenic heat production in the crust occurs over a significant crustal thickness, the analysis will underestimate the heating (and weakening) of the crust as it thickens, so that Am will be too high and Ar too low. The effects of radiogenic heat production on length-scales of deformation are discussed further in Appendix G.

Diffusion of the temperature perturbation due to the thickening will increase the crustal geotherm back to its steady-state, pre-thickening value. Diffusion processes in the crust can be shown to operate over timescales on the order of:

$$\tau \sim \frac{S^2}{\kappa} \sim 30\,\mathrm{My}$$

(Carslaw and Jaeger, 1959), where τ is the time for the initial perturbation to decay to 1/e of its initial value, towards the steady state ($t \to \infty$) value; κ is the diffusivity; and S is the length-scale of the perturbation, which is is taken to be the initial crustal thickness. The increase in the crustal geotherm with time for a crust thickened homogeneously and instantaneously by factor f can be found using an approximate expression derived by England and Thompson (1984) (England and Thompson, 1984, Appendix B, equation (B18b)). The resultant change in geotherm with time since thickening, for f=2, is shown in figure 63(b).

For the basally-driven model, the simple case shown in figure 63 must be modified to include the effect of the continued movement and detachment of crust and mantle lithosphere (i.e. the thickening process cannot be assumed to occur instantaneously, cf. England and Thompson (1984)). This effect is particularly important on the pro-side of the plate boundary, where mantle lithosphere is converging and subducting with convergence velocity V_P. (Note that this discussion and the following analysis assume that V_P is constant throughout the episode of convergence). Mantle lithosphere which underthrusts the thickened crust before subducting will tend to maintain the temperature at the base of the crust at its pre-diffusional value (figure 64(a)), which in this case is 450 °C. As the pro-mantle lithosphere moves underneath the thickened crustal region, heat flow from the mantle asthenosphere (indicated by squiggly arrows on the figure) will cause the gradual heating up of both the crust and mantle lithosphere. The increase in basal temperature will cause a decrease in Am locally, as indicated by the change in pattern underneath the thickened region of figure 64(a).

Figure 64: Illustration of the effect of the continued motion and subduction of mantle lithosphere on diffusion of the crustal geotherm for crust which has doubled in thickness. (a) At small normalized convergence, t', showing how (for a high Péclet number) the movement of cool mantle lithosphere into the pro-side of the plate boundary keeps the Moho cool compared to the retro-side. Squiggly lines indicate heating from the mantle lithosphere, and the various patterns in the weak basal detachment layer represent local values for Am. (b) A later convergence time, where the extent of thickened crust has grown, and is assumed to have developed symmetrically about the singularity. The top part of (b) shows the thickened crust, with corresponding crustal and mantle lithosphere residence times as noted. The lower part of (b) is a graphical representation of the variation in residence times with across-strike position. The mantle lithosphere residence time is shown by the dashed line with fill, and the crustal residence time by the solid line. (c) same as (b) but assuming most crustal thickening takes place on the pro-side of the plate boundary; (d) same as (b) assuming most thickening occurs on the retro-side. Case (d) corresponds most closely with numerical results later in the section.

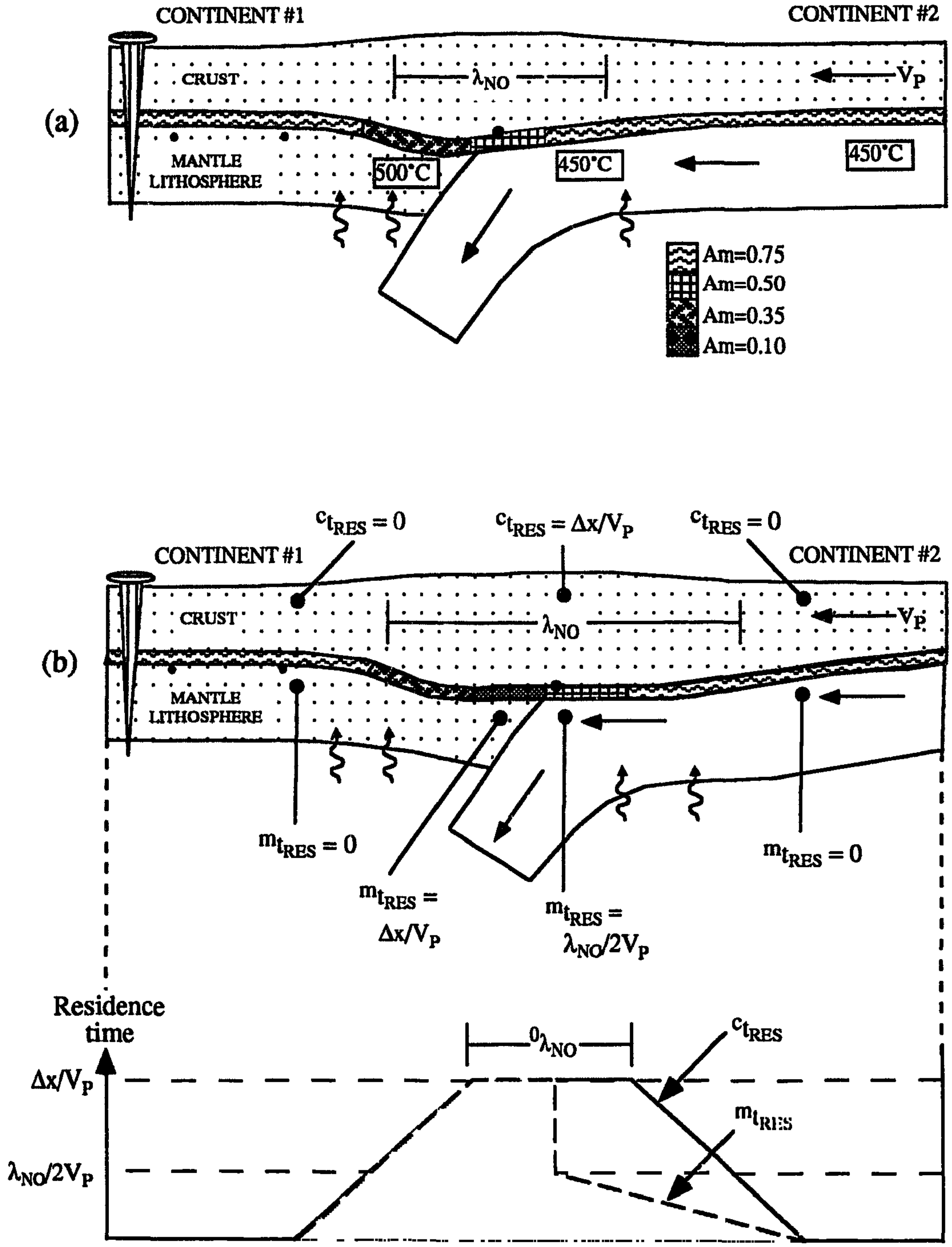
(a)
CONTINENT #1
CONTINENT #2
CRUST
λ_{NO}
V_P
MANTLE LITHOSPHERE
500°C
450°C
450°C
Am=0.75
Am=0.50
Am=0.35
Am=0.10
(b)
$^{c}t_{RES} = 0$
$^{c}t_{RES} = \Delta x/V_P$
$^{c}t_{RES} = 0$
CONTINENT #1
CONTINENT #2
CRUST
λ_{NO}
V_P
MANTLE LITHOSPHERE
$^{m}t_{RES} = 0$
$^{m}t_{RES} = \Delta x/V_P$
$^{m}t_{RES} = \lambda_{NO}/2V_P$
$^{m}t_{RES} = 0$
Residence time
$\Delta x/V_P$
$\lambda_{NO}/2V_P$
$^{0}\lambda_{NO}$
$^{c}t_{RES}$
$^{m}t_{RES}$

Figure 64(a,b)

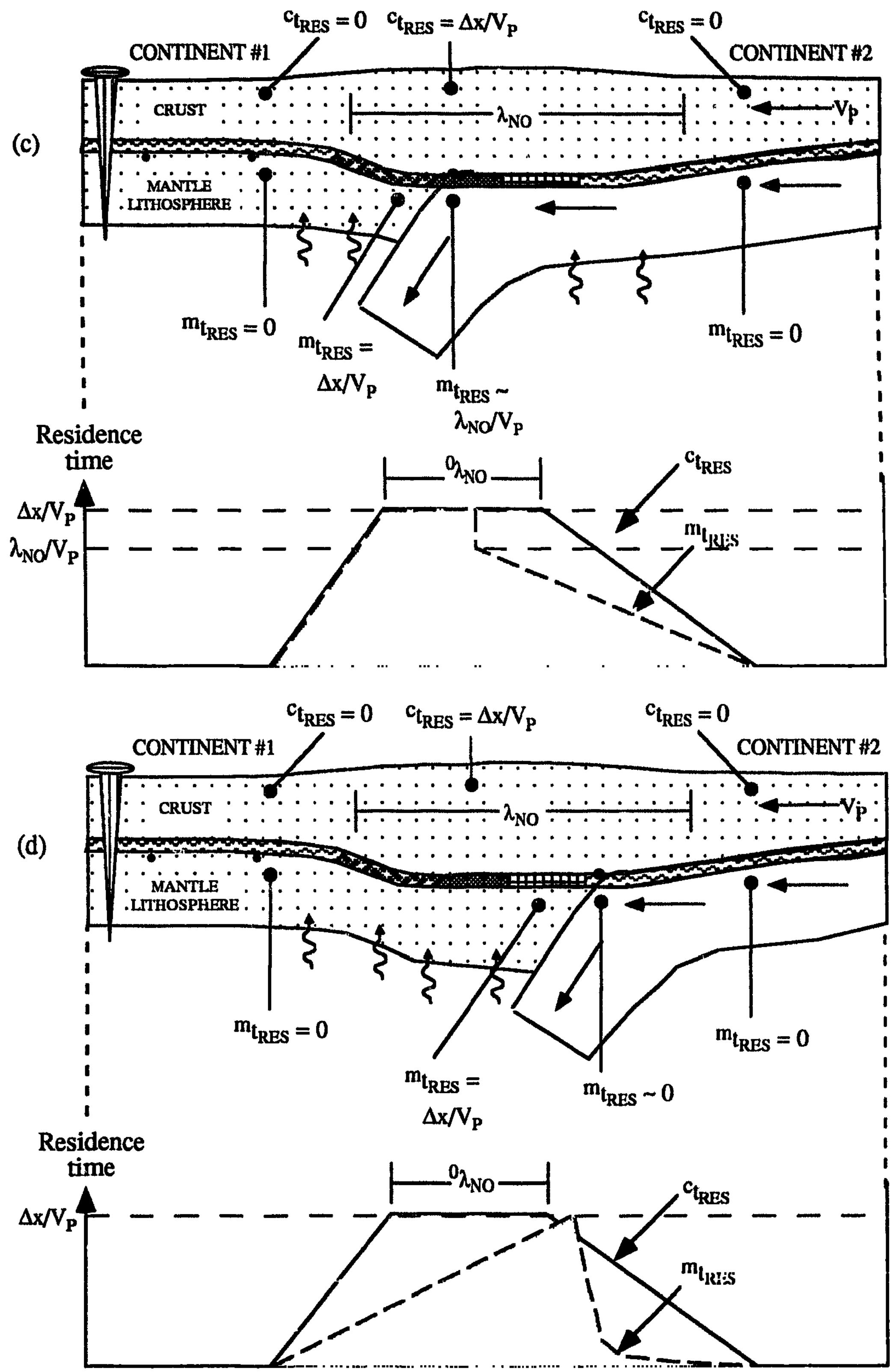
(c)
$^{c}t_{RES} = 0$
$^{c}t_{RES} = \Delta x/V_P$
$^{c}t_{RES} = 0$
CONTINENT #1
CONTINENT #2
CRUST
λ_{NO}
V_P
MANTLE
LITHOSPHERE
$^{m}t_{RES} = 0$
$^{m}t_{RES} = \Delta x/V_P$
$^{m}t_{RES} \sim \lambda_{NO}/V_P$
$^{m}t_{RES} = 0$
Residence time
$\Delta x/V_P$
λ_{NO}/V_P
$^{0}\lambda_{NO}$
$^{c}t_{RES}$
$^{m}t_{RES}$
(d)
$^{c}t_{RES} = 0$
$^{c}t_{RES} = \Delta x/V_P$
$^{c}t_{RES} = 0$
CONTINENT #1
CONTINENT #2
CRUST
λ_{NO}
V_P
MANTLE
LITHOSPHERE
$^{m}t_{RES} = 0$
$^{m}t_{RES} = \Delta x/V_P$
$^{m}t_{RES} \sim 0$
$^{m}t_{RES} = 0$
Residence time
$\Delta x/V_P$
$^{0}\lambda_{NO}$
$^{c}t_{RES}$
$^{m}t_{RES}$

Figure 64(c,d)

The effective time for which diffusion acts on the crust and mantle lithosphere can be illustrated using the concept of *residence time* (figure 64(b-d)). The mantle residence time, ${}^{m}t_{RES}$, is defined as the amount of time for which a particular part of the mantle lithosphere has been in residence under a region with approximately doubled crustal thickness. In figure 64(b), where crustal thickening has developed symmetrically about the plate boundary, ${}^{m}t_{RES}$ is zero beyond the thickened region. On the pro-side of the plate boundary, ${}^{m}t_{RES}$ increases to a value of $(\lambda_{NO}/2V_P)$ before the pro-mantle lithosphere subducts at the singularity. In contrast, on the retro-side of the plate boundary, mantle lithosphere near the singularity is effectively stationary, and has been in residence under thickened crust since the start of convergence (assuming that the initial thickening, over length-scale $\lambda'_{NO}\big|_{t'=0}$, occurs rapidly in comparison to thermal diffusion). The mantle residence time for this region is therefore equal to the time since convergence began, $\Delta x/V_P$, where Δx is the amount of convergence.

Residence time for the crust, ${}^{c}t_{RES}$, is in general different to mantle residence time, because of the detachment between the crust and mantle lithosphere layers (figure 64(b)). Crustal residence time is defined as the amount of time since a particular column of crust was thickened to approximately twice its initial value. The residence time ${}^{c}t_{RES}$ is a maximum for the region which was initially within a crustal deformation length-scale $\lambda'_{NO}\big|_{t'=0}$ of the plate boundary, and decreases to either side of this region.

The two residence times are illustrated in the bottom part of figure 64(b) for the symmetrically-thickening case. This part of the figure plots crustal and mantle residence times vs. distance across-strike. ${}^{c}t_{RES}$ reaches a maximum of $\Delta x/V_P$ over a distance equal to the initial deformation length-scale, $\lambda'_{NO}\big|_{t'=0}$, and decreases to zero on either side of this region. In contrast, ${}^{m}t_{RES}$ decreases abruptly at the singularity from the retro- to the pro-side of the plate boundary, because of the movement of cool mantle lithosphere into the pro-side at convergence velocity, V_P. The rest of figure 64 shows equivalent cases assuming that most thickening occurs on the pro-side (figure 64(c)), and the retro-side (figure 64(d)) of the plate boundary. The magnitude and location of the differences between crustal and mantle lithosphere residence times depends on the distribution of thickening about the plate boundary.

Table 13 summarizes the predicted increase in T_{moho} and corresponding decrease in Am with maximum crustal residence time, $\Delta x/V_P$, caused by diffusion of the thermal perturbation after doubling the thickness of the crust (the temperature calculation is performed using a one-dimensional finite element model, which is described below and in Appendix G). As residence time increases, the local value for Am diminishes (by an order of magnitude for ${}^{max}t_{RES}$ = 90 My). The exponential decrease in Am with increasing temperature means that for $T_{moho} > 600$ °C, Am will be approximately constant for further increases in temperature (figure 19(a)), so that the initial temperature increase at the Moho will be most important in changing crust-mantle coupling characteristics. The decrease in Am is expected to cause an increase in the thickening rate away from the plate boundary. In the last two columns of Table 13, the maximum residence time is converted into convergence amounts for incident velocites of 1 and 5 cm/yr, using the assumption that maximum residence time ${}^{max}t_{RES} = \Delta x/V_P$.

Table 13: A simple scale analysis showing the decrease in Am with convergence

maximum crustal residence time (My)	maximum T_{moho} (°C)	minimum Am	equivalent convergence (km): u_0=1 cm/yr	equivalent convergence (km): u_0=5 cm/yr
0	450	0.75	0	0
10	521	0.29	100	500
20	551	0.19	200	1000
35	583	0.13	350	1750
45	600	0.10	450	2250
50	608	0.09	500	2500
90	655	0.05	900	4500

Table 13 shows the maximum possible decrease in Am with convergence assuming the Moho temperature is best represented by the crustal residence time. The true change in Am with convergence will be a function of position, and also depends on the residence time for the mantle lithosphere.

(ii) Numerical Calculations of the Effect of Thickening

The calculations illustrated in Table 13 are approximate, and if length-scale estimates were computed directly from Table 13, they would give an over-estimate of the diffusional effect because the computations neglect regions with strong crust-mantle coupling outside of the thickened zone. A better method to find the effect of thermal relaxation is to use a numerical finite element code (Braun, 1988), which solves the one-dimensional time-dependent heat flow equation (Appendix G), and couples the thermal and mechanical effects directly in the thin-sheet code. The advantage of the numerical method is that it can incorporate the effects discussed above (the continued motion and thickening of the crust and mantle lithosphere) directly, by solving for a temperature array throughout the crust and mantle lithosphere. A numerical implementation also allows a local Ampferer number to be found for every horizontal location, so that regions outside of the thickened orogen can retain strong crust-mantle coupling.

The details of the numerical thermal method are given in Appendix G, and involve the following simplifying assumptions:

1] The heat conduction equation is solved in the vertical dimension only (lateral heat conduction is neglected because of the large horizontal spatial scale of the problem);

2] Radiogenic heat production in the crust is neglected; if included, results for the decrease in T_{moho} with convergence would not change significantly (Appendix G).

3] The relationship between T_{moho} and Am from figure 19(a) is used to find the equivalent change in the local Ampferer number with time for each timestep. The use of figure 19(a) involves the assumption that the plot is valid for crust which has thickened to twice its initial value. In addition, note that the plot (figure 19(a)) was derived for a uniform layer of wet feldspar. Other assumed crustal compositions would change the relationship between Am and T_{moho}, but are not investigated in this thesis.

4] The change in crustal strength due to stretching of the crustal geotherm (before diffusion) is neglected in the calculations, except where it affects the strength of the basal detachment layer. Before diffusion, a crust of thickness $2S_0$ will have a maximum strength twice that of the equivalent undeformed crust, because the depth of the brittle-ductile transition will have increased. The doubling in crustal strength will initially reduce Am and Ar by a factor of 2. As the geotherm diffuses back to a steady-state value, the maximum crustal strength will return to its pre-thickened value, and Ar will return to its pre-thickened value, with the decrease in Am caused only by the weakening of the basal detachment layer. The effect of the initial decrease in Am and Ar with crustal thickening is neglected in the crust, because the simultaneous decrease in Am and Ar are assumed to counteract each other. If included, the change in parameter values would slightly change the increase in length-scales for small amounts of convergence.

The combined thermal/mechanical thin-sheet code is used in part (iii) of this sub-section, to determine the increase in basally-driven length-scales with convergence.

(iii) The Increase in Basally-Driven Deformation Length-Scale with Convergence

The calculations outlined above and in Appendix G are used in this sub-section to estimate how the change in crust-mantle coupling with convergence influences the deformation length-scale. To recapitulate briefly, the assumptions made for this analysis are: (i) Lateral heat conduction is neglected in the (1D) thermal calculations; (ii) The initial geotherm is assumed to give a temperature at the Moho of 450 °C, and crustal radiogenic heat production is not included in geotherm calculations; (iii) The effect of changes in crustal strength with thickening on parameters Ar and Am is neglected (except in the weak basal layer).

The effect of the diffusion of the geotherm is demonstrated in figure 65, for initial parameter values Am=0.75, Ar=5, n=3, and a convergence velocity V_P=1 cm/yr. Figure

Figure 65: Comparison of crustal thickness, S, after 1500 km of convergence, for a case where there is no thermal relaxation (top), and the same case but with thermal relaxation, and a convergent velocity of 1 cm/yr (lower part of figure). The arrows and dots under the figures represent velocities of 1 cm/yr and zero, respectively. The singularity point is indicated by the filled circle. Vertical exaggeration on the figure is 4, and other parameter values are n=3 and Ar=5, with an initial Ampferer number of 0.75. The effect of isostasy has not been included on the figure for ease of qualitative comparison; however, locally compensated cases would attain the same crustal thickening, provided the scaling number Ar remained the same.

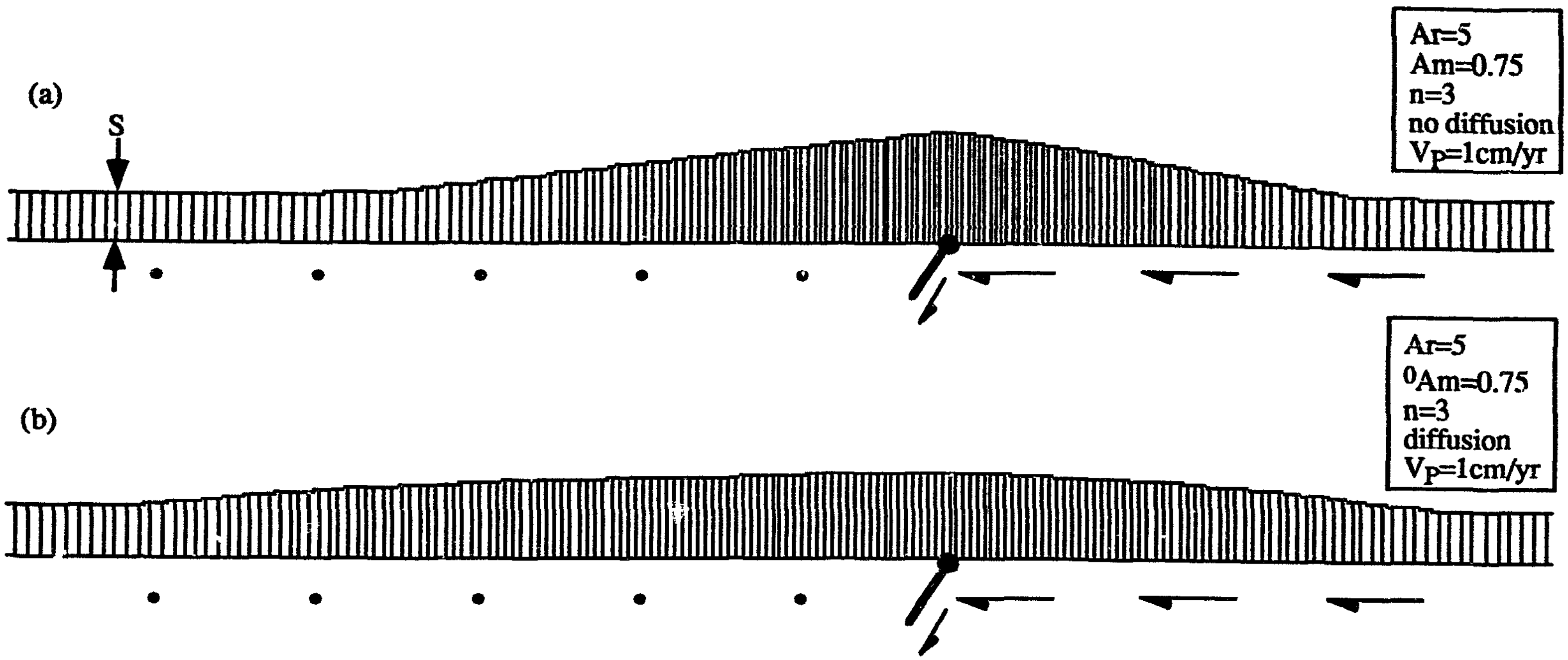

(a)
S
Ar=5
Am=0.75
n=3
no diffusion
Vp=1cm/yr
(b)
Ar=5
0Am=0.75
n=3
diffusion
Vp=1cm/yr

Figure 65

65(a) shows the distribution of crustal thickening for a case with no thermal relaxation, for 1500 km of convergence. The case with no change in the geotherm with thickening may be contrasted with a model which uses the numerical approximations outlined in Appendix G to incorporate diffusional effects, shown in figure 65(b). Both cases are shown with isostatic compensation effects removed, for ease of comparison.

The differences between figure 65(a) and (b) indicate the effect of thermal relaxation on crust-mantle coupling. Firstly, in the case with diffusion (figure 65(b)), crustal deformation extends over a wider region. Secondly, the case with the diffusion shows a pronounced asymmetry, with most thickening occurring on the retro-side of the plate boundary. The movement of cool mantle lithosphere into the pro-side of the boundary keeps the Moho temperature close to 450 °C, so that crust-mantle coupling remains high on the pro-side, whereas detachment increases preferentially on the retro-side, where mantle lithosphere is stationary and can heat up on timescales comparable to the those for crustal thickening. Finally, the case with diffusion (figure 65(b)) develops a plateau over the detached retro-side of the plate boundary, that is not present in the case without thermal relaxation (figure 65(a)).

A systematic analysis of numerical results such as that shown in figure 65(b), for deformation length-scales vs. convergence, is shown in figure 66(a). Results are shown for a range of possible values of Ar (Ar=1, 5) and convergent velocities (V_P=1, 5 cm/yr). The diffusional effect is significant for large amounts of convergence, and has a similar effect on length-scales to the Ar effect (figure 62, cf. figure 66), which was examined in the previous sub-section and is also incorporated into these results. Figure 66(b) compares the predicted length-scale increase to data from the natural examples of chapter five (figure 56). Since Ar values between 1 and 5 are considered acceptable, and most geological rates of convergence are between 1 and 5 cm/yr, data points that plot in the shaded area between the length-scale curves for these limits indicate agreement between the model and data.

The effect of thermal relaxation on crustal deformation style is important in terms of the shape and asymmetry of the deformation (e.g. figure 65), as well as for the trend of increasing length-scales (figure 66). An interesting effect observed during weakening of the crust-mantle detachment (not shown on the figures) is the change to uniform pure-shear thickening in the plateau region, where Am is close to zero. The more strongly coupled regions on either side of the plateau act as 'bookends' which squeeze the crust in between like an accordion. Therefore, even after crust in the plateau region becomes totally detached from the mantle lithosphere, it still undergoes some contraction. The continued compressive environment suggests that a *steady-state* decrease in crust-mantle coupling, such as that investigated here, cannot provide a general mechanism for the extensional collapse of orogens (Dewey, 1988). However, the model results do not rule out the possibility that contraction and extension may occur together over different parts of the model domain (e.g. results from chapter three, figure 20(a), which shows simultaneous extension (near the surface) and contraction (deeper in the model crust) over part of the model domain, for the cross-sectional, plane-strain viscous model).

The agreement shown in this and the preceding sub-section between data and the basally-driven model (figure 66), demonstrates that a combination of gravity acting on thickened crust, and diffusive heating of thickened crust, may provide a possible explanation for the trend in the data.

Figure 66: (a) The predicted basally-driven length-scale curves for 1 and 5 cm/yr convergent velocities, and Ar=1 and 5, with diffusion of the crustal geotherm. (b) Comparison of basally-driven predictions with the natural data. Range of predicted curves (from Ar=1, 5 cm/yr to Ar=5, 1 cm/yr) is shaded.

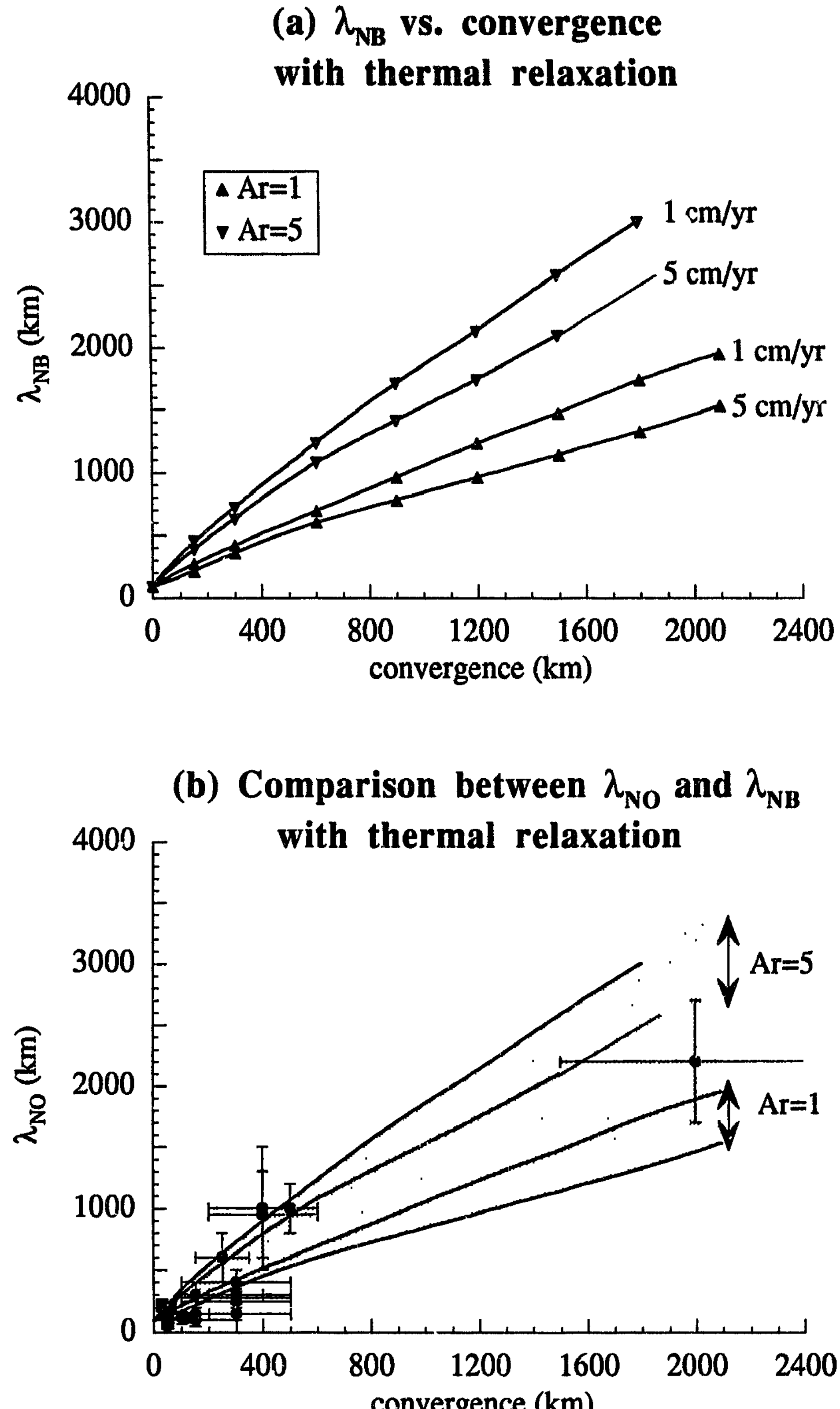
(a) λ_{NB} vs. convergence
with thermal relaxation
λ_{NB} (km)
convergence (km)
Ar=1
Ar=5
1 cm/yr
5 cm/yr
1 cm/yr
5 cm/yr
(b) Comparison between λ_{NO} and λ_{NB}
with thermal relaxation
λ_{NO} (km)
convergence (km)
Ar=5
Ar=1

Figure 66

§ 6.3 Comparison of Model Predictions with the Evolution of the Tibetan Plateau

The remoteness of the locality, and lack of constraining seismic and geologic data, have so far prevented the construction of a detailed history for the tectonic evolution of the Tibetan Plateau (Dewey et al., 1988). However, the combination of a large along-strike extent of collision (D~3000 km), a rapid rate of collision (~ 5 cm/yr), and large amounts of convergence since the initial collision of India and Eurasia (~2000 km), make the Himalayan-Tibetan system the best example of a large-scale orogenic system currently on Earth (Molnar and Tapponnier, 1975; England and Houseman, 1986) (figure 67).

In this section, the predicted evolution of model length-scales with convergence is tested against evidence for the spatial development (with time) of the Tibetan Plateau. The model length-scale predictions are based on the qualitative results from chapter four and section 6.2, for the development and change in length-scale dependences with increased convergence. The comparison is performed for each of the possible deformation styles, and include (for the basally-driven case) the modifications for changing Am with convergence investigated in section 6.2. The predictions for each case are summarized below, and then compared to the evolution of the India-Eurasia collision. The general purpose of this section is to determine whether more accurate estimates of length-scale evolution would provide constraints on the mechanics of collision for such a large-scale system.

Figure 67: The India-Eurasia collision, simplified from a figure by Peltzer and Tapponnier (1988). The position of major thrust and strike-slip faults is indicated. The stippled region indicates extensively thickened topography (~over 1500m elevation). MCT refers to the Main Central Thrust in the Himalayas.

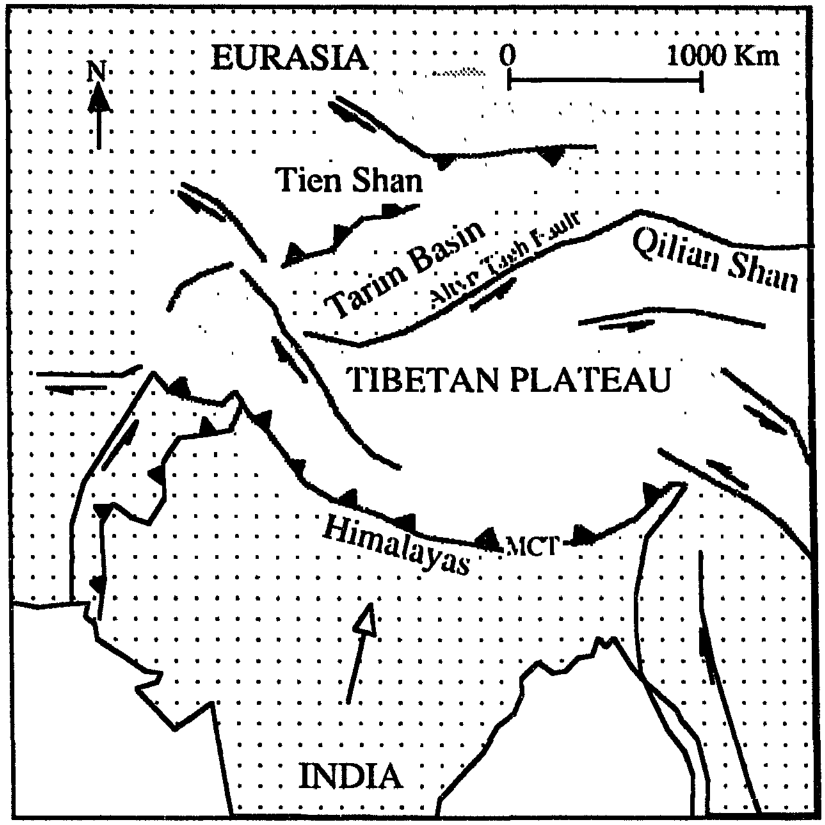
EURASIA
N
0
1000 Km
Tien Shan
Tarim Basin
Altyn Tagh Fault
Qilian Shan
TIBETAN PLATEAU
Himalayas
MCT
INDIA

Figure 67

Model Predictions

(i) Side-Driven Model Predictions

The change in deformation length-scales with t' for the side-driven case was found to depend on the relative effects of n, the power-law exponent for the lithosphere (the higher n, the more likely mass will become concentrated just in front of the indenter), and Ar, the Argand number, which controls the amount of lateral tectonic escape of mass away from the indenter. The cases investigated in chapter four (figures 39, 40) did not show an increase in the deformation length-scale, as measured by thickening, with convergence. If the system is dominated by strain-rate weakening effects in front of the indenter, the length-scale actually *decreases* with t', and if Ar is large so that gravity effects dominate the system, the length-scale stays constant or also decreases with t', because of the tectonic escape along-strike. The results shown in figures 39 and 40 would be modified somewhat for different-shaped (kinematic) indenters (cf. section 4.4 and the results of England and Houseman (1986)), as I show later in this section, and the length-scale may actually increase with t' for a sufficiently large Ar (Ar >>1). However, the increase is small compared to the equivalent basally-driven increase.

Thermal relaxation is unlikely to be important for the side-driven whole-lithosphere case, because if the lithosphere thickens uniformly in response to stress applied by an indenter, lithospheric temperatures will heat up on a diffusive timescale of $\tau \sim L^2/\kappa =$ 320 Ma (where L is the thickness of the lithosphere, ~ 100 km), which is much larger than orogenic timescales. The average values of Ar and n are therefore unlikely to change significantly for the side-driven case, unless there is an additional heating mechanism (e.g. convective removal of thickened mantle lithosphere (England and Houseman, 1988). The predictions for evolution of a large-scale orogenic system, if controlled by whole-lithosphere, indenter mechanics, are therefore:

1. Small changes in deformation length-scale with t' (depending on Ar, and the shape of the indenter).

2. No significant change in Ar, n during syn-orogenic thickening, although a plateau may form in regions which have thickened significantly.

(ii) Basally-Driven Model Predictions

Unlike the side-driven case, an orogen whose deformation is controlled by detachment and subduction of underlying mantle lithosphere is expected to grow away from the plate boundary with normalized convergence, t' for all values of the Argand number. The increase in length-scale is initially caused by the effects of gravity on crustal thickness gradients (Ar), but as discussed in the last part of section 6.2, the increase may also depend on the heating of the weak layer (at the Moho) with time, from the diffusion of the thickened crustal geotherm, as illustrated in figures 65-66.

Because there are no variations in the velocity boundary condition along-strike for the basally-driven case investigated in this thesis, there is no lateral tectonic escape, so that for a normally convergent system, there will be no strike-slip component of deformation. The predictions for evolution of a large-scale orogenic system, if controlled by subduction of underlying mantle lithosphere with no along-strike variations, are therefore:

1. The length-scale of deformation will increase with t', according to the type of relationship illustrated in figure 66.
2. Orogens which have a relatively high rate of convergence (≥ 5 cm/yr) will grow outwards more slowly with normalized convergence, than those with slower rates of convergence (due to the effect of thermal relaxation).
3. There will be no lateral movement of mass along the plate boundary.

More generally, a basally-controlled system may also have along-strike variations in the plate boundary; these variations will allow tectonic escape of mass away from the converging zone, and the system will then become similar in behaviour to the mixed model predictions discussed below.

(iii) Mixed Model Predictions

The mixed model has a deformation length-scale which, as shown in chapter four, is controlled by either indenter mechanics or mantle lithosphere kinematics, depending on the relative sizes of the predicted length-scale for each case. For typical ($D >> S_0$) along-strike dimensions of the velocity boundary condition, the deformation length-scale will therefore be controlled by the basal boundary condition, and will grow with t' according to the predictions discussed for (ii) above. Eventually, when the indenter length-scale limit (D) is approached, the extent of deformation increases more slowly with t', and further growth of the orogen will be mainly by lateral escape of mass along-strike. The predictions for evolution of a large-scale orogenic system, if controlled by mixed boundary conditions, are therefore:

1. Initially, Am will be relatively large (~0.75 if the geotherm is assumed to be ~ 15 °C/km, giving a starting deformation length-scale of ~ 90 km for n=3). For all but the smallest along-strike velocity boundary conditions, D, orogens are basally controlled.
2. As the orogen grows, the length-scale increases because of (i) the effect of gravity on crustal thickness contrasts (Ar), and (ii) decreasing Am (as discussed in section 6.2) with thickening.
3. Eventually, the deformation length-scale will approach the side-driven limit, and orogen growth will become controlled by indenter mechanics. The tectonic escape component will increase as this limit is reached.
4. Therefore, it is expected that the convergent zone will start as a long, narrow orogen; it will grow outwards with convergence; as Am decreases, there will be increased tectonic escape, with a transition to a length-scale controlled by indenter mechanics. The transition to side-driven behaviour implies that strike-slip faulting

may become dominant over some part of the thickened crust, and large growth across-strike will cease (i.e. the orogen will seek to grow laterally instead).

Comparison of Predictions to the Tibetan Plateau

Numerous studies of the development of the Tibetan Plateau (figure 67) exist in the literature, many of which allow different interpretations (see for example the ongoing debate over the amount of mass lost by lateral extrusion (tectonic escape), vs. crustal thickening (Tapponnier et al., 1982, cf. Dewey et al., 1988)). Despite these differences, and the lack of a proven mechanism for the development of the Tibetan Plateau, there is general agreement that the onset of significant continental thickening occurred at about 45 Ma, and that deformation has propagated northwards across Tibet since that time (Molnar and Tapponnier, 1977; Dewey et al., 1989b). (Note that the actual start of collision is not well constrained, and may have begun as early as 60 Ma in some areas (e.g. Beck et al., 1995)). I follow the tentative reconstructions of Dewey et al. (1988) and Mercier et al. (1987) for the timing of various events which can be gleaned from the geological record. Although some of the details of these reconstructions may prove to be incorrect, I believe that the general sequence of events is well enough constrained to facilitate a qualitative comparison with the predictions made above.

According to Dewey et al. (1988), the uplift of the Tibetan Plateau was accomplished in three main stages. The first stage involved convergence of about 1000 km between 45 and 30 Ma, conjectured to have occurred by northward-propagating crustal shortening and deformation. The evidence that thickening propagated northwards with time, rather than occurring synchroneously across the Tibetan Plateau, is sparse, and based on evidence from the northern edge of the Plateau (Molnar et al., 1987). During stage one, Tibetan crust doubled its thickness to ~ 65 km, over a total across-strike distance of about 1000 km.

Stage two began when further thickening to the north was blocked at ~ 30 Ma by the strong lithosphere of the anomalous Tarim Basin, which acted as a 'spacer' to transfer thickening out to the Tien Shan mountain belt. In Tibet, north-south shortening by thrusting changed to shortening by conjugate strike-slip faulting, with small amounts of east-west extrusion. The evidence for a change from north-south shortening to strike-slip faulting after 30 Ma is based on dating of fault structures, paleomagnetic data, and geometrical mass-balancing arguments (Dewey et al., 1989b). Mercier et al. (1987) estimate that the change occurred somewhat later, at ~20 Ma. Thrusting along the MCT (Main Central Thrust) in the Himalayas also began at ~ 25-20 Ma (Mercier et al., 1987), and thickening may have propagated southwards into the Himalayas at this time (Dewey et al., 1988). Note that there is evidence that convergence and extension occurred contemporaneously in the northern Himlayas during the Miocene (Burg and Chen, 1984; Burchfiel and Royden, 1985), indicating possible decoupling between different levels of the crust (Burchfiel and Royden, 1991).

For the last 5 Ma (stage three), north-south shortening has continued north of Tien Shan; east-west extension has occurred on the Plateau, with conjugate strike-slip faulting, for at least the last 2 Ma (Armijo et al., 1982, 1986), and uplift of up to 2 km may have occurred. The rapid uplift episode has been inferred (i) from paleobotanical and paleoclimatological evidence (Li et al., 1981; Xu, 1981), (ii) from cooling (exhumation) ages of fission track data in the Himalayas (Zeitler, 1985), and (iii) from timing of extensional features and recent volcanics on the Plateau (Molnar and Tapponnier, 1975; Chen and Molnar, 1977) . The debate over the extent of Pliocene to Recent uplift of the Tibetan Plateau, and its implications for mantle dynamics and crustal extension, has not been resolved (e.g. England and Houseman, 1988; Burchfiel and Royden, 1991; Molnar et al., 1993; Willett and Beaumont, 1994), and will not be addressed in this discussion.

The crucial points which can be compared to the predictions made at the start of this sub-section, are the increase in deformation length-scale with convergence across-strike, and the timing and amount of tectonic escape on the Plateau. The rough estimates from Dewey et al. (1988) are summarized in a figure which plots length-scale vs. convergence (figure 68), and compares the data to model predictions. The length-scale data from before the Pliocene are sparse, and a best-fit linear relationship has been fitted to the data points, based on the conjectures of Dewey et al. (1988). This assumption (of a linear increase in length-scale before the Pliocene) remains a major weak point of any comparison between data and models for evolution of the Tibetan Plateau, as will be shown below.

Figure 68: (a) A comparison of the evolution of length-scales for the Tibetan Plateau (solid circles, and best-fit line, based on Dewey et al., 1988), with predictions from the side-driven model. Side-driven length-scale predictions are shown for Ar=1 and 5, (dashed lines), with the region in between shaded. (b) Comparison with the basally-driven model, for Ar=1 and 5 (dashed lines). Basally-driven length-scale predictions are from section 6.2 for a velocity of 5 cm/yr. Am decreases from 0.75 to 0.3 as convergence increases. (c) Figure illustrating the construction of the mixed model length-scale predictions (dashed line) for Ar=5. The limiting length-scale predictions for the side-driven and basally-driven models (solid lines) are also shown. The transition region between basal and indenter control for the mixed model is estimated by eye, and so is approximate. The unfilled circles represent the beginning of the transition zone for each case. (d) Comparison between the mixed model predictions for Ar=1, 5 (constructed as in (c)) and the evolution of length-scales for the Tibetan Plateau. The unfilled circles indicate that significant strike-slip faulting is expected to initiate at these convergence times, and will be ongoing (as indicated by the arrows). Significant strike-slip faulting is predicted as the deformation length-scale becomes controlled by the side-driven length-scale limit.

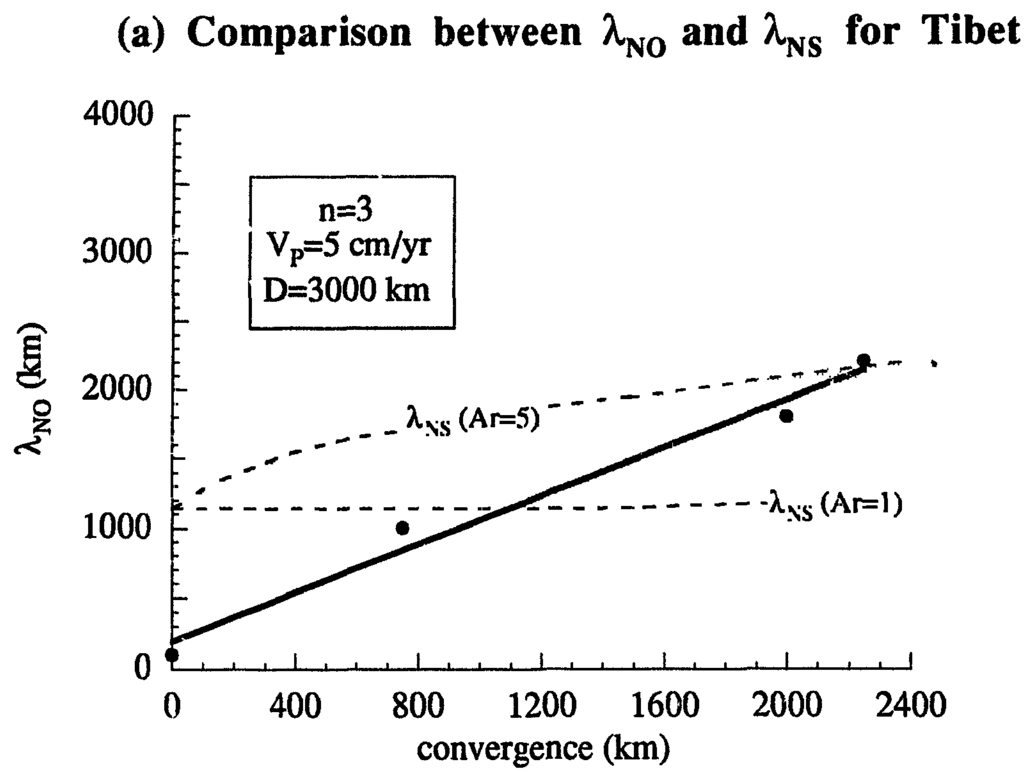
(a) Comparison between λ_{NO} and λ_{NS} for Tibet
n=3
V_P=5 cm/yr
D=3000 km
λ_{NS} (Ar=5)
λ_{NS} (Ar=1)
λ_{NO} (km)
convergence (km)
0
1000
2000
3000
4000
0
400
800
1200
1600
2000
2400

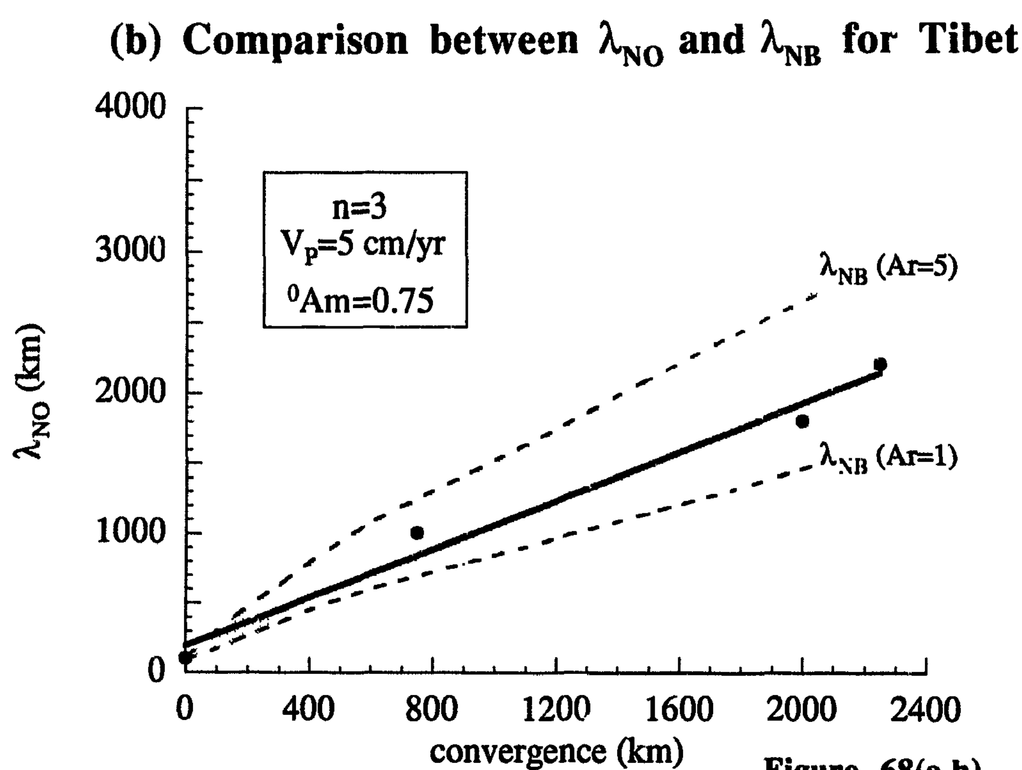
(b) Comparison between λ_{NO} and λ_{NB} for Tibet
n=3
V_P=5 cm/yr
^{0}Am=0.75
λ_{NB} (Ar=5)
λ_{NB} (Ar=1)
λ_{NO} (km)
convergence (km)
0
1000
2000
3000
4000
0
400
800
1200
1600
2000
2400

Figure 68(a,b)

(c) Construction of mixed curves

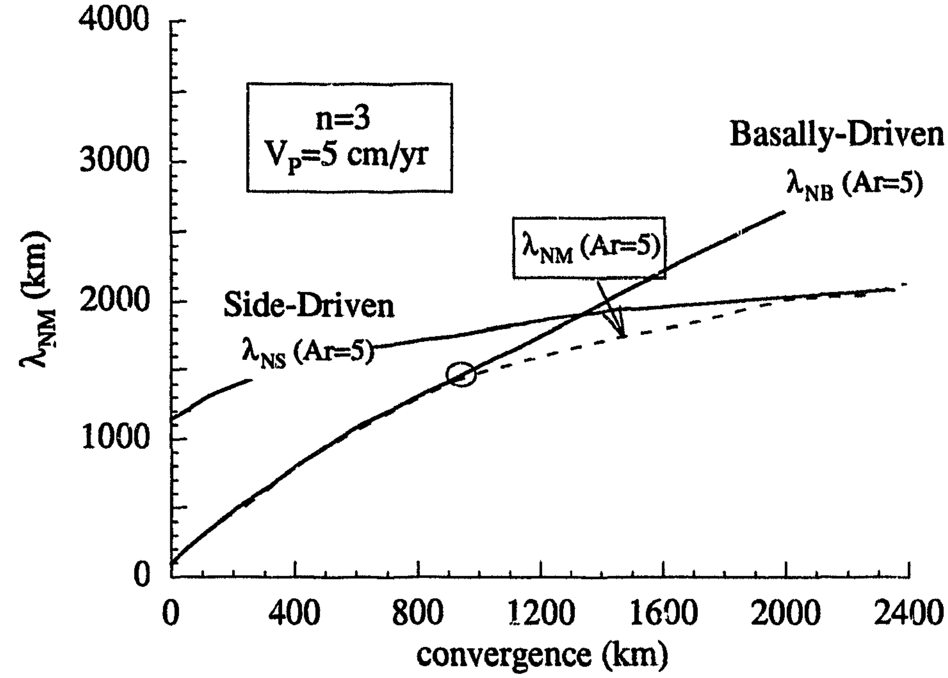

(d) Comparison between λ_{NO} and λ_{NM} for Tibet

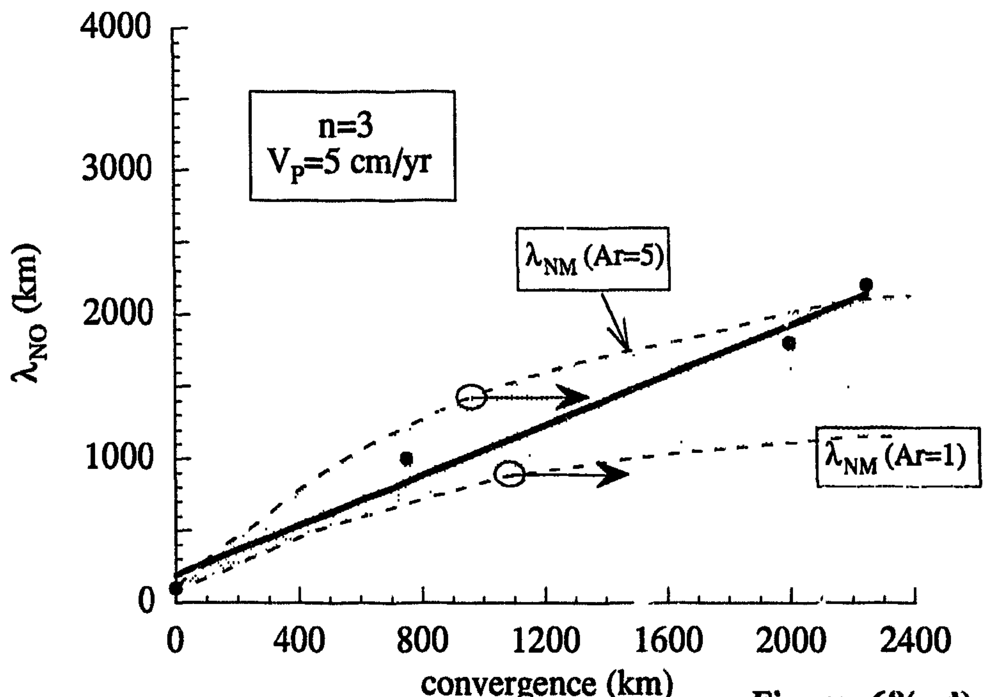

Figure 68(c,d)

In figure 68(a), the estimated increase in length-scale with convergence for the Tibetan Plateau (solid circles and best-fit, thick line) is compared to numerically derived results for the side-driven model. Model predictions for two values of Ar (Ar=1, 5), using the indenter shape of figure 36(d) in chapter four, and n=3, are shown by the dashed lines on the figure. Ar=1 and 5 are taken to bracket the geologically realistic values for the Argand number, based on the experiments of chapter three using a wet feldspar crust, and previous numerical studies of the Tibetan Plateau (England and Houseman, 1986). The region between the two bracketing values for Ar is shown shaded, and suggests the probable range for side-driven length-scale predictions. As discussed previously, even for high values of Ar, side-driven length-scales do not increase very fast with convergence, because of the tectonic escape term. The side-driven predictions in figure 68(a) are in agreement with current length-scale estimates for the Tibetan Plateau for Ar~5; however, if the conjecture that Tibetan length-scales of deformation increased approximately linearly with convergence in stage 1 is correct, the side-driven predictions do not fit the early evolution of the Tibetan Plateau.

The length-scale estimates of Dewey et al. (1988) are compared to the basally-driven model results in figure 68(b). The basally-driven length-scale predictions are taken from the results outlined in section 6.2 (figure 66), with V_P=5 cm/yr; Am therefore decreases from ~ 0.75 to 0.3 over the convergence interval of ~ 2000 km. As for the side-driven case, length-scale predictions are shown for Ar=1 and Ar=5, with the region between the two curves shaded. The filled circles and best-fit thick line represent the estimates of Dewey et al. (1988). The agreement between the shaded region and the length-scale estimates for the Tibetan Plateau indicates that the basally-driven model, with no along-strike mass movement, is a valid alternative to the side-driven model of England and Houseman (1986).

The construction of equivalent length-scale estimates for the mixed model is illustrated in figure 68(c), for Ar=5, and with an indenter length-scale of 3000 km and an

Ampferer number which decreases from ~0.75 to 0.3 as the temperature at the Moho increases. Although for small convergence times (chapter four) mixed model length-scales are ~1/2 the equivalent basally-driven length-scales when deformation is controlled by subduction of underlying mantle lithosphere, in this analysis I assume the length-scales are roughly equal. This assumption is based on the growing asymmetry of a basally-driven orogen with time, so that for both basally-driven and mixed models, thickening occurs mostly on the retro-side of the plate boundary. The mixed model therefore has length-scale limits: (i) the basally-driven length-scale for an equivalent Ar, and Am which decreases with convergence; and (ii) the side-driven length-scale for an equivalent Ar. The construction of the estimated length-scale increase for the mixed model is based on these limits, as illustrated in figure 68(c), using the transition criteria established in chapter four. The mixed model curve in the figure has not been derived numerically, but by best-fit to the limiting basally-driven and side-driven cases. Therefore, the construction is approximate, and is meant to indicate the trend in the length-scale increase with convergence. The solid lines are the side-driven and basally-driven limits for Ar=5. The unfilled circle represents the approximate convergence amount at which the mixed curve (for a given Ar) diverges from the basally-driven prediction.

Mixed model curves estimated in the manner shown in figure 68(c) are compared to the estimates of Dewey et al. (1988) in figure 68(d), for Ar=1 and 5. The region between the two mixed curves for Ar=1, 5 is shaded. The correspondence between the mixed curve with Ar=5 and the data indicates that this model is also a possible explanation for the evolution of the Tibetan Plateau with convergence. An interesting feature of the plot is the location of transition from basal control towards the side-driven limit (unfilled circles). The unfilled circles represent the approximate convergence amount at which strike-slip faulting is expected to become important, as the mixed model adjusts to the limit imposed by the finite along-strike length-scale, D. The point at which the length-scale diverges from basal control is therefore taken to predict the onset of strike-slip faulting on the Tibetan Plateau. The strike-slip faulting is expected to continue for convergence amounts greater than the start of the transition region, as indicated by the arrows. For the best-fit curve with Ar=5, the onset of significant strike-slip faulting is expected to occur after ~1000 km of convergence, which may be compared with the estimates of Dewey et al. (1988) and Mercier et al. (1987), for strike-slip faulting initiation at ~ 30 Ma (Dewey et al., 1988) and ~ 20 Ma (Mercier et al., 1987), respectively, corresponding to amounts of convergence of 750 km and 1250 km.

This result suggests that a combination of indenter mechanics and basal forcing may be able to explain first-order style of thickening on the Tibetan Plateau. However, given the tentative nature of the geological evidence, these comparisons are not conclusive. In particular, the conjectured northward progression of shortening and thickening across the Tibetan Plateau is not well constrained (Molnar et al., 1987; England and Searle, 1986; Shackleton and Chengfa, 1988). The comparison could be improved if we had a better knowledge of the uplift history of the Tibetan Plateau, especially the timing and spatial extent of various stress regimes, and the length-scale of deformation at various points in the evolution of the thickened region. For instance, conclusive evidence for an increase in deformation length-scales for the Plateau similar to the suggested increase shown in figure 68, for small convergence (<1000 km), could be used to distinguish more easily between an orogen which is controlled by indenter mechanics from the outset, compared to an orogen which is initially controlled by subduction of mantle lithosphere, and grows out to the limit imposed by the finite extent of the indenter.

In addition to the cautions expressed above, it should be noted that none of the models by themselves are able to explain the inferred sudden uplift, increased volcanism, and extensional features which have developed on the Plateau over the past ~2-5 Ma. This requires an appeal to either convective removal of thickened mantle lithosphere for the side-driven case (England and Houseman, 1988), or retreat of the subducting mantle lithosphere towards Asia (Willett and Beaumont, 1994), to initiate a rapid heating event under the Plateau.

§ 6.4 Recapitulation: Physical Styles of Behaviour of Convergent Lithosphere

The styles of behaviour of the crust or lithosphere in convergent and strike-slip settings investigated in this thesis are based on two main styles of forcing, the whole-lithosphere side-driven (indenter) and basally-driven (mantle lithosphere subduction) models, as well as a mixed model, which has indentation from the side and detachment of mantle lithosphere. Although the physical settings leading to each of the model assumptions have been discussed individually earlier in the thesis, section 6.4 attempts to bring the models together in a physically consistent manner, in order to summarize the conditions under which a particular model style will best represent the behaviour of the lithosphere at a plate boundary.

Convergent Plate Boundaries

The different assumptions which produce model styles for a convergent zone are illustrated in figure 69 as a flow diagram. The first-order difference which controls behaviour is whether the mantle lithosphere is assumed to thicken and deform, as shown in the left-hand side of the figure, or to subduct, as shown on the right-hand side. Within each of these subsets of behaviour, another important control on deformation style is the relative strength of the crust and/or mantle lithosphere on either side of the plate boundary zone. The indenter model assumes that the strengths are very different, so that one side of the plate boundary indents the other side without significant deformation (case LI ≡ 'lithospheric indenter', the side-driven case). Whole-lithosphere deformation with *no* significant differences in strength across the plate boundary (case LX) is not physically possible, because there would be no reason for deformation to localize near the plate boundary.

For the alternative end-member style (right-hand side of figure 69), mantle lithosphere subducts. The polarity of the subduction may depend on the relative crust-mantle coupling on either side of the plate boundary. A difference in strength between the crust and weak detachment layers on either side of the plate boundary is likely to lead to a combination of indenter and basally-driven mechanics, giving the mixed model that was investigated in chapter four (figure 69, case CI ≡ 'Crustal Indenter'). If there is no significant contrast in strength and crust-mantle coupling across the plate boundary, crust on both sides of the plate boundary will deform, in a manner dictated by the basal

---

Figure 69: A flow diagram indicating the different assumptions that lead to the various model styles for convergent plate boundaries investigated in this thesis. The first choice for a convergent system is whether mantle lithosphere thickens along with the crust (left-hand choice), or detaches and subducts (right-hand choice). If the mantle lithosphere thickens, and the average lithospheric strength on one side of the plate boundary is much stronger than the other, case LI is the result: the whole-lithosphere, indenter, side-driven case. If mantle lithosphere thickens but there is little difference in strength across the plate boundary (case LX), deformation will not necessarily localize at the plate boundary; this case is not investigated. Taking the right-hand assumption, that mantle lithosphere detaches and subducts, leads to two alternative choices for deformation style. CI is the mixed case, where significant differences in strength and coupling on either side of the plate boundary lead to a combination of indenter and basally-driven mechanics. If there are no significant strength differences (case CB), crustal deformation will be basally driven and will not depend on the along-strike length-scale.

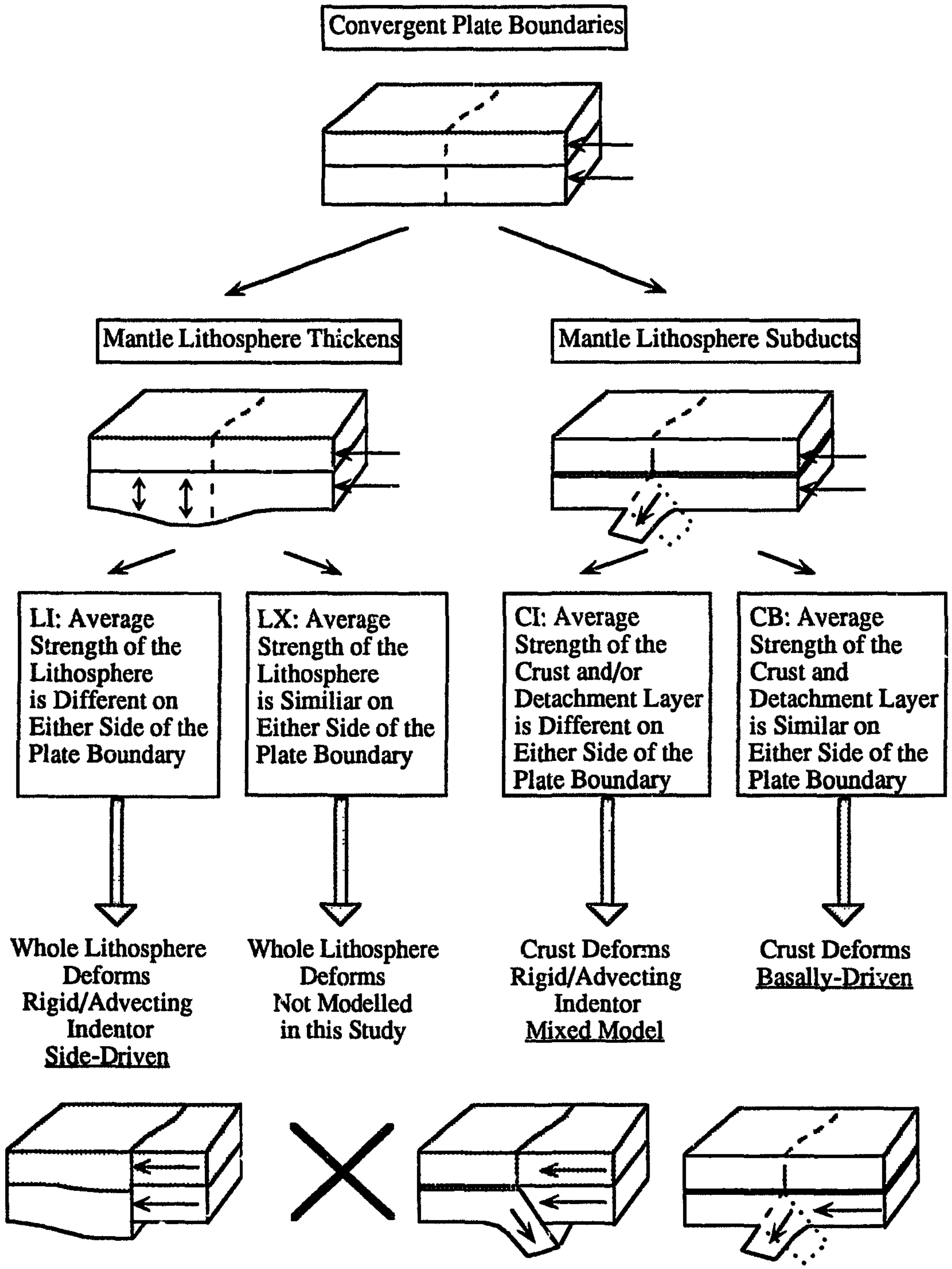
Convergent Plate Boundaries
Mantle Lithosphere Thickens
Mantle Lithosphere Subducts
LI: Average Strength of the Lithosphere is Different on Either Side of the Plate Boundary
LX: Average Strength of the Lithosphere is Similiar on Either Side of the Plate Boundary
CI: Average Strength of the Crust and/or Detachment Layer is Different on Either Side of the Plate Boundary
CB: Average Strength of the Crust and Detachment Layer is Similar on Either Side of the Plate Boundary
Whole Lithosphere Deforms Rigid/Advecting Indentor Side-Driven
Whole Lithosphere Deforms Not Modelled in this Study
Crust Deforms Rigid/Advecting Indentor Mixed Model
Crust Deforms Basally-Driven

Figure 69

boundary conditions (case CB ≡ 'Crust driven by Base', the basally-driven case). Note that for the cases CI and CB, there are two possibilities for the polarity of mantle subduction. The subduction polarity shown for CI is considered most likely for the mixed model (see discussion at the end of this section), whereas either choice of polarity for mantle lithosphere subduction in the basally-driven case (CB) is possible. The two choices for subduction polarity impose different kinematical constraints on the deforming crust, as will be discussed later in this section.

Strike-Slip Plate Boundaries

Figure 70 illustrates an equivalent flow-diagram of possible mechanical behaviours in strike-slip settings. As for the convergent case, if the whole lithosphere deforms and is much stronger on one side of the plate boundary than the other, the system will be driven by indenter mechanics, and length-scales will depend on the lateral extent of the strike-slip boundary conditions (figure 70, case LI). Case LX, for whole-lithosphere deformation with no contrasts in strength across the plate boundary, may be possible if there is a strain-weakened vertical contact at the boundary (e.g. Molnar, 1992), but is not considered in this thesis.

If the mantle lithosphere detaches from the crust (right-hand panel of figure 70), and the crustal strength and crust-mantle coupling on either side of the plate boundary are different, the system will behave according to the mixed boundary conditions, where the deformation length-scale will be controlled by the minimum predicted length-scale from the indenter and basal mechanics (case CI). If there is no strong difference in strength across the plate boundary, the crust will be basally-driven (case CB). The geometry of the contact between the two plates in the mantle lithosphere is unknown, but it is conjectured that, since most strike-slip boundaries considered in this thesis have a small compressive component of motion, the contact in the mantle will be angled in a similar manner to the convergent cases illustrated in figure 69.

Figure 70: The equivalent flow diagram (to figure 69) for strike-slip plate boundaries. If the whole lithosphere is assumed to deform on the same horizontal length-scale (left-hand choice), and there are different strengths on either side of the plate boundary, the deformation will best be modelled by the whole-lithosphere side-driven indenter model (case LI). As for figure 69, the whole lithosphere case where there are no significant strength differences across the plate boundary (case LX) is not modelled in this study. The right-hand column, which assumes that the mantle lithosphere is detached from the crust along a weak simple-shear layer, leads to two alternative styles: case CI, where significant strength differences across the plate boundary lead to a combination of indenter and basally-driven mechanics, and case CB, which is solely basally-driven.

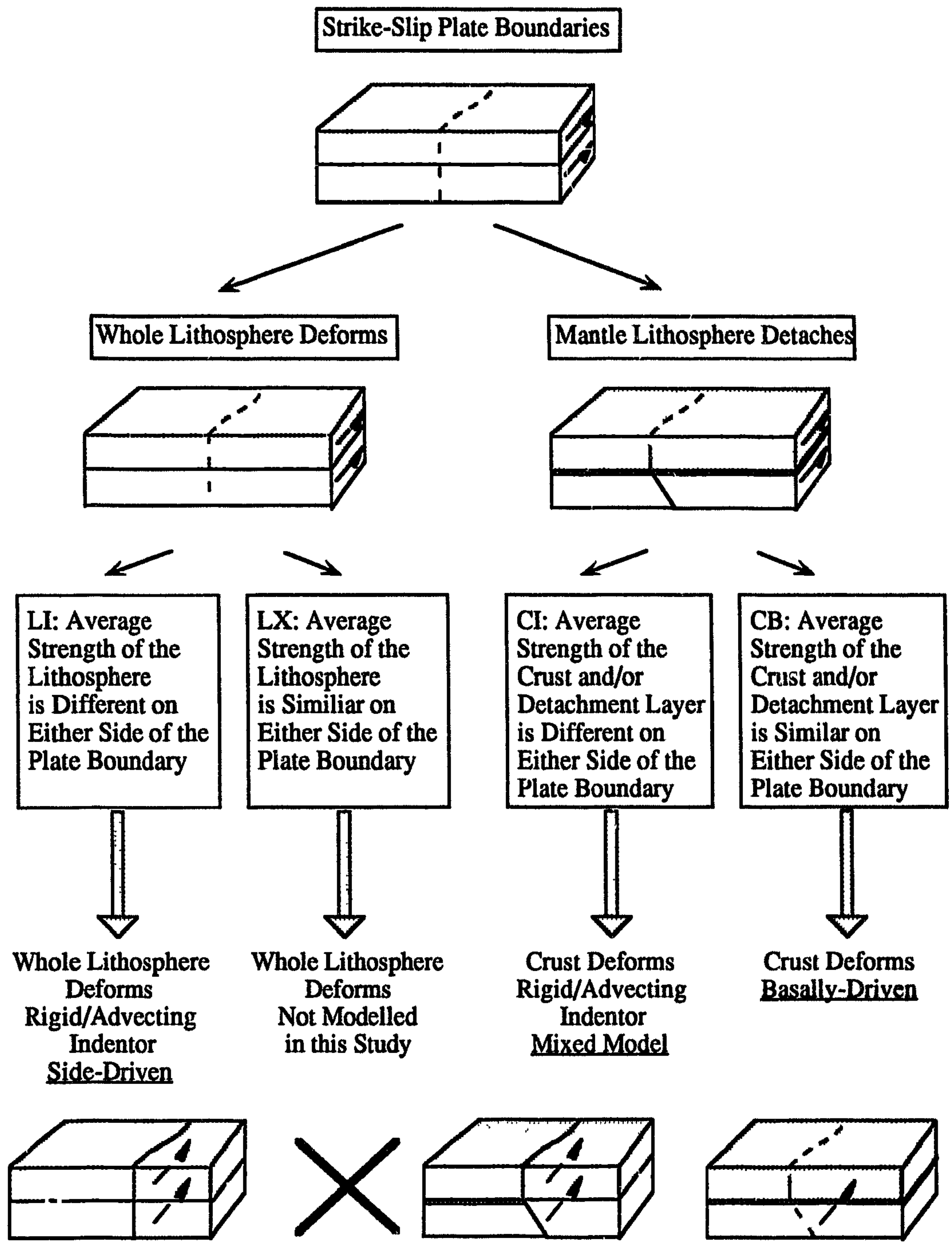
Strike-Slip Plate Boundaries
Whole Lithosphere Deforms
Mantle Lithosphere Detaches
LI: Average Strength of the Lithosphere is Different on Either Side of the Plate Boundary
LX: Average Strength of the Lithosphere is Similiar on Either Side of the Plate Boundary
CI: Average Strength of the Crust and/or Detachment Layer is Different on Either Side of the Plate Boundary
CB: Average Strength of the Crust and/or Detachment Layer is Similar on Either Side of the Plate Boundary
Whole Lithosphere Deforms Rigid/Advecting Indentor Side-Driven
Whole Lithosphere Deforms Not Modelled in this Study
Crust Deforms Rigid/Advecting Indentor Mixed Model
Crust Deforms Basally-Driven

Figure 70

Intra-continental vs. Active Margin Plate Boundary Development

A continental plate boundary may develop within an initially homogeneous plate due to in-plate stresses, or may occur at an already existing, active (subduction) plate boundary when relative plate motions cause two continental plates, (or a continent and island arc/ oceanic plateau) to collide. Examples of the former, intra-continental type include the Kapuskasing structural zone (convergent setting) and the northern Anatolian Fault (strike-slip setting). The crust on either side of the plate boundaries in these examples appears to have a similar geological and thermal history. Examples that have evolved from active margins include the India-Asia collision (convergent setting) and the San Andreas Fault Zone (strike-slip setting).

The site of plate boundary development may determine the style of deformation, and whether it is controlled by indentation or mantle subduction, as illustrated in figures 69 and 70. Intra-continental development of a plate boundary is less likely to produce different crustal and detachment strengths across the boundary, although it is possible that intra-plate stresses may reactivate deformation on an old plate boundary within the craton. For most intra-continental settings, however, there will be no significant strength contrasts across the newly formed plate boundary, so that the initial deformation may be controlled by basally-driven mechanics. If this conjecture is correct, length-scales of intra-continental deformation for small amounts of convergence should show little dependence on along-strike length-scales (D).

Conversely, continental collision or strike-slip plate boundaries developing on active subduction margins are very likely to inherit significant differences in crustal strength and crust-mantle coupling across the boundary zone. Strength differences will arise not only because of the abutment of continental lithospheric plates which may have originated in very different settings, and experienced different thermal and tectonic evolutions, but also because of the transient thermal effects at active subduction boundaries. For instance, when India collided with Eurasia, the (Lhasa) Eurasian margin had been the site of active oceanic subduction for over 80 My (Ricou, 1994), and is likely to have developed a fairly high heat flow due to effects of the subducting slab, whereas the passive northern margin of India was probably much stronger and cooler, with strong coupling between the crust and mantle lithosphere. Differences in strength across such a collisional plate boundary may produce deformation which initially follows the whole lithosphere indenter, or mixed indenter/mantle detachment model, as illustrated in figure 69.

The speculations discussed above lead to the testable prediction that intra-continental plate boundaries will have a deformation length-scale which does not depend on, and in general is much less than, the predicted side-driven length-scale. This seems to be in agreement with convergent and strike-slip boundaries which have developed in situ, such as the Kapuskasing convergent zone, and the Levant and Anatolian fault zones; length-scales for these cases are all significantly under the length-scale predicted by the side-driven thin sheet model. Examples of collisional plate boundaries which developed at active margins have length-scales on or below the side-driven prediction (e.g. the Zagros length-scale is just above, and the Urals length-scale is below, the predicted length-scale; the San Andreas and Chaman fault zones lie on the side-driven prediction), which is in agreement with length-scales for deformation controlled by a combination of indenter and basal detachment mechanics. Alternatively, the trend in the data can also be explained solely in terms of the basally-driven model, with larger deformation length-scales predicted at evolved active margins because of higher thermal gradients (and therefore lower values of the Ampferer number) at disturbed, vs. undisturbed, plate boundaries.

The Transition from Oceanic Subduction to Continental Convergence, and the Polarity of Mantle Lithosphere Subduction for the Mixed and Basally-Driven Cases

The transition from an active subduction margin to a continental collisional plate boundary is a common evolutionary sequence for orogenic belts. An active subduction margin has a number of first-order controls which determine crustal behaviour on the continental side. The most important, as discussed in chapters 1 and 2, is the movement of the trench relative to the stable cratonic interior (Doglioni, 1992; Royden, 1993a, 1993b). Retreating subduction zones may be characterized by extensional features, and do not involve significant thickening of the crust. In contrast, if the trench moves towards the continental landmass, the margin is an advancing subduction zone, and conservation of mass requires that the continental crust and mantle lithosphere must either be thickened, or lost from the system by subduction and/or lateral tectonic escape. Advancing subduction and continental collision therefore may produce similar styles of thickening for continental crust.

(i) Advancing Oceanic Subduction

Some conceptual possibilities for the advancing subduction case which conserve mass in the mantle lithosphere are illustrated in figure 71. In the top figure, both the crust and mantle lithosphere of the continental plate (continent #1) thicken together. The trench moves with velocity V_S, and if the oceanic lithosphere is much stronger than continent #1, it will act as a rigid indenter. This case is therefore directly analogous to the side-driven models of England and McKenzie (1982). The bottom panel of figure 71 shows an alternative conceptual model, which also conserves mass, and in which the continental lithospheric mantle is entrained by, and subducts with, the oceanic lithosphere. The idea that some of the mantle lithosphere of continent #1 subducts follows from the 'ablative subduction' concept of Tao and O'Connell (1992), and should be possible provided the crust and mantle of continent #1 are separated by a weak detachment layer. Figure 71(b) is directly analogous to the mixed model introduced in chapter four, where the mantle lithosphere (of continent #1) is assumed to detach from the crust over a region adjacent to a rigid indenter (oceanic lithosphere). Although the sense of subduction in the two cases (figure 41, chapter four, cf. figure 71(b)) appears to differ, the subduction of oceanic lithosphere does not enter into the equivalent model for figure 71(b) directly, and by adding an opposite velocity $-V_S$ to the advancing subduction case, it can be seen that the ablative subduction of continental mantle lithosphere (figure 71(b)) applies the same horizontal kinematic boundary condition to the base of the continental crust as for the case where mantle subduction polarity is towards the indenter (figure 41). Note that in figure 71(b) the detachment zone moves towards the stable continental interior with velocity V_S, along with the indenting oceanic lithosphere.

Figure 71: Two alternatives for advancing subduction; (a) continental mantle lithosphere thickens and deforms with the crust, according to the whole-lithosphere side-driven model; (b) continental mantle lithosphere follows the oceanic lithosphere downwards according to the ablative subduction ideas of Tao and O'Connell (1992). In both (a) and (b), mass is conserved in the mantle lithosphere. V_P is the incident velocity of the oceanic lithosphere, and V_S is the velocity of the trench relative to the stable continental interior (represented by the nail). The dark shaded region in (b) represents a detachment layer between crust and mantle lithosphere.

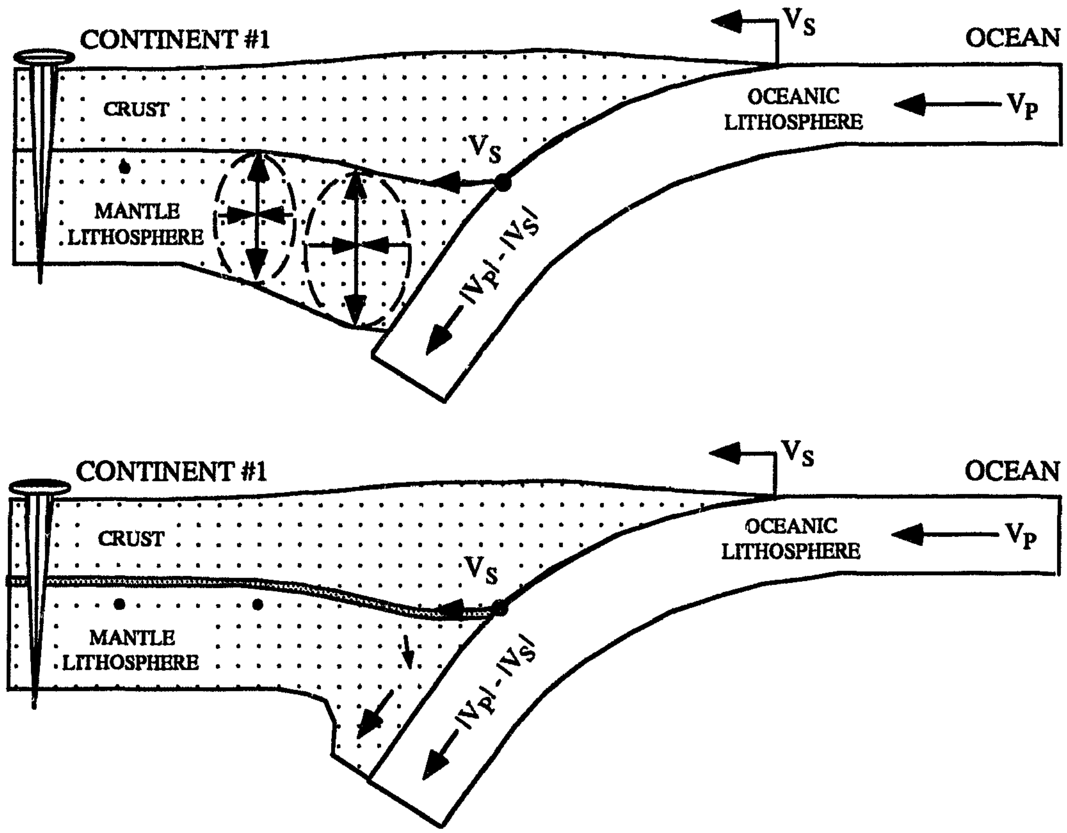
CONTINENT #1
OCEAN
V_S
CRUST
OCEANIC LITHOSPHERE
V_P
V_S
MANTLE LITHOSPHERE
$|V_P| - |V_S|$
CONTINENT #1
OCEAN
V_S
CRUST
OCEANIC LITHOSPHERE
V_P
V_S
MANTLE LITHOSPHERE
$|V_P| - |V_S|$

Figure 71

(ii) Continent-continent collision

The initial stages of collision between two continental landmasses generally occur as the result of a continent being 'rafted in' towards an active subduction margin. As discussed in the previous sub-section, strength differences (and therefore, in the limit, some form of indenter mechanics) are likely across the plate boundary. The early stages of collision will be controlled by the kinematics of the preceding oceanic subduction zone, and there may be an attempt to subduct continental crust ('A'-type subduction), which will be resisted by buoyancy forces. Eventually the kinematics of the system will change to the thickening of some part of the converging crust, with three possible modes of deformation for the underlying mantle lithosphere (figure 72), assuming that significant strength differences still exist across the plate boundary.

Figure 72: Three possibilities for the deformation of lithosphere (continent #1) which is being indented by a much stronger continental lithosphere (continent #2, represented by white layers). (a) whole lithosphere deformation according to the side-driven model. The strong continental lithosphere deforms primarily by elastic flexure, and is not modelled. (b) Case where the mantle lithosphere on the strong (indenting) continent #2 side detaches and subducts. (c) Case where the mantle lithosphere on the weaker (continent #1) side detaches and subducts. Mass is conserved in the mantle lithosphere in all cases. The original position of the singularity at the start of deformation is shown by the unfilled circle for (a-c), and linked between plots by the dashed straight line. The dashed profiles on figure 72 (a) and (c) show the original position of continent #2. The dark shaded region in (b) and (c) represents a detachment layer between crust and mantle lithosphere.

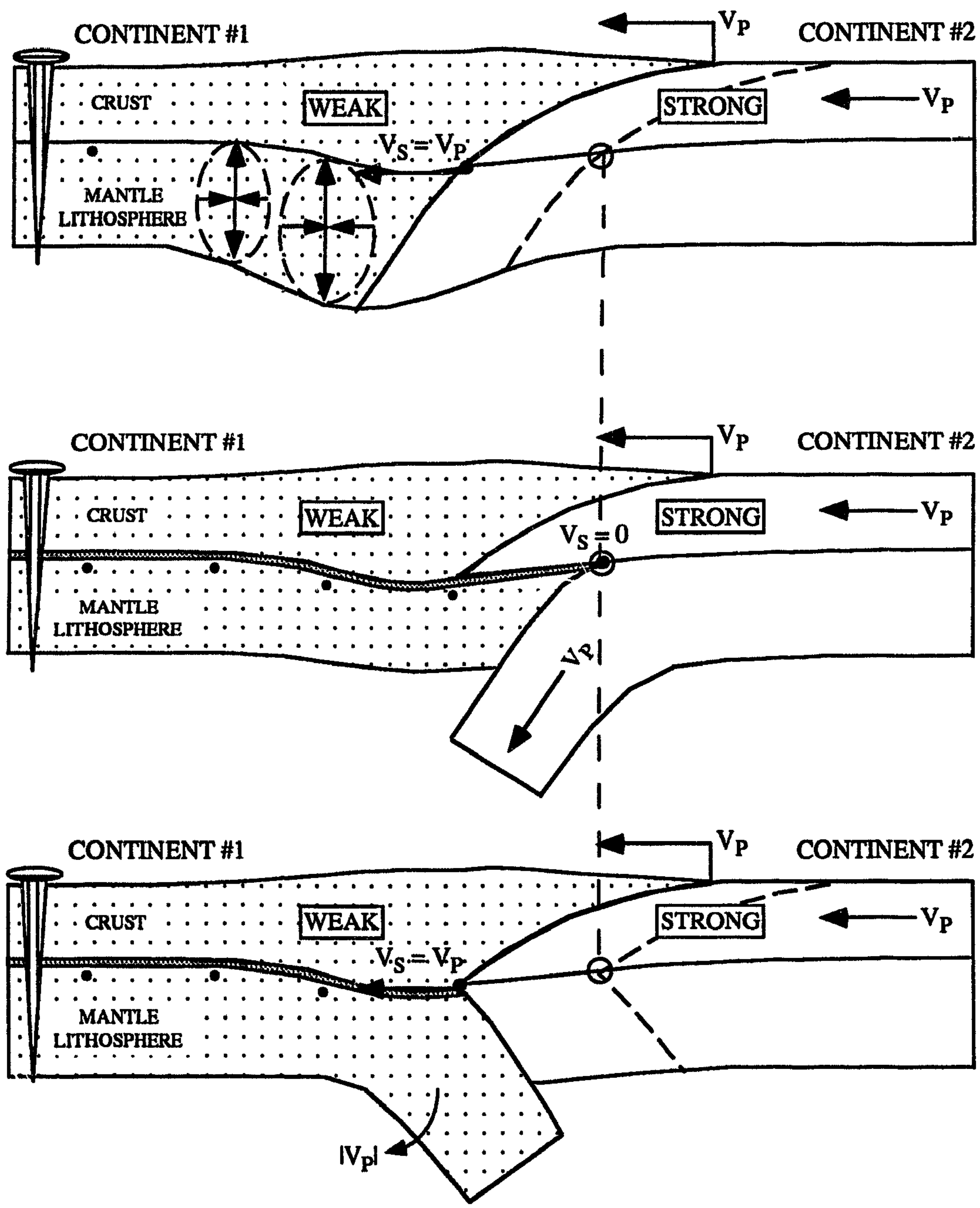
CONTINENT #1
VP
CONTINENT #2
CRUST
WEAK
STRONG
VP
VS = VP
MANTLE
LITHOSPHERE
CONTINENT #1
VP
CONTINENT #2
CRUST
WEAK
STRONG
VP
VS = 0
MANTLE
LITHOSPHERE
VP
CONTINENT #1
VP
CONTINENT #2
CRUST
WEAK
STRONG
VP
VS = VP
MANTLE
LITHOSPHERE
|VP|

Figure 72

Figure 72(a) illustrates the deformation style in which the mantle lithosphere of continent #1 (which was previously adjacent to an active margin) thickens and deforms along with the crust, over a length-scale determined by the along-strike variation in indenter velocity, D, of the rigid, strongly-coupled (continent #2) lithospheric plate (LI model, cf. figure 71(a)). In figure 72(b), the mantle lithosphere detaches from the crust and subducts towards continent #1, following the remaining oceanic lithosphere downwards. Conservation of mantle lithospheric mass dictates that, as the stronger (continent #2) crust indents into the weaker side, the point of detachment for the subducting mantle lithosphere will separate from the crustal position of the plate boundary, so that indenter and subduction-driven mechanics will become separated. This mechanism therefore injects the strong, indenting crust of continent #2 into continent #1. Although possible, no geophysical data strongly suggest this configuration at any recently converging plate boundaries.

Figure 72(c) suggests an alternative detachment symmetry, in which mantle lithosphere subduction polarity is flipped, and detachment and subduction occurs in the direction of continent #2, the stronger, indenting side. I consider the asymmetry represented by figure 72(c) to be probable, because the effective Ampferer number for the side of the plate boundary which was initially an active margin (continent #1), with associated volcanics and high heat-flow, is likely to be lower than for the passive margin side (continent #2). The weaker coupling between crust and mantle lithosphere for continent #1 will make it easier for the mantle lithosphere on this side to detach and subduct. Conservation of mantle lithospheric mass predicts that the point of detachment will move along with the indenting crust, so that the stronger mantle lithosphere acts as a 'ram' to split the weaker lithospheric plate along the detachment layer. (However, once subduction of continent #1 mantle lithosphere is initiated, the subduction pull from the negatively buoyant mantle lithosphere may keep the process going). From the reference frame of the stable continental interior of continent #1, the singularity or detachment point of the subducting mantle lithosphere appears to retreat as the stronger indenter (continent #2) advances, so that $V_S=V_P$.

Note that in both figure 72(a) and 72(c), the detachment point retreats with velocity $V_S=V_P$, but that in figure 72(b) $V_S=0$, and the injecting crustal tip has velocity V_P. The configurations shown in figure 72 are similar to the set of alternative models for the deformation of the Tibetan Plateau, summarized in figure 2 of Willett and Beaumont (1994). The above analysis, which considers model cases based on the relative velocities and deformation style of the mantle lithosphere, ties these models together into a consistent series of mechanical styles.

The proposed flip in subduction polarity during the change from oceanic subduction to continental collision for the mixed model, as shown in figure 72(c), is in agreement with the suggestion made by Willett and Beaumont (1994) for the evolution of the Tibetan Plateau (figure 67). They suggest that during the India-Eurasia collision, the sense of subduction changed from subduction of oceanic lithosphere towards Eurasia, to subduction of Eurasian mantle lithosphere towards India. Evidence in favour of this polarity flip comes from the position of the continental suture, which is much closer to the Indian side of the plate boundary, indicating that most of the continental mass on the Plateau is derived from Eurasia. From the reference frame of Siberia, subduction of Eurasian mantle lithosphere will move continental crust towards India, keeping the continental suture close to the initial site of collision. Note that, as Willett and Beaumont (1994) also cautioned, the side-driven indenter model (LI on figure 69, also shown as figure 72(a)) provides an equally valid explanation for the position of the suture, if India is indenting Eurasia.

If strength differences across a continental convergence zone are small, the deformation of the lithosphere may follow the basally-driven deformation style (figure 69, case CB). As discussed above, this is most likely for plate boundaries which develop in intra-continental settings. Either polarity choice for mantle lithosphere subduction is possible, if the crust-mantle coupling is (initially) similar everywhere. The two choices are illustrated in figure 73(a) and (b). In figure 73(a), mantle lithosphere from continent #2 subducts towards continent #1. In the reference frame of the stable interior of continent #1, the velocity of the singularity is zero, and continent #2 is the 'pro'-lithosphere. Figure 73(b) illustrates the alternative case where the mantle lithosphere of continent #1 detaches and subducts towards continent #2. In the reference frame of the stable interior of continent #1, the velocity of the singularity is V_P, with retreat of the subduction towards continent #1. However, in the reference frame of the stable interior of continent #2 (obtained by adding $-V_P$ to all velocity vectors), the velocity of the singularity is zero (figure 73(c)). The two cases (figure 73(a) and 73(b,c)) are therefore equivalent, except for the direction of convergence, and they will have opposite asymmetries in crustal deformation style when viewed from the same reference frame (Beaumont et al., 1994a, 1994b).

Figure 73: Three possibilities for the deformation of crust which is driven by detachment and subduction of underlying mantle lithosphere. (a) continent #1 stationary; subduction of pro-mantle lithosphere from continent #2, at velocity V_P. The singularity is stationary (V_S=0). (b) Continent #1 is stationary, but the mantle lithosphere of continent #1 subducts; V_S=V_P. (c) The equivalent case to (b), from the reference frame of the singularity; V_S=0 and the pro-mantle lithosphere of continent #1 subducts. The symmetry of case (a) is opposite to cases (b) and (c). The dark shaded region represents a detachment layer between crust and mantle lithosphere.

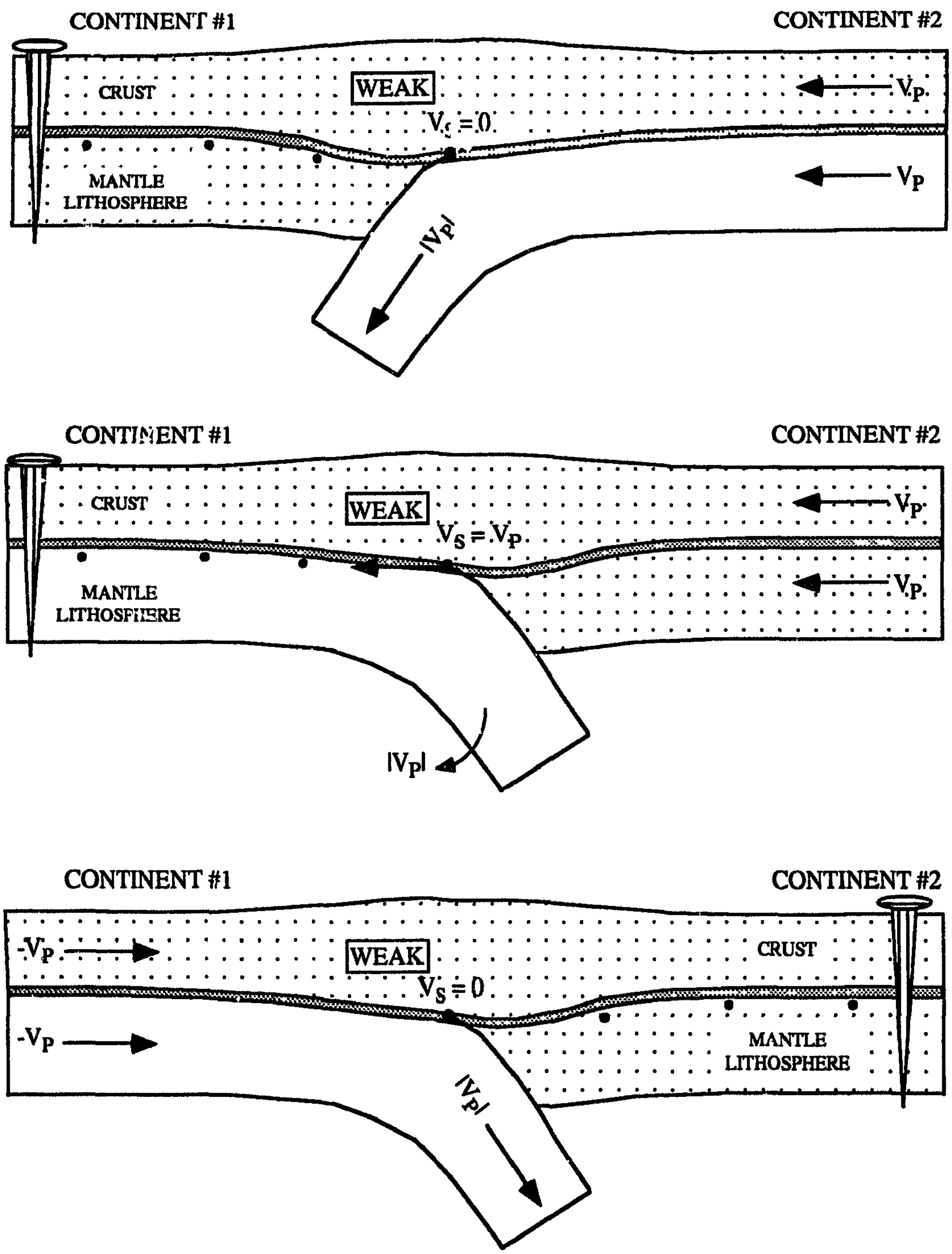
CONTINENT #1
CONTINENT #2
CRUST
WEAK
$V_S = 0$
V_P
V_P
MANTLE
LITHOSPHERE
$|V_P|$
CONTINENT #1
CONTINENT #2
CRUST
WEAK
$V_S = V_P$
V_P
V_P
MANTLE
LITHOSPHERE
$|V_P|$
CONTINENT #1
CONTINENT #2
$-V_P$
WEAK
$V_S = 0$
CRUST
$-V_P$
MANTLE
LITHOSPHERE
$|V_P|$

Figure 73

Summary of Conceptual Basis for Models

The conceptual models illustrated in figures 69 and 70 provide a template of behavioural styles which give a framework for the real behaviour of continental lithosphere at convergent zones. They cannot represent the true complexity of the lithosphere, but may provide some insight into processes which exert a first-order control on deformation. Evidence from studies of mantle dynamics is not conclusive enough to determine which of the model styles is physically more likely, and whether convergent deformation will cause the mantle lithosphere to recycle into the asthenosphere by a steady-state process, as suggested for the mixed and basally-driven models, or cycle through a different series of behaviours with time, depending on transient thermal and physical parameters (e.g. the convective instability behaviour explored by Houseman et al. (1981)).

§ 6.5 Summary

The purpose of chapter six is to tie together a number of the threads investigated throughout the thesis. The chapter started by extending the length-scale studies from chapters four and five to large convergence times. By incorporating a one-dimensional thermal routine into the thin-sheet code, it was shown that the Ampferer number (i.e. crust-mantle coupling) is likely to change for the basally-driven model at large convergence times. An approximate study of the increase in length-scale with convergence was in agreement with the trend found in the natural data in chapter five.

The predicted increase in length-scales with convergence were used in a comparison between the evolution of the largest-scale orogen on earth, the Tibetan Plateau, and the side-driven, basally-driven, and mixed models. Although all three models styles were admissible given the lack of knowledge of deformation history on the Tibetan Plateau, the mixed model gave the best agreement with the data. It is suggested that the change from a basally-driven limit to indenter mechanics with convergence may explain the onset of strike-slip faulting on the Tibetan Plateau.

The recapitulation summarized the different physical settings likely for each of the model styles investigated in chapters four and five. In particular, an effort was made to predict possible mechanical styles based on the inherited properties of continental lithosphere. Given that most collisional plate boundaries develop on previously active oceanic subduction zones, it was concluded that the indenter or mixed styles of deformation are most likely to be representative of collisional processes on Earth.

Chapter Seven

CONCLUSIONS

This thesis has investigated styles of crustal deformation using the premise that interactions at convergent plate boundaries will fall between two main end-member styles of behaviour. The fundamental assumption behind this approach is that the lithosphere behaves as a partially coupled system. A simple viscous thin-sheet representation of the crust has been developed to investigate these two end-members, using velocity boundary conditions applied at the side and base of the model domain.

The side-driven (whole-lithosphere) end-member follows from the work of previous modellers (e.g. England and McKenzie, 1982), and assumes that the crust and mantle lithosphere deform together with no shear between them (figure 69, LI). The basally-driven end-member (figure 69, CB) is equivalent to the models of Willett et al. (1993), but investigates deformation in the planform for cases which have relatively little cross-sectional shear. One of the benefits of simplifying the basally-driven case to study planform effects has been the development of a scaling number, the Ampferer number, to describe the relative coupling between the crust and mantle lithosphere. Using a simple scaling technique, a straightforward, and often analytical, analysis is possible, and can be used to determine the controls on deformation length-scales for a basally-driven orogen.

The results of the scaling analysis, and the comparison between model predictions and length-scale measurements from natural examples, are summarized overleaf.

§ 7.1 Summary

1. Two contrasting end-member styles of deformation at a convergent/strike-slip plate boundary are investigated using the simple thin-sheet model. The behaviour of the lithosphere for the side-driven model can be characterized in terms of the parameters Ar (the dimensionless Argand number), n (the average power-law exponent for viscous creep in the lithosphere), and D (the along-strike length-scale of the indenter). In contrast, the basally-driven model uses a new dimensionless number (the Ampferer number, Am) to parameterize the effect of the detaching mantle lithosphere on overlying crust. The deformation of the crust for this case is characterized in terms of Am, Ar, and n.
2. Model crust which deforms according to the side-driven model assumptions has deformation length-scales (at small convergence times) which depend on D, Ar, and n. Deformation length-scales become unbounded as $D \to \infty$. The length-scale for normally convergent plate boundaries is approximately four times as large as the length-scale for strike-slip plate boundaries, given the same set of parameter values. For oblique convergence, the ratio of normal and transcurrent deformation length-scales is in general between 4 and 1, depending on the value for n, and the obliquity of convergence.
3. Model crust which deforms according to the basally-driven model assumptions has deformation length-scales (at small convergence times) which depend on Am, Ar, and n. Deformation length-scales become unbounded as $Am \to 0$. The length-scale for normally convergent plate boundaries is approximately twice the length-scale for strike-slip plate boundaries, given the same set of parameter values. For oblique convergence, the ratio of normal and transcurrent deformation length-scales is in general between 2 and 1, depending on the value for the power-law exponent, n, and the obliquity of convergence.

4. A combination of the basally and side-driven cases (the 'mixed' case) is used to represent a case where mantle lithosphere detaches, and crust on one side of the plate boundary is much stronger, so that there is a combination of basal forcing and indenter mechanics. Length-scale dependences for this case are a combination of the side-driven and basally-driven cases, which act as limiting bounds.
5. Growth of normal deformation length-scales with increasing convergence for the basally-driven model is much more likely than for the side-driven model. For the basally-driven model, the magnitude of the length-scale increase depends on the value of Ar. For the side-driven model, lateral tectonic escape away from the indenter prevents large increases in length-scales normal to the plate boundary.
6. A comparison at small convergence times of the length-scale predictions for the side- and basally-driven models, with length-scales and aspect ratios for natural plate boundary examples, is inconclusive in determining the more likely driving mechanism for crustal deformation.
7. The increase in deformation length-scales of natural examples with convergence is best explained in terms of the basally-driven model, with a decrease in the crust-mantle coupling with convergence, as the crust thickens and the base of the crust heats up.
8. Qualitative comparisons between the growth in deformation length-scales with time predicted for the side-, basally-driven, and mixed models, with the conjectured evolution of the Tibetan Plateau, suggests that a combination of basal forcing and indenter mechanics may best explain the observed deformation.
9. Given the large uncertainties in determining length-scales, and the evolution of length-scale in time for natural examples, it is concluded that the length-scale analysis cannot emphatically determine whether mantle lithosphere thickens or detaches and subducts during plate boundary interactions.

§ 7.2 A Cautionary Note

Results from the thesis are dependent on the simplifying assumptions and approximations that have been made. For instance, the simplifications concerning the rheology of the lithosphere for both the side-driven and basally-driven models are dubious. The end-member models assume that the rheology of the crust or lithosphere can be represented, in an average sense, by a power-law viscous sheet. This prevents the representation of cross-sectional shear zones in the crust. The rheological properties of the lithosphere make likely the existence of internal detachment zones along weak layers, so that the whole-lithosphere models of England and McKenzie (1982) may be unrealistic; however, the assumption of the basally-driven model, that the mantle lithosphere subducts without significant ductile deformation, is also unlikely. The consequences of detachment occurring at a different site to the Moho (e.g. Ord and Hobbs, 1989; England and Houseman, 1988; Beaumont et al., 1994a), or between multiple layers, have not been investigated for the basally-driven model. The true behaviour of the lithosphere will be a combination of some of the properties inherent in the side-driven and basally-driven cases. Until observations can determine the true behaviour of the lithosphere, firm conclusions should not be drawn from model results.

All of the models assume that plate boundary processes occur in a continuous manner in time and space, with local isostatic compensation and continued convergence or strike-slip motion. This is certainly an over-simplification of real plate boundary interactions. Tectonic forcing may be episodic, and the type of compensation may change as crust thickens. No attempt is made in this thesis to examine how the removal of thickened mantle lithosphere by convective instability, as proposed by Houseman et al. (1981), will affect length-scales of deformation. Similarly, the change in symmetry of an orogen during convergence, due to a change in the direction of mantle lithosphere subduction (Willett and Beaumont, 1994), has not been investigated. Post-convergent extension and its effect on the length-scale of convergent orogens has been neglected in the analyses of chapters five and six.

The effect of erosion and deposition at the earth's surface has not been investigated in the thesis. Such an investigation would be limited to large planform scales (>3x the crustal thickness) by the thin-sheet model requirements, and so would only be able to incorporate surface processes using diffusive mass transport. Diffusive surface processes could be incorporated into the model fairly easily, however, as described in chapter two.

Results from the scale analysis suggest that there are some predictable differences between deformation controlled by indenter (side-driven) mechanics, and by detachment and subduction of mantle lithosphere. These differences were explored in some detail in chapter four, and were extended to large convergence times in chapter six. In principle, the different predictions could be used to distinguish between different styles of driving mechanism for crustal deformation at convergent and strike-slip settings. The results from the latter half of this thesis, however, indicate that the search for proxy indicators of mantle lithosphere dynamics at plate boundaries must continue. These results suggest that the continuation of simple length-scale analyses such as those conducted in this thesis may have reached their useful limit. In particular, a major difficulty in interpreting scale analysis results is the large choice of parameter values (for example, choices for n, the power-law exponent, which is generally assumed to be between 3 and 10, but may decrease for thickened crust). Most of the trends found in the length-scales for natural examples can be satisfactorily explained by any of the models, given an appropriate choice for the parameters Ar, Am, and n.

Problems also occurred in finding sufficient natural examples to test the model predictions. This is particularly the case for large-scale normally convergent examples, and strike-slip settings. Many candidate examples could not be used in the scale analysis, because their evolution was too complex, or unknown. However, even if a larger number of natural examples of convergent and strike-slip settings could be found, it is unlikely that the comparison to the simple model predictions would be any more conclusive.

§ 7.3 Future Directions

Despite the limitations discussed above, the simple approach taken in this thesis has allowed the investigation of some possible first-order controls on deformation style in convergent settings. In order to advance our knowledge of crustal and mantle processes at plate boundaries, I believe that more detailed studies of deep crustal and mantle lithosphere structure are required. Imaging of the mantle lithosphere by seismic tomography and other methods may provide some direct information on what happens to the mantle in convergent zones. Better constraints on times of uplift and exhumation of rocks, as well as timing of movement along fault and thrust structures; detailed gravity, magnetic and heat-flow surveys; and many other useful field techniques for crustal deformation may help to determine good proxy measures of mantle processes. Recent advances in computational techniques have made possible much more detailed numerical models, which can compute displacements and deformation for complex, layered rheologies and coupled thermo-mechanical systems. Comparison of these models with deep geophysical data and the metamorphic history of exhumed rocks may also provide better constraints than simple length-scale analyses, to refine our concepts of how the lithosphere deforms.

Appendices

Appendix A

The Effect of the Shear Traction on the Integrated Vertical Force Balance

The vertical force balance equation (4) contains a term in $\partial\tau_{zx}/\partial x$ (= $\partial\tau_{xz}/\partial x$), and this appendix investigates whether this term will have a significant effect on the integrated vertical force balance. Integrating with respect to z gives:

$$p(z) = P_0 - \int_0^z \rho g\, dz' + \int_0^z \frac{\partial\tau_{zx}}{\partial x} dz' + \int_0^z \frac{\partial\tau_{zz}}{\partial z'} dz'$$

As stated in chapter 2, the model assumption is that where the elastic mantle lithosphere is below yield, it acts as a thin elastic beam in compensating the load of the thickened crust (Appendix B). At greater depths, below the elastic region, it is assumed that the mantle is isolated from the shear traction by the elastic beam, and that this region is hydrostatic. Therefore only the deviatoric stress gradients in the crust need to considered. The integrated pressure over the lithosphere is:

$$P_L = \int_{\text{lithosphere}} \left(P_0 - \int_0^z \rho g\, dz' \right) dz + \int_{\text{crust}} \left(\int_0^z \frac{\partial\tau_{zx}}{\partial x} dz' + \int_0^z \frac{\partial\tau_{zz}}{\partial z'} dz' \right) dz$$

The shear stress τ_{zx} is zero at the top of the crust, and equal to the applied shear traction, T^b_{xz}, at the base of the crust. Using the simplifying approximation that within the crust the shear stress varies linearly between these two values, and that $z^* = z+L-w$, gives:

$$\int_0^S \int_0^{z^*} \frac{\partial\tau_{xz}}{\partial x} dz'\, dz^* \equiv \int_0^S \int_0^{z^*} \frac{\partial T^b_{xz}}{\partial x} \left(1 - \frac{z^*}{S}\right) dz'\, dz^* = \frac{\partial T^b_{xz}}{\partial x} \frac{S^2}{3}$$

The vertically integrated term in $\partial\tau_{xz}/\partial x$ (neglecting gradients in crustal thickness, and using eq. (9)) is therefore:

$$\frac{\mu_b}{h}\frac{S^2}{3}\frac{\partial(\bar{u}-u_m)}{\partial x}$$

To determine whether this term is important, it is compared with the vertically integrated term in $\partial\tau_{zz}/\partial z$. This term may be found from incompressibility and assuming a linear viscous relationship in the crust, to be:

$$S\bar{\tau}_{xx} = 2\mu_c S\frac{\partial\bar{u}}{\partial x}$$

Normalizing the vertically integrated deviatoric stress terms as in section 3 gives:

$$\int_{z^*=0}^{z^*=S}\int_{0}^{z^*}\frac{\partial\tau_{xz}}{\partial x}dz'\,dz^* \cong \frac{\mu_b S_0{}^2 u_0}{3h\lambda_m}\frac{\partial(\bar{u}'-u_m')}{\partial x'} \qquad \text{...(A1)}$$

$$\int_{z^*=0}^{z^*=S}\int_{0}^{z^*}\frac{\partial\tau_{zz}}{\partial z'}dz'\,dz^* \cong \frac{2\mu_c S_0 u_0}{h}\frac{\partial\bar{u}'}{\partial x'} \qquad \text{...(A2)}$$

The ratio of (A1)/(A2), assuming that the horizontal derivatives of $\bar{u}'$ and $(\bar{u}' - u_m')$ are of the same magnitude, is approximately:

$$\frac{\mu_b S_0}{6\mu_c h}$$

Provided the effective basal strength μ_b/h is much less than the effective crustal strength μ_c/S_0, the contribution of the basal traction term (A1) to the vertical force balance may be negl[illegible]d.

Appendix B

The Isostatic Balance for a Thin-Sheet Crust Compensated by an Elastic Mantle Lithosphere

The deflection w of an elastic beam due to loading with excess crustal thickness S is given by:

$$D\frac{\partial^4 w}{\partial x^4} + (\rho_m - \rho_c)gw = \rho_c g(S - w) \qquad \text{...(B1)}$$

(Turcotte and Schubert, 1982), where D is the flexural rigidity of the beam:

$$D = \frac{Et_e^3}{12(1 - \nu^2)}$$

and E is Young's modulus (~ 70 GPa for the upper mantle), t_e is the elastic thickness of the beam (between 0 and 25km for the lithosphere in zones of collision), and ν is Poisson's ratio (~0.25). For the locally compensated case, (B1) reduces to:

$$w_{IS} = \frac{\rho_c}{\rho_m} S$$

Assuming a harmonic loading function $S = S_0 \cos(2\pi x/\lambda_N)$, where λ_N is the wavelength of the crustal thickness variations, the deflection w is given by:

$$w = \frac{\left(\rho_c/\rho_m\, S\right)}{1 + \frac{D}{\rho_m g}\left(\frac{2\pi}{\lambda_N}\right)^4} = \left(\rho_c/\rho_m\, S\right)\left(1 - \frac{\lambda_f^4}{\lambda_N^4 + \lambda_f^4}\right) = w_{IS} + w_f$$

(Turcotte and Schubert, 1982), where λ_f is the flexural wavelength:

$$\lambda_f = 2\pi\left(\frac{D}{\rho_m g}\right)^{\frac{1}{4}}$$

The perturbation, w_f, with respect to the locally compensated deflection of the Moho, w_{IS}, due to excess crustal thickness S is therefore:

$$w_f = \frac{\rho_c S}{\rho_m}\left(\frac{\lambda_f^4}{\lambda_f^4+\lambda_N^4}\right)$$

The requirement for less than 5% error in the pressure gradient term in eq. (6) caused by neglecting w_f, is:

$$\left(\frac{\rho_m g}{2}\frac{\partial w_f^2}{\partial x} \Big/ \frac{\rho_c g\phi}{2}\frac{\partial S^2}{\partial x}\right) = \frac{\rho_c}{\rho_m\phi}\frac{\lambda_f^8}{(\lambda_f^4+\lambda_N^4)^2} \leq 0.05$$

i.e.:

$$\lambda_N \geq \left(\sqrt{\frac{20\rho_c}{\phi\rho_m}}-1\right)^{\frac{1}{4}}\lambda_f \approx 1.8\lambda_f$$

In general, for crustal density $\rho_c = 2800$ kg m^{-3} and mantle density $\rho_m = 3300$ kgm^{-3}, the wavelength of thickening must therefore be greater than ~$230 t_e^{3/4}$ for less than 5% error in the pressure gradient term. For an elastic thickness t_e=10km (D=6×10^{21} Nm), this condition requires the wavelength of crustal thickening to be at least 230km (approx. 8 times the crustal thickness). For t_e=25 km (D=1×10^{23} Nm), λ_N must be at least 460 km. The results in chapter 3 show that when the mantle detachment length-scale λ_m is of order S_0 (the initial crustal thickness), the basally-driven thin-sheet model is a good approximation provided the deformation length-scale $\lambda_N \geq 4S_0$ (5% error) to $12S_0$ (1% error), due to the requirement that shear stresses in the crust must be small. Consequently, the assumption of local isostatic compensation imposes about the same restriction as that of chapter 3 on the range of length-scales which may be investigated using the model.

Appendix C

Derivation of the Governing Equation for a Non-Linear Crustal Rheology

A non-linear viscous rheology is described by the constitutive relation:

$$\tau_{ij} = B\dot{E}^{(1/n-1)}\dot{\varepsilon}_{ij} \qquad \text{...(C1)}$$

where, for a crustal thin-sheet, $B=B_c$ is the averaged temperature dependent parameter for the crust (England and McKenzie, 1982), and the vertically averaged second invariant of the strain-rate tensor $\bar{\dot{E}}$ is:

$$\bar{\dot{E}} = \left(\frac{1}{2}\left(\bar{\dot{\varepsilon}}_{xx}{}^2 + \bar{\dot{\varepsilon}}_{yy}{}^2 + \bar{\dot{\varepsilon}}_{zz}{}^2\right) + \bar{\dot{\varepsilon}}_{xy}{}^2\right)^{\frac{1}{2}}$$

Substituting the expression (C1) into the modified version of the force balance (eq. (7)), and assuming that the thin basal layer through which traction is transmitted also obeys a non-linear viscous rheology with $B=B_b$ and the same power-law exponent, the two dimensional normalized form for the ith velocity component ((i, j)= (x, z)) is:

$$2\frac{\partial}{\partial x_i'}\left(S'\bar{\dot{E}}'^{\frac{1}{n}-1}\frac{\partial \bar{u}_j'}{\partial x_j'}\right) + \frac{\partial}{\partial x_j'}\left(S'\bar{\dot{E}}'^{\frac{1}{n}-1}\left(\frac{\partial \bar{u}_i'}{\partial x_j'} + \frac{\partial \bar{u}_j'}{\partial x_i'}\right)\right) = \text{Ar}\,\frac{\partial S'^2}{\partial x_i'} + \text{Am}(\bar{u}_i' - u_{mi}')^{\frac{1}{n}} \qquad \text{...(C2)}$$

where repeated indices imply summation, the normalized strain-rate invariant is:

$$\bar{\dot{E}}' = \bar{\dot{E}}\frac{\lambda_m}{u_0}$$

and:

$$Ar = \frac{\rho_c g \phi S_0 \lambda_m}{2B_c u_0}\left(\frac{\lambda_m}{u_0}\right)^{\frac{1}{n}-1} \qquad Am = \frac{B_b \lambda_m{}^2}{B_c h S_0}\left(\frac{\lambda_m}{h}\right)^{\frac{1}{n}-1}$$

The non-linear case can therefore be described in terms of four dimensionless numbers: Ar, Am, t' and power-law exponent n. The effect of using a power-law viscous rheology in the model is described in chapters 2 and 3.

Appendix D

The Finite Element Method

The linear equation (13) may be separated into a partial differential equation in **u** on the right hand side, and the remainder, as follows:

$$2\frac{\partial}{\partial x_i'}(S'\frac{\partial \bar{u}_j'}{\partial x_j'}) + \frac{\partial}{\partial x_j'}(S'\frac{\partial \bar{u}_i'}{\partial x_j'} + S'\frac{\partial \bar{u}_j'}{\partial x_i'}) - \mathrm{Am}\,\bar{u}_i' = \mathrm{Ar}\frac{\partial S'^2}{\partial x_i'} - \mathrm{Am}\,u_{mi}' \qquad \text{...(D1)}$$

The solution to this equation P(**u**)=**R** over a domain Ω, may be approximated by discretizing all quantities within the domain into a finite number of nodes and elements (figure D1(a)). The governing equation is solved for the crustal velocities at the nodes, subject to the specified velocity conditions along the boundaries of the domain.

The equation to be solved (eq. D1) is reduced to a series of finite equations at the nodes, using the method of weighted residuals:

$$P(\mathbf{u}) = \mathbf{R} \quad \longrightarrow \quad \int_\Omega P(\hat{\mathbf{u}}).N_p\, d\Omega = \int_\Omega \hat{\mathbf{R}}.N_p\, d\Omega \qquad \text{...(D2)}$$

where N_p are the weighting functions, and the crustal velocity field, **u**(x,y), is replaced by the *trial solution*, $\hat{\mathbf{u}}$, at the nodes. For the Galerkin finite element method, the weighting functions, N_p, are the same as the domain interpolation functions (also called *basis functions)* for the trial solution, so that:

$$\hat{\mathbf{u}} = \sum_{p=1}^{n} N_p u_p \qquad \text{...(D3)}$$

where n is the maximum number of nodal parameters (number of nodes in the domain multiplied by the number of degrees of freedom of the solution), and u_p are the system nodal parameters. A velocity at a given point is thus described by interpolation between the nodal parameters at neighbouring nodes. The choice of interpolation function for a second order partial differential equation such as eq. (13) is the bilinear hat function (figure D1(b)).

Substituting the expression for the trial solution (eq. D3) into the weighted sum of the residuals (eq. D2), gives:

$$\int_{\Omega} P(\sum_{p} N_p u_p).N_q \, d\Omega = \int_{\Omega} \hat{\mathbf{R}}.N_q \, d\Omega$$

The differential operator P is linear, so that the order of summation and integration may be reversed to give:

$$\sum_{p} u_p \int_{\Omega} P(N_p).N_q \, d\Omega = \int_{\Omega} \hat{\mathbf{R}}.N_q \, d\Omega$$

This equation is formulated in terms of the *global coordinates* over the domain, and p and q refer to global node numbers. The global system to be solved can also be written as:

$$\sum_{p} K_{pq} u_p = F_q$$

$$\text{where} \qquad K_{pq} = \int_{\Omega} P(N_p).N_q \, d\Omega; \qquad F_q = \int_{\Omega} R.N_q \, d\Omega \qquad \text{...(D4)}$$

K_{pq} is the global system stiffness matrix.

The usefulness of the finite element technique is derived from assembling the global system of equations (D4) from the equivalent equations at the element sub-domain level (i.e. over the *local* domain). The stiffness matrix from equation (D4) may be written:

$$K_{pq} = \sum_{e=1}^{\substack{\text{total number}\\ \text{of elements}}} K^e_{ij}$$

where $$K^e_{ij} = \int_e P(N_i)N_j \, dx\, dy$$

The summation is over the total number of elements in the domain. K^e_{ij} is the local stiffness matrix, and i and j represent the local nodal parameter numbering.

By a suitable transformation of coordinate systems, the evaluation of the stiffness matrix at the local (element) level using numerical integration techniques becomes routine. An appropriate choice of isoparametric mapping (x,y)→(r,s) allows the element to be be transformed to a unit square whose centre is at (r, s)= (0,0) (figure D1(c)). Then the local (element) stiffness matrix is:

$$K^e_{ij} = \int_{e'} P'(N'_i)N'_j \, J \, dr\, ds$$

where the dashes represent the mapping from (x,y) to (r,s), and J is the Jacobian of the transformation. The operator P' is related to P by the chain rule of differentiation. The integrals are evaluated by utilizing Gaussian quadrature (i.e. by summing the weighted values at the Gauss points). The interpolation functions and their derivatives may be pre-computed for the reference element, so that the problem of evaluating the integrals is reduced to the determination of the Jacobian of the transformation for each element, which may be computed using the shape functions and the cartesian values of the local coordinates.

The element stiffness matrices are assembled into a global matrix, K_{pq}, and the right-hand side is similarly assembled. The Dirichlet boundary conditions for the velocity field (i.e. prescribed velocities on the boundaries) at a given nodal point are inserted by the addition of a large number to the diagonal of the stiffness matrix, and adding the same large number multiplied by the prescribed velocity to the left hand side of the equation. Neumann boundary conditions (i.e. prescribing the normal components of the derivative of a velocity to be zero on the domain boundary, also called *Natural* boundary conditions) are satisfied automatically in the calculation. The stiffness matrix is a symmetric, positive definite, banded matrix, and these properties reduce the number of equations that need to be solved. The solution to the global equation (D4) is found using straightforward matrix solver routines.

Figure D1: (a) A schematic illustration of the discretization of a domain, $\Omega(x,y)$, into nodes and elements. (b) Illustration of the interpolation function for quadrilateral elements. The interpolation function for nodal parameter p (= degree of freedom) is interpolated linearly to zero at all adjacent nodes. (c) An element e may be mapped from (x,y) to (r,s) using a bilinear transformation function. The shape functions and their derivatives in (r,s) space are the same for each transformed element. The shape functions are also used as interpolation functions, to interpolate positions and velocities for the nodal parameters.

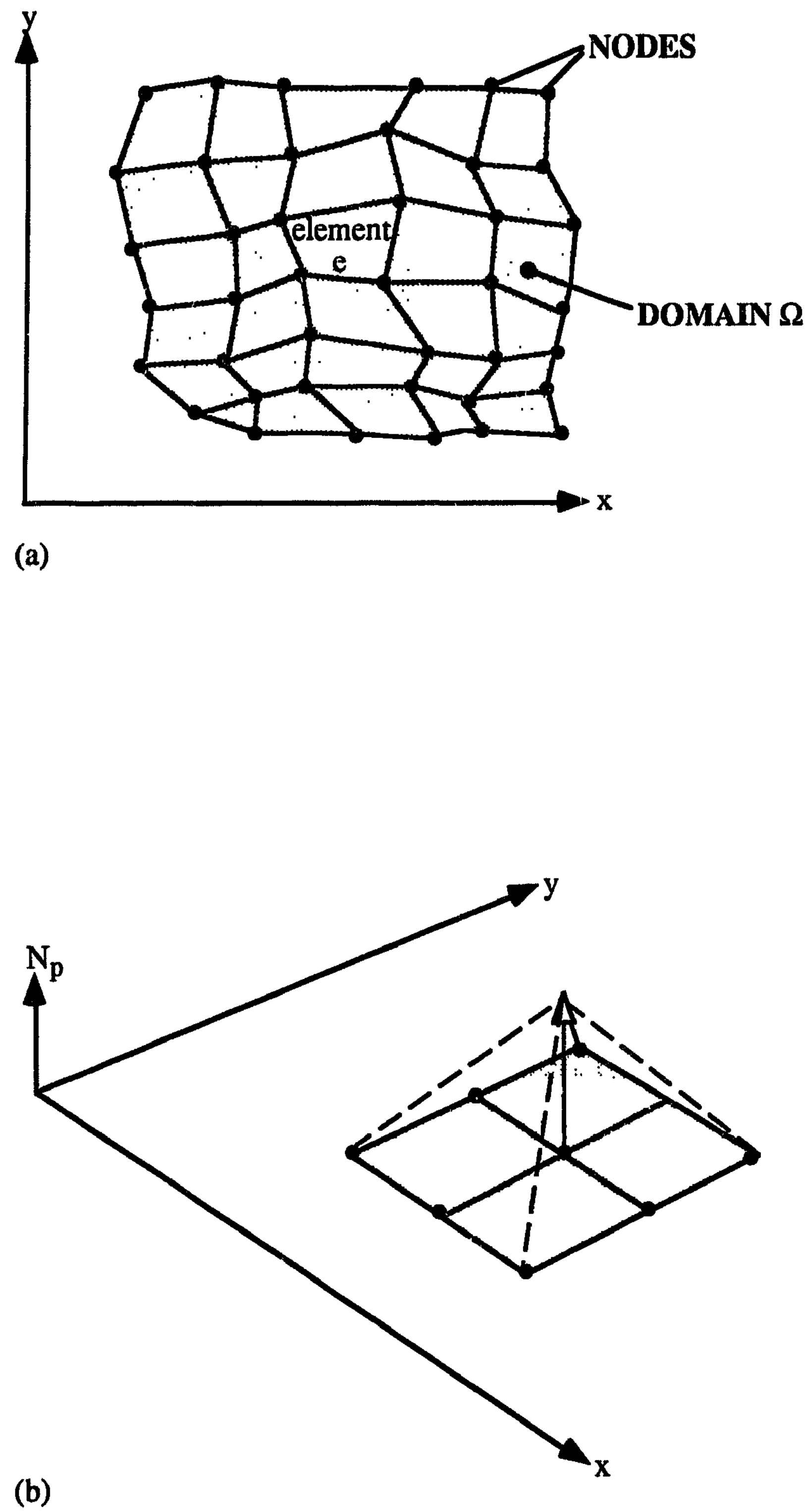

Figure D1(a, b)

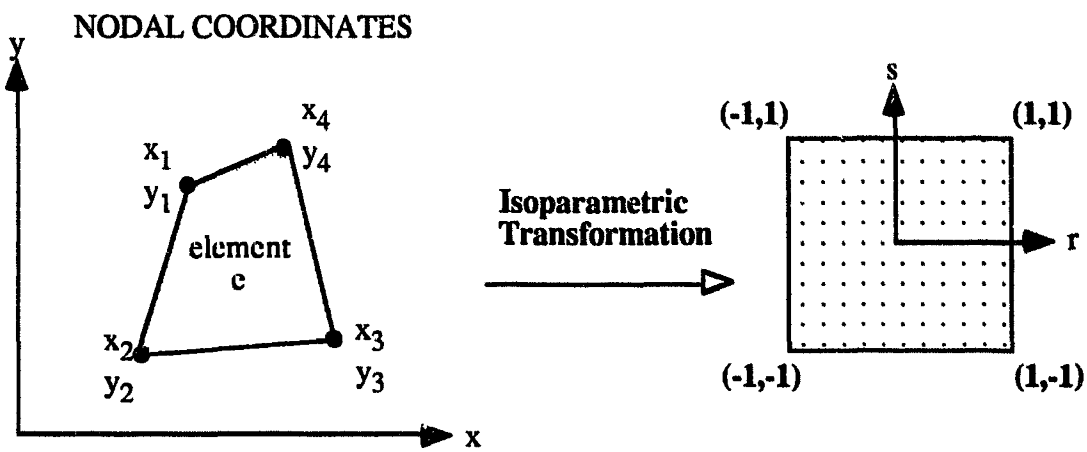

$$x(r, s) = \sum_{i=1}^{4} N_i^e(r, s)\, x_i$$

$$y(r, s) = \sum_{i=1}^{4} N_i^e(r, s)\, y_i$$

where:

$$N_1^e = \frac{1}{4}(1+r)(1+s)$$

$$N_2^e = \frac{1}{4}(1-r)(1+s)$$

$$N_3^e = \frac{1}{4}(1-r)(1-s)$$

$$N_4^e = \frac{1}{4}(1+r)(1-s)$$

N_i^e are the shape functions

and:

$$\hat{u}^e = \sum_{i=1}^{4} N_i^e(r, s)\, u_i$$

$$\hat{v}^e = \sum_{i=1}^{4} N_i^e(r, s)\, v_i$$

N_i^e are the bilinear interpolation functions

Figure D1(c)

Appendix E

Derivation of Natural Length-Scales of Deformation

Neglecting crustal gradient terms in $\partial S/\partial x$, the linear viscous eq. (12) in the text may be written as:

$$2S'\frac{\partial}{\partial x_i'}\left(\frac{\partial \bar{u}_j'}{\partial x_j'}\right) + S'\frac{\partial}{\partial x_j'}\left(\frac{\partial \bar{u}_i'}{\partial x_j'} + \frac{\partial \bar{u}_j'}{\partial x_i'}\right) = Am\left(\bar{u}_i' - u_{mi}'\right) \qquad \text{....(E1)}$$

where ((i, j)=(x, z)). In the case of normal convergence with no variation along strike, the only non-zero component of the strain-rate tensor $\dot{\varepsilon}_{ij}'$ is $\partial\bar{u}'/\partial x'$, and assuming that $S'\sim 1$, (E1) becomes:

$$4\frac{\partial^2 \bar{u}'}{\partial x'^2} - Am\,\bar{u}' = -\,Am\,u_m' \qquad \text{....(E2)}$$

By Fourier Transforms, the solution to this equation is:

$$\bar{u}' = \frac{\sqrt{Am}}{2}\exp\left(-\frac{\sqrt{Am}}{2}|x'|\right) * u_m' \qquad \text{....(E3)}$$

where * indicates that the forcing term $u'_m(x)$ is convolved with a term containing the natural response in the crust. For normal convergence with infinitely extending boundary conditions along strike, this means that the crustal response normal to the boundary, as measured by the normal velocity component $\bar{u}'(x)$ and also its derivative $\dot{\varepsilon}_{xx}'$, dies away with a normalized length-scale given by $2/\sqrt{Am}$, and that the full-width normalized length-scale for the orogen is therefore $4/\sqrt{Am}$.

In the case of transverse motion that does not vary along strike, the only non-zero term in strain-rate tensor $\dot{\varepsilon}_{ij}'$ is $(1/2)\partial\bar{v}'/\partial x'$, and eq. (E1) becomes:

$$\frac{\partial^2 \overline{v}'}{\partial x'^2} - \mathrm{Am}\,\overline{v}' = -\mathrm{Am}\,v'_m \qquad \text{....(E4)}$$

which, by a similar process, yields a normalized natural full-width response length-scale of $2/\sqrt{\mathrm{Am}}$ for a model with transcurrent boundary conditions. For a linear vi cous model, the ratio of natural length-scales for normal:transcurrent deformation is therefore 2 provided the Ampferer number is not too large. If $\lambda_{NB} < \lambda_m$ (Am > 1) the problem is forced by the base, so the ratio tends to 1. For very small values of the Ampferer number, the solution becomes dominated by the side boundary conditions. In this case, the deformation has no natural length-scale.

The non-linear two dimensional equivalent to (E1) is:

$$2S'\frac{\partial}{\partial x'_i}\left(\overline{\dot{E}}'^{\frac{1}{n}-1}\frac{\partial \overline{u}'_j}{\partial x'_i}\right) + S'\frac{\partial}{\partial x'_j}\left(\overline{\dot{E}}'^{\frac{1}{n}-1}\left(\frac{\partial \overline{u}'_j}{\partial x'_i} + \frac{\partial \overline{u}'_i}{\partial x'_j}\right)\right) = \mathrm{Am}\left(\overline{u}'_i - u'_{mi}\right)^{\frac{1}{n}} \qquad \text{....(E5)}$$

where crustal gradients have been neglected. For normal convergence, the strain-rate invariant $\overline{\dot{E}}'$ may be replaced by $\partial\overline{u}'/\partial x'$, and (E5) reduces to:

$$4S'\frac{\partial}{\partial x'}\left(\frac{\partial \overline{u}'}{\partial x'}\right)^{\frac{1}{n}} = \mathrm{Am}\left(\overline{u}' - u'_m\right)^{\frac{1}{n}} \qquad \text{....(E6)}$$

To find the natural response length-scale for this case, note that the natural length-scale for the linear problem could also have been found by solving the homogeneous differential equation (i.e. neglecting the forcing velocity u'_m). Assuming that this can also be done for n>1, and again that $S' \sim 1$, the equation:

$$4\frac{\partial}{\partial x'}\left(\frac{\partial \overline{u}'}{\partial x'}\right)^{\frac{1}{n}} = \mathrm{Am}\,\overline{u}'^{\frac{1}{n}}$$

is solved by assuming an exponential function for the natural response $u'_{natural}$, which has solution:

$$\overline{u}'_{natural} \cong \exp(-\left(\frac{n\,\mathrm{Am}}{4}\right)^{\frac{n}{n+1}}|x'|)$$

The full-width normalized length-scale for normal deformation, as measured by the normal velocity component $\overline{u}'(x)$ and its derivative $\dot{\varepsilon}'_{xx}$, is therefore given by:

$$\lambda'_{NB} = 2\left(\frac{4}{n\,\mathrm{Am}}\right)^{\frac{n}{n+1}}$$

For transverse motion along strike, (E5) equivalently reduces to:

$$2S'\frac{\partial}{\partial x'}\left(\frac{1}{2}\frac{\partial \overline{v}'}{\partial x'}\right)^{\frac{1}{n}} = \mathrm{Am}\left(\overline{v}' - v'_m\right)^{\frac{1}{n}} \qquad \text{....(E7)}$$

Solving for the natural response by neglecting v'_m, gives:

$$\overline{v}'_{natural} \cong \exp(-2\left(\frac{n\,\mathrm{Am}}{4}\right)^{\frac{n}{n+1}}|x'|)$$

and the full-width transcurrent length-scale is therefore:

$$\lambda'_{TB} = \left(\frac{4}{n\,Am}\right)^{\frac{n}{n+1}}$$

The ratio of length-scales for normal: transcurrent deformation for n>1 is thus seen to be the same as the linear case, i.e. $\alpha = 2$. It should be noted that these natural solutions are only valid for λ_{NB}, $\lambda_{TB} >> \lambda_m$. As $n \rightarrow \infty$, the second derivative in the equations drops out, deformation in the crust operates on the forcing length-scale λ_m, and the normal: transcurrent ratio tends to 1.

Normal Deformation Length-scale for $t' > 0$

For normalized convergence times $t' > 0$, the effect of gravity on crustal thickness contrasts may no longer be neglected. The equation (12) for normally incident convergence is:

$$4S'\frac{\partial^2\bar{u}'}{\partial x'^2} + 4\frac{\partial S'}{\partial x'}\frac{\partial \bar{u}'}{\partial x'} = 2\,Ar\,S'\frac{\partial S'}{\partial x'} + Am\,(\bar{u}' - u'_m) \qquad \text{...(E8)}$$

An approximate analytical solution to this equation may still be found, for the case where S' is still relatively close to 1. The continuity equation (14):

$$\frac{\partial S'}{\partial t'} = -\frac{\partial (S'\bar{u}')}{\partial x'}$$

reduces to:

$$\frac{\partial S'}{\partial t'} = -\frac{\partial \bar{u}'}{\partial x'}$$

provided $\partial S'/\partial x'$ is still $<< \partial \overline{u}'/\partial x'$, which will be true for S' still close to 1. Substituting this approximation into an expression for $\partial S'/\partial x$:

$$\frac{\partial S'}{\partial x'} = \int_0^{t'} \frac{\partial^2 S'}{\partial t' \partial x'} dt' = -\int_0^{t'} \frac{\partial^2 \overline{u}'}{\partial x'^2} dt'$$

allows the expression (E8) to be written as:

$$4\frac{\partial^2 \overline{u}'}{\partial x'^2} = -2\,\mathrm{Ar}\int_0^{t'} \frac{\partial^2 \overline{u}'}{\partial x'^2} dt' + \mathrm{Am}\,\overline{u}' \qquad \text{....(E9)}$$

where the term in $\partial S'/\partial x'$ on the left hand side of (E8) and the forcing velocity term have been neglected, and $S' \sim 1$. Using the further approximation that:

$$\int_0^{t'} \frac{\partial^2 \overline{u}'}{\partial x'^2} dt' \approx \frac{\partial^2 \overline{u}'}{\partial x'^2} t'$$

gives:

$$\frac{\partial^2 \overline{u}'}{\partial x'^2} = \left(\frac{\mathrm{Am}}{4 + 2\,\mathrm{Ar}\,t'} \right) \overline{u}'$$

with solution:

$$\overline{u}' = \exp\left(-\frac{\sqrt{\mathrm{Am}}}{2} \sqrt{\frac{2}{2 + \mathrm{Ar}\,t'}} |x'|\right)$$

giving a full-width length-scale of:

$$\lambda'_{NB} \approx \frac{4}{\sqrt{Am}}\sqrt{1+\frac{Ar\,t'}{2}} = \lambda'_{NB}\Big|_{t'=0}\sqrt{1+\frac{Ar\,t'}{2}}$$

for the normal velocity component $\overline{u}'(x)$ and its derivative $\dot{\varepsilon}'_{xx}$, where $\lambda'_{NB}\big|_{t'=0}$ is the normal deformation length-scale at $t'=0$.

For a non-linear rheology, the equivalent expression to (E9) is:

$$\frac{4}{n}\left(\frac{\partial \overline{u}'}{\partial x'}\right)^{\frac{1}{n}-1}\frac{\partial^2 \overline{u}'}{\partial x'^2} + 2Ar\int_0^{t'}\frac{\partial^2 \overline{u}'}{\partial x'^2}dt' = Am\,\overline{u}'^{\frac{1}{n}} \qquad ..(E10)$$

which cannot be solved easily analytically.

Appendix F

Examples Used in Length-Scale Analyses

The Albany-Fraser Orogen

The amalgamation of western Australian cratons in the Proterozoic initiated the Albany-Fraser orogeny along the southeast margin of western Australia (Myers, 1990). High-grade metamorphism indicates that significant crustal thickening and exhumation accompanied the collision. An along-strike dimension D>1500 km is a minimum estimate because of subsequent overprinting by the Paterson Orogeny (Myers, 1990). The across-strike length-scale λ_{NO} is estimated to be 250±50 km.

The Alleghanian Orogen

During the Permian (290-250 Ma), the collision of Gondwana and Laurentia along the eastern edge of proto-North America produced a major period of Appalachian mountain building, the Alleghanian orogeny. This event, and the contemporaneous Variscan orogeny in Europe (Ziegler, 1988), formed an internal suture for the Pangaean supercontinent.

It is believed that the Alleghanian orogeny involved significant crustal thickening and shortening, although the exact amounts are not well constrained (Ziegler, 1988). I use a convergence estimate of 400±200 km. The collisional boundary with Africa extended over 1600±300 km, and terminated in complicated strike-slip deformation at either end (Lefort, 1989). The northern strike-slip region connected Alleghanian deformation to the adjoining Variscan orogen (Ziegler, 1988). The width of Alleghanian deformation, estimated from deformation in eastern North America and west Africa (LeFort, 1989), is approximately 950±350 km.

The European Alpine System

The contraction of the Paleo-Tethys ocean during the late Permian and early Triassic resulted in a series of collisions between island arcs, and subsequently continental masses, comprising the European Alpine system (the Carpathanians, the Apennines, the Hellenides, and the Southern, Western and Eastern Alps). The timing and inter-relations between the formation of these mountain chains is complex. The Carpathanians, Apennines and Hellenides formed in a retreating subduction environment, and collision ceased shortly after all oceanic lithosphere was consumed (Royden, 1993a). Therefore, only the Eastern, Western and Southern Alps, which formed as a result of the terminal continent-continent collision, are used in the length-scale analysis.

I take the along-strike length D to be 600±100 km, from the western termination of the Alps near the Apennines, to the Pannonian Basin in the east. The region has a moderate curvature, which is neglected in the measurement of D. An across-strike deformation length-scale of 150±50 km can be estimated from the current position of deformation fronts (Royden, 1993a). Structural data indicate combined post-collisional shortening in the Southern and Eastern Alps of several hundred kilometres (Royden, 1993a). I assume 200±50 km of shortening. The maximum present-day crustal thickness is ~50 km (Trümpy, 1980), and therefore is likely to have been > 50 km at the peak of orogenic activity (20-30 Ma).

The Anatolian Fault Systems

The continued convergence between Arabia and Eurasia has caused the lateral motion of Turkey westwards, away from areas of crustal thickening, along the Northern and Eastern Anatolian strike-slip faults (Jackson and McKenzie, 1984). The Northern Anatolian Fault Zone has a length of 1000±100 km, and deformation appears to be confined to a narrow zone, no more than 30±20 km wide, with surface expression of the fault over a few kilometres (Jackson and McKenzie, 1984). The Eastern Anatolian Fault

Zone has an along-strike length of 500±50 km. There is a small component of compression along most of the Eastern Anatolian Fault Zone (Kiratzi, 1993). Transcurrent deformation also seems to be restricted to a narrow zone (30±20 km), and there is a suggestion of strain partitioning due to the occurrence of thrust faulting over a slightly wider (50±20 km) area (Kiratzi, 1993).

The (Neogene) Andes

The Andes are a present-day example of an oceanic-continental plate boundary, with the subduction of the Nazca plate beneath South America causing net compression of crust between the trench and the South American craton. The eastward movement of the trench with respect to the stable interior is occurring at somewhere between 2-10 mm/yr (Suárez et al., 1983). The topography of the Andes is spectacular, with significant areas at over 3km in elevation. The variation in topographic features and relief along-strike can be roughly correlated with the dip of the subducting slab (Jordan et al., 1983). The central Bolivian Andes extend to a distance of about 800 km from the fore-arc region, and form a plateau of moderate relief. To either side of the Bolivian Andes, the slab dips less steeply, and the mountains are more rugged, but extend only ~400 km from the fore-arc region.

The convergence velocity of the trench, v_t, relative to South America, does not vary significantly in magnitude or direction along the plate boundary (Dewey and Lamb, 1992). I therefore take the along-strike length-scale D from lat. 5°S to 45°S (Jordan et al., 1983), which roughly corresponds to the along-strike extent of the Nazca plate, and is a distance of 4500±500 km. The curvature of the orogen is accounted for in estimates of D and λ_{NO}. The present Andean deformation is thought to have been created over the past 20 Ma, with net shortening estimates ranging from 150 to 350 km (Isacks, 1988).

The Banda Arc

At the southern edge of the South China Sea, an arcuate trench system stretches from the Andaman Sea to New Guinea. The eastern limit of the trench system, the Banda Arc, is thought to have ceased oceanic subduction very recently (within the last 3 Ma according to Johnston and Bowin, 1981), and is the site of an ongoing collision between the Banda arc and the northern Australian margin. The along-strike extent of collision is bounded to the west by the transition from Australian continental to oceanic crust, and to the east by the New Guinea trench/arc system, giving D=1500±200 km.

Deformation associated with the arc-continent collision has moved progressively from continental margin sediments, into the volcanic island arc (Johnston and Bowin, 1981). Total convergence is estimated at 150±50 km, and the across-strike deformation length-scale is approximately the same (150±50 km). The small time interval since the continental margin has entered the subduction zone implies that subduction of oceanic lithosphere may still be occurring underneath Timor (Johnston and Bowin, 1981). According to Karig et al. (1987), in many ways the deformation of the Banda arc still resembles a normal subducting-arc system, because the transition to arc-continent collision is so recent.

Focal mechanisms suggest that a back-arc basin which formed before the collision, the Banda Basin, is presently being extruding laterally in response to the north-south convergence across the arc (McCaffrey and Abers, 1991).

The Capricorn Orogen

The assembly of Gondwana in the Proterozoic involved several suturing collisions between cratonic masses in southwestern Australia (Unrug, 1992). Of these, the Capricorn orogen represents the best-preserved of the Proterozoic orogenic belts (Myers, 1990). A complete section is exposed along the western part of the orogen and its margins. Strike-slip faulting along the western part of the orogen may indicate an oblique component to the collision, or late-stage tectonic escape (Tyler and Thorne, 1990).

A minimum estimate for the along-strike length-scale D is constrained by the dimensions of the Pilbara and Yilgarin cratons, and later overprinting by the Paterson Orogeny, to be > 1100 km. The across-strike deformation length-scale $\lambda_{NO} = 280 \pm 50$ km (Myers, 1990). The amount of convergence is unknown, but from the exposed metamorphic grades and inferred uplift histories, it was probably significant.

The Chaman Fault Zone (The Sulaiman Fold Belt)

The convergence between India and Eurasia has created a system of transform faults on either side of the Indian continent. The dextral fault system to the west, which includes the active Chaman fault, is deformed over a width of 120±80 km (Lawrence et al., 1981). The transform boundary is 800±100 km long, from the west Himalayan syntaxis to the Makran fold belt.

A jog in the plate boundary near the mid-point of the transform boundary is marked by the Zhob convergent zone. This 220±50 km-long zone has an across-strike width of 220±50 km (Lawrence et al., 1981). Displacement is on the order of several 10s of kms, with large rotations occurring in the Pliocene and early Pleistocene, analogous to the rotations of the Transverse Ranges, California. At the southern end of the Chaman Fault Zone, the plate boundary changes to the slightly oblique advancing subduction of oceanic crust (Lawrence et al., 1981), in the Makran Convergent Zone. The Makran fold belt extends from the Chaman Transform to the Persian Gulf, a distance of 900±100 km. Associated deformation extends inland for 250±50 km.

The Damaran Orogen

Continental collision between the Congo and Kalahari cratons in southern Africa occurred in the Late Proterozoic (Kukla and Stanistreet, 1991). Because the cratons remained sutured together after collision, it is possible to recontruct the dimensions of the orogen.

The lateral extent of the Damaran orogen is constrained by the dimensions of the Kalahari craton, to give D = 800±200 km. Across-strike deformation can be reconstructed using sediment sequences deposited in the Khomas trough, and positions of imbricate thrusting (Kukla and Stanistreet, 1991). These estimates give λ_{NO} = 120±50 km. The total amount of convergence is unknown, but was probably around 100 km (Kukla and Stanistreet, 1991).

The Great Slave Lake shear zone

The Great Slave Lake shear zone (GSLsz) is a 25 km-wide dextral zone of mylonites (Reinhardt, 1969; Hanmer and Lucas, 1985), which is believed to be a major, 1300 km long continental transform, bounding the Early Proterozoic collision between the Slave and Rae Provinces (the Thelon orogeny) (Hoffman, 1987). The relationship between the major topographic expression of the Thelon orogeny (the Queen Maud Uplift) and the GSLsz, is conjectured to be similar to the present-day association between the Tibetan Plateau and the bounding Chaman and Saigang transform faults (Hoffman, 1987).

Deflection of magnetic anomalies across the shear zone suggest that there has been at least 300-700 km of right-lateral offset. The across-strike width of the transcurrent deformation is likely to be under-estimated by the width of the mapped mylonite shear zone. I use the apparently continuous offsets of anomalies from the published magnetic anomaly map of North America (Geol. Surv. Canada), and from the offset of the Taltson and Thelon magmatic arcs, to estimate the approximate width of shearing, giving λ_{TO} = 80±40 km.

The Kibaran Belt

The Kibaran belt marks the contact between the Congo and Tanzanian cratons, and was deformed in the Middle Proterozoic. The length of the Belt is 1500±300 km, and the deformation attains a width of 280±50 km (Pohl, 1987). The amounts of crustal convergence and thickening are not known.

The Levant Fault

The Levant Fault, also known as the Dead Sea Transform, is a left-lateral transform fault that links the extensional Red Sea rift zone to the Zagros mountains, a distance of 1000±100 km (Garfunkel et al., 1981). Small variations in the angle of the fault have caused areas of extension (pull-apart basins, e.g. the Dead Sea) and compression (e.g. the Lebanon Mountains) to develop.

The formation of the Levant transform in the Cenozoic accompanied the breakup of the African-Arabian continent (Garfunkel, 1981). Since the onset of faulting, a minumum estimate of 105 km of sinistral displacement has occurred over a narrow zone, estimated to be no more than 30 km wide, and often marked at the surface by only one major fault strand (Garfunkel, 1981). The 150±30 km-long compressive bend near the mid-section of the Levant shear zone has caused the strike-slip faulting to splay out over a width of 50±30 km, with compressive deformation in the Lebanon and Anti-Lebanon mountains extending a little further (80±30 km).

The Najd Shear Zone

The Najd fault system developed in the Late Precambrian in Arabia and Egypt. The origin of the Najd shear zone as a continental transform system has been variously ascribed to collisional tectonics during a major Late Precambrian continent-continent collision, or to extension tectonics and rifting at the north-western end of the shear zone (Stern, 1985). The complex system of left-lateral strike-slip faults and ductile shear zones has an exposed length of 1100 km, from the eastern margin of the Red Sea to Yemen (Stern, 1985). Alignments with faults on the South Yemen coast and extrapolations using satellite imagery (Sultan et al., 1988) suggest a total length of over 2000 km (Moore, 1979).

The New Quebec Orogen

Dextral oblique collision between the Superior and Rae provinces occurred in the Early Protrozoic (ca. 1850 Ma). The along-strike extent of the ensuing orogeny is over 800 km, constrained at the southern end by deformation from the Mid-Proterozoic Grenvillian orogeny, and at the northern end by the termination of the Superior Province (Van Kranendonk et al., 1993).

The across-strike extent of the New Quebec orogen is 100±30 km. Amounts of convergence and crustal thickening are not well constrained, but were probably small, based on maximum pressure estimates from exhumed rocks and the limited width of the orogen.

The New Zealand Southern Alps

The South Island of New Zealand is the site of an oblique continent-continent collision between the Pacific and Australian plates. Convergent shortening of 50±35 km (Walcott, 1984) has been accommodated in the modern Southern Alps since the mid-Miocene (10 Ma). The surface trace of collision is marked by the Alpine Fault, which has undergone both thrusting and dextral strike-slip motion. Along-strike displacements of ~ 480km since the early Miocene (23 Ma) have occurred along the Alpine Fault (Kamp, 1986). The plate convergence vector varies along-strike due to the proximity of the pole of rotation. Convergence can be resolved into parallel and normal components of 0.7 and 3.6 cm/yr, respectively, in the central portion of the collisional boundary (DeMets et al., 1990).

At the northern end of the Southern Alps, the collision zone changes to subduction of the Pacific plate along the Hikurangi subduction zone. The southern extent of collision is bounded by the Puysegur trench, an ocean-continent convergent boundary. These limits give an estimate for D of 500±100 km. Across-strike normal and transcurrent deformation occur over length-scales of less than 100 km, with significant displacement along the Alpine Fault (Walcott, 1978). Strain does not appear to be partitioned over most of the collision boundary (Braun and Beaumont, submitted).

Papua and Western New Guinea

The Melanesian Arc has been colliding with the Australian continental margin since the Miocene (15 Ma), forming a zone of oblique collision on the island of New Guinea (Smith, 1990). The convergence is taken up in a complex faulted region, with compressional and strike-slip features which may be partitioned (McCaffrey and Abers, 1991). The ~45° obliquity of convergence is caused by the south-east motion of the Pacific plate relative to the northwards moving Australian plate.

The lateral extent of collision can be estimated from the dimensions of the Melanesian Arc, giving D = 1500±200 km. Focal mechanisms suggest that across-strike normal deformation and thickening is distributed over the New Guinea Highlands, a distance of 200±50 km, whereas strike-slip deformation may be confined to a dual system of faults on either side of the Highlands, with much smaller length-scales of 50±30 km (McCaffrey and Abers, 1991). The total amount of shortening and convergence since the initaition of collision across New Guinea is estimated to be 60±20 km (Abers and Lyon-Caen, 1990), with a maximum crustal thickness of 55±10 km (Smith, 1990).

The Paterson Orogen

The Paterson orogen resulted from the collision and accretion of a suspect terrane (possibly part of the central Australian craton) with Western Australia in the Middle Proterozoic. The orogen is dominated by thrusts, accompanied by sinistral faults which may indicate an oblique component of collision (Myers, 1990). The amount of crustal thickening is uncertain, but probably significant.

The along-strike dimension of the belt is 1300±300 km, the eastern extent of the western Australian craton. The width of normal deformation, estimated from the location of thrust belts, is 250±100 km (Myers, 1990).

The Patos-Seridó System

During the amalgamation of the Gondwana supercontinent in the NeoProterozoic (Unrug, 1992), collision between Brazil and Africa initiated the Brasiliano-pan-African orogeny. A complex system involving strain transfer at a continental scale developed in northeastern Brazil (Corsini et al., 1991). This system includes east-west trending dextral ductile strike-slip faults (the Patos shear zone), linked with a northeast-trending transpressional fold belt (the Seridó belt) in the east.

The Patos shear zone is up to 30 km wide and several hundred kms long, giving $D = 400 \pm 100$ km and $\lambda_{TO} = 30 \pm 5$ km. Using the width of the ductile shear zone as an estimate for across-strike deformation gives a minimum length-scale only. The shear zone merges into the slightly tranpressive Seridó belt, which has an along-strike dimension $D > 300$ km, and an across-strike width of 100 km, which is again a minimum estimate. Strain does not appear to be partitioned in the Seridó belt, and strike-slip movement is accommodated along with compression, in a flower-structure system of faults (Corsini et al., 1991).

The Pyrenees

The Pyrenees form a part of the Alpine collision belt, where the Iberian and European plates collided between the Late Cretaceous and Early Miocene (Muñoz, 1992). Palinspastic restorations suggest shortening amounts of 125±25 km for the upper crust. The ECORS seismic profile across the central Pyrenees, when combined with balanced cross-sections, indicates a mid-crustal detachment layer at ~15 km depth, with the lower crust subducting along with the mantle lithosphere (Muñoz, 1992).

The across-strike dimension of the thickening is 120±20 km. D is constrained by the dimensions of the Iberian plate to be 400±100 km. Convergence was predominantly normal to the plate boundary (Decourt et al., 1986). Maximum crustal thickness in the central Pyrenees is constrained by the ECORS profile to be ~ 50±10 km.

The San Andreas Fault

The San Andreas Fault is the major surface expression of the transform fault boundary between the Pacific and North American plates. The present strike-slip boundary is 1200±100 km long (Wallace, 1990), and formed as a result of the northward migration of the Mendocino Triple Junction in the last 25-30 Ma (Furlong, 1993). For most of its length, the plate boundary is predominantly strike-slip, with a small component of compression which has caused thrust faulting and folding over a width of about 200±50 km (Stein and Yeats, 1989). A bend near the southern end of California is responsible for an area of increased convergence, corresponding to the position of the Transverse Ranges (Bird and Piper, 1980).

Paleomagnetic data indicates that Cenozoic transcurrent deformation extends between 100-200 km from the plate boundary (Sonder et al., 1986; Wallace, 1990). I take the length-scale of transcurrent deformation to be 100±50 km. Note that these long-term estimates constrast with more recent geodetic estimates of deformation (summarized by Furlong and Hugo, 1989), which suggest that transcurrent deformation is restricted to within 30 km of the plate boundary.

Taiwan

Taiwan is located at the convergent plate boundary between an island arc and the Chinese continental margin. To the north of the island, the Philippine sea plate is subducting beneath the continental Eurasian plate at the Ryukyu trench. To the south, the South China Sea is subducting at the Manila Trench. Convergence is oblique, with approximately equal components of motion normal and parallel to the plate boundary. Onset of the collision varies along-strike from 4 Ma in northern Taiwan, to Recent in southernmost Taiwan (Suppe, 1987), with convergence estimates of 300±50 km to 0 km from north to south, and crustal thickness increasing from 30 km (Chinese continental margin) to 40 km (Lu and Malavieille, 1994). Strike-slip movement is estimated to be 360 km over the last 4 Ma.

The along-strike extent of collision is approximately 200±50 km, constrained by the position of the Ryukyu amd Manila trenches. Thrusting and uplift is presently occurring over a length-scale of 100±50 km (Suppe, 1987). Strain partitioning is conjectured from the high density of strike-slip faults near the centre of the island (Lu and Malavieille, 1994), with an across-strike length-scale for transcurrent motion of approximately 50±20 km.

The Thelon Orogen

During the Early Proterozoic amalgamation of Laurentia, an oblique collision between the Rae and Slave provinces (Hoffman, 1989) created the Thelon orogeny with accompanying uplift of a hinterland plateau (the Queen Maud uplift). Hoffman (1987) estimated the total along-strike extent of the dextral collision at ~1.9 Ga to be 3200 km; however, the deformation may only be traced continuously from the Great Slave Shear Zone in the south, to the end of the Slave craton in the north, giving a conservative minimum strike length D>1500 km. The Great Slave Shear Zone marks the southern end of the Slave-Rae collision, and is thought to have experienced 600-700 km of dextral offset during the collision. Post-collisional movement of approximately 100 km occurred along the brittle McDonald and Bathurst Fault zones (Hoffman, 1989). There is no strong evidence for strain partitioning during the Thelon orogeny. The width of deformation is approximately 300±100 km. Crustal thickening amounts must have been significant, creating the Queen Maud Uplift which is thought to be a small-scale analogue to the Tibetan Plateau. High exhumation rates and large sediment transport distances indicate that the Thelon orogen experienced considerable erosion (Hoffman and Grotzinger, 1993).

The Tibetan Plateau

The ongoing continental collision between India and Eurasia is responsible for the formation of the high Tibetan Plateau, which has average elevations over 4000 m and is bordered to the south by the Himalayan mountain range. Since the onset of continental convergence in the Eocene between 60 and 40 Ma, India is estimated to have moved 2000±500 km relative to the Eurasian craton, in a direction approximately normal to the plate boundary. The Indus-Tsangpo suture, located ~ 300 km from the southern limit of deformation, is believed to mark the surficial contact between Indian and Eurasian crust.

The lateral extent of collision is somewhat more than the distance between the syntaxes, 3000±500 km. The across-strike extent of deformation as measured by crustal thickening and recent estimates of uplift (Chen et al., 1991), is 2200±500 km, excluding the Tarim Basin, which is assumed to act as a rigid 'spacer'. The current stress regime over the southern part of the Plateau is extensional (Burchfiel and Royden, 1985; Mercier et al., 1987).

The Torngat Orogen

Sinistral oblique collision between the Nain and Rae provinces occurred in what is now eastern Labrador shortly before the New Quebec orogeny to the west, at ca. 1860 Ma (Van Kranendonk et al., 1993). Deformation may have occurred in more than one stage, because the sinistral shearing seems to have taken place in an already thickened crust, along the Abloviak shear zone at 1845 Ma (Mengel and Rivers, 1991).

The along-strike extent of the orogen is determined by the lateral extent of the Nain Province at the northern end, and overprinting by Grenvillian deformation at the southern end, giving D>600 km. Deformation occurs over across-strike distance of 100±30 km. Peak pressures of 10 kbar in metamorphosed rocks now at the surface indicate that the crust was at least 35 km thick; total amounts of crustal thickening and convergence were probably small.

The Trans-Hudson Orogen

The Trans-Hudson orogen, in its broadest definition, sutured together the cratons to form Laurentia in the Early Proterozoic (1.9-1.85 Ga) (Hoffman, 1989). The main exposed segment is in Manitoba, and occurred along an oblique sinistral collision between the Hearne-Wyoming and Superior cratons. From the southern extension, which is overprinted by the Central Plains orogen, to the dog-leg bend, a minimum estimate for D is 1500 km. The width of deformation is 400±100 km. The amount of crustal thickening and convergence is unknown, but thought to be significant.

The Urals

The deeply eroded Ural mountains are a relict of the continental collision between the Siberian plate and Laurussia in the late Permian (approximately 245 Ma (Ziegler, 1993)). The Ural tectonic zone stretches for 2500±500 km from north of the Caspian Sea, to the Barents Sea (Dymkin and Puchkov, 1984). The deformed zone is 300±100 km wide (Dymkin and Puchkov, 1984) and includes a tectonic melange, or suture, called the Main Uralian Deep Fault (MUDF), which dips steeply to the east. A belt of Paleozoic island-arc and ophiolitic assemblages in the Eastern Urals were formed on an active subduction boundary.

The amount of post-collisional convergence is unknown. It was probably significant. Present crustal thicknesses in the Urals increase from a regional value of 40 km to over 50 km (Ryzhiy et al., 1992). High pressure rocks, including eclogite facies, are exhumed near the MUDF, and high-temperature amphibolite facies assemblages occur to the east. Later stages of the collision may have involved a significant dextral component of motion (Zonenshain et al., 1990).

The Variscan Orogen

The Variscan orogen resulted from the formation of the supercontinent Pangaea in the Carboniferous and Permian (365-325 Ma), which produced dextral oblique collision between Gondwana and Fennoscandia/Baltica. The Variscan fold belt had an arcuate shape, with major oroclinal bending and wrench faulting. The western limit of the Variscan deformation is taken to be the location of intense strike-slip transport, along the Tornquist Line, (Lefort, 1989). To the east, the extent of the collision is less clear. Ziegler (1988) suggested that deformation continued beyond the zone of collision between Africa and Eurasia, but a more conservative estimate for D is to locate the eastern end at the site where Gondwana continental crust merged into the proto-Tethys ocean (see figure 55(d)). These limits give D=2000±500 km. Structural indicators, palinspastic restorations, and plate reconstructions (Ziegler, 1988) suggest that deformation extended over a distance of 1000±500 km, although the involvement of Iberia in the orogeny is not yet clear. A minimum estimate for convergence amounts during deformation is given by LeFort (1993) using shortening estimates for French crust. Results from seismic imaging in this case indicate at least 150 km of convergence (50% shortening), but since the study only examined a part of the Variscan deformation, total amounts of convergence will probably be greater. I use an estimate for total convergence of 400±200 km.

The Zagros Mts

The Zagros fold belt in Iran formed as a result of the northward movement of the Arabian/African continent, and the subsequent closure of the Neo-Tethys ocean, during the Alpine-Himalayan orogeny. Some debate exists over the timing of the change from subduction of Arabian oceanic lithosphere to continental collision between the Arabian margin and Eurasia. The current theory is that inital collision occurred at the northern end of the Arabian promontory in the mid-late Eocene (45-36 Ma) (Hempton, 1987), and that the contact spread eastwards from the Bitlis to the Zagros suture during the early Miocene (22 Ma). Crustal stacking of the thinned Arabian continental margin is thought to have delayed the spread of deformation to the north until ca. 15 Ma. The convergence and associated volcanics eventually caused the thickening of the Iranian and Anatolian plateaus, and uplift and deformation in the Caucasus mountains (Philip et al., 1989). Further convergence initiated 'extrusion tectonics', to the west along the northern and eastern Anatolian fault systems, and to the east along the Zagros suture, increasing the relative obliquity of the Arabia-Eurasia collision.

The collision zone extends laterally from the Persian Gulf to the junction with the Anatolian Fault in Turkey, giving a length-scale D = 1900±200km. Estimates for the extent of across-strike deformation, derived from crustal uplift rates and seismicity (England and Jackson, 1989), range from 800km in the north, between the Bitlis suture and the Caucasus mountains, to 1200 km in the south, between the Zagros simply folded belt and the Kopet Dagh. Convergence since collision in the Eocene is estimated to be 500±150km (from reconstructions of Hempton, 1987), with maximum crustal thicknesses of 50±5 km. It is estimated that over half of the mass added due to convergence has escaped laterally along the strike-slip fault system.

Appendix G

Incorporation of a 1D Numerical Thermal Code in the Mechanical Model

The change in Moho temperature with time, at each location in the thin-sheet model, is calculated using a one-dimensional thermal finite element code written by Jean Braun (Braun, 1988). Details of the numerical temperature routine are described by Braun (1988). Inputs to the code are: the initial temperature field as a function of depth, T(z) (°C), the distribution and magnitude of radiogenic heat production in the crust, A(z) (Wm^{-3}), the thermal conductivity of the lithosphere, k ($Wm^{-1}{}^{\circ}C^{-1}$), the dynamic specific heat, ρc ($kgm^{-1}s^{-2}{}^{\circ}C^{-1}$), and the heat flux from the mantle asthenosphere, Q^* (Wm^{-2}). The code solves the one-dimensional time-dependent heat-flow equation:

$$\rho c \frac{\partial T}{\partial t} = k \frac{\partial^2 T}{\partial z^2} + A \qquad \text{...(G1)}$$

In order to compute the thermal relaxation of the Moho in a region of thickened crust, the numerical code must calculate the temperature field at the detachment layer. As discussed in section 6.2, differential motion between the model crust and mantle lithosphere will mean that, in general, the two layers have different residence times. This will create an incremental discontinuity in temperature at the Moho, over length-scale h, where h is the thickness of the detachment layer (on the order of 1 km thick). In the numerical implementation of diffusion, this temperature discontinuity thermally relaxes at each timestep, so that the temperature of the weak layer can be assumed to be near uniform.

The thermal code is incorporated into the thin sheet model by creating an array of crustal temperatures T(z) for each thin-sheet element. A vertical resolution of 11 nodal points for the temperature array is used in the crust. In order to compute the geotherm correctly as a function of horizontal position, depth, and time, the crustal temperature array must be matched to the underlying mantle lithosphere temperature field at each timestep, before computing the incremental change in temperature. Figure G1 illustrates how this is accomplished. The basal grid, which is Eulerian and has a fixed velocity distribution at the basal nodes, is assigned a temperature array for each basal element, also with a resolution of 11 nodes. There are therefore two temperature arrays for each horizontal location: the crustal temperature array, $T_c(z)$, and the mantle lithosphere temperature array, $T_b(z)$. At each time-step, the position of each crustal element is found with respect to the underlying basal grid, and the temperature arrays of corresponding crustal and basal elements are combined to form a temperature array for the lithosphere, T(z), at each horizontal position. The one-dimensional heat conduction equation is solved, for a time increment equal to the mechanical timestep, for this temperature array. The updated T(z) is then split into its component crustal and basal temperature arrays ($T_c(z)$ and $T_b(z)$).

Once the updated temperature arrays have been computed, the local Ampferer number (Am(x)) for each crustal element is found using an empirical relationship derived from figure 19(a), as follows:

$$\mathrm{Am} \approx (316.4)\exp\left(\frac{-T_{moho}}{(74.4)}\right) \qquad \text{...(G2)}$$

The local Am values are used in the thin-sheet computation, which proceeds as detailed in chapter two. Once the grid has been solved for horizontal displacement and thickening of the crust, the positions of the temperature arrays must be updated. The vertical position of the temperature nodes changes with time, according to the thickening of the crustal element, so that after thickening by factor f, the new temperature nodal depths z'_i (i=1 to 11) for an element will be:

$$z'_i = f\, z_i$$

In the mantle lithosphere temperature grid, the vertical spacing between temperature nodes does not change with time, since there is no mantle thickening. The depth of the top basal node is set to the depth of the corresponding bottom crustal node at each time-step. Since the crustal grid is Lagrangian, the crustal temperature array is automatically advected horizontally with time. However, the basal grid is Eulerian, and so the basal temperature array must be advected according to the basal velocity field. Advection is performed using simple interpolation routine.

Once the positions of the temperature arrays have been updated, the local Am for each crustal element is ready to be computed for the next timestep, and the process described above is repeated. In summary, the numerical method and approximations used in the thermal/mechanical code are as follows:

(i) At each timestep, the temperature arrays for the crust and mantle lithosphere are computed using eq. (G1) for each crustal column, and the corresponding basal element over which it resides at that timestep;

(ii) The crustal and basal temperature are reset according to the new temperature array at that location. The local value of Am for each crustal element is computed using eq. (G2).

(iii) The displacements are solved, and crustal thickness is updated in the usual way;

(iv) The basal temperat ield is advected according to the basal velocity field.

The parameters used in the thermal calculation are as follows:

$A(z) = 0\ Wm^{-3}$(no radiogenic heat production in the crust)

$\rho c(z) = 2.5x10^{-6}\ kgm^{-1}s^{-2}{}^{\circ}C^{-1}\ (\forall\ z)$

$k(z) = 2.25\ Wm^{-1}{}^{\circ}C^{-1}\ (\forall\ z)$

$Q^* = 0.03375\ Wm^{-2}$

initial temperature array: $T(z)=0.015z$, giving a temperature at the Moho of 450°C

Values for k and ρc are taken from England and Thompson (1984). The mantle heat flux, Q^*, is chosen to give an initial geothermal gradient of 15 °Ckm^{-1}.

For simplicity, radiogenic heat production in the crust is neglected; however, when calculations are performed with a 15 km thick radiogenic heat-producing layer (and $A = 2 \times 10^{-6}$ Wm^{-3}, with $Q^* = 0.02625$ Wm^{-2} so that the initial Moho temperature is still 450 °C), the difference in length-scale predictions, compared to calculations which neglect radiogenic heat production, is less than 5% after a normalized convergence of 70. This result indicates that radiogenic heat production in the crust does not significantly affect the increase in Moho temperature with thickening, provided the mantle heat flux Q^* is adjusted accordingly. The initial agreement in length-scale predictions is expected, since the mantle heat flow in each case has been adjusted to give the same temperature at the base of the (unthickened) crust. The lack of a length-scale discrepancy after large amounts of convergence is probably a result of competing effects on length-scales from scaling factors Am and Ar. The case which includes radiogenic heating in the crust, will heat up (and weaken) more rapidly than the case where A=0, so that Am will not decrease as fast. However, Ar will increase more rapidly as the crust thickens. The changes in Am and Ar seem to roughly cancel out the expected change in length-scale due to the extra radiogenic heat production. Also, the coupling between crust and mantle lithosphere near the edges of the deforming region, which is expected to be the most important area in controlling length-scales (the 'bookend' effect, discussed in chapter six), will not be greatly affected by the radiogenic heating, because the extra radiogenic heat production associated with crustal thickening has had little time to cause a large difference in the effective parameter values Am and Ar.

An illustration of the change in temperature array with time, for a crustal element which is initially over the detachment point, is shown in figure G2. The geotherm initially steepens, as the crust thickens at the advective limit (t'=0 to 10). Once the thickening rate for the element decreases, thermal relaxation causes the geotherm to shallow with time (t'=10 to 50). The depth of the Moho with respect to the surface changes with time, as shown by the filled circles on the figure.

Figure G1: A schematic illustration of the temperature arrays used in the thermo-mechanical model. At each timestep, a temperature array for each lithospheric column is assembled from separate temperature arrays in the crust and mantle lithosphere, for crustal and basai elements which are in contact with each other. The combined temperature array is used to solve the one-dimensional transient heat flow equation (G1), and the resulting temperatures are used to reset the crustal and basal temperature arrays before elements are advected. S is crustal thickness for the element indicated; M is the thickness of the mantle lithosphere; Q^* is the heat flow from the mantle asthenosphere.

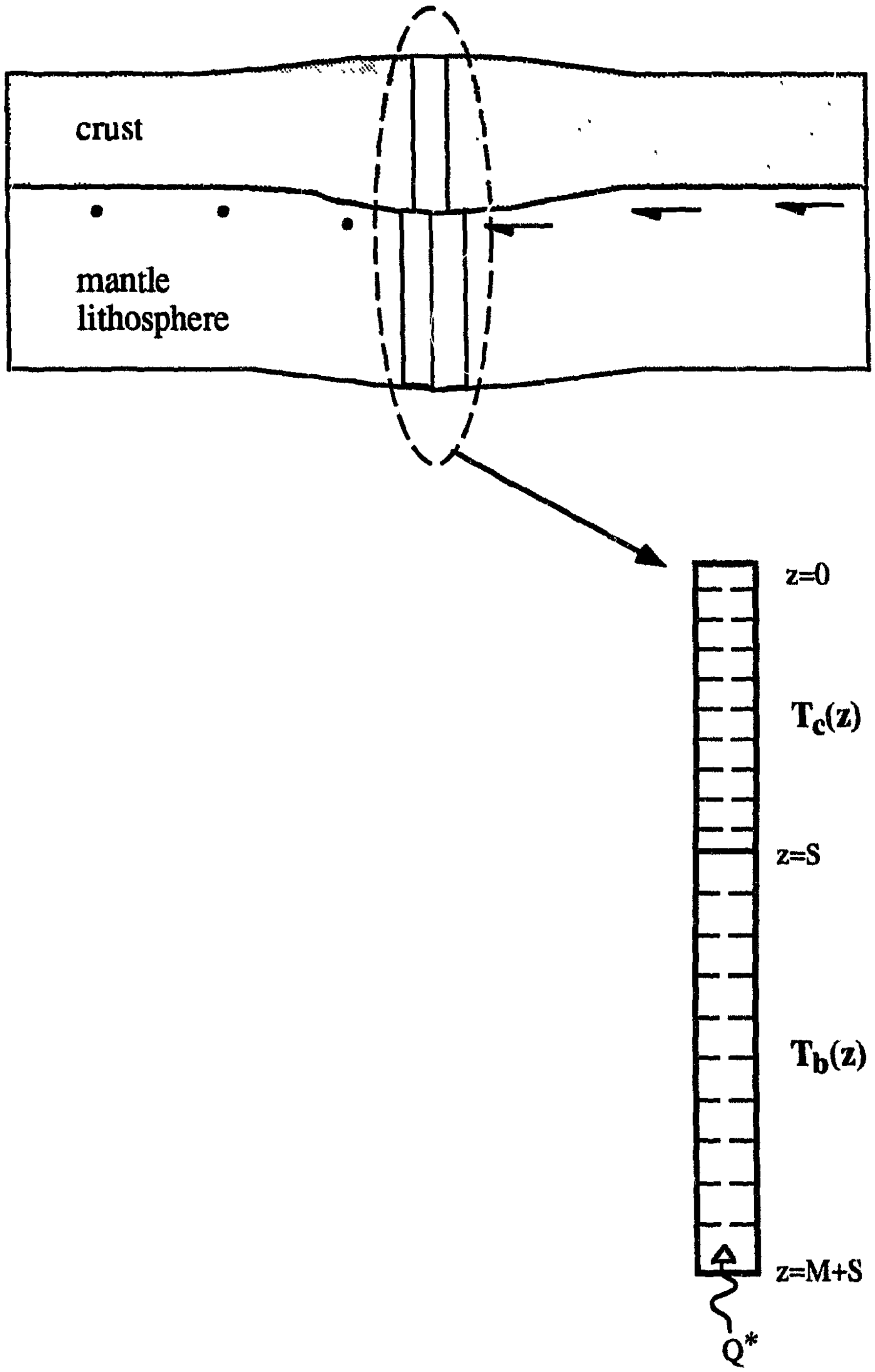

Figure G1

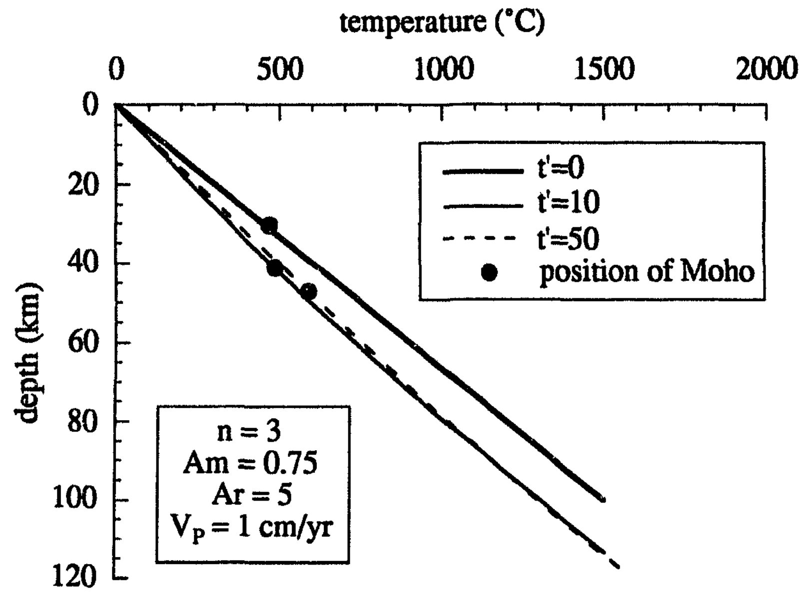

Figure G2: Change in the geotherm with normalized convergence, for a crustal element initially above the mantle detachment zone. Crustal temperatures are shown vs. depth, along with the corresponding mantle lithosphere temperatures from a corresponding basal column at each timestep. The position of the Moho is indicated by the filled circle. Note that this figure shows the change in temperature with convergence for an incident velocity V_P=1 cm/yr. For the case where V_P=5 cm/yr, the effects of thermal relaxation with convergence are reduced.

References

Abers, G., and Lyon-Caen, H., 1990. Regional gravity anomalies, depth of the foreland basin, and isostatic compensation of the New Guinea Highlands, *Tectonics*, **9**, 1479-1493.

Akin, J., 1986, *Finite element analysis for undergraduates*, Academic Press, 319pp.

Alonso, J.L., and Teixell, A., 1992. Forelimb deformation in some natural examples of fault-propagation folds, In: *Thrust Tectonics* (edited by McClay, K.R.), Chapman and Hall, London, 175-180.

Ampferer, O., 1906. Über das Bewegungsbild von Faltengebirgen, *Jb. k. k. Geol. Reichsanst.*, **56**, 539-622.

Ampferer, O., and Hammer, W., 1911. Geologischer Querschnitt durch die Ostalpen vom Allgäu zum Gardasee, *Jb. k. k. Reichsanst.*, **61**, 531-710.

Argand, E., 1924. La tectonique de l'Asie. In: *C.R. Congr. Géol. Int.*, Belgique, 1922, 171-372.

Armijo, R., Tapponnier, P., Mercier, J.L., and Han, T., 1982. A field study of Pleistocene rifts in Tibet, *EOS*, **63**, 1093.

Armijo, R., Tapponnier, P., Mercier, J.L., and Han, T., 1986. Quaternary extension in southern Tibet: field observations and tectonic implications, *J. geophys. Res.*, **91**, 13803-13872.

Bally, A.W., and Oldow, J.S., 1984. *Structural Styles and the Evolution of Sedimentary Basins, Short Course,* 1984 Fossil Fuels of Europe Conference and Exhibition, AAPG, 238pp.

Barr, T.D., and Dahlen, F.A., 1989. Steady-state mountain building 2. Thermal structure and heat budget, *J. geophys. Res.*, **94**, 3923-3947.

Beaumont, C., Fullsack, P. and Hamilton, J., 1992. Erosional control of active compressional orogens, In: *Thrust Tectonics* (edited by McClay, K.R.), Chapman and Hall, London, 1-18.

Beaumont, C., Fullsack, P. and Hamilton, J., 1994a. Styles of crustal deformation caused by subduction of the underlying mantle, *Tectonophys.*, **232**, 119-132.

Beaumont, C., Willett, S., Fullsack, P. and Hamilton, J, 1994b. Progress report on geodynamical modelling of crustal deformation in compressional orogens, In: *Alberta Basement Transects Workshop (Feb 14-15)* (edited by Ross, G.M.), Lithoprobe Report **37**,1-39.

Beaumont, C. and Quinlan, G., 1994. A geodynamic framework for interpreting crustal scale seismic reflectivity patterns in compressional orogens, *Geophys. J. Int.*, **116**, 754-783.

Beaumont, C., Kamp, P.J.J., Hamilton, J., and Fullsack, P., submitted. The continental collision zone, South Island New Zealand; comparison of geodynamical models and observations.

Beck, M.E., 1983. On the mechanism of tectonic transport in zones of oblique subduction, *Tectonophys.*, **93**, 1-11.

Beck, R.A., and 13 others, 1995. Stratigraphic evidence for an early collision between northwest India and Asia, *Nature*, **373**, 55-58.

Bird, P., 1978a. Finite element modeling of lithosphere deformation: the Zagros collision orogeny, *Tectonophys.*, **50**, 307-336.

Bird, P., 1978b. Initiation of intracontinental subduction in the Himalaya, *J. geophys. Res.*, **83**, 4975-4987.

Bird, P., 1989. New finite element techniques for modeling deformation histories of continents with stratified temperature-dependent rheology, *J. geophys. Res.*, **94**, 3967-3990.

Bird, P. and Baumgardner, J., 1984. Fault friction, required stress, and crust-mantle coupling in southern California from finite element models, *J. geophys. Res.*, **89**, 1932-1944.

Bird, P. and Piper, K., 1980. Plane-stress finite-element models of tectonic flow in southern California, *Phys. Earth Planet. Int.*, **21**, 158-175.

Bird, P., Toksöz, M.N., and Sleep, N.H., 1975. Thermal and mechanical models of continent-continent convergence zones, *J. geophys. Res.*, **80**, 4405-4416.

Bott, M.H.P., 1982. *The interior of the Earth: its structure, constitution and evolution*, Elsevier Sci. Publ. (2nd edition), Amsterdam.

Brace, W.F. and Byerlee, J.D., 1966. Stick slip as a mechanism for earthquakes, *Science*, **153**, 990-992.

Braun, J., 1988. *Styles of continental extension: Results from numerical experiments*, Unpublished PhD thesis, Dalhousie University.

Braun, J., 1993. Three dimensional numerical modeling of compressional orogenies; thrust geometry and oblique convergence, *Geology*, **21**, 153-156.

Braun, J., 1994. Three-dimensional numerical simulations of crustal-scale wrenching using a non-linear failure criterion, *J. Struct. Geology*, **16**, 1173-1186.

Braun, J. and Beaumont, C., submitted. Three dimensional numerical experiments of strain partitioning at oblique plate boundaries: implications for contrasting tectonic styles in California and South Island, New Zealand, *J. geophys. Res.*

Buck, W.R., and Sokoutis, D., 1994. Analogue model of gravitational collapse and surface extension during continental convergence, *Nature*, **369**, 737-740.

Burchfiel, B.C., and Royden, L.H., 1985. North-south extension within the convergent Himalayan region, *Geology*, **13**, 679-682.

Burchfiel, B.C., and Royden, L.H., 1991. Tectonics of Asia 50 years after the death of Emile Argand, *Eclogae geol. Helv.*, **84**, 599-629.

Burg, J.P., and Chen, G.M., 1984. Tectonic and structural zonation of southern Tibet, China, *Nature*, **311**, 219.

Byerlee, J.D., 1968. Brittle-ductile transition in rocks, *J. geophys. Res.*, **73**, 4741-4750.

Carslaw, H.S., and Jaeger, J.C., 1959. *Conduction of heat in solids*, (2nd edition), Oxford, Clarendon Press.

Carter, N.L., and Tsenn, M.C, 1987. Flow properties of continental lithosphere, *Tectonophys.*, **136**, 27-63.

Carter, N. L., Kronenberg, A.K., Ross, J.V., and Wiltschko, D.V., 1990. Control of fluids on deformation of rocks, In: *Deformation Mechanisms, Rheology and Tectonics* (edited by Knipe, R.J. and Rutter, E.H.), GSA Spec. Publ. **54**, 1-13.

Chapple, W.M., 1978. Mechanics of thin-skinned fold-and-thrust belts, *Geol. Soc. Am. Bull.*, **89**, 1189-1198.

Chase, C.G., 1988. Fluvial landsculpting and the fractal dimension of topography, *EOS*, **69**, 1207.

Chase, C.G., 1992. Fluvial landsculpting and the fractal dimension of topography, *Geomorphology*, **5**, 39-57.

Chen, W.P., and Molnar, P., 1977. Constraints on the seismic wave velocity structure beneath the Tibetan plateau and their tectonic implications, *J. geophys. Res.*, **86**, 5937-5962.

Chen, Y., Cogne, J., Courtillot, V., Avouac, J., Tapponnier, P., Wang, G., Meixiang, H.Y., Li, M., Wei, C., and Buffetaut, E., 1991. Paleomagnetic study of Mesozoic continental sediments along the northern Tien Shan (China) and heterogeneous strain in Central Asia, *J. geophys. Res.*, **96**, 4065-4082.

Colman, S.M., and Watson, K., 1983. Ages estimated from a diffusion equation model for scarp degradation, *Science*, **221**, 263-265.

Condie, K.C., and Rosen, O.M., 1994. Laurentia-Siberia connection revisited, *Geology*, **22**, 168-170.

Cook, F., and Varsek, J.L., 1994. Orogen-scale decollements, *Rev. Geophys.*, **32**, 37-60.

Corsini, M., Vauchez, A., Archanjo, C., and de Sá, E.F.J., 1991. Strain transfer at continental scale from a transcurrent shear zone to a transpressional fold belt: the Patos-Seridó system, northeastern Brazil, *Geology*, **19**, 586-589.

Cowan, D.S., 1994. Alternative hypotheses for the mid-Cretaceous paleogeography of the western Cordillera, *GSA Today*, **4**, 181-186.

Dahlen, F.A., 1984. Noncohesive critical Coulomb wedges: An exact solution, *J. geophys. Res.*, **89**, 10215-10133.

Dahlen, F.A., and Barr, T.D., 1989. Steady-state mountain building 1. Deformation and mechanical energy balance, *J. geophys. Res.*, 3906-3922.

Dahlen, F.A., and Suppe, J., 1988. Mechanics, growth and erosion of mountain belts, *Geol. Soc. Am. Spec. Paper* , **218**, 161-178.

Davis, D., Suppe, J., and Dahlen, F.A., 1983. Mechanics of fold-and-thrust belts and accretionary wedges, *J. geophys. Res.*, **88**, 1153-1172.

Decourt, J, and 18 others, 1986. Geological evolution of the Tethys belt from the Atlantic to the Pamirs since the Lias, *Tectonophys.*, **123**, 241-315.

DeMets, C., Gordon, R.G., Argus, D.F., and Stein, S., 1990. Current plate motions, *Geophys. J. Int.*, **101**, 425-478.

Dewey, J.F., 1988. Extensional collapse of orogens, *Tectonics*, **7**, 1123-1139.

Dewey, J.F., Shackleton, R.M., Chengfa, C., and Yiyin, S., 1988. The tectonic evolution of the Tibetan Plateau, *Phil. Trans. R. Soc. Lond.*, **327**, 379-413.

Dewey, J.F., Helman, M.L., Turco, E., Hutton, D.H.W., and Knott, S.D., 1989a. Kinematics of the western Mediterranean, In: *Alpine Tectonics*, GSA Spec. Publ. **45**, 265-283.

Dewey, J.F., Cande, S., and Pitman, W.C., 1989b. Tectonic evolution of the India/Eurasia collision zone, *Eclogae geol. Helv.*, **82**, 717-734.

Dewey, J.F. and Lamb, S.H., 1992. Active tectonics of the Andes, *Tectonophys.*, **205**, 79-95.

Dietrich, W.E., Wilson, C.J., Montgomery, D.R., and Romy Bauer, J.M., 1992. Erosion thresholds and land surface morphology, *Geology*, **20**, 675-679.

Doglioni, C., 1992. Main differences between thrust belts, *Terra Nova*, **4**, 152-164.

Dongarra, J.J., Bunch, J.R., Moler, C.B., and Stewart, G.W., 1979. *Linpack Users Guide*, Society for Industrial and Applied Mathematics, Philadelphia.

Dymkin, A.M., and Puchkov, V.N., 1984. Ancient Urals- new problems, *Episodes*, **7**, 33-37.

Ellis, S., Fullsack, P., and Beaumont, C., 1995. Oblique convergence of the crust driven by basal forcing: implications for length-scales of deformation and strain partitioning in orogens, *Geophys. J. Int.*, **120**, 24-44.

England, P., Houseman, G. and Sonder, L., 1985. Length scales for continental deformation in convergent, divergent, and strike-slip environments: analytical and approximate solutions for a thin viscous sheet model, *J. geophys. Res.*, **90**, 4797-4810.

England, P. and Houseman, G., 1985. The influence of lithospheric strength heterogeneities on the tectonics of Tibet and surrounding regions, *Nature*, **315**, 297-301.

England, P. and Houseman, G., 1986. Finite strain calculations of continental deformation. 2. Comparison with the India-Asia collision zone, *J. geophys. Res.*, **91**, 3664-3676.

England, P. and Houseman, G., 1988. The mechanics of the Tibetan Plateau, *Phil. Trans. R. Soc. Lond.*, **326**, 301-319.

England, P. and Houseman, G., 1989. Extension during continental convergence, with application to the Tibetan Plateau, *J. geophys. Res.*, **94**, B12, 17561-17579.

England, P. and Jackson, J., 1989. Active deformation of the continents, *Ann. Rev. Earth Planet. Sci.*, **17**, 197-226.

England, P. and McKenzie, D., 1982. A thin viscous sheet model for continental deformation, *Geophys. J. R. astr. Soc.*, **70**, 295-321.

England, P. and McKenzie, D., 1983. Correction to: a thin viscous sheet model for continental deformation, *Geophys. J. R. astr. Soc.*, **73**, 523-532.

England, P., and Molnar, P., 1991. Inferences of deviatoric stress in actively deforming belts from simple physical models, *Phil. Trans. R. Soc. Lond.*, **337**, 151-164.

England, P., and Searle, M.P., 1986. The Cretaceous-Tertiary deformation of the Lhasa Block and its implications for crustal thickening in Tibet, *Tectonics*, **5**, 1-14.

England, P., and Thompson, A.B., 1984. Pressure-Temperature-time paths of regional metamorphism I. Heat transfer during the evolution of regions of thickened continental crust, *J. Petrology*, **25**, 894-928.

Etheridge, M.A., Rutland, R.W.R., and Wyborn, L.A.I., 1987. Orogenesis and tectonic process in the early to middle Proterozoic of northern Australia, In: *Precambrian lithospheric evolution* (edited by Kröner, A.), AGU Geodyn. Ser., **17**, 131-147.

Evans, B., and Dresen, G., 1991. Deformation of Earth materials - 6 easy pieces, *Rev. Geophys.*, **29**, 823-843.

Fitch, T.J., 1972. Plate convergence, transcurrent faulting and internal deformation adjacent to Southeast Asia and Western Pacific, *J. geophys. Res.*, **77**, 4432-4460.

Flemings, P.B., and Jordan, T.E., 1989. A synthetic stratigraphic model of foreland basin development, *J. geophys. Res.*, **94**, 3851-3866.

Forsyth, D., and Uyeda, S., 1975. On the relative importance of the driving forces of plate motion, *Geophys. J. R. astr. Soc.*, **43**, 163-200.

Fullsack, P., 1995. An arbitrary Lagrangian-Eulerian formulation for creeping flows and applications in tectonic models, *Geophys. J. Int.*, **120**, 1-24.

Furlong, K.P., and Hugo, W.D., 1989. Geometry and evolution of the San Andreas fault zone in northern California, *J. geophys. Res.*, **94**, 3100-3110.

Furlong, K.P., 1993. Thermal-rheologic evolution of the upper mantle and the development of the San Andreas fault system, *Tectonophys.*, **223**, 149-164.

Garfunkel, Z., 1981. Internal structure of the Dead Sea leaky transform (rift) in relation to plate kinematics, *Tectonophys.*, **80**, 81-108.

Garfunkel, Z., Zak, I., and Freund, R., 1981. Active faulting in the Dead Sea rift, *Tectonophys.*, **80**, 1-26.

Goetze, C., and Evans, B., 1979. Stress and temperature in the bending lithosphere as constrained by experimental rock mechanics, *Geophys. J. R. Astr. Soc.*, **59**, 463-478.

Handy, M.R., 1989. Deformation regimes and the rheological evolution of fault zones in the lithosphere; the effects of pressure, temperature, grainsize and time, *Tectonophys.*, **163**, 119-152.

Handy, M.R., 1990. The solid-state flow of polymineralic rocks, *J. geophys. Res.*, **95**, 8647-8661.

Handy, M.R., 1994. Flow laws for rocks containing two non-linear viscous phases: a phenomenological approach, *J. Struct. Geol.*, **16**, 287-301.

Hanks, T.C., Bucknam, R.C., Lajoie, K.R., and Wallace, R.E., 1984. Modification of wave-cut and faulting-controlled landforms, *J. geophys. Res.*, **89**, 5771-5790.

Hanmer, S., and Lucas, S.B., 1985. Anatomy of a ductile transcurrent shear: the Great Slave Lake shear zone, District of MacKenzie, NWT (preliminary report), In: *Current research, Part B*, GSC paper **85-1B**, 7-22.

Hempton, M.R., 1987. Constraints on Arabian plate motion and extensional history of the Red Sea, *Tectonics*, **6**, 687-705.

Hirth, G., and Tullis, J., 1992. Dislocation creep regimes in quartz aggregates, *J. Struct. Geol.*, **14**, 2, 145-159.

Hirth, G and Tullis, J., 1994. The brittle-plastic transition in experimentally deformed qu aggregates, *J. geophys. Res.*, **99**, 11731-11747.

Hoffman, P.F., 1987. Early Proterozoic foredeeps, foredeep magmatism, and Superior-type iron-formations of the Canadian Shield, In: *Proterozoic Lithospheric Evolution* (edited by Kroner, A.), AGU Geodyn. Ser., **17**, 85-98.

Hoffman, P.F., 1988. United plates of America, the birth of a craton: early Proterozoic assembly and growth of Laurentia, *Ann. Rev. Earth Planet. Sci.*, **16**, 543-603.

Hoffman, P.F., 1989. Precambian geology and tectonic history of North America, In: *The Geology of North America- an Overview* (edited by Bally, A.W. and Palmer, A.R.), GSA, 447-512.

Hoffman, P.F. and Grotzinger, J.P., 1993. Orographic precipitation, erosional unloading, and tectonic style, *Geology*, **21**, 195-198.

Hoffman, P.F., 1991. Did the breakout of Laurentia turn Gondwanaland inside out? *Science*, **252**, 1409-1412.

Houseman, G. and England, P., 1986. Finite strain calculations of continental deformation 1. method and general results for convergent zones, *J. geophys. Res.*, **91**, 3651-3663.

Houseman, G., McKenzie, D., and Molnar, P., 1981. Convective instability of a thickened boundary layer and its relevance for the thermal evolution of continental convergent belts, *J. geophys. Res.*, **86**, 6115-6132.

Irwin, W.P., 1990. Chapter 3, Geology and plate development, In: *The San Andreas Fault System*, U.S. Geol. Surv. Prof. paper **1515**, 61-80.

Isacks, B.L., 1988. Uplift of the central Andean Plateau and bending of the Bolivian Orocline, *J. geophys. Res.*, **93**, 3211-3231.

Jackson, J.A., 1992. Partitioning of strike-slip and convergent motion between Eurasia and Arabia in Eastern Turkey and the Caucasus, *J. geophys. Res.*, **97**, 12471-12479.

Jackson, J.A., and McKenzie, D.P, 1984. Active tectonics of the Alpine-Himalayan belt between western Turkey and Pakistan, *Geophys. J. R. Astron. Soc.*, **77**, 185-264.

Jadoon, I.A.K., Lawrence, R.D., and Lillie, R.J., 1994. Seismic data, geometry, evolution, and shortening in the active Sulaiman fold-and-thrust belt of Pakistan, southwest of the Himalayas, *AAPG Bulletin*, **78**, 758-774.

Jaeger, J.C., and Cook, N.G.W., 1979. *Fundamentals of rock mechanics*, (3rd ed.), Chapman and Hall, London.

Jamieson, R.A., and Beaumont, C., 1988. Orogeny and metamorphism: a model for deformation and pressure-temperature-time paths with application to the central and southern Appalachians, *Tectonics*, **7**, 417-445.

Jamieson, R.A., and Beaumont, C., 1989. Deformation and metamorphism in convergent orogens: a model for uplift and exhumation in metamorphic terrains, In: *Evolution of Metamorphic Belts* (edited by Daly, J. S., et al.), Geol. Soc. Spec. Publ., **43**, 117-129.

Johnson, D. D., and Beaumont, C., 1995. Preliminary results from a planform kinematic model of orogen evolution, surface processes, and the development of clastic foreland basin stratigraphy, In: *SEPM Spec. Publ. on stratigraphic development in foreland basins* (edited by Dorobek, S., and Ross, G.), in press.

Johnston, C.R., and Bowin, C.O., 1981. Crustal reactions resulting from the mid-Pliocene to Recent continent-island arc collision in the Timor region, *BMR J. Austr. Geol. Geophys.*, **6**, 223-243.

Jordan, T.E., Isacks, B.L., Allmendinger, R.W., Brewer, J.A., Ramos, V.A., and Ando, C.J., 1983. Andean tectonics related to geometry of the subducted Nazca plate, *Geol. Soc. Am. Bull.*, 341-361.

Kamp, P.J.J., 1986. The mid-Cenozoic Challenger Rift System of western New Zealand and its implications for the age of Alpine fault inception, *Geol. Soc. Am. Bull.*, **97**, 255-281.

Karig, D.E., Barber, A.J., Charlton, T.R., Klemperer, S., and Hussong, D.M., 1987. Nature and distribution of deformation across the Banda Arc-Australian collision zone at Timor, *Geol. Soc. Am. Bull.*, **98**, 18-32.

Kazmi, A., 1979. Active fault systems of Pakistan, In: *Geodynamics of Pakistan* (edited by Farah, A., and DeJong, K.A.), Geological Survey of Pakistan, Quetta, 285-294.

Kiratzi, A.A., 1993. A study on the active crustal deformation of the North and East Anatolian Fault Zones, *Tectonophys.*, **225**, 191-203.

Kirby, S.H., 1985. Rock mechanics observations pertinent to the rheology of the continental lithosphere and the localization of strain along shear zones, *Tectonophys.*, **119**, 1-27.

Kooi, H., and Beaumont, C., 1994. Escarpment evolution on high-elevation rifted margins; insights derived from a surface processes model that combines diffusion, advection and reaction, In: *J. geophys. Res special issue on Tectonics and Topography,* **99**, 12191-12209.

Koons, P.O., 1990. The two-sided orogen: collision and erosion from the sandbox to the Southern Alps, New Zealand, *Geology*, **18**, 679-682.

Kukla, P.A., and Stanistreet, I.G., 1991. Record of the Damaran Khomas accretionary prism in central Namibia: refutation of an "ensialic" origin of a Late Proterozoic orogenic belt, *Geology*, **19**. 473-476.

Lawrence, R.D., Khan, S.H., DeJong, K.A., Farah, A., and Yeats, R.S., 1981. Thrust and strike slip fault interaction along the Chaman transform zone, Pakistan, In: *Thrust and Nappe Tectonics* (edited by McClay, K.R. and Price, N.J.), Geol. Soc. Lond. Spec. Publ., **9**, 363-370.

Lefort, J.-P., 1989. *Basement correlation across the North Atlantic*, (English Edition translated by Carpenter, M.S.N.), Springer-Verlag, 148pp.

Lefort, J.-P., 1993. Image globale de la croûte continentale française entre le Brabant et le Pays Basque, [Global image of the French Continental crust between Brabant and the Basque Country], *Bull. Centres Rech. Explor.-Prod. Elf Aquitaine*, **17**, 39-52.

Li, J., Li, B., Wang, F., Zhang, Q., Wen, S., and Zheng, B., 1981. The process of the uplift of the Qinghai-Xizang Plateau, In: *Geological and Ecological Studies of Qinghai-Xizang Plateau*, Beijing, Science Press, **1**, 111-118.

Lobkovsky, L. I. and Kerchman, V.I., 1991. A two-level concept of plate tectonics; applications to geodynamics, In: *The achievements of plate tectonics in the USSR* (edited by Zonenshain, L.P.), Tectonophys., **199**, 343-374.

Lu, C-Y., and Malavieille, J., 1994. Oblique convergence, indentation and rotation tectonics in the Taiwan Mountain Belt: insights from experimental modelling, *Earth Planet. Sci. Letters*, **121**, 477-494.

Malavieille, J., 1984. Modélisation expérimentale des chevauchements imbriqués: Application aux chaînes des montagnes, *Societe Geologique de France Bulletin*, **26**, 129-138.

Mandl, G., 1988. *Mechanics of tectonic faulting*, Developments in Structural Geology 1, Elsevier, 407pp.

McCaffrey, R., and Abers, G.A., 1991. Orogeny in arc-continent collision; the Banda arc and western New Guinea, *Geology*, **19**, 563-566.

McCaffrey, R., 1992. Oblique plate convergence, slip vectors, and forearc deformation, *J. geophys. Res.*, **97**, 8905-8915.

McKenzie, D.P., and Jackson, J., 1983. The relationship between strain rates, crustal thickening, paleomagnetism, finite strain and fault movements within a deforming zone, *Earth Planet. Sci. Lett.*, **65**, 182-202.

Mengel, F., and Rivers, T., 1991. Decompression reactions and P-T conditions in high-grade rocks, Northern Labrador: P-T-t paths from individual samples and implications for Early Proterozoic tectonic evolution, *J. Petrol.*, **32**, 139-167.

Mercier, J., Armijo, R., Tapponnier, P., Carey-Gailhardis, E., and Lin, H.T., 1987. Change from late Tertiary compression to Quaternary extension in southern Tibet during the India-Asia collision, *Tectonics*, **6**, 275-304.

Minster, J.B., and Jordan, T.H., 1978. Present-day plate motions, *J. geophys. Res.*, **83**, 5331-5354.

Molnar, P. and Tapponnier, P., 1975. Cenozoic tectonics of Asia: effects of a continental collision, *Science*, **189**, 419-426.

Molnar, P., and Tapponnier, P., 1977. Relation of the tectonics of eastern China to the India-Eurasia collision; application of slip-line field theory to large-scale continental tectonics, *Geology*, **5**, 212-216.

Molnar, P., Burchfiel, B.C., Liang, K-U., and Zhao, Z., 1987. Geomorphic evidence for active faulting in the Altyn Tagh and northern Tibet and qualitative estimates of its contribution to the convergence of India and Eurasia, *Geology*, **5**, 249-253.

Molnar, P., 1992. Brace-Goetze strength profiles, the partitioning of strike-slip and thrust faulting at zones of oblique convergence, and the stress-heat flow paradox of the San Andreas fault, In: *Fault Mechanics and Transport Properties of Rocks*, Academic Press Ltd, 435-459.

Molnar, P., England, P., and Martinod, J., 1993. Mantle dynamics, uplift of the Tibetan Plateau, and the Indian Monsoon, *Rev. Geophys.*, **31**, 357-396.

Moore, J.M., 1979. Tectonics of the Najd transcurrent fault system, Saudi Arabia, *J. Geol. Soc. London*, **136**, 441-454.

Moretti, I., and Turcotte, D. L., 1985. A model for erosion, sedimentation, and flexure with applications to New Caledonia, *J. Geodyn.*, **3**, 155-168.

Muñoz, J.A., 1992. Evolution of a continental collision belt: ECORS-Pyrenees crustal balanced cross-section, In: *Thrust Tectonics* (edited by McClay, K.R.), 235-246, Chapman and Hall.

Myers, J., 1990. Precambrian tectonic evolution of part of Gondwana, southwestern Australia, *Geology*, **18**, 537-540.

Nash, D.B., 1980. Forms of bluffs degraded for different lengths of time in Emmet County, Michigan, U.S.A., *Earth Surf. Proc.*, **5**, 331-345.

Norrie, D. H., and deVries, G., 1978. *An introduction to finite element analysis*, Academic Press, 301pp.

Norris, R.J., Koons, P.O., and Cooper, A.F., 1990. The obliquely-convergent plate boundary in the South Island of New Zealand: Implications for ancient collision zones, *J. Struc. Geol.*, **12**, 715-725.

Oldow, J.S., Bally, A.W., Lallement, H.G.A., and Leeman, W.P., 1989. Phanerozoic evolution of the North American Cordillera; United States and Canada, In: *The Geology of North America- an Overview* (edited by Bally, A.W., and Palmer, A.R.), GSA, 139-232.

Oral, M.B., Reilinger, R.E., Toksöz, M.N., King, R.W., Barka, A.A, Kinik, I., and Lenk, O., 1995. Global positioning system offers evidence of plate motions in eastern Mediterranean, *EOS, Transactions, AGU*, **76**, 9-11.

Ord, A. and Hobbs, B.E., 1989. The strength of the continental crust, detachment zones and the development of plastic instabilities, In: *Deformation of Crustal Rocks* (edited by Ord, A.), Tectonophys., **158**, 269-289.

Paola, C., Heller, P. L., and Angevine, C. L., 1992. The large-scale dynamics of grain-size variation in alluvial basins, 1: Theory, *Basin Research*, **4**, 73-90.

Paterson, M.S., 1990. *Deformation mechanisms, rheology and tectonics, Geol. Soc. Spec. Publ.*, **54**, 299.

Peltzer, G., and Tapponnier, P., 1988. Formation and evolution of strike-slip faults, rifts, and basins during the India-Asia collision: an experimental approach, *J. geophys. Res.*, **93**, 15085-15118.

Philip, H., Cisternas, A., Gvishiani, A., and Gorshkov, A., 1989. The Caucasus: an actual example of the initial stages of a continental collision, *Tectonophys.*, **161**, 1-21.

Platt, J.P., Leggett, J.K., Young, J., Raza, H. and Alam, S., 1986. Dynamics of orogenic wedges and the uplift of high-pressure metamorphic rocks, *GSA Bull.*, **97**, 1037-1053.

Platt, J., 1993. Mechanics of oblique convergence, *J. geophys. Res.*, **98**, 16239-16256.

Pohl, W., 1987. Metallogeny of the northeastern Kibaran belt, Central Africa, *Geol. J.*, **22**, 103-119.

Ranalli, G., 1987. *Rheology of the Earth*, Allen and Unwin, 366pp.

Ranalli, G. and Murphy, D.C., 1987. Rheological stratification of the lithosphere, *Tectonophys.*, **132**, 281-295.

Reinhardt, E.W., 1969. Geology of the Precambrian rocks of Thubin Lakes map area in relationship to the McDonald Fault system, District of MacKenzie, *Geol. Survey of Canada Paper* **69-21**, 29pp.

Ricou, L-E., 1994. Tethys reconstructed: plates, continental fragments and their boundaries since 260 Ma from central America to south-eastern Asia, *Geodin. Acta*, **7**, 169-218.

Royden, L.H., and Burchfiel, B.C., 1989. Are systematic variations in thrust belt style related to plate boundary processes? (The Western Alps versus the Carpathanians), *Tectonics*, **8**, 51-61.

Royden, L. H., 1993a. The tectonic expression of slab pull at continental convergent boundaries, *Tectonics*, **12**, 303-325.

Royden, L.H., 1993b. Evolution of retreating subduction boundaries formed during continental collision, *Tectonics*, **12**, 629-638.

Royden, L.H., submitted. Coupling and decoupling of crust and mantle in convergent orogens: implications for strain partitioning in the crust.

Rutter, E.H., and Brodie, K.H., 1988. Experimental "syntectonic" dehydration of serpentinite under conditions of controlled pore water pressure, *J. geophys. Res.*, **93**, 4907-4932.

Rutter, E.H., and Brodie, K.H., 1991. Lithosphere rheology- a note of caution, *J. Struct. Geol.*, **13**, 363-367.

Ryzhiy, B.P., Druzhinin, V.S., Yunusov, F.F., and Ananyin, I.V., 1992. Deep structure of the Urals region and its seismicity, *Phys. Earth Planet. Int.*, **75**, 185-191.

Salel, J.F., and Séguret, M., 1994. Late Cretaceous to Palaeogene thin-skinned tectonics of the Palmyrides belt (Syria), *Tectonophys.*, **234**, 265-290.

Shackleton, R.M., and Chengfa, C., 1988. Cainozoic uplift and deformation of the Tibetan Plateau; the geomorphological evidence, In: *The geological evolution of Tibet; report of the 1985 Royal Society- Acadima Sinica geotraverse of the Qinghai-Xizang Plateau* (edited by Chengfa, C., et al.), Acad. Sin., Beijing, China, Phil. Trans. R. Soc. Lond., **327**, 365-377.

Shelton, G., and Tullis, J., 1981. Experimental flow laws for crustal rocks, *EOS*, **62**, 396.

Sibson, R.H., 1982. Fault zone models, heat flow and the depth distribution of earthquakes in the continental crust, *Bull. seism. Soc. Am.*, **72**, 151-163.

Smith, R.I., 1990. Tertiary plate tectonic setting and evolution of Papua New Guinea, In: *Proc. 1st PNG Petroleum Convention* (edited by Carman, G.J.), Port Moresby, 229-244.

Sonder, L., England, P. and Houseman, G., 1986. Continuum calculations of continental deformation in transcurrent environments, *J. geophys. Res.*, **94**, 10331-10346.

Sonder, L.J., and England, P., 1986. Vertical averages of rheology of the continental lithosphere: relation to thin sheet parameters, *Earth Planet. Sci. Letters*, **77**, 81-90.

Stein, R.S., and Yeats, R.S., 1989. Hidden earthquakes, *Sci. Am.*, **260**, 48-57.

Stern, R.J., 1985. The Najd fault system, Saudi Arabia and Egypt: A Late Precambrian rift-related transform system?, *Tectonics*, **4**, 497-511.

Stockmal, G.S., 1983. Modelling of large scale accretionary wedge deformation, *J. geophys. Res.*, **88**, 8271-8287.

Strehlau, J., and Meissner, R., 1987. Estimation of crustal viscosities and shear stresses from an extrapolation of experimental steady-state flow data, In: *Composition, Stucture, and Dynamics of the Lithosphere-Asthenosphere System* (edited by Fuchs, K., and Froidevaux, C.), Geodynamics series 16.

Suárez, G., Molnar, P., and Burchfiel, B.C., 1983. Seismicity, fault plane solutions, depth of faulting, and active tectonics of the Andes of Peru, Ecuador, and southern Colombia, *J. geophys. Res.*, **88**, 10403-10428.

Sultan, M., Arvidson, R.E., Duncan, I.J., Stern, R.J., and Kaliouby, B.E., 1988. Extension of the Najd shear system from Saudi Arabia to the central eastern desert of Egypt based on integrated field and Landsat observations, *Tectonics*, **7**, 1291-1306.

Suppe, J., 1987. The active Taiwan mountain belt, In: *The Anatomy of Mountain Ranges*, Princeton University Press, 277-293.

Tao, W.C., and O'Connell, R.J., 1992. Ablative subduction: a two-sided alternative to the conventional subduction model, *J. geophys. Res.*, **97**, 8877-8904.

Tapponnier, P. and Molnar, P., 1976. Slip-line theory and large scale continental tectonics, *Nature*, **264**, 319-324.

Tapponnier, P., Peltzer, G., Le Dain, A.Y., Armijo, R., and Cobbold, P., 1982. Propagating extrusion tectonics in Asia: new insights from simple experiments with plasticine, *Geology*, **10**, 611-616.

Tikoff, B., and Teyssier, C., 1994. Strain modeling of displacement-field partitioning in transpressional orogens, *J. Sruct. Geol.*, **16**, 1575-1588.

Trümpy, R., 1980. *Geology of Switzerland, a guidebook, part A: An outline of the geology of Switzerland*, Wepf and Company, Basel, Switzerland.

Turcotte, , D. L. and Schubert, G., 1982. *Geodynamics- Applications of continuum physics to geological problems*, John Wiley and Sons, New York.

Tyler, I.M., and Thorne, A.M., 1990. The northern margin of the Capricorn orogen, Western Australia- an example of an early Proterozoic collision zone, *J. Struct. Geology*, **12**, 685.

Unrug, R., 1992. The supercontinent cycle and Gondwanaland assembly: component cratons and the timing of suturing events, *J. Geodyn.*, **16**, 215-240.

Van Kranendonk, M.J., St-Onge, M.R., and Henderson, J.R., 1993. Paleoproterozoic tectonic assembly of northeast Laurentia through multiple indentations, *Precamb. Res.*, **63**, 325-347.

Vilotte, J. P., Daignieres, M. and Madariaga, R., 1982. Numerical modeling of intraplate deformation: simple mechanical models of continental collision, *J. geophys. Res.*, **87**, 10709-10728.

Walcott, R.I., 1978. Geodetic strains and large earthquakes in the axial tectonic belt of North Island, New Zealand, *J. geophys. Res.*, **83**, 4419-4429.

Walcott, R.I., 1984. The kinematics of the plate boundary zone through New Zealand: a comparison of short- and long-term deformations, *Geophys. J. R. astr. Soc.*, **79**, 613-633.

Walcott, R.I., 1993. Neogene tectonics and kinematics of western North America, *Tectonics*, **12**, 326-333.

Wallace, R.E., 1990. 1. General features, In: *The San Andreas Fault System* (edited by Wallace, R.E.), US Geol. Surv. Prof. Paper **1515**, 3-12.

Walley, C.D., 1988. A braided strike-slip model for the northern continuation of the Dead Sea Fault and its implications for Levantine tectonics, *Tectonophys.*, **145**, 63-72.

Wdowinski, S., O'Connell, R. J. and England, P., 1989. A continuum model of continental deformation above subduction zones: application to the Andes and the Aegean, *J. geophys. Res.*, **94**, 10331-10346.

Westaway, R., 1994. Present-day kinematics of the Middle East and eastern Mediterranean, *J. geophys. Res.*, **99**, 12071-12090.

Willett, S., 1992. Dynamic and kinematic growth and change of a Coulomb wedge, In: *Thrust Tectonics* (edited by McClay, K.R.), Chapman and Hall, 1-18.

Willett, S., Beaumont, C. and Fullsack, P., 1993. A mechanical model for the tectonics of doubly vergent compressional orogens, *Geology*, **21**, 371-374.

Willett, S. and Beaumont, C., 1994. Subduction of Asian lithospheric mantle beneath Tibet inferred from models of continental collision, *Nature*, **369**, 642-645.

Willgoose, G., Bras, R. L., and Rodriguez-Iturbe, I., 1991a. Results from a new model of river basin evolution, *Earth Surf. Proc. Landforms*, **16**, 237-254.

Willgoose, G., Bras, R. L., and Rodriguez-Iturbe, I., 1991b. A coupled channel network growth and hillslope evolution model 1. Theory, *Water Resources Res.*, **27**, 1671-1684.

Wilson, J.T., 1965. A new class of faults and their bearing on continental drift, *Nature*, **207**, 343-347.

Windley, B.F., 1984. *The Evolving Continents*, John Wiley and Sons.

Xu, R., 1981. On paleobotanical evidence for continental drift and the Himalayan uplift, In: *Studies on the Period, Amplitude, and Type of the Uplift of the Qinghai-Xizang Plateau*, Science Press, Beijing, 17-23.

Zhao, W., and Morgan, W. J., 1987. Injection of Indian crust into Tibetan lower crust: a two-dimensional finite element model study, *Tectonics*, **6**, 489-504.

Zeitler, P.K., 1985. Cooling history of the NW Himalaya, Pakistan, *Tectonics*, **4**, 127-151.

Ziegler, P.A., 1988. Post-Hercynian plate reorganization in the Tethys and Arctic-North Atlantic domains, In: *Triassic-Jurassic rifting, continental breakup and the origin of the Atlantic Ocean and passive margins, part B* (edited by Manspeizer, W.), Developments in Geotectonics, **22**, 711-755.

Ziegler, P.A., 1993. Plate-moving mechanisms: their relative importance, *J. Geol. Soc. Lond.*, **150**, 927-940.

Zienkiewicz, O.C., 1977. *The finite element method*, McGraw-Hill, 787pp.

Zonenshain, L.P., Kuzmin, M.I., and Natapov, L.M., 1990. *Geology of the USSR: a plate tectonic synthesis*, AGU Geodynamics Series (Washington), **21**, 242pp.